Modeling, Estimation, and Control of Helicopter Slung Load System

Bisgaard, Morten

Publication date:
2008

Document Version
Publisher's PDF, also known as Version of record

Modeling, Estimation, and Control of Helicopter Slung Load System

Ph.D. thesis

Morten Bisgaard

Department of Electronic Systems
Section for Automation and Control
Aalborg University
Fredrik Bajers Vej 7, 9220 Aalborg East, Denmark

Modeling, Estimation, and Control of Helicopter Slung Load System
Ph.D. thesis

ISBN 87-90664-34-5
November 2007

This thesis was typeset using LaTeX 2_ε in `report` document class.

Preface

This thesis is submitted as partly fulfillment of the requirements for the Doctor of Philosophy at the Section of Automation and Control, Department of Electronic Systems, Aalborg University, Denmark. The work has been carried out in the period September 2004 to November 2007 under the supervision of Associate Professor Jan Dimon Bendtsen and Associate Professor Anders la Cour-Harbo.

Aalborg University, November 2007
Morten Bisgaard

Abstract

Modeling, Estimation, and Control of Helicopter Slung Load System

This thesis treats the subject of autonomous helicopter slung load flight and presents the reader with a methodology describing the development path from modeling and system analysis over sensor fusion and state estimation to controller synthesis. The focus is directed along two different application branches: Generic cargo transport using a helicopter slung load system and landmine clearing using helicopter slung load deployed mine detector. This is reflected in the methodology and contributions of this thesis where some are shared by the two branches and some are specific for each branch.

This first major contribution of this thesis is the development of a complete helicopter and slung load system model that is shared between the two branches. The generic slung load model can be used to model all body to body slung load suspension types and gives an intuitive and easy-to-use way of modeling and simulating different slung load suspension types. It further includes detection and response to wire slacking and tightening, it models the aerodynamic coupling between the helicopter and the load, and can be used for multi-lift systems with any combination of multiple helicopters and multiple loads.

To enable slung load flight capabilities for general cargo transport, an integrated estimation and control system is developed for use on already autonomous helicopters. The estimator uses vision based updates only and needs little prior knowledge of the slung load system as it estimates the length of the suspension system together with the system states. The controller uses a combined feedforward and feedback approach to simultaneously prevent exciting swing and to actively dampen swing in the slung load.

For the mine detection application an estimator is developed that provides full system state information, including slung load heading. A linear trajectory tracking controller for the generic helicopter slung load system is devised using an optimal approach and it can be tuned to any given suspension system. To generate a full system reference for the controller, a trajectory mapping algorithm is developed. It is capable of mapping a desired slung load trajectory to a feasible full state reference based on the dynamic and kinematic system behavior.

The methods and algorithms developed in this thesis are validated by systematic simulation and flight testing, and the results presented throughout the thesis show very good agreement between theory and practice.

Synopsis

Modellering, estimering og kontrol til helikopter slung load system

Denne afhandling omhandler autonom flyvning med helicopter slung load systemer og præsenterer en metodik der beskriver system udvikling fra modellering og system analyse, over sensor fusion og tilstands estimering, til kontroller design. To forskellige udviklingsgrene præsenteres: Flyvning med generisk slung load og landmine detektion med helikopter slung load system.

Et hoved bidrag for denne afhandling er udviklingen af en komplet helikopter og slung load model. Den generiske slung load model kan bruges til at modellere alle body-to-body ophængssystemer og giver en intuitiv måde at modeller og simulerer slung load systemer på. Den inkludere modellering af snor kollaps og kollision, aerodynamisk kobling mellem helikopter og load og kan benyttes til modellering af multibody systemer med flere helikoptere eller flere loads.

Til generel slung load flyvning udvikles et integreret estimator og kontrol system til brug på autonome helikoptere. Estimatoren benytter udelukkende vision baserede målinger og behøver kun lidt information om selve systemet da den estimere den vigtigste system parameter, længden på ophængssnoren, sammen med system tilstandende. Kontrolleren benytter en kombineret feedforward og feedback fremgangsmåde til at undgå at eksitere og samtidigt aktivt undertrykke load svingninger.

Til minedetektion udvikles en estimator der giver full tilstandsinformation for helikopter slung load systemet, inklusiv slung load attitude. En linear kontroller til tracking af trajektorier udvikles udvilkes til et generisk helikopter slung load system. Til generering af en reference vektor til kontrolleren udvikles en trajektorie mapping algoritme. Denne er i stand til at mappe en givet slung load trajektorie til en fuld system reference baseret på systemets dynamiske og kinematiske egenskaber.

Metoder og algoritmer udviklet i denne afhandling er valideret gennem systematisk simulering og test flyvning, og resultaterne der præsenteres viser god overenstemmelse mellem teori og praksis.

Acknowledgments

I would like to acknowledge my supervisors Jan Dimon Bendtsen and Anders la Cour-Harbo for their continuous support and guidance during the past three years and for being patient with my sometimes intensive involvement in other projects. Jan has been a great help in solving many theoretical problems encountered during this research. A special acknowledgment is due for the huge dedication of Anders to the helicopter project. Without his many hours working in the laboratory the helicopter would not be flying today and without his dedication to learning the art of helicopter flying there would be no one to fly it. Thanks!

I would like thank everyone, students as well as employees at Aalborg University and others, who have helped at flight tests and with the development of the helicopter. A special thanks goes to my office-mate and colleague Lars Alminde for many great discussions of crazy ideas over the years.

I was a guest at Georgia Institute of Technology during the summer 2006 and I would like to thank Professor Eric Johnson for making this stay possible. Thanks are due to the entire team working on the GTMax for helping me with flight testing the slung load and finally I would like to say thanks to office-mates at Georgia Tech for making the stay highly enjoyable.

Finally the greatest acknowledgment goes to Jannie for her support and patience during these three long years.

Contents

Nomenclature

General Nomenclature

m	Mass
g	Gravitational acceleration
$\boldsymbol{\omega}$	Angular velocity vector
$\boldsymbol{v}$	Translational velocity vector
$\boldsymbol{a}$	Translational acceleration vector
$\boldsymbol{\alpha}$	Angular acceleration vector
$\boldsymbol{T}_{be}$	Transformation matrix from e to b
$\boldsymbol{\theta}$	Euler angle vector ($[\phi \;\; \theta \;\; \psi]^T$)
$\boldsymbol{R}$	Position vector ($[x \;\; y \;\; z]^T$)
$_b$	General body coordinate system index
$_h$	Helicopter body coordinate system index
$_l$	Load body coordinate system index
$_e$	Earth fixed coordinate system index
$_{mr}$	Main rotor coordinate system index
$_{tr}$	Tail rotor coordinate system index
$\tilde{x}$	Measurement of x
$\hat{x}$	Estimate of x
$\bar{x}$	Reference of x
$\dot{x}$	Time derivative of x

Helicopter Modelling Nomenclature

$\boldsymbol{X}$	System state vector
Ω	Rotor angular velocity vector ($[\Omega_{mr} \;\; \Omega_{tr}]^T$)
$\boldsymbol{S}$	Actuator input vector ($[S_{\text{col}} \;\; S_{\text{lat}} \;\; S_{\text{lon}} \;\; S_{\text{tr}}]^T$)
$\theta_{\text{col}}, \theta_{\text{lat}}, \theta_{\text{lon}}, \theta_{tr}$	Collective, lateral cyclic, longitudinal cyclic and tail collective pitch
$\theta_{lat,mr}, \theta_{lon,mr}$	Bell-Hiller adjusted main rotor cyclic pitch
K_g	Gyro controller P gain
ω_{tail}	Input reference to gyro controller

$\boldsymbol{a}_{mr}$	Main rotor flapping angle vector ($[a_{\text{con}}\ a_{\text{lat}}\ a_{\text{lon}}]^T$)
$\boldsymbol{a}_{st}$	Stabilizer bar flapping angle vector ($[a_{\text{lat,st}}\ a_{\text{lon,st}}]^T$)
ω_{tail}	Yaw rate tail gyro reference
R_{mr}	Main rotor radius
R_{tr}	Tail rotor radius
θ_r	Local blade element pitch
θ_t	Blade twist angle
r	Distance to blade element
b	Number of blades
φ	Blade azimuth station
e	Virtual hinge offset
β	Blade flapping angle
C_L	Blade coefficient of lift
α	Blade angle of attack
c	Blade cord
U_p, U_t	Vertical and horizontal blade velocity
ρ	Air density
γ	Blade lock number
M_b, I_b	First and second blade mass moment
F	General force
D	Drag force
T, C_T	Thrust force and dimensionless thrust coefficient
p	Pressure
χ_s	Wake skew angle
λ, λ_{tr}	Main and tail rotor induced inflow ratio
v_i	Induced inflow
μ	Rotor advance ratio
K_s	Blade restrain constant
Ri, R_o	Stabilizer bar paddle inner and outer radius
K_B, K_H	Bell and Hiller gain
A	Area
d	Drag coefficient
K_{tf}	Factor of tail fin in tail rotor wake
$\boldsymbol{D}, \boldsymbol{K}, \boldsymbol{J}, \boldsymbol{E}, \boldsymbol{G}$	Flapping equation matrices
$\boldsymbol{R}_{fw}$	Position of the far wake relative to helicopter hub
$\boldsymbol{R}_{wl}$	Position of load relative to the far wake
$\boldsymbol{V}^{'}$	Near wake velocity vector
$\boldsymbol{V}^{''}$	Far wake velocity vector
R_{ma}	Wake cross section major axis radius
R_{mi}	Wake cross section minor axis radius
K_{con}	Wake contraction factor
w	Wake coordinate system index

Slung Load Modelling Nomenclature

$\boldsymbol{M}$	Positive definite symmetric generalised mass matrix
$\boldsymbol{Q}$	Generalised force vector
$\boldsymbol{A}$	Jacobian of the constraint function
$\boldsymbol{q}$	Generalised coordinates
$\boldsymbol{b}$	Acceleration independent part of constraint function
$\boldsymbol{L}$	Wire vector
$\boldsymbol{I}$	Inertia tensor
$\boldsymbol{F}$	Force vector
$\boldsymbol{\tau}$	Torque vector
$\boldsymbol{N}$	Normalised wire vector
$\boldsymbol{a}_n$	Numerical correction term
g	Constraint equation
J	Impulse
k_s	Numerical correction spring constant
c_d	Numerical correction damper constant
K_e	Collision elasticity constant
l	Length of wire
$_c$	Constrained index
$_u$	Unconstrained index
$_i$	Wire number index
$_j$	Helicopter number (in multi-lift systems) index
$_1$	Before collision index
$_2$	After collision index
$_n$	Number of system coordinates index
$_m$	Number of constraints index

Model Analysis and Verification Nomenclature

ξ	Flight condition ($[V \;\; \gamma_w \;\; \gamma_{\text{fp}} \;\; \dot{\psi}_{\text{trim}}]^T$)
V	Flight condition speed
γ_w	Flight condition sideslip angle
γ_{fp}	Flight condition plane angle
$\dot{\psi}_{\text{trim}}$	Flight condition yaw angular velocity

State Estimation and Sensor Fusion Nomenclature

θ_p, ϕ_p	Slung load angles (vision system)
p_y, p_z	Slung load pixel position
D_p	Pixel position to slung load

α_{FOV}	Camera field of view
P_{FOV}	Number of pixels related to α_{FOV}
$\boldsymbol{R}_{cl}$	Position of load relative to camera
ψ_{cam}	Vision system measured slung load yaw
$\boldsymbol{\mathcal{X}}, \boldsymbol{\mathcal{Z}}$	State and measurement sigma point
$\hat{\boldsymbol{x}}, \hat{\boldsymbol{z}}$	Predicted state and measurement vector
W	Sigma point weight
$\lambda_u, \beta_u, \alpha_u, \kappa_u$	UKF scaling parameters
$\boldsymbol{P}$	Covariance matrix
$\boldsymbol{K}$	Kalman gain
$\boldsymbol{B}$	Bias vector
$\tilde{\boldsymbol{R}}_{\text{gps}}$	GPS position measurement
$\tilde{\boldsymbol{v}}_{\text{gps}}$	GPS velocity measurement
$\tilde{\boldsymbol{M}}_{\text{mag}}$	Magnetometer measurement
$\tilde{\boldsymbol{W}}_{\text{virt}}$	Virtual wire sensor measurement
$\boldsymbol{M}_{ref}$	Magnetic field reference
$\boldsymbol{v}_w$	External wind
$\tilde{\boldsymbol{a}}_{\text{IMU}}$	IMU acceleration measurement
$\tilde{\boldsymbol{\omega}}_{\text{IMU}}$	IMU rate measurement
θ_w, ϕ_w	Slung load wire angles

Slung Load Swing Damping Control Nomenclature

$\mathcal{V}$	Residual vibration
λ_i	The i'th eigenvalue
ω_{ni}	Eigenvalue i natural frequency
ζ_i	Eigenvalue i damping
A_i	Amplitude of impulse
$*$	Convolution
τ_d	Controller time delay parameter
G_d	Controller gain parameter

Trajectory Tracking Slung Load Control Nomenclature

$\boldsymbol{e}, \boldsymbol{e}_i$	Error and integral error
L_c, L_i	Controller gains
κ_{λ_i}	Eigenvalue condition number
ν	Slung load swingout angle
r_l	Slung load turn radius
a_{cf}	Centrifugal acceleration
$\delta x, \delta y, \delta z$	Slung load position relative to helicopter

Part I

Introduction

This part gives a general introduction to the background and motivation of this research. A review of the literature in the different fields examined in this thesis is given and a general methodology combining the contributions is presented. Furthermore, it gives an introduction to the two different helicopter test platforms used to verify the contributions of this thesis.

Chapters

Chapter 1

Introduction

This chapter presents the background and motivation for this PhD study and discusses the application of helicopter slung load flight and the problems associated with this. It further introduces landmine detection as a new slung load application and discusses the landmine problem in general. Then the contributions and methodology of this study are presented and finally an outline of the thesis is given.

1.1 Background and Motivation

A helicopter is a highly versatile aerial vehicle and its unique flying characteristics enables an intriguing ability to carry loads hanging in wires underneath the helicopter. Flying with an underslung load is known as either slung load or sling load flight and it is widely used for different kinds of cargo transport, especially since the development of heavy-lift helicopters like the CH-47 Chinook and the CH-54 Skycrane in the middle 1960's. Since then helicopters have been used for a vast number of different towing assignments ranging from fire-fighting applications over animal transport to container-hauling (see figure 1.1). However, flying a slung load can be a very challenging and sometimes hazardous task as a slung load significantly alters the flight characteristics of the helicopter. The pendulum-like behavior of the slung load gives a high risk of pilot induced oscillations that can result in dangerous situations [Hoh *et al.*, 2006]. Furthermore, unstable oscillations can occur at high speeds due to the different aerodynamic shapes of the slung loads. There is therefore, from helicopter pilots and from the aerospace industry in general, a large interest in technologies that can reduce the challenge in operating helicopter slung loads.

This thesis focuses on the development of an autonomous helicopter capable of operating with a slung load. The specific focus areas in this work is taken along two parallel roads. One road will focus on enabling slung load flight in autonomous helicopters for general cargo transport in applications similar to those shown in figure 1.1. The other

Figure 1.1: Top left: UH-60 Black Hawk with a container load. Top right: Eurocopter Super Puma used for fire fighting. Bottom left: Bell 212 with slung load. Bottom right: CH-47 Chinook towing a Lynx fuselage.

road will focus on slung load trajectory tracking in application where full control of the slung load yaw angle is necessary. One such application is described in the next section.

1.2 Landmine Detection

The land mines used in modern warfare can trace their lineage all the way back to the simple non-explosive caltroops employed by the armies of ancient history. The development of the modern landmine started in 1726 when the German military historian H. Frieherr von Flemming invented history's first pressure operated landmine - however in was not until the first world war that the landmine became a widely used weapon in response to the newly developed armored tank. During the second world war the evolution of the landmine accelerated, introducing technologies like the jumping mine and the non-metal mine. During conflicts around the world since the second world war, land mines have been used extensively, most significantly in places like Korea, Vietnam, Angola, Cambodia and Afghanistan, but also countries such as Greece and Denmark figure on the list of mine-affected nations (see figure 1.2 [Human Rights Watch, 2004]).

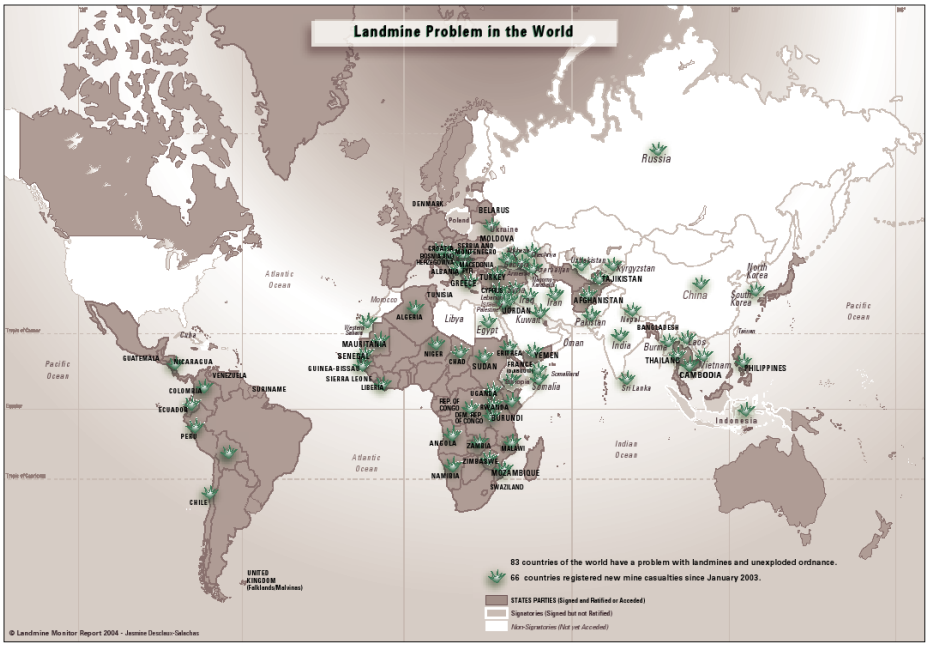

Figure 1.2: A map of the landmine affected nations of the world [Human Rights Watch, 2004].

There is a number of characteristics of the landmine, which makes it a favorable weapon and a global problem. A landmine is a very cheap and simple weapon to produce and deploy, but it is very difficult and expensive to detect and destroy. It is a highly effective defensive weapon which, without great cost or effort, can be used to protect military installations and slow enemy advance through terrain. However, mines do not distinguish between the enemy they were intended for and other people; often innocent civilians becomes the victims (see figure 1.3).

Figure 1.3: Victims of landmines [Human Rights Watch, 2004].

The mines also stay behind to attack the enemy even when the forces that deployed them have retreated. This leads to another major problem with landmine: Their ability to lay dormant and yet operational in the ground for very long periods of time – even long after the conflict they were deployed in has ended. In 1960 a number of simple landmines placed during the American Civil Wars was found – still ready to kill after almost century in the ground [Stephan, 2004]. This means that a mine-affected country cannot easily return to normal peace conditions as the reconstruction can be severely impeded by the mine danger.

More than 300 million mines have been deployed worldwide since 1939 and about 2.5 million more are laid down each year. Since 1975, more than 1 million people have been severely maimed or killed by land mines and 70 more are added each day. Estimates of the cost for removing these mines if the deployment were to be stopped today is in the area of 35 billion US dollars – furthermore with the methods applied today only about 100,000 mines are cleared each year, which means that it will take about 1000 years to clear the mines that are presently in the ground [Human Rights Watch, 2004].

1.2.1 Current Mine Detection Technologies

For a mine detection system the most important parameter is the detection-ratio which must be very close to a 100% in civilian operations (UN standards specific $> 99.6\%$ [McAslan, 2004]) as a missed mine can be lethal for the mine clearing operation and subsequent use of the land. However, also other parameters are of great significance: It is necessary to do the mine detection at a sufficiently high rate in order for the detection method to be of any practical use and it is also very important that the method produces has a very low false detections rate.

Today many different options exist for mine detection and all of them have different kinds of weaknesses. For an in depth discussion of the different technologies and methods either used today or being developed see [Mächler, 1995], [Gros and Bruschini, 1996], and [U.S. Department of Defense, 2001].

A often used and effective method is manually prodding the ground at a shallow angle with a rigid metal probe, but it is very slow (see figure 1.4). Metal detectors has been

Figure 1.4: Mine clearance by hand is a difficult and dangerous job.

extensively used in mine detection and is a very effective method when the mines contain sufficient metal. However, many modern mines contain only very little metal and therefore the metal detector can only be used for certain mine types. Also dogs are used today for mine detection – a trained dog can smell very small amounts of explosives which enables them to detect all mine-types. However, they are very expensive to train and the reliability cannot meet the UN requirements.

One of the best known mine detection and clearance methods is using a plough, roller or flail mounted on a modified tank or truck (see figure 1.5). The method is known as mechanical demining and originates from military use where the objective is to quickly clear a way though a mine field. The equipment for the method is very expensive both to purchase and to maintain and it can only meet the UN requirements in certain terrain types, whereas in other terrain types the efficiency decade dramatically. This approach

Figure 1.5: The demining flail truck build by Hydrema.

has only little correlation with other methods like metal detectors and these can therefore be used in combination to raise the total detection rate.

A common disadvantage of the methods mentioned above is that to deploy them it is necessary to move into the mine field, touch the ground, and thereby risk a accidental mine detonation.

1.2.2 Autonomous Aerial Mine Detection Platform

Using an aerial platform for deploying mine detection equipment has the considerable advantage over a ground based vehicle that it needs no direct contact with the ground and thus yields no risk of the mines being detonated in the detection process. A ground based vehicle must make sure that it does not detonate the mines if it drives on top of them. This can be done by either making sure that the vehicle cannot detonate the mines by only leaving a very light pressure on the ground or by simply driving around the detected mines. Another advantage of an aerial platform over a ground based vehicle is that it is less dependent on the type of terrain that it operates in. In figure 1.6 four different mine infected terrains are shown.

In the first terrain, which is from Afghanistan, the area is open and heavy machinery like the mine flail can be used. The second terrain is from Africa and also exhibit a reasonable open landscape with some vegetation where it is possible to deploy ground base vehicles. The lower left picture shows an obstacle in the terrain from the former Jugoslavia in which most ground based vehicles would not be able to operate. The lower right picture shows a typical area in Asia during the rain season which makes the use of ground based vehicles either extremely difficult or even impossible. An aerial platform would be able to operate in all of these terrains without being affected by the different terrain conditions. The helicopters unique flying characteristics makes it well suited for such an application.

In order for most mine detecting sensors to operate efficiently they must be deployed close to the ground. This operation height can lead to quite dangerous situations for the

Figure 1.6: Four different terrain types infected with land mines. Top left: Afghanistan area, Top right: African bush, Bottom left: Trench in former Jugoslavia, Bottom right: Wet area in Cambodia [U.S. Department of Defense, 2001].

helicopter where rotor blades can come in contact with low vegetation like small bushes. Therefore, a slung load setup is advantageous such that the mine detection equipment is suspended underneath the helicopter (see figure 1.7).

1.3 Helicopter Terminology

To aid the reader unfamiliar with general helicopter theory a short introduction to helicopter terminology is given here. For further information about general helicopter operation and theory [Prouty, 1989] is a good place to start.

A standard helicopter has two rotors: The main rotor which provides lift and translational control and the tail rotor which counters the torque of the main rotor and provides heading control. The lift – also known as the thrust – is generated by the main rotor pushing air downwards. The motion of this air is called the induced inflow or the rotor wake.

The control inputs to the rotor are the pitch on the blades. The main rotor is controlled though the swash plate, which transforms the actuator inputs in the nonrotating helicopter frame to the rotating blades. When the swash plate is moved up and down it alters the pitch equally on all blades, known as collective pitch, which controls the lift generated

Figure 1.7: The mine detection principle with the detection equipment in the slung load close to ground.

by the main rotor. When the swash plate is tilted it changes the blade pitch depending on where the blade is in the rotation. This is known as cyclic pitch and controls the direction of the thrust vector such that lateral and longitudinal control is achieved. The tail rotor is controlled through collective pitch alone.

The forces acting on the rotor causes the blades to bend and move in difference directions. The horizontal bending motion of the blades in the rotor plane is known as lagging and the vertical bending motion out of the rotor plane is known as flapping. The flapping motion must be allowed to accommodate for the difference in lift in each side of the rotor disc in forward flight generated by the difference in local velocity of the advancing and retreating blade. Furthermore, the flapping generates large in-plane Coriolis forces and to relieve these, an in-plane hinge that allows free blade lag is included on most helicopters.

On smaller helicopter an additional rotor known as a stabilizer bar can often be found. The flapping of the stabilizer bar is coupled to the cyclic pitch of the main rotor and it has the effect of slowing down the helicopter dynamics. In a sense it works as a rate controller for the helicopter. The three helicopter rotors are shown on figure 1.8.

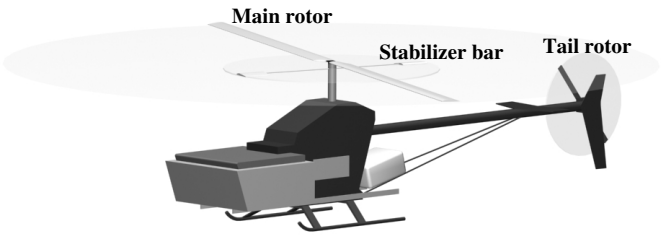

Figure 1.8: The rotor systems of the helicopter.

1.4 Previous Work

Here we present a review of existing literature on the topics of this thesis. First we look at the literature on dynamic helicopter modeling and slung load modeling. Helicopter modeling for control purposes is a well established topic in the literature, while the slung load modeling literature is more focused on stability analysis. We then look at estimation and control literature, mainly for helicopters without slung load as literature on control and estimation for slung load systems is sparse.

1.4.1 Helicopter Modeling

Helicopter modeling has been a major research topic for more than 80 years ever since the first auto-gyros in the early twentieth century. The modeling efforts have been concentrated in the first-principle direction ranging from simple models based on momentum theory to highly advanced FEM modeling of the rotor wake. The large range of different modeling techniques are initiated by the many different scopes of the research work. Some examples are: Models created for a simulation tool used in pilot training, models for structural analysis, models for stability analysis of a new helicopter design and models intended for control purposes. This review will focus on models that in complexity are in the range that can be used for piloted simulation and for control purposes.

There are a number of different books available which treats the theory of helicopters and a good starting point for understanding helicopter theory is [Prouty, 1989]. It focuses on rather simple modeling intended for understanding the helicopter rather than simulating it. It includes simple force equation and quasi steady state flapping equations. Likewise [Bramwell, 1976] gives a good introduction to the basic equations needed for understanding the theory behind helicopter operation, but does not discuss more advanced theory.

A very comprehensive treatment of helicopter modeling is [Johnson, 1980], which treats everything from simple hover equations to rotary wake modeling. It presents the

theory in a high detail level and covers almost all interesting parts of helicopter modeling like autorotation, stall etc. Due to its comprehensiveness it can be somewhat difficult to extract the important parts for a model from it, but it is an excellent starting point for the modeling. In [Padfield, 1996] the focus is on modeling directed at simulation and control and a good presentation of the basic equation is given, whereas the more advanced parts of the modeling are only briefly touched upon.

Parallel with the books a quite large number of articles and reports have been published that often focuses on specific parts of the helicopter theory. A comprehensive treatment of the flapping dynamics is given in [Chen, 1980], which uses blade element theory for the derivation of the second order dynamic equations. These flapping equations are used in [Chen, 1979] and [Talbot *et al.*, 1982], where a complete helicopter model for simulation purposes is presented. Blade element theory is used to derive the forces and moments. In [Heffley and Mnich, 1988] a simple model is presented which focuses on improving computational effort. It includes first order modeling of the flapping and thrust generation from main and tail rotor as well as simple aerodynamic drag from all surfaces.

One of the most widely used non-uniform dynamic inflow models can be found in [Pitt and Peters, 1981] which treats the inflow as a three state first order system. A useful survey of this as well as other non-uniform inflow models can be found in [Chen, 1990]. In [Kim *et al.*, 1990] a high order model is created including flap, lag, and inflow dynamics and the model is verified using frequency response data. One of the more recent helicopter models published is [Civita, 2002], which is mainly based on the previously discussed literature. It calculates the flapping and rotor forces and moments using blade element theory and uses non-uniform dynamic inflow from [Pitt and Peters, 1981]. Parameters are identified using frequency response data. In [Gavrilets *et al.*, 2001a] a simple model is derived for aggressive flight with uniform inflow and first order flapping dynamics. A frequency response system identification approach is taken in [Mettler *et al.*, 2002] where simple first principle relations are used to determine a parametrized model for a helicopter that includes the influence of the stabilizer bar.

1.4.2 Slung Load Modeling

One of the very first to consider the dynamics of an object being towed through air was [Glauert, 1930] and he discovered the stability problems involved in such a task. He identified that short wires and low load mass was factors that could lead to instabilities of the slung load system. The first study in a complete helicopter slung load system was performed by [Lucassen and Sterk, 1965]. The analysis was limited to 3 degrees of freedom hover and excluded load aerodynamics, but is nevertheless the first to consider the coupling between helicopter and slung load. In the following two decades a large number of different researchers have considered the stability of slung load systems through analytical studies as well as experimental testing. Almost all studies have focused on determining a stable region of flight with respect to slung load parameters to avoid instabilities ([Poli and Cromack, 1973], [Prabhakar, 1978], [Sampath, 1980], [Ronen *et al.*, 1986], [Fusato

et al., 2002]). Some have analyzed certain parameters such as the shape of the load itself in order to reduce instabilities, including considering different stabilizing implements like gyroscopes, fins, and drogues ([Micale and Poli, 1973], [Fester *et al.*, 1977], [Sheldon, 1977]).

Common for most of the models developed in these studies is that they are somewhat limited and focused directly at stability analysis in a bounded region. In [Poli and Cromack, 1973] a 10 state linearized model is presented which assumes no coupling of lateral and longitudinal motion. The model only deals with single-point suspension and forward flight and the study concludes that a long wire is needed for stability, but it also concluded contrary to [Glauert, 1930] that a low load mass is a requirement for stability. A study in how a gyroscope and fins can be utilized to stabilize the load was conducted in [Micale and Poli, 1973] and it found both implements beneficial in most situations. [Fester *et al.*, 1977] performed experimental test using forced oscillations in a wind tunnel to obtain stability information. The dynamics and flowfield of the helicopter was ignored and the conclusion was that a two-wire suspension system solved some of the single-wire stability problems and thus provides an adequate suspension system.

A more extensive model is found in [Prabhakar, 1978] where Newton-Euler equations are used to describe an inverted-V suspension system and includes a helicopter model based on stability-derivatives. The model assumes inflexible and inextensible wires and describes the system by constraining the full 12 degrees of freedom system to 9 and notes the difficulties in obtaining an adequate model reaction to yaw-motion.

A major work was the PhD thesis by [Sampath, 1980] which used a Lagrange formulation of the problem and as one of the first created a complete set of 12 degrees of freedom equations of motion which included all body-to-body suspension schemes. Aerodynamic models of both helicopter and load were included as well as wires implemented as inflexible, but extensible by considering them as springs with viscous damping. Also modeled was the possibility of wire collapse, but not wire collision, which is the situation where the wire goes from being slack to being taut. In [Ronen *et al.*, 1986] a Newtonian approach is applied to develop a full model of single-point suspension systems where rotor downwash on the load as well as unsteady aerodynamics of the load were taken into account. The stability of a buoyant quad-rotor vehicle with a slung load is considered in [Nagabhushan, 1983] and concludes that the system is hover stable, but identifies possible instabilities during cruise.

One of the most comprehensive treatments of slung load modeling can be found in [Cicolani and Kanning, 1992] and [Cicolani *et al.*, 1995] where specific simulation models for different kinds of single- and multiple-point suspension systems as well as multi lift systems (more than one helicopter) are developed. Both suspension systems with elastic and inelastic wires are treated using an explicit constraint method which separates the motion due to the wire stretching from the motion due to the coupled rigid-body dynamics. In a recent publication [Stuckey, 2002], the single point suspension type models found in [Cicolani and Kanning, 1992] have been implemented and simulated.

For an elaborate survey of the different research in this area see [Sampath, 1980]

where many older references dealing with different kinds of stability analysis have been treated.

1.4.3 Estimation and Sensor Fusion

State estimators and sensor fusion algorithms for autonomous helicopters have been the subject of quite some research for the past two decades, but with respect to slung load systems there are almost no published results. For helicopter state estimation, a number of different approaches have been tried over the years, using both model free and model based methods. However, most work has been based on a model free approach as helicopter models are often highly non-linear, quite complex to work with, and have rather high computational requirements.

In [Rock *et al.*, 1998] position, velocity, and attitude determination is demonstrated using a four antenna carrier-phase differential GPS (CDGPS) setup. The very high accuracy of the CDGPS made it possible to achieve position estimates with an accuracy of 3 cm and attitude estimates with an accuracy of a couple of degrees. A system for estimating attitude based on rate gyros and inclinometers fused through a complementary filter is demonstrated in [Baerveldt and Klang, 1997]. With the complementary filter, which fuses high bandwidth information from the gyros with low bandwidth information from the inclinometers, attitude accuracy of a couple of degrees is achieved. Another model-free approach is given in [Jun *et al.*, 1999], which describes the use of a Kalman filter driven by accelerations and rates measured by an IMU along with data from GPS and compass as sensor inputs. The idea is to use a simple kinematic model driven by the measured rates for attitude estimation and a simple rigid body dynamic model driven by the measured accelerations for position and velocity estimation. Similar approaches are discussed in [Gavrilets *et al.*, 2001b] and [Saripoalli *et al.*, 2003], where gyro bias estimation is added to the Kalman filter.

Custom attitude estimation algorithms developed for sparse resource systems are presented in [Musial *et al.*, 2004], where acceleration and magnetic field measurements are fused to yield an attitude prediction, a CDGPS is used to adjust for dynamic accelerations and rate gyros are used for state updates. Further, it is demonstrated that the custom algorithms shows accuracies comparable with those of a standard EKF setup, but using less computations. In recent years a new type of nonlinear estimator, known as the unscented Kalman filter (UKF), has become increasingly popular. In [van der Merwe *et al.*, 2004] the UKF is used in an IMU driven setup with GPS and barometric data as sensor inputs and it is found to exhibit superior accuracy compared to traditional EKF solutions. In [Matsuoka *et al.*, 2005] the GPS system is replaced with a triangulation system based on visual cameras, which fused with IMU measurements yields position estimates usable in closed loop.

However, while it is clear that a lot of research has gone into state estimation in helicopter UAV systems, the published work on state estimation in slung load systems is very sparse. In [Dukes, 1973b] the difficulty in reliably estimation slung load states is briefly

mentioned. To the best of the author's knowledge, the only publication that considers the design of state estimation for slung load systems is [Gupta and Bryson, 1976]. It discusses a hover control system for a helicopter with a slung load and suggests using an attitude measurement, the angles of a measurement cable from the helicopter to the ground and the angles of the suspension cable as sensor input to a linear Kalman filter.

1.4.4 Autonomous Helicopter Control

Control of helicopters is by no means a new research area and several research groups around the world have attempted different control strategies during the past years. It is however not until within the last years that the first real successful results have been shown.

A review of the literature on control system design for autonomous helicopters shows that a very wide range of control design techniques have been tried. However, if the different most successful strategies are reviewed, a common trait quickly becomes apparent. The most active and successful projects have discarded traditional non-linear control strategies like feedback linearization or sliding model control.

An adaptive trajectory tracking controller is presented in [Johnson and Kannan, 2005] where approximate inverse dynamics together with a neural network being used to cancel system dynamics. The actual design is done using a cascaded principle with a attitude controlling inner loop and a translational controlling outer loop. PD feedback from a reference model error is used to suppress disturbances and shape the two loops. A technique called pesudocontrol hedging is used to protect the adaptation process from actuator saturation. The controller has been tested on a wide range of flying vehicles and has shown excellent tracking performance in a very wide flight envelope, while being robust to changes in vehicle parameters.

Nonlinear Model Predictive Control based on a neural network is used in conjunction with State Dependent Riccati Equation control in [Wan and Bogdanov, 2001] for high bandwidth helicopter control. The SDRE controller provides robust stabilization of the helicopter while the neural MPC provides high performance. The use of Nonlinear Model Predictive Control – and also State Dependent Riccati Equations – as a mean of stabilizing the helicopter has the disadvantage that a highly intensive computational effort is needed for real time implementation of the control scheme. It can indeed be quite difficult to achieve real time control of a small high-bandwidth helicopter with such methods. Therefore, [Bogdanov *et al.*, 2004] proposes a control system based only on SDRE, but with a nonlinear feedforward compensation to account for model simplifications and good tracking performance is shown using two different helicopters.

Gain scheduled robust control is presented in [Civita, 2002] where $\mathcal{H}_\infty$ loop shaping theory is used to design a set of linear controllers which are scheduled based on the system gain margin. The controller is verified in a number of flight maneuvers and shows good tracking performance in a wide flight envelope. Nonlinear Model Predictive Control based on a simple first principle model is presented in [Shim *et al.*, 2002] and through

the use of an efficient optimization formulation a real time implementation of the controller is achieved. The controller is verified in different flight scenarios and shows good performance.

In [Ng *et al.*, 2004] reinforced learning techniques are used to first learn a helicopter model and then learn a controller that successfully performs sustained inverted hovering. [Shim *et al.*, 1998] gives a review of three different approaches for helicopter control: Robust linear MIMO control, fuzzy control with evolutionary training, and nonlinear tracking control based on feedback linearization. Not surprisingly it concludes that the nonlinear controller shows better performance away from hover. The design of the nonlinear controller is elaborated in [Koo and Sastry, 1998]. Aggressive aerobatic flight is shown in [Gavrilets *et al.*, 2002] where the control approach is inspired by recorded maneuvers flow by human pilot. A hybrid control strategy is used to switch between open loop prerecorded aerobatic maneuvers and LQ designed close loop controllers for cruise between maneuvers.

1.4.5 Slung Load Control

A number of different publications on control of helicopter slung load systems exist, but actual flight verification is very sparse in the literature. In [Dukes, 1973a] feedback from the load wire rates to either main rotor thrust angles or to attachment point position is analyzed. It is concluded that feedback to rotor input gives only limited performance while feedback to the attachment point position is more advantageous. The problem of state estimation for slung load systems are mentioned in [Dukes, 1973b] and to overcome this problem an open loop control approach is suggested. This open loop control method resembles input shaping (see [Singh and Singhose, 2002]) in the sense that the controller is designed such that excitation of the resonant modes is avoided, in this case by using appropriate spaced triangular pulses as control input. In [Gupta and Bryson, 1976] a LQR controller are designed for a S-61 Sikorsky helicopter for near hover stabilization with a single wire suspension. SISO controllers are designed for the lateral and longitudinal axis taking wind disturbances into account. The resulting design is left untested, but stability and performance analysis shows satisfying results. An active control system mounted on the actual slung load is proposed in [Raz *et al.*, 1989]. It consists of two vertical aerodynamic control surfaces intended to dampen oscillation on the load yaw and lateral axis in a single wire suspension system. Controller design is done using LQR and it is shown through linear analysis that the system is capable of stabilizing the system up to quite high airspeeds.

Robust control is used in [Faille and Weiden, 1995] for stabilization of a helicopter with a point mass slung load. Controller design is done based on a reduced order linear model using $\mathcal{H}_\infty$ synthesis and it is shown through simulation to be able to stabilize the system. Receding Horizon Optimal control is suggested in [Schierman *et al.*, 2000] and preliminary simulation results is presented. A recent publication is [Oh *et al.*, 2006] which looks at a helicopter carrying a cable suspended robot that is controlled through a

number of adjustable length cables. The nonlinear control design is done independently for the helicopter and for the load system and therefore relies on a controllable suspension system.

Twin lift system has also been the focus of some research through the past decades. In [Rodriguez and Athans, 1986] a LQG control design is developed for a twin lift system with spreader bar and single load. The controller uses a master/slave configuration of the helicopters and simulations shows that the controller is capable of stabilizing the system and tracking velocity references. Robust control on a similar system is also applied in [Reynolds and Rodriguez, 1992] where $\mathcal{H}_\infty$ is used and simulation is used to verify that the system can track velocity references. A feedback linearization scheme is presented in [Mittal *et al.*, 1991] where a twin lift system without spreader bar is considered. The controller is designed to adapt to an unknown slung load mass and simulations is used to show that the system is stabilized by the controller.

For smaller scale helicopter the 1997 AUVSI International Aerial Robotics Competition showed autonomous flight with a slung load. The winning entry by Carnegie Mellon [Miller *et al.*, 1997] demonstrated object collection by a controllable suspension system with PID controllers for helicopter and slung load system. Feedforward control was used to compensate for helicopter motion in the slung load control, while the helicopter controller was unaware of the slung load.

1.5 Contributions of this Thesis

The following summarizes the main contributions of this thesis.

Generic slung load model A generic slung load model has been derived, which can be used to model all body to body slung load suspension types. The model gives an intuitive and easy-to-use way of modeling and simulating different slung load suspension types and it includes detection and response of wire slacking and tightening, and aerodynamic coupling between the helicopter and the load. Furthermore, the model can easily be used for multi-lift systems with any combination of multiple helicopters and multiple loads. A numerical stabilization algorithm is derived and implemented in the model and a trim algorithm for the entire helicopter/slung load system is developed. The model has been published in [Bisgaard *et al.*, 2006] (awarded best technical paper award at AIAA conference) and [Bisgaard *et al.*, 2007a].

Adaptive slung load estimator A state estimator for a yaw decoupled slung load system designed to augment the IMU driven estimator found in many autonomous helicopters. The process model used for the estimator is a simple 4 state acceleration driven pendulum. Sensor input for the filter is provided by a vision based system that measures the position of the slung load. The estimator needs little prior knowledge of the system as it estimates the length of the suspension system together with

the system states and can thereby adapt the model. This work has been published in [Bisgaard *et al.*, 2007c].

Full slung load state estimator A state estimator for a generic helicopter based slung load system designed to deliver full rigid body state information for both helicopter and load. Two different approaches are investigated: One based on a parameter free kinematic model and one based on a full aerodynamic helicopter and slung load model. The kinematic model approach uses acceleration and rate information from two IMUs, one on the helicopter and one on the load, to drive a simple kinematic model. A virtual sensor method is developed to maintain the constraints imposed by the wires in the system. The full model based approach uses a complex aerodynamic model to describe the helicopter together with the generic slung load model. A method is devised to reduce the execution time of the process model in the unscented Kalman filter. It has been published in [Bisgaard *et al.*, 2007b].

Swing damping slung load control This is a combined feedforward and feedback controller designed to simultaneously prevent exciting swing in the slung load from helicopter motion and to actively dampen swing. It is created to use in combination with the adaptive slung load estimator and relies on an existing inner loop helicopter controller. The feedforward is based on an robust input shaping approach which filters trajectories to the helicopter controller such that it does not cause slung load swing. The feedback is based on a delayed proportional feedback approach that directly can account for eventual delays in sensor systems etc. Both the feedforward and feedback are designed to handle varying wire length and together with the adaptive slung load estimator they form an integrated control system.

Trajectory tracking slung load control A controller system for a generic helicopter slung load system capable of generating and tracking slung load trajectories. The controller is designed using LQR techniques and stabilizes the helicopter and slung load using state feedback. It can handle suspension systems both with and without yaw coupling and can indeed be tuned to any body to body suspension system. A trajectory mapping algorithm to generate a full system reference based on a desired slung load trajectory is developed. The mapping is divided into two parts, a kinematic mapping of circular flight and a dynamic mapping during velocity changes.

Publications of the latter two items are under preparation and will be published in near future.

1.6 Methodology

In this section we present a methodology for autonomous helicopter slung load flight based on the contribution of this thesis. Earlier in this chapter two system design lines

were introduced: Generic cargo transport using a helicopter slung load system and landmine clearing using helicopter slung load deployed detector system. These two applications result in two different branches that will be investigated in this thesis:

Swing damping control This scenario is characterized by a suspension system that uses a single attachment point on the helicopter and by unknown slung load parameters. There is no specific tracking requirement for the slung load, but stable flight must be ensured, which is done through keeping load swing at an acceptable level. This branch is focused on enabling slung load flight in already autonomous helicopters.

Trajectory tracking control This scenario is characterized by known slung load parameters and often utilized a multi-wire suspension system that allows yaw control of the load. High precision trajectory tracking for the slung load is required and control system synthesis is done for the entire system.

Given these two branches, we here present a proposal for integrated design of an autonomous helicopters capable of carrying slung loads. The method is formulated as a step-by-step procedure for the theoretical work from analysis to flight ready system, depending on the specific branch. The procedure is illustrated in figure1.9.

The procedure flow for the two branches share the first two steps. First step is the modeling of both helicopter and slung load and as the same helicopter is used for both branches the same model can be used. The slung load model derived in this thesis is capable of modeling a wide range of suspension systems and is therefore well suited for both branches. The second step in the procedure is to determine the parameters for the model and while this step in not treated rigorously in this thesis, a similar approach can nevertheless be used for both branches. For more rigorous treatment of this step see [Mettler *et al.*, 2002] and [Civita, 2002].

For the swing damping branch the next point is to achieve helicopter stand alone autonomy by design controller and estimator for it. This element is not treated in this thesis, but is treated thoroughly in the literature, see e.g. [Johnson and Kannan, 2005] and [Wan and Bogdanov, 2001]. Given the autonomous helicopter, the next steps are design of the slung load estimator and the actual swing damping controller. For the trajectory tracking branch the design of estimator and controller is done for the entire system with helicopter and slung load together.

1.7 Thesis Outline

This section provides the reader with an overview of the chapters found in this thesis. It divide into five parts: Introduction, Modeling, Estimation and Control, Discussion and Conclusion, and Appendixes. The majority of the thesis is gathered in two parts: Part II Modeling and Part III Estimation and Control and most contributions of this thesis are described in these two parts.

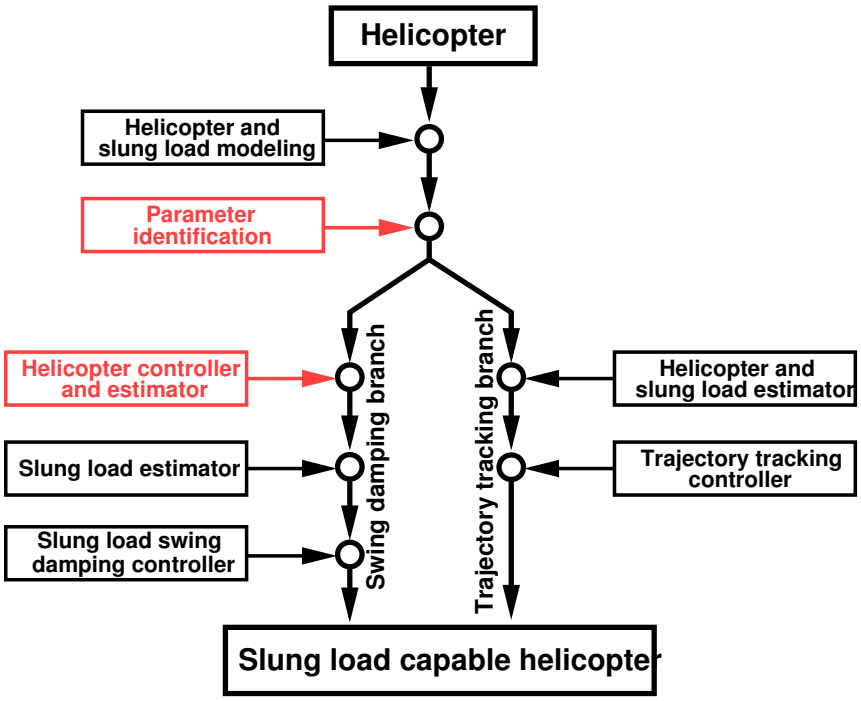

Figure 1.9: The work flow to slung load capable helicopter as developed in this thesis. Black text elements are treated rigorously in this thesis, while red text element are only treated superficially.

Part I Introduction :

Chapter 1 Introduction is this chapter which gives the background and motivation to this research. A review is given of the literature in the different fields examined in this thesis and a general methodology combining the contributions is presented.

Chapter 2 System Description gives an introduction to the two different helicopter test platforms used to verify the contributions of this thesis.

Part II Modeling :

Chapter 3 Helicopter Modeling contains a derivation of the helicopter model and the aerodynamic coupling between helicopter and slung load.

Chapter 4 Slung Load Modeling gives a derivation a generic slung load model which is one of the major contributions of this thesis.

Chapter 5 Model Analysis and Verification presents a verification of the model against flight data. Furthermore, it provides the reader with a analysis and discussion of the model and the behavior of the helicopter slung load system.

Part III Estimation and Control :

Chapter 6 State Estimation and Sensor Fusion presents the development of two different estimators: One for augmenting existing helicopter estimators and one for full helicopter slung load systems.

Chapter 7 Swing Damping Slung Load Control presents the design of a combined feedforward and feedback controller design for dampening swing in slung loads.

Chapter 8 Trajectory Tracking Slung Load Control provides a control design for tracking trajectories with a helicopter slung load system. The controller is designed using a linear optimal approach and a trajectory mapping algorithm is developed to generate a full state reference for the controller.

Part IV Conclusion :

Chapter 9 Conclusion and Future Work contains a summary and conclusion of the thesis, a discussion of the thesis contributions, and considerations about future work.

Part V Appendixes :

Appendix A Main and Tail Rotor Equations contains the full equations for the main and tail rotor used in the helicopter model.

Appendix B Model Parameters provides the parameter set for main test platform used in this research.

Chapter 2

System Description

Two different helicopter slung load systems are used for testing and both are described in this chapter: The AAU Bergen Industrial Twin helicopter and the Georgia Tech GTMax. The AAU Bergen helicopter is developed during the course of this research and the helicopter hardware and software are described. The GTMax which has been made available for this work by Georgia Institute of Technology is discussed briefly.

2.1 The AAU Bergen Industrial Twin Helicopter

The baseline helicopter used for the research is a modified Bergen Industrial Twin, which is an off-the-shelf radio controlled (RC) helicopter with a 52 cc, 8 HP engine targeted for heavy duty hobby and semi-professional use. The main requirement for the helicopter is that it must be large enough to carry substantial slung loads of several kilograms, while still bring well within the 25 kg weight limit imposed that the Danish Civil Aviation Administration on hobby RC aerial vehicles (BL9-04). The physical parameters of the helicopter is presented in appendix B.

The mechanical modifications of the stock helicopter consists of equipping it with computer, sensors and other hardware necessary for autonomous flight as well as a slung load suspension system. The main focus being to create a reliable platform for carrying different slung loads. The system has been engineered with the objective of keeping the bottom side of the helicopter free from everything but the suspension system. Therefore the computer, sensors and other hardware has been placed in the from and the back of the helicopter as it can be seen in figure 2.1.

The helicopter has been equipped with two aluminum profiles along the sides: These are used to mount the heavy equipment and the slung load suspension system. In the front a custom instrumentation box holds and shield most of the different hardware systems of the helicopter and on top of the instrumentation box the main computer is mounted.

Figure 2.1: The modified Bergen Industrial Twin developed as test platform in this research.

2.1.1 The Hardware

The hardware system of the helicopter can be divided into two different categories: The stock instrumentation used on the unmodified helicopter for the RC control system and the custom instrumentation necessary for autonomous flight. An overview of the hardware system is given in figure 2.2.

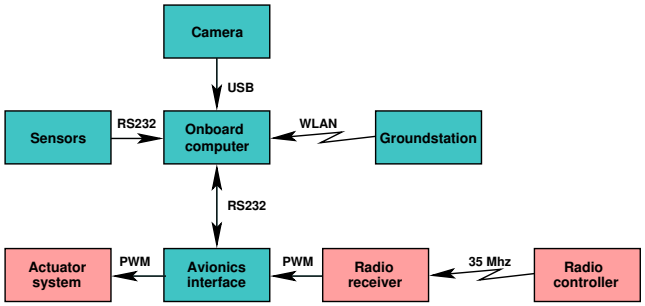

Figure 2.2: Overview of the hardware system on the helicopter. Red boxes: Original instrumentation. Green boxes: Custom instrumentation.

The interface between the original and the custom instrumentation system is an avionics board that enables switching between manual and autonomous control. This means that either the helicopter can be controlled manually through the RC transmitter or autonomously by the onboard computer. The avionics interface is placed between the actuator system and the RC receiver and can be used to record the control signals when in manual flight. Though a switch on the RC transmitter, the helicopter can be changed into autonomous mode. The computer is a standard Dell D400 1.8 GHz laptop computer and

can be controlled from the groundstation through a WLAN interface. An Edgeport 8R USB to serial adapter provides the computer with 8 RS232 serial interface ports.

The sensor suite for the helicopter has been chosen to provide baseline information for estimating the full state vector of the helicopter. A GPS provides position and velocity measurements, a magnetometer gives attitude information and a IMU provides inertial information. The GPS is a Novatel OEM4-G2L stand-alone unit, but using the satellite-based differential augmentation system EGNOS, it can produce position and velocity measurements of the helicopter at an rate of 20 Hz and a position accuracy better than 1 m. As magnetometer, a Honeywell HMR2300 is used. It delivers high accuracy 3-axis magnetic field measurements at 50 Hz. The IMU is an O-Navi Falcon GX unit capable of delivering 3-axis acceleration and rate measurements at 50 Hz.

To provide state information for the slung load a downward looking camera is mounted on the helicopter. The camera is a uEye UI-1410 with a resolution of up to 640x480 pixels in monochrome which through a DMA interface is capable of delivering full size pictures at up to 35 Hz and faster at lower resolutions. Furthermore, the slung load is equipped with an IMU similar to the one on the helicopter.

The actuator system of the helicopter consists of five servo motors and a main power plant (engine) as shown in figure 2.3. Three servos are used to control collective and cyclic

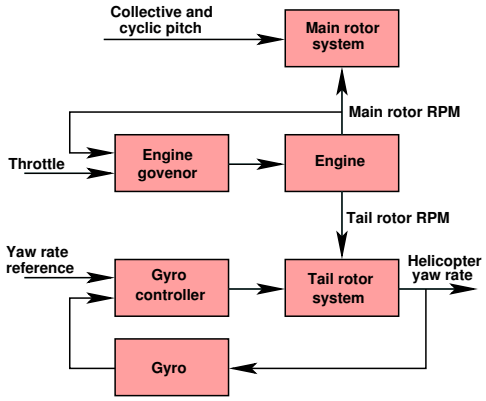

Figure 2.3: Overview of the actuator system on the helicopter.

pitch on the main rotor, one servo controls throttle on the engine, and one servo controls collective pitch on the tail rotor. A Futaba GV-1 govenor is used to keep a constant rotation on the engine and thus a constant rotation on main and tail rotor. Furthermore, a Futaba GY-611 is used as inner loop controller on the helicopter yaw rate which through a gyro and a controller stabilizes the yaw axis of the helicopter.

2.1.2 The Slung Load

The slung load suspension system is mounted underneath the helicopter between the aluminum profiles. Two suspension points are implemented symmetrically infront and behind of the main rotor and a beam can be mounted between them for single point suspension. The suspension points are glider tow hooks capable of releasing the wires even under high tension.

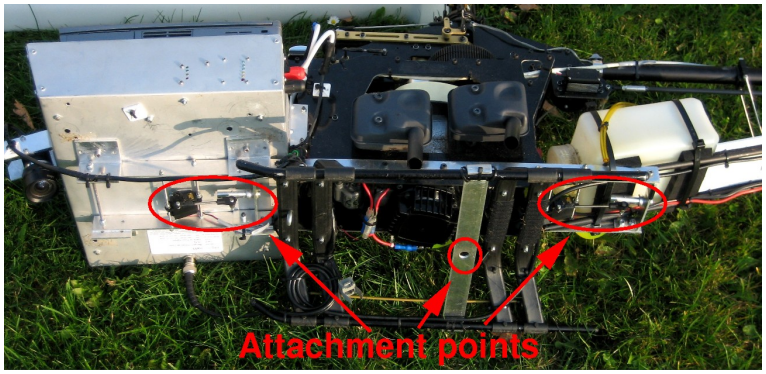

Figure 2.4: The suspension system underneath the helicopter.

The slung load itself can of course be a wide range of objects with different masses and shapes, but for demonstration purposes two different slung loads are devised: One for yaw-coupled suspensions like for the mine detection application and one for single wire cargo transport. Both are shown in figure 2.5 and the helicopter in flight with the dual wire slung load is shown in figure 2.6.

Figure 2.5: The demonstration slung loads. To the left the single wire slung load and to the right the dual wire slung load.

Figure 2.6: The AAU Bergen Industrial Twin flying with the dual wire demonstration slung load.

2.1.3 The Software

Figure 2.7 identifies the software components developed for the helicopter and groundstation. The centerpiece of the software system is the shared memory running on the helicopter. It ties the software together and works as a buffer that enables asynchronous execution between the different processes. The sensor server collects data from the many different sensors on the helicopter and whenever new data is available it delivers it to the shared memory. The vision systems collects images from the camera, performs image processing and places the results in the shared memory. The two software systems, on the helicopter and on the groundstation respectively, are coupled together by a client/server TCP/IP connection. This connection synchronizes the shared memory on the helicopter with the one on the groundstation. Data like sensor measurements, estimates, and control signals are send to the groundstation for visualization and commands to control the helicopter software is send the other way.

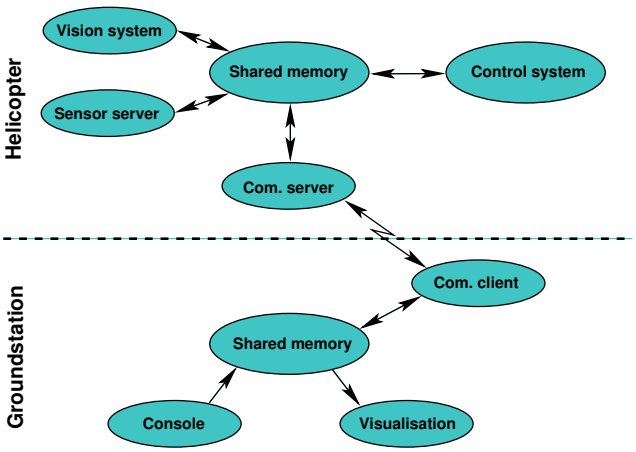

Figure 2.7: Overview of the software on the helicopter and groundstation.

The Control System

The control system contains a state estimator, a path planner and a controller. Currently the AAU Bergen Twin features a linear state feedback controller that is capable of hover and slow (< 10 m/s) trajectory flight. Implementation is done using a soft real-time process using partly auto generated code from the Matlab/Simulink toolbox Real-Time Workshop (RTW) by Mathworks. The RTW toolbox is primarily intended for rapid prototyping and eases the transition from simulation to implementation. It is capable of generating C or C++ code from a Simulink block diagram and can compile it into a Linux binary by using the Linux Soft Real-Time Target (LNX). LNX (by Dan D. V. Bhanderi) uses the POSIX real-time clocks to generate periodic signals that wakes the control process at every execution step. By using this, and by changing the process priority to the highest possible level, soft real-time execution is achieved.

Custom C or C++ code is include through the use of Simulink S-functions and this makes it possible to interface the Simulink block diagram to the shared memory and to write the calculated control signals to the avionics board.

The Groundstation

The groundstation software consists of a command-line console interface and a combined graphical and text-based visualization interface. The console is used for commanding the aircraft, e.g. for uploading a new flight trajectory reference or to change parameters the vision algorithm. The text-based visualization provides an easy overview of the different key variables of the helicopter like sensor measurements, control signals, estimated states, vision system data, etc. The graphical visualization interface is im-

plemented as a Simulink block diagram that provides graphs and plots of selected data. A 3D representation of the helicopter is further integrated into the Simulink block diagram. The graphical representation is implemented using the Irrlicht 3D engine (See http://irrlicht.sourceforge.net for more info) and uses the estimated helicopter and slung load position and attitude to show the motion in 3D.

2.1.4 The Simulation Tool

The simulation tool used is a Simulink implementation of the models, estimators, and controllers derived in this thesis. Sensors are modeled using realistic noise, quantization, delays, etc. As mentioned earlier the onboard software also uses a Simulink interface and thereby it is possible to use the exact same controller, estimator, and similar both in the simulation and onboard. This minimizes problems with implementations between simulation and real flight. For visualization the 3D representation from the groundstation is used.

2.2 The Georgia Institute of Technology GTMax

The Georgia Tech GTMax shown in figure 2.8 is based on the Yamaha RMAX helicopter developed for agricultural work. It weighs around 100 kg, have a 3 m rotor diameter, and is a fully autonomous system using an IMU driven state estimator and an adaptive controller described in [Johnson and Kannan, 2005]. It is used for testing part of the swing

Figure 2.8: The Georgia Tech GTMax.

damping controller branch and is equipped with an AXIS-213 Pan-Tilt-Zoom camera with a 40° field of view used for the vision system. The slung load used in the flight tests is a 5.5 kg bucket suspended in a 7 m wire.

Part II

Modeling

This parts provides a derivation of a model that describes the helicopter, the aerodynamic coupling between helicopter and slung load, and the slung load system itself. Furthermore, a verification and analysis of the model is presented.

Chapters

Chapter 3

Helicopter Modeling

In this chapter a model of the aerodynamic characteristics of the helicopter and the slung load is created. First the background and overall approach for the modeling is established. Then the actual model is derived, focusing first on the rotor dynamics, then on the force generation, and finally on the aerodynamic coupling between the helicopter and the slung load.

3.1 Model Overview

From a modeling perspective the helicopter consists of a body that generates drag, a tail fin and tail plane that generates drag, and a set of rotors. The helicopter used in this research have three different rotors: The main rotor, the tail rotor, and the stabilizer bar. The main rotor provides lift, the tail rotor provides yaw control of the helicopter, and the stabilizer bar works as a rate feedback system that stabilizes and slows down the dynamics of the helicopter.

3.1.1 Modeling Requirements

In order to determine the best choice of model for the purpose of this project it is necessary to establish the requirements and the purpose for the model. The purpose is threefold:

- Real time simulation
- Model based estimation
- Controller design

For use in simulation a high fidelity model is required which still needs to be sufficiently computational efficient to be executed in real-time as it is furthermore intended for slung

load pilot training. For use in a model based estimator it is necessary for the model to be able to run much faster that real-time on the onboard computer. This means that the choice of modeling approach and complexity is a compromise between how accurate the model describes the system and how fast it can be executed on a computer.

3.1.2 Model Structure

The model is structured following the natural flow from the actuator inputs to the helicopter and slung load motions and consists of four primary building blocks. These are actuator system, rotor dynamics, force and torque generation and rigid body dynamics.

Actuator System The actuator system makes it possible to operate the helicopter by manipulating the control surfaces of the helicopter, i.e. the blades of the main and tail rotor. The actuator system (see section 2.1.1 on page 28) consists of three servos to control the main rotor pitch, one servo and governor to control the engine, and one servo with gyro and controller for the tail rotor pitch.

Rotor Dynamics The motions of the main rotor and the stabilizer bar are very significant in determining the forces and moments generated by the rotor. The primary motion of the blades is the flapping and it is modeled using second order dynamics.

Force and Torques Generation In this block the motions of the rotors and the helicopter and slung load are calculated into forces and torques. These consists of two major contributions: The forces and torques originating from the rotors and the drag forces and torques from the helicopter and slung load surfaces.

Rigid Body Dynamics Consists of the describing dynamic and kinematic equations of the helicopter and slung load. It maps from the input forces and torques to the helicopter and slung load motion. This motion is the helicopter and slung load position, attitude, velocity, and rate which are collected in the rigid body state vector.

The simplified primary model flow is illustrated in figure 3.1.

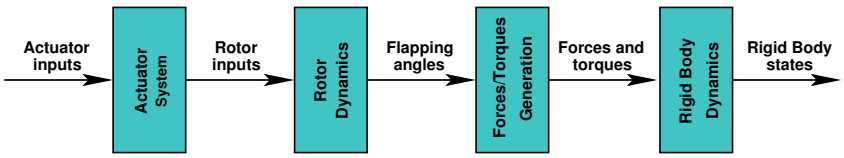

Figure 3.1: The overall model structure.

3.2 Coordinate Systems

All coordinate systems (or reference frames) used in this thesis are, unless otherwise noted, right hand Cartesian coordinate systems. The rigid body model is derived with respect to an initially fixed reference frame denoted the earth fixed frame (the variable x measured in the earth fixed frame is ${}^{e}x$). This reference frame is equivalent to the Universal Transverse Mercator coordinate system (UTM) with the x-axis pointing north (UTM northing), the y-axis pointing east (UTM easting) and the z-axis point down. This ensure that the system position calculated in the earth fixed frame can be related directly to the output of the GPS. However for simplicity in the position representations used in this work, the origin of the earth fixed frame is offset to an arbitrary position close to the starting point of the helicopter. Furthermore, body fixed coordinate systems are defined at the center of mass (CM) for each object present in the system, i.e. one for each helicopter (${}^{h}x$ or ${}^{h1}x$, ${}^{h2}x$, . . .) and one for each slung load (${}^{l}x$ or ${}^{l1}x$, ${}^{l2}x$, . . .). A generalized body fixed frame is denote as ${}^{b}x$. An illustration of the reference frames are shown in figure 3.2 which shows the helicopter with a slung load.

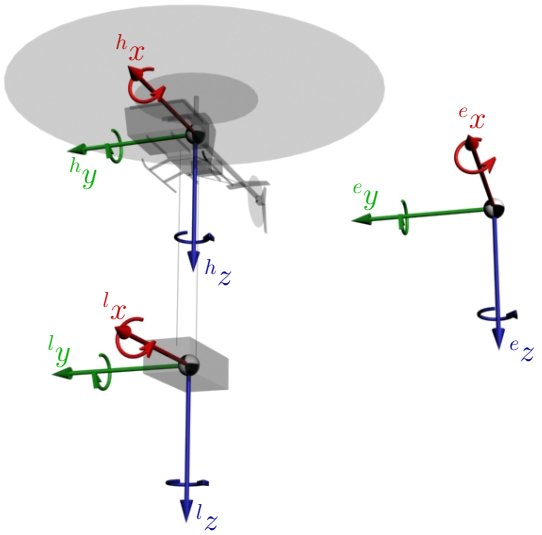

Figure 3.2: Illustration of the earth fixed, the helicopter body fixed, and load body fixed reference frames.

For each rotor a reference frame is defined that is aligned with the helicopter body fixed frame, but offset to the center of the specific rotor hub. For the main rotor this is denoted ${}^{mr}x$ and for the tail rotor this is denoted ${}^{tr}x$. The rigid body dynamics is

derived using the CM fixed coordinate systems, but the modeling of rotor dynamics etc. are derived using rotor fixed coordinate systems. For these calculations it is necessary to map the body motion to velocities on the rotors. The rotor positions are illustrated on figure 3.3 and it is assumed that the stabilizer bar and the main rotor are placed in the same position.

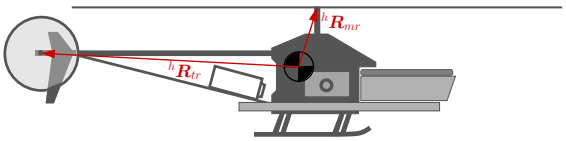

Figure 3.3: The positions of the rotors.

$$ {}^{mr}\boldsymbol{v}_{mr} = {}^{h}\boldsymbol{v}_{h} + {}^{h}\boldsymbol{\omega}_{h} \times {}^{h}\boldsymbol{R}_{mr} \tag{3.1} $$

$$ {}^{tr}\boldsymbol{v}_{tr} = {}^{h}\boldsymbol{v}_{h} + {}^{h}\boldsymbol{\omega}_{h} \times {}^{h}\boldsymbol{R}_{tr} \tag{3.2} $$

Similar the local velocities can be calculated for the empennage surfaces of the helicopter like the tail fin and tail plane.

3.3 Modeling Approach

The first choice we must make is between a first principle and a system identification approach. A model based on system identification like the one developed in [Mettler *et al.*, 2002] is quite comprehensive and precise enough for high bandwidth control, but it does not present a good understanding of the underlying theory and operation of a helicopter. For this research we believe that an important aspect of the modeling is the insight it gives into helicopter theory and a first principle approach is therefore chosen.

The rotor is the governing part of the helicopter and it is the one that requires most attention in the modeling phase. The rotor forces and moments are traditionally (and in most of the cited references) found using blade element analysis which is a simple and efficient approach. It gives the opportunity of including the desired effects on the rotor depending on the desired level of complexity and then integrating the elements. As the method is appropriate and well tested it will be used in this work. The flapping can be modeled either as quasi-steady state or as dynamic and while the steady state equations are much simpler than the dynamic equations it is nevertheless the latter that will be used. As mentioned in both [Chen, 1980] and [Johnson, 1980] the flapping dynamics are underdamped and important to the rotor behavior, especially for rotors with a large virtual hinge-offset, which is the case for the hinge-less Bergen Industrial Twin and indeed for most model helicopters.

The inflow modeling can be done either using a uniform steady state approach or a non-uniform dynamic approach. The uniform steady state approach is the traditional

method derived from momentum theory and is widely used in the literature for simple models like [Heffley and Mnich, 1988] and [Talbot *et al.*, 1982]. The non-uniform dynamic approach is only seldom found in models intended for estimation and control purposes, but is included in [Civita, 2002]. Non-uniform inflow yields a more precise flapping description and by including the dynamics a better description of the coupling between the fuselage and the rotor. However, based on test results presented in [Johnson, 1980] and [Chen, 1990] we believe that the added modeling complexity by including the non-uniform and dynamic inflow distribution is not worth the added accuracy of the model. A uniform momentum based approach is therefore taken.

In the modeling reverse flow, compressibility, and stall effects are neglected and inflow is modeled as uniform and static. Bladed lag is negelcted and flapping is modeled as rigid around a hinge and only the first harmonic is considered. Furthermore, flade flapping and blade local angle of attack are assumed small. These assumptions are similar to the ones in [Chen, 1980] and [Talbot *et al.*, 1982]. Both mention that experimental studies have shown an analysis based on these assumption is valid up to an advance ratio of up to

$$\mu_h = \frac{{}^hV_h}{\Omega_{mr} R_{mr}} \approx 0.3 \, .$$

3.4 Actuator Dynamics

The actuator system is used to manipulate the control surfaces, i.e. the main and tail rotor pitch, of the helicopter through the swash plate. It consists of the five servos, the engine and the two innerloop hardware controllers as illustrated in figure 2.3 on page 29. The servos are modeled as linear second order dynamic

$$\frac{\theta_{col}}{S_{col}} = \frac{K_{col}\omega_{col}^2}{s^2 + 2\zeta_{col}\omega_{col} + \omega_{col}^2} \tag{3.3}$$

$$\frac{\theta_{lat}}{S_{lat}} = \frac{K_{lat}\omega_{lat}^2}{s^2 + 2\zeta_{lat}\omega_{lat} + \omega_{lat}^2} \tag{3.4}$$

$$\frac{\theta_{lon}}{S_{lon}} = \frac{K_{lon}\omega_{lon}^2}{s^2 + 2\zeta_{lon}\omega_{lon} + \omega_{lon}^2} \tag{3.5}$$

$$\frac{\theta_{tr}}{S_{tr}} = \frac{K_{tr}\omega_{tr}^2}{s^2 + 2\zeta_{tr}\omega_{tr} + \omega_{tr}^2} \tag{3.6}$$

with rate and travel limits imposed. In reality the mapping from servo input to swash plate angle is non-linear due to the mechanical connection of the servos to the swash plate. On the Bergen Industrial Twin the mixing is done in such a way that each servo controls one pitch degree of freedom – this means that one servo controls the collective pitch, one servo controls the lateral cyclic pitch and one servo controls the longitudinal cyclic pitch. The non-linearities of the actuator system arise from the link connections between the servos and swash plate. However, to simplify the actuator modeling these non-linear mappings

are found through experimental system identification and simply canceled in the interface software to the actuators.

It is assumed that the engine governor is capable of keeping the engine running at a desired RPM, and flight tests shows that it is indeed capable of doing so. This means that it can simple be modeled as delivering a speed to the main rotor Ω_{mr}. The tail rotor is connected through a gear (gear ratio K_{tr}) to the main rotor

$$\Omega_{tr} = K_{tr}\Omega_{mr} \, . \tag{3.7}$$

The same simplification is not possible with regard to the gyro system that controls the pitch on the tail rotor. It is capable of keeping a stable yaw rate of the helicopter, but at the same time the tail rotor also generate forces, most significantly the thrust, which will pull the helicopter sideways. Therefore the tail rotor controller must be included and it is modeled as a P controller with the gain K_g. Thereby, the input to the model is not directly to the tail rotor actuator, but instead

$$S_{tr} = K_g(\omega_{\text{tail}} - {}^h\omega_h) \, , \tag{3.8}$$

where ω_{tail} is the reference input to yaw rate controller and ${}^h\omega_h$ is the helicopter yaw rate.

3.5 Blade Element Analysis

In order to derive the equations that describes the flapping of the blades and generated forces, it is necessary to examining the aerodynamics forces on a small element of the blade. By integration this can then be used to find the resulting aerodynamic forces and torques of the blade. This method is known as "blade element method" and examples of it can be found in most classical literature like [Bramwell, 1976], [Johnson, 1980], and [Prouty, 1989].

In figure 3.4 a rotor hub and a blade can be seen with the small blade element dr and the aerodynamic lift from this element dL. On full scale helicopters the blades are

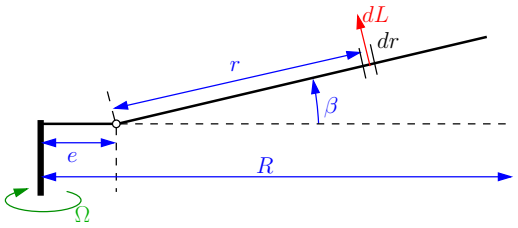

Figure 3.4: The rotor hub and rotor blade with the small blade element dr.

mounted using hinges that allows the blades to flap, but on most model-helicopters - and

on the Bergen Industrial Twin - no physical flap-hinges are present and the flapping are instead achieved by the flexibility of the blades. However, it is still possible to model these flexible blades as stiff with a virtual flapping hinge which according to [Johnson, 1980] typically are equivalent to a hinge offset of about 10% of the blade length. The hinge offset is shown in figure 3.4 as e. The distance from the hinge to the blade element is denoted r and the length of the entire blade is denoted R.

A rotor consists of a number of blades b which rotates around a center hub. The blades rotates with the angular rate Ω and the position in the rotation – known as the azimuth station – is defined φ. The pitch angle of each blade in the rotor is controlled by the swash plate, which transform the body fixed actuator control angles to harmonic varying flapping angles for the blades. At any given azimuth station, the pitch of a point on a rotor blade can be described by

$$\theta_r = \theta_{col} - \theta_{lat}\cos(\varphi) - \theta_{lon}\sin(\varphi) + \theta_t\frac{e+r}{R}\,, \tag{3.9}$$

which maps the lateral and longitudinal pitch inputs (θ_{lat}, θ_{lon}) on the swash plate to the blade. The collective pitch input θ_{col} is independent of the azimuth station, and so is the blade twist θ_t. The blade twist defines how the blade profile changes the pitch along the blade.

The flapping motion of the main rotor can be described by a first harmonic Fourier series as a function of the blade azimuth station

$$\beta = a_{con} - a_{lon}\cos(\varphi) + a_{lat}\sin(\varphi)\,, \tag{3.10}$$

which consists of the coning angle a_{con} as well as the longitudinal a_{lon} and lateral a_{lat} flapping angles. The time-derivatives of (3.10) are needed in the blade element analysis and can be found using the fact that $\varphi = \Omega t$, where t is time

$$\dot{\beta} = \dot{a}_{con} - (\dot{a}_{lon} - a_{lat}\Omega)\cos(\varphi) + (a_{lat} + a_{lon}\Omega)\sin(\varphi)\,, \tag{3.11}$$

$$\ddot{\beta} = \ddot{a}_{con} - (\ddot{a}_{lon} - 2\dot{a}_{lat}\Omega - a_{lon}\Omega^2)\cos(\varphi) + (\ddot{a}_{lat} + 2\dot{a}_{lon}\Omega - a_{lat}\Omega^2)\sin(\varphi)\,. \tag{3.12}$$

The definitions of the flapping and control angles are illustrated on figure 3.5 in relation to the hub plane and to the tip path plane. The tip path plane is described by the motion of the rotor blade tips and the angle of this is not affected by the coning as this is constant throughout an entire rotation.

3.5.1 Stabilizer Bar

As mentioned earlier the stabilizer bar is introduced to slow down the dynamics and improve the stability of the helicopter. It is in effect a small tethering rotor that receives its pitch inputs directly from the swash plate and the flapping of the stabilizer bar is then linked to the pitch input of the main rotor. This means that instead of the pitch input of

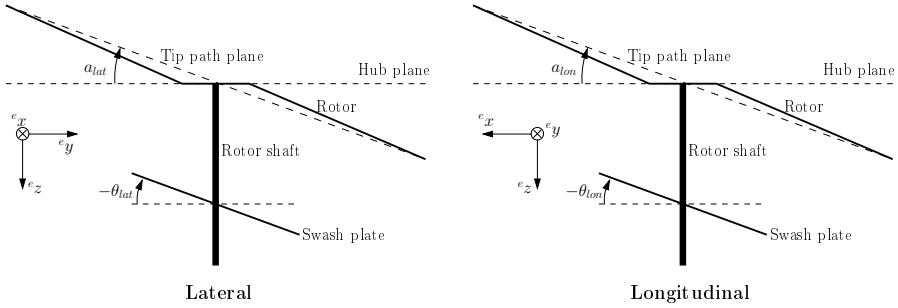

Figure 3.5: Definition of the flapping and control angles.

the main rotor coming directly from the swash plate, it is instead mixed in such a way that some comes from the swash plate and some comes from the flapping of the stabilizer bar – this is know as a Bell-Hiller system. Using this system, (3.9) for the main rotor changes to

$$\begin{aligned}\theta_r = \theta_{col} &+ K_B(-\theta_{lat}\cos(\varphi) - \theta_{lon}\sin(\varphi)) \\ &- K_H(a_{lon,sb}\sin(\varphi) + a_{lat,sb}\cos(\varphi)) + \theta_t\frac{e+r}{R}\,,\end{aligned} \tag{3.13}$$

where K_B is the Bell-factor and K_H is the Hiller-factor. Collecting the lateral and longitudinal elements (3.13) can be formulated as

$$\theta_r = \theta_{col} - \theta_{lat,mr}\cos(\varphi) - \theta_{lon,mr}\sin(\varphi)) + \theta_t\frac{e+r}{R}\,, \tag{3.14}$$

where

$$\begin{aligned}\theta_{lat,mr} &= \theta_{lat}K_B - a_{lat,sb}K_H\,, \\ \theta_{lon,mr} &= \theta_{lon}K_B - a_{lon,sb}K_H\,.\end{aligned}$$

3.5.2 Basic Aerodynamic Analysis

Figure 3.6 shows a closer inspection of a blade cross section. It shows the two forces affecting the infinitesimal blade element dr: The lift dL and the drag dD. The lift is defined as the force perpendicular to the direction of the blade velocity V_b, whereas the drag is parallel to the blade velocity. The lift on a small blade element can be described in a similar fashion as the standard air-drag equation know from basic physics as

$$dL = \frac{1}{2}\rho V_b^2 C_L c\ \ dr\,. \tag{3.15}$$

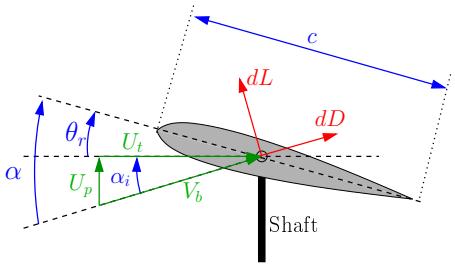

Figure 3.6: Cross section of the blade showing the blade element forces.

This means that the drag is dependent on the air density ρ, the blade velocity squared, the size of the blade, in this case the cord length c, as well as the blade lift curve slope C_L. The local coefficient of lift can be approximated as being proportional to the blade angle of attack α by a constant known as the lift coefficient C_l and (3.15) becomes

$$dL = \frac{1}{2}\rho V_b^2 C_l \alpha c \;\; dr \, . \tag{3.16}$$

Furthermore, it can be seen from figure 3.6 that the angle of attack is equal to the sum of the pitch angle θ_r and the local inflow angle α_i. This means that the angle of attack can be described by

$$\begin{aligned} &\alpha = \theta_r + \alpha_i \Leftrightarrow \\ &\alpha = \theta_r + \arctan\left(\frac{U_t}{U_p}\right) \, , \end{aligned} \tag{3.17}$$

where α_i is formulated using the horizontal (U_t) and vertical (U_p) elements of V_b. Using the assumption that vertical velocity of the blade U_p is much smaller than the forward velocity U_t ($|U_t| >> |U_p|$), which follows from an assumption of the induced velocity being much smaller that the rotational velocity of the blade, (3.17) reduces to

$$\alpha \approx \theta_r + \frac{U_t}{U_p} \, . \tag{3.18}$$

Using the same assumption it is possible to describe V_b as

$$V_b = \sqrt{U_t^2 + U_p^2} \simeq U_t \, , \tag{3.19}$$

which leads to the final description of the lift as

$$dL = \frac{1}{2}\rho U_t^2 C_l c\Big(\theta_r + \frac{U_t}{U_p}\Big) \;\; dr \, . \tag{3.20}$$

The drag on the blade element dD can be described similar to the lift

$$dD = \frac{1}{2}\rho V_b^2 C_d c \;\; dr \;, \tag{3.21}$$

where C_d is the blade drag coefficient.

Two different contributions can be identified for the horizontal blade velocity. The rotation of the blade around the shaft is the main contribution, but also helicopter motion contribute. The contribution from the helicopter motion can be expressed as the main rotor hub translational velocities ${}^{mr}v_{x_{mr}}$ and ${}^{mr}v_{y_{mr}}$ mapped to the blade by the blade azimuth station and together with element from the blade rotation it forms U_t as

$$U_t = {}^{mr}v_{x_{mr}} \sin(\varphi) - {}^{mr}v_{y_{mr}} \cos(\varphi) + \Omega_{mr}(e + r cos(\beta)) \;. \tag{3.22}$$

Defining the rotor advance ratios μ_x and μ_y as the ratio between the helicopter velocity horizontal velocities and the blade forward velocity, and by assuming small angles on the blade flapping, (3.22) can be reformulated as

$$\begin{aligned} U_t &\simeq {}^{mr}v_{x_{mr}} \sin(\varphi) - {}^{mr}v_{y_{mr}} \cos(\varphi) + \Omega(e + r) \\ &\simeq \Omega_{mr} R_{mr} \left(\frac{e + r}{R} + \mu_x sin(\varphi) - \mu_y cos(\varphi) \right) \;, \end{aligned} \tag{3.23}$$

where

$$\mu_x = \frac{{}^{mr}v_{x_{mr}}}{\Omega_{mr} R_{mr}}, \qquad \mu_y = \frac{{}^{mr}v_{y_{mr}}}{\Omega_{mr} R_{mr}} \;.$$

The vertical blade velocity consists of several elements, most significantly the induced velocity from the rotor (v_i). Another component can be identified as the flapping motion $\dot{\beta}$ of the blade itself, and finally the motion of the helicopter must be taken into account. This can be divided into two parts, one from the translational motion and one from the rotational. The mapping of the main rotor hub motion to U_p is illustrated in figure 3.7. Summing the elements, U_p can be expressed as

$$\begin{aligned} U_p =& {}^{mr}v_{z_{mr}} \cos(\beta) - v_i \cos(\beta) - {}^{mr}v_{x_{mr}} \sin(\beta) \cos(\varphi) - {}^{mr}v_{y_{mr}} \sin(\beta) \sin(\varphi) - \dot{\beta} r \\ &+ (e + r)({}^{mr}\omega_{x_{mr}} \cos(\varphi) - {}^{mr}\omega_{y_{mr}} \sin(\varphi)) \;. \end{aligned} \tag{3.24}$$

By applying small angle approximation on β and by defining the inflow ratio λ as the ratio between the actual velocity of the rotor along the z-axis and the blade forward velocity, (3.24) is formulated as

$$\begin{aligned} U_p &\simeq {}^{mr}v_{z_{mr}} - v_i - {}^{mr}v_{x_{mr}} \beta \cos(\varphi) - {}^{mr}v_{y_{mr}} \beta \sin(\varphi) - \dot{\beta} r + \\ &\quad (e + r) {}^{mr}\omega_{x_{mr}} (\cos(\varphi) - {}^{mr}\omega_{y_{mr}} \sin(\varphi)) \end{aligned} \tag{3.25}$$

$$\begin{aligned} &\simeq \Omega R \Big(\lambda - \mu_x \beta \cos(\varphi) - \mu_y \beta \sin(\varphi) \Big) - \dot{\beta} r + \\ &\quad (e + r)({}^{mr}\omega_{x_{mr}} \cos(\varphi) - {}^{mr}\omega_{y_{mr}} \sin(\varphi)) \;, \end{aligned} \tag{3.26}$$

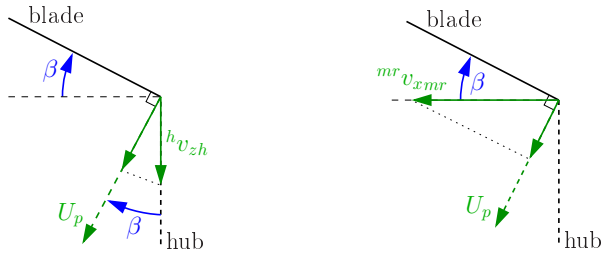

Figure 3.7: Main rotor hub translational motions projected onto U_p.

where

$$\lambda = \frac{{}^{mr}v_{zmr} - v_i}{\Omega_{mr} R_{mr}} \, .$$

A useful parameter to introduce is the blade lock number

$$\gamma = \frac{\rho C_l c R_{mr}^4}{I_b} \, , \tag{3.27}$$

which describes the relationship between the aerodynamic and the centrifugal force of the blade. The lock number describes the damping of the rotor flapping, where a high blade inertia equals a small lock number which yields low rotor damping.

3.6 Rotor Dynamics

The rotor dynamics are dominated by the blade flapping which is governed by a number of different torques working of the rotor blades.

3.6.1 Rotor Torques

In order to determine the dynamic flapping motion we use an equilibrium equation of the blade torques

$$\tau_a + \tau_{cf} + \tau_\beta + \tau_{cor} + \tau_R + \tau_{ba} + \tau_{bn} = 0 \tag{3.28}$$

where the torques in order of appearance are: Aerodynamic torque, centrifugal torque, inertial torque, Coriolis torque, restraining torque, and torque from body angular and normal acceleration. As the restraining torque of the flexible blades on the Bergen Twin is quite significant, the torque originating from the gravity is ignored.

Aerodynamic Torque

The aerodynamic torque is the primary torque and it originates from the lift force acting on a blade as shown in figure 3.4. The torque around the flapping hinge is found by integrating the lift dL over the blade length from e to R and multiplying with the lever r. This yields

$$\begin{aligned} \tau_a &= \int_0^{R-e} r \;\; dL \Leftrightarrow \\ \tau_a &= \int_0^{R-e} \frac{1}{2}\rho U_t^2 C_l c\Big(\theta_r + \frac{U_t}{U_p}\Big) r \;\; dr \; . \end{aligned} \tag{3.29}$$

The evaluated integral is shown in appendix A on page 231.

Centrifugal Torque

The centrifugal torque originates from the centrifugal force acting on the blade elements which is a consequence of the rotor spinning in relation to the main rotor coordinate system. The centrifugal force acts perpendicular to the rotation axis and as the blade flaps this results in a torque around the flapping hinge as illustrated in figure 3.8. The

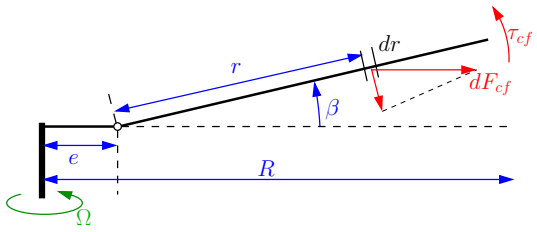

Figure 3.8: The centrifugal force dF_{cf} of the small blade element dr.

centrifugal force can be described by the standard equation

$$F = \frac{v^2}{r} m \tag{3.30}$$

where m is the object mass, r is the radius of the circular motion, and v is the velocity of the object perpendicular to the axis of rotation. We can then formulate this equation for a blade element as

$$\begin{aligned} dF_{cf} &= -\frac{\Omega(e + r\cos(\beta))^2}{e + r\cos(\beta)} dm_b \Leftrightarrow \\ dF_{cf} &= -\Omega^2(e + r\cos(\beta)) dm_b \end{aligned}$$

The torque can then determined by projecting the force perpendicularly to the blade and integrating over the blade elements

$$\begin{aligned}\tau_{cf} &= \int r\sin(\beta)\ \ dF_{cf} \Leftrightarrow \\ \tau_{cf} &= -\Omega^2 \int (e \cdot r \cdot dm + r^2 dm_b \cos(\beta))\sin(\beta)\,, \end{aligned} \tag{3.31}$$

which evaluates to

$$\tau_{cf} = -\Omega^2(eM_b + I_b\cos(\beta))\sin(\beta)\,, \tag{3.32}$$

where M_b is the first mass moment and I_b is the second mass moment of the blade (moment of inertia). Assuming a small flapping angle, the centrifugal force can be approximated as

$$\tau_{cf} \simeq -\Omega^2(eM_b + I_b)\beta\,. \tag{3.33}$$

Flapping Torque

The torque due to the flapping the blade originates from the blade angular acceleration around the flapping hinge and can be expressed as

$$\tau_\beta = -I_b\ddot{\beta}\,. \tag{3.34}$$

Coriolis Torque

The Coriolis torque originating from the Coriolis force and is a consequence of the blade element moving in the rotating main rotor frame. The Coriolis force can for a general object be calculated as

$$F_{cor} = -2m(\omega \times v)\,, \tag{3.35}$$

where m is the mass of the object, ω is the angular velocity of the reference system, and v is the velocity of the object. For the helicopter the rotating reference frame is given by pitch and roll angular velocities (${}^{mr}\omega_{xmr}$ and ${}^{mr}\omega_{xmr}$) and the velocity of the blade element originates from the blade spinning as illustrated on figure 3.9. Therefore we calculate the Coriolis force acting on a blade element as

$$dF_{cor} = -2({}^{mr}\omega_{y_{mr}}\cos(\varphi) + {}^{mr}\omega_{xmr}\sin(\varphi))\Omega(e + r\cos(\beta))\ \ dm_b\,. \tag{3.36}$$

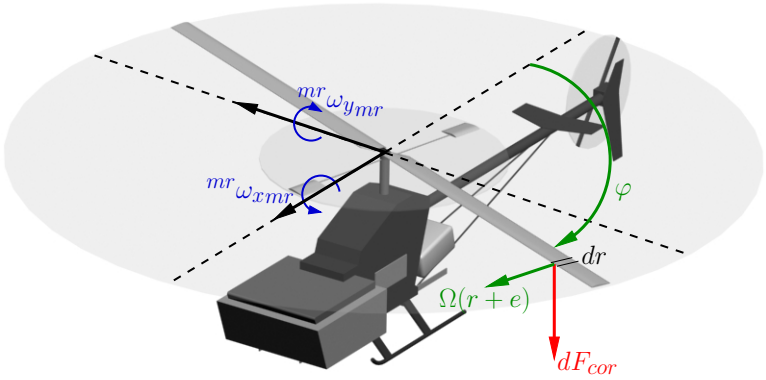

Figure 3.9: The Coriolis force on a blade element.

The Coriolis torque is then found by integration and by again assuming a small flapping angle

$$\begin{aligned}
\tau_{cor} &= \int r \;\; dF_{cor} \\
&= -2(^{mr}\omega_{y_{mr}} \cos(\varphi) + {}^{mr}\omega_{x_{mr}} \sin(\varphi))\Omega \int (e \cdot r \cdot dm_b + r^2 dm_b \cos(\beta)) \\
&= -2(^{mr}\omega_{y_{mr}} \cos(\varphi) + {}^{mr}\omega_{x_{mr}} \sin(\varphi))(eM_b + I_b \cos(\beta)) \\
&\approx -2(^{mr}\omega_{y_{mr}} \cos(\varphi) + {}^{mr}\omega_{x_{mr}} \sin(\varphi))(eM_b + I_b)\,. \qquad (3.37)
\end{aligned}$$

Restrain Torque

The torque due to the flexing of the blade is modeled as a spring in the hinge with the spring constant K_s (see figure 3.10)

$$\tau_R = -K_s \beta\,. \qquad (3.38)$$

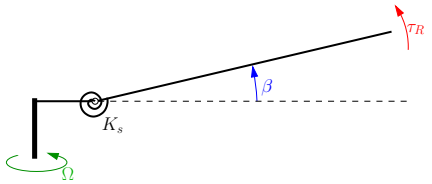

Figure 3.10: The restrain torque from the flexing of the blade.

Body Angular Torque

The force on a blade element originating from the helicopter angular acceleration around the x and y axis is

$$dF_{ba} = r({}^{h}\dot{\omega}_{y_h}\cos(\varphi) - {}^{h}\dot{\omega}_{xh}\sin(\varphi))\ \ dm_b\ . \tag{3.39}$$

This integrates to a torque as

$$\begin{aligned}\tau_{ba} &= \int\ \ dF_{ba} \\ &= \int r^2({}^{h}\dot{\omega}_{y_h}\cos(\varphi) - {}^{h}\dot{\omega}_{xh}\sin(\varphi))\ \ dm_b \\ &= ({}^{h}\dot{\omega}_{y_h}\cos(\varphi) - {}^{h}\dot{\omega}_{xh}\sin(\varphi))I_b\ .\end{aligned} \tag{3.40}$$

Body Normal Torque

As the helicopter accelerates along the body fixed z axis a force is generated on the blade elements

$$dF_{bn} = {}^{h}a_{zh}\ \ dm_b\ . \tag{3.41}$$

This can be formulated using rigid body states as

$$dF_{bn} = ({}^{h}\dot{v}_{zh} - {}^{h}v_{xh}{}^{h}\omega_{y_h} + {}^{h}v_y{}^{h}\omega_{xh})\ \ dm_b\ , \tag{3.42}$$

which takes the rotating coordinate frame of the helicopter into account. The torque can then be calculated

$$\begin{aligned}\tau_{bn} &= \int r\ \ dF_{bn} \\ &= ({}^{h}\dot{v}_{zh} - {}^{h}v_{xh}{}^{h}\omega_{y_h} + {}^{h}v_y{}^{h}\omega_{xh})\int r\ \ dm_b \\ &= M_b({}^{h}\dot{v}_{zh} - {}^{h}v_{xh}{}^{h}\omega_{y_h} + {}^{h}v_y{}^{h}\omega_{xh})\ .\end{aligned} \tag{3.43}$$

3.6.2 Flapping

The describing dynamics of the rotor flapping can now be obtained by using the different torques derived above.

Main Rotor Flapping Equation

For the main rotor the different torques are substituted into (3.28) together with (3.10), (3.11), and (3.12). A series of trigonometric equations is applied and all higher harmonics, like $\sin(2\varphi)$, are discarded. To find the tip-path plane dynamics, the elements which contains $\sin(\varphi)$ is equated to yield the equation for $\ddot{a}_{lat}$, the elements which contains $\cos(\varphi)$ is equated to yield the equation for $\ddot{a}_{lon}$, and the constant elements are equated to yield the equation for $\ddot{a}_{con}$. The resulting second order equation can be formulated as

$$\ddot{\boldsymbol{a}}_{mr} + \boldsymbol{D}_{mr}\dot{\boldsymbol{a}}_{mr} + \boldsymbol{K}_{mr}\boldsymbol{a}_{mr} = \boldsymbol{J}_{mr}\boldsymbol{\theta}_{mr} + \boldsymbol{E}_{mr}\lambda + \boldsymbol{G}_{mr} \tag{3.44}$$

where

$$\boldsymbol{a}_{mr} = \begin{bmatrix} \ddot{a}_{con} \\ \ddot{a}_{lon} \\ \ddot{a}_{lat} \end{bmatrix}, \quad \boldsymbol{\theta}_{mr} = \begin{bmatrix} \theta_{col} \\ \theta_{lat,mr} \\ \theta_{lon,mr} \end{bmatrix}.$$

The resulting flapping equations are shown in expanded form in appendix A on page 231.

Stabilizer Bar Flapping Equation

The flapping of the stabilizer bar is a very important element of the helicopter model due to the Bell-Hiller mixing system mentioned earlier. The flapping dynamics is derived in the same manner as for the main rotor with certain differences. Because the stabilizer bar is a tethering rotor, i.e. it can pivot freely like a seesaw in the rotor hub, no coning can occur, there is no hinge offset, and the restrain torque can be omitted. The torque equilibrium is similar to (3.28) for the main rotor

$$\tau_{a,sb} + \tau_{cf,sb} + \tau_{\beta,sb} + \tau_{cor,sb} + \tau_{ba,sb} + \tau_{bn,sb} = 0 \tag{3.45}$$

with the restrain torque omitted. As it can be seen on figure 3.11 the aerodynamic lifting areas of the stabilizer bar are small paddles mounted on the end of a bar. Thus, when deriving the aerodynamic torque, the integration is done from R_i to R_o

$$\tau_{a,sb} = \int_{R_i}^{R_o} dL_{sb} \cdot r \;\; dr \tag{3.46}$$

The flapping equation is similar to the main rotor equation

$$\ddot{\boldsymbol{a}}_{sb} + \boldsymbol{D}_{sb}\dot{\boldsymbol{a}}_{sb} + \boldsymbol{K}_{sb}\boldsymbol{a}_{sb} = \boldsymbol{J}_{sb}\boldsymbol{\theta}_{sb} + \boldsymbol{E}_{sb}\lambda + \boldsymbol{G}_{sb} \tag{3.47}$$

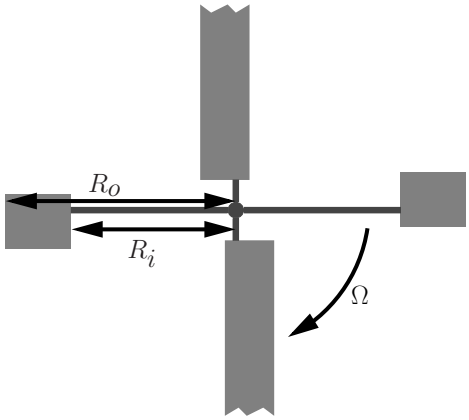

Figure 3.11: The stabilizer bar.

where

$$\boldsymbol{a}_{sb} = \begin{bmatrix} \ddot{a}_{lon,sb} \\ \ddot{a}_{lat,sb} \end{bmatrix}, \quad \boldsymbol{\theta}_{mr} = \begin{bmatrix} \theta_{lat} \\ \theta_{lon} \end{bmatrix} .$$

The resulting equations are shown in expanded form in appendix A on page 231.

Tail Rotor Flapping

As with the stabilizer bar, the tail rotor can be modeled in a similar fashion as the main rotor, but for the tail rotor the main difference is that it only has a collective pitch input. Due to the small size of the tail rotor it is judged that its dynamics are sufficiently fast to be negleced. Furthermore, the blades are quite stiff compared to the size of the rotor which result in very small flapping angles and steady state flapping for the tail rotor is therefore also neglected.

3.7 Force and Torque Generation

The two main force generators are the main and tail rotor, the stabilizer bar is assumed to produce only neglectable forces. Forces are also generated by drag on the helicopter and slung load fuselage and helicopter empennages. The rotor forces and torques are derived in the rotor coordinate systems and the derivations are done using blade element theory like with the flapping equations.

3.7.1 Main Rotor Forces and Torques

The most dominant force is the thrust along the z-axis ($T = -F_z$) and the most dominant torque is the around the same axis. However, for the main rotor also the forces and torques along and around the x- and y-axis are quite significant. The forces generated by the the main rotor are assumed to be primarily generated by the aerodynamic lift dL and drag dD (given by (3.16) and (3.21)) on the blades and other contributions from blade flapping etc. are neglected. The aerodynamic contributions are found by projecting dL and dD onto the rotor coordinate system, integrating along the blade, and finally integrating around one blade revolution. Initially dL and dD for a blade element is projected onto a vertical and horizontal axis as illustrated in figure 3.12. These projected forces are then further

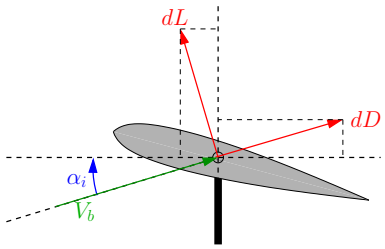

Figure 3.12: The projection of the blade element forces.

projected in the vertical and horizontal plane by the flapping angle β and the azimuth station φ as shown in figure 3.13 and 3.14. By using these projections we can find the

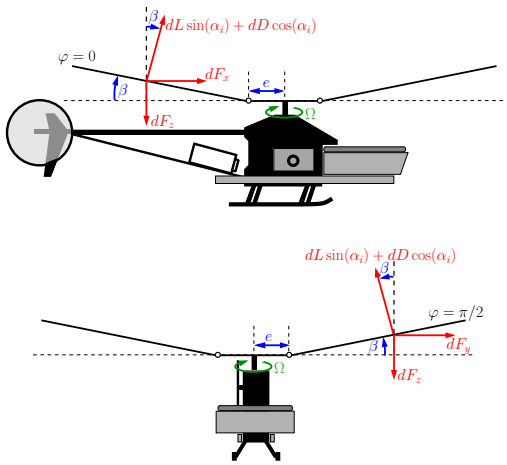

Figure 3.13: Vertical projection of the blade forces, right side and front view.

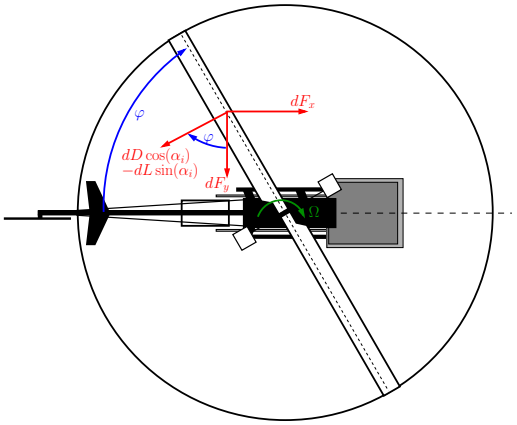

Figure 3.14: Horizontal projection of the the blade forces, top view.

infinitesimal forces along the rotor frame axis as

$$\begin{aligned} dF_{x_{mr}} &= -(dD\cos(\alpha_i) - dL\sin(\alpha_i))\sin(\varphi) + (dL\cos(\alpha_i) + dD\sin(\alpha_i))\sin(\beta)\cos(\varphi)\ , \\ dF_{y_{mr}} &= (dD\cos(\alpha_i) - dL\sin(\alpha_i))\cos(\varphi) + (dL\cos(\alpha_i) + dD\sin(\alpha_i))\sin(\beta)\sin(\varphi)\ , \\ dF_{z_{mr}} &= -(dL\cos(\beta)\cos(\alpha_i) + dD\cos(\beta)\sin(\alpha_i))\ . \end{aligned} \tag{3.48}$$

The complexity of the infinitesimal force double integration can greatly be reduced by using small angle approximations on β and α_i as with the derivations of the flapping equations. Furthermore, it is assumed that the lift component of the total force is much greater than the drag component $dL >> dD$. Seen from a physical point of view this means that the model is incapable of handling stall. Using these assumptions the infinitesimal force equations can be simplified to

$$\begin{aligned} dF_{x_{mr}} &= -dD\sin(\varphi) + dL(\beta\cos(\varphi) + \alpha_i\sin(\varphi))\ , \\ dF_{y_{mr}} &= dD\cos(\varphi) + dL(\beta\sin(\varphi) - \alpha_i\cos(\varphi))\ , \\ dF_{z_{mr}} &= -dL\ . \end{aligned}$$

The infinitesimal forces are then integrated over r along the blade from 0 to $R-e$. Averaging over one revolution is then done by integration over φ from 0 to 2π and dividing with

2π and finally the resulting forces are found by multiplying with the number of blades b

$$F_x = \frac{bc}{2\pi}\frac{\rho}{2}\int_0^{2\pi}\int_0^{R-e} U_t^2\Bigg(- C_d\sin(\varphi) + C_l\Big(\theta_r + \frac{U_p}{U_t}\Big) \Big(\beta\cos(\varphi) + \frac{U_p}{U_t}\sin(\varphi)\Big)\Bigg)\ dr d\varphi\,, \tag{3.49}$$

$$F_y = \frac{bc}{2\pi}\frac{\rho}{2}\int_0^{2\pi}\int_0^{R-e} U_t^2\Bigg(C_d\cos(\varphi) + C_l\Big(\theta_r + \frac{U_p}{U_t}\Big) \Big(\beta\sin(\varphi) - \frac{U_p}{U_t}\cos(\varphi)\Big)\Bigg)\ dr d\varphi\,, \tag{3.50}$$

$$F_z = -\frac{bc}{2\pi}\frac{\rho}{2}C_l\int_0^{2\pi}\int_0^{R-e} U_t^2\Big(\theta_r + \frac{U_t}{U_p}\Big)\ dr d\varphi\,. \tag{3.51}$$

The torques generated by the main rotor can, like the forces, be divided into a primary part that originates from the aerodynamic forces and a part that originates from flapping and similar. For the torque around the z-axis only aerodynamic components are considered and other effects are neglected. Furthermore, effects from the lag hinge are neglected and the blade is considered a stiff rod seen from above. Around the x- and y-axis the blades are modeled as flapping around a spring restrained hinge and both the aerodynamic element and the element from the restrain spring are including in the torque derivation. Other contributions from e.g. blade flapping acceleration are neglected.

The contribution by the drag and lift to the torque around the z-axis is shown on figure 3.14 and the infinitesimal torque can then be found as

$$d\tau_z = -(e+r)(dD\cos(\alpha_i) - dL\sin(\alpha_i))\,, \tag{3.52}$$

which reduces to

$$d\tau_z = -(e+r)(dD - dL\alpha_i)\,, \tag{3.53}$$

through small angle approximation. The final torque is found as

$$\tau_z = \frac{bc}{2\pi}\frac{\rho}{2}\int_0^{2\pi}\int_0^{R-e} U_t^2(r+e)\Bigg(- C_d + C_l\frac{U_p}{U_t}\Big(\theta_r + \frac{U_p}{U_t}\Big)\Bigg)\ dr d\varphi\,. \tag{3.54}$$

The aerodynamic lift contribute to the lateral and longitudinal torque through the lever given by the hinge offset as shown on figure 3.15. The aerodynamic torque for a blade can be described as

$$\tau_{aero} = eL\cos(\beta)\,, \tag{3.55}$$

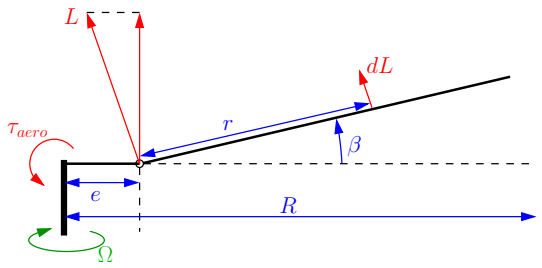

Figure 3.15: The aerodynamic lift contribution to the torque around the hub.

which can be mapped to the lateral and longitudinal torques and reduced through the previously mentioned small angle approximation on the flapping angles to

$$\tau_{aerox} = eL\sin(\varphi)\,, \tag{3.56}$$
$$\tau_{aeroy} = -eL\cos(\varphi)\,. \tag{3.57}$$

The torque caused by the blade restrain is given as

$$\tau_{res} = K_s\beta\,, \tag{3.58}$$

for one blade. This can be mapped onto the lateral and longitudinal axis as

$$\tau_{resx} = K_s\beta\sin(\varphi)\,, \tag{3.59}$$
$$\tau_{resy} = K_s\beta\cos(\varphi)\,, \tag{3.60}$$

through the blade azimuth station. The total lateral and longitudinal torques are found as the sum of the aerodynamic and the restrain component. The aerodynamic component is found by calculating the lift L as in the derivation of the thrust. The restrain component is found by averaging (3.59) and (3.60) over one revolution and multiplying with the number of blades

$$\tau_x = \frac{bc}{2\pi}\frac{\rho}{2}eC_l\int_0^{2\pi}\int_0^{R-e}U_t^2\left(\theta_r+\frac{U_p}{U_t}\right)\sin(\varphi)\;\;drd\varphi\;+\;\frac{b}{2\pi}K_s\int_0^{2\pi}\beta\sin(\varphi)\;\;d\varphi\,, \tag{3.61}$$

$$\tau_y = -\frac{bc}{2\pi}\frac{\rho}{2}eC_l\int_0^{2\pi}\int_0^{R-e}U_t^2\left(\theta_r+\frac{U_p}{U_t}\right)\cos(\varphi)\;\;drd\varphi\;+\;\frac{b}{2\pi}K_s\int_0^{2\pi}\beta\cos(\varphi)\;\;d\varphi\,. \tag{3.62}$$

The results of (3.49) - (3.51), (3.54), (3.61), and (3.62) can be found in appendix A on page 231.

3.7.2 Tail Rotor Forces and Torques

For the tail rotor only the most significant components, the thrust $F_{y_{tr}}$ and the respective torque around the thrust axis $\tau_{y_{tr}}$, are modeled. It is furthermore assumed that within the flight-envelope of the helicopter, the downwash from the main rotor has a negligible effect on the tail rotor. It is also assumed that the induced velocity from the tail rotor is much larger than the helicopter velocities such that the assumption $U_{ttr} >> U_{p_{tr}}$ holds. The

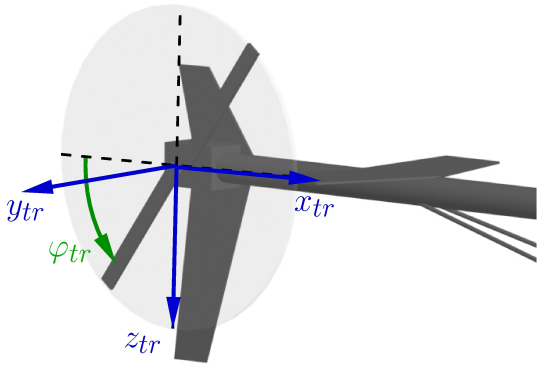

Figure 3.16: Close up on the tail rotor.

derivations of the tail rotor force and torque is analogue to the derivations for the main rotor without the flapping elements. The tail rotor blade horizontal and vertical velocity components is found as

$$U_{ttr} = \Omega_{tr} R_{tr} \left(\frac{r_{tr}}{R_{tr}} + \mu_{x\,tr} \sin(\varphi_{tr}) + \mu_{z\,tr} \cos(\varphi_{tr}) \right) , \tag{3.63}$$

$$U_{p_{tr}} = \Omega_{tr} R_{tr} \lambda_{tr} + r_{tr} \left({}^{tr}\omega_z \cos(\varphi_{tr}) + {}^{tr}\omega_x \sin(\varphi_{tr}) \right) , \tag{3.64}$$

where

$$\lambda_{tr} = \frac{{}^{tr}v_y - v_{itr}}{\Omega_{tr} R_{tr}} ,$$

$$\mu_{x\,tr} = \frac{{}^{tr}v_x}{\Omega_{tr} R_{tr}} ,$$

$$\mu_{z\,tr} = \frac{{}^{tr}v_z}{\Omega_{tr} R_{tr}} .$$

The thrust force and torque is found as

$$F_{ztr} = -\frac{b_{tr}c_{tr}}{2\pi}\frac{\rho}{2}C_{ltr}\int_0^{2\pi}\int_0^{R_{tr}} U_{ttr}^2\Big(\theta_{rtr} + \frac{U_t tr}{U_{ptr}}\Big)\ dr_{tr}d\varphi_{tr}\ , \tag{3.65}$$

$$\tau_{ztr} = \frac{b_{tr}c_{tr}}{2\pi}\frac{\rho}{2}$$
$$\int_0^{2\pi}\int_0^{R_{tr}} U_{ttr}^2 r_{tr}\left(-C_{dtr} + C_{ltr}\frac{U_{ptr}}{U_{ttr}}\Big(\theta_{rtr} + \frac{U_{ptr}}{U_{ttr}}\Big)\right)\ dr_{tr}d\varphi_{tr}\ . \tag{3.66}$$

3.7.3 Fuselage Forces

The fuselage forces, both from the helicopter and the load, originates from air drag. The drag forces are defined along the body coordinate system axis and are assumed to act in the body CM and thus causing no torques. They can be calculated using the standard quadratic drag function which describes the drag as proportional to the square of the speed

$${}^bD_{xb} = -\frac{\rho}{2}d_{xb}A_{xb}|{}^bv_{xb}|{}^bv_{xb}\ , \tag{3.67}$$

$${}^bD_{yb} = -\frac{\rho}{2}d_{yb}A_{yb}|{}^bv_{yb}|{}^bv_{yb}\ , \tag{3.68}$$

$${}^bD_{zb} = -\frac{\rho}{2}d_{zb}A_{zb}|{}^bv_{zb} - {}^bv_{ib}|({}^bv_{zb} - {}^bv_{ib})\ , \tag{3.69}$$

where b indicates a generic body, i.e. ${}^lv_{il}$ is the induced inflow at the slung load in the load body coordinate frame.

3.7.4 Empennage Forces

Three different empennage surfaces are considered on the helicopter: The tail plane and fin and the box in the nose of the helicopter is considered as a front plane. These surfaces are modeled as flat plates without any aerodynamic profile to provide lift and they are therefore considered to only generate drag. The tail and front plans are placed such that they are in the wake of the main rotor and the tail fin is placed such that part of it is in the wake of the tail rotor which is accounted for by using the factor K_{tf}. The three drag forces are calculated as

$$D_{tf} = -\frac{\rho}{2}d_{tf}A_{tf}|({}^{tr}v_{y_{tf}} - v_{itr}K_{tf})|({}^{tr}v_{y_{ft}} - v_{itr}K_{tf})\ , \tag{3.70}$$

$$D_{tp} = -\frac{\rho}{2}d_{tp}A_{tp}|({}^{tp}v_{ztp} - v_i)|({}^{tp}v_{ztp} - v_i)\ , \tag{3.71}$$

$$D_{fp} = -\frac{\rho}{2}d_{fp}A_{fp}|({}^{fp}v_{z_{fp}} - v_i)|({}^{fp}v_{z_{fp}} - v_i)\ . \tag{3.72}$$

3.8 Induced Inflow

Momentum theory assumes that the rotor behaves like a circular wing and thrust is generated when the rotor moves air downwards through what is assumed to be a virtual tube as illustrated in figure 3.17. The induced inflow is directly related to the thrust force which

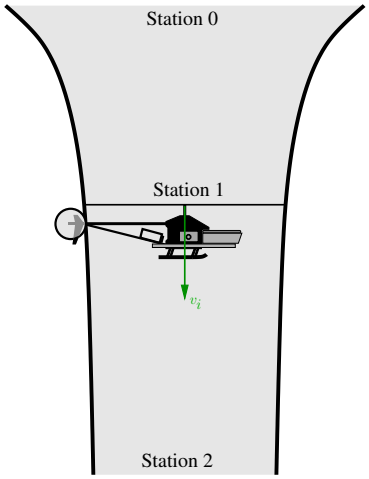

Figure 3.17: The airflow through the rotor from station 0 to station 2 in hover.

for the main rotor is defined as

$$T = -{}^{mr}F_{z_{mr}} \, . \tag{3.73}$$

The amount of thrust generated is determined by the change of momentum for the air when it is moved by the rotor from station 0 far above the helicopter (upstream) to station 2 far below the helicopter (downstream). As the tube that the air moves in is assumed to be a closed system, the law of conservation of mass states that the mass flux at station 0 must be equal to the mass flux at station 2. Thus the change in momentum is purely generated by

$$\Delta v = v_2 - v_0 \, , \tag{3.74}$$

which is the change in air velocity though the tube. By assuming that the air is at rest far upstream at station 0, the velocity change reduces to

$$\Delta v = v_2 \, . \tag{3.75}$$

This means that the thrust can be described as

$$\begin{aligned} T &= \dot{m}\Delta v \\ &= \dot{m}v_2 \end{aligned} \tag{3.76}$$

where $\dot{m}$ is the mass flux of the air. The mass flow can be described as product of the velocity of the air through the rotor v_i, the area it passes through A, and the air density ρ, which means that (3.76) can be formulated as

$$T = \rho A v_i v_2 \, . \tag{3.77}$$

To relate (3.77) to the induced velocity, a second thrust equation is derived using pressure considerations. Thrust can be described as the pressure change over the rotor

$$T = \Delta p A \, . \tag{3.78}$$

The pressure change is equal to the difference between the pressure at station 0 (p_0) and at station 2 (p_2). At station 0 the air is in rest and only the static pressure contribute

$$p_0 = p_{\text{static}} \tag{3.79}$$

At station 2 the pressure is equal to the static pressure plus the dynamic pressure added by the increased velocity described by 3.75. Using Bernoulli's equation the pressure at station 2 then becomes

$$p_2 = p_0 + \frac{1}{2}\rho v_2^2 \, , \tag{3.80}$$

which yields a pressure change of

$$\Delta p = \frac{1}{2}\rho v_2^2 \, . \tag{3.81}$$

This means that (3.78) becomes

$$T = \frac{1}{2}\rho A v_2^2 \tag{3.82}$$

and by using this together with (3.77) it is found that the air velocity at station 2 is twice the air velocity at the rotor

$$\begin{aligned} \frac{1}{2}\rho A v_2^2 &= \rho A v_i v_2 \Leftrightarrow \\ v_2 &= 2 v_i \, . \end{aligned} \tag{3.83}$$

The theory is derived using a hover situation assumption, but according to [Johnson, 1980] validation against more advanced vortex theory and experimental data shows good agreement over a very wide flight envelope. The equation can therefore be extended to encompass non-hover conditions as shown in figure 3.18. The results derived above using pressure considerations and Bernoulli's equation are still valid as the pressure change over the rotor is generated by the induced inflow. However, for a non-hover flight condition, (3.77) changes to

$$T = \rho A U v_2 \, , \tag{3.84}$$

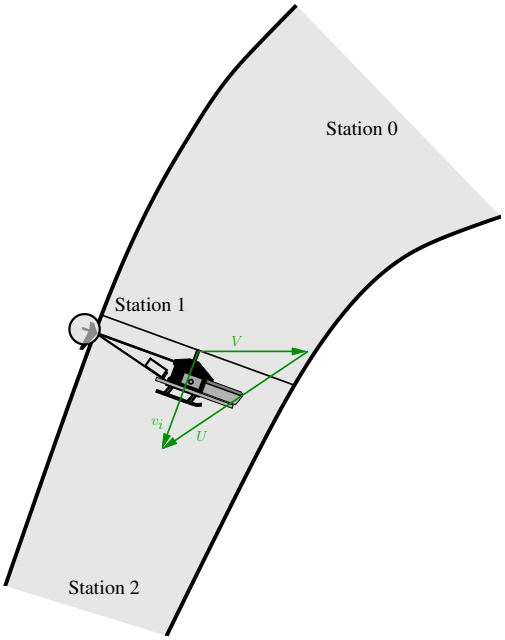

Figure 3.18: The airflow through the rotor in flight.

where U is the rotor speed through the air and is defined for the main rotor as

$$U = \sqrt{{}^{mr}v_{x_{mr}}{}^2 + {}^{mr}v_{y_{mr}}{}^2 + ({}^{mr}v_{z_{mr}} - v_i)^2}\,. \tag{3.85}$$

Using (3.83) the final thrust / induced inflow relation becomes

$$\begin{gathered} T = 2\rho A U v_i \Leftrightarrow \\ v_i = \frac{T}{2\rho A\sqrt{{}^{mr}v_{x_{mr}}{}^2 + {}^{mr}v_{y_{mr}}{}^2 + ({}^{mr}v_{z_{mr}} - v_i)^2}}\,, \end{gathered} \tag{3.86}$$

A dimensionless thrust coefficient C_T is in introduced

$$C_T = \frac{T}{\rho A(\Omega_{mr} R_{mr})^2}\,, \tag{3.87}$$

together with μ_x, μ_y, and μ_z as the advance ratio coefficients. These expressions are then

substituted into the inflow ratio λ

$$\begin{aligned}\lambda &= \frac{{}^{mr}v_{z_{mr}} - v_i}{\Omega_{mr} R_{mr}} \\ &= \frac{{}^{mr}v_{z_{mr}}}{\Omega_{mr} R_{mr}} - \frac{C_T(\Omega_{mr} R_{mr})}{2\sqrt{({}^{mr}v_{z_{mr}}{}^2 + {}^{mr}v_{y_{mr}}{}^2) + ({}^{mr}v_{z_{mr}} - v_i)^2}} \\ &= \mu_z - \frac{C_T}{2\sqrt{(\mu_x^2 + \mu_y^2) + \lambda^2}}\,, \end{aligned} \tag{3.88}$$

To solve this equation to find λ an iterative Newton-Raphson approach can be taken as described in [Johnson, 1980], but here a analytical approach is taken. The equation is reformulated as

$$f(\lambda) = \lambda - \mu_z + \frac{C_T}{2\sqrt{(\mu_x^2 + \mu_y^2) + \lambda^2}} = 0\,, \tag{3.89}$$

and solved using Maple to a fourth order equation which yields four solutions. The real part of the solutions are back-substituted into (3.89) and the smallest function value provides the correct lambda.

The tail rotor induced inflow is analog to the main rotor inflow and can be derived as

$$\lambda_{tr} = \mu_{y_{tr}} - \frac{C_{Ttr}}{2\sqrt{({\mu_{x_{tr}}}^2 + {\mu_{z_{tr}}}^2) + \lambda_{tr}^2}}\,. \tag{3.90}$$

3.8.1 Rotor Downwash Effects on Load

The modeling of the interaction between load and main rotor wake is done using [Ronen *et al.*, 1986] as inspiration. It is assumed that the load is at all time either outside the wake or in the far wake.

Wake Geometry

The purpose of determining the wake geometry is to be able to predict whether the load is inside or outside the wake. One way to consider the wake is a contracting cylinder as illustrated in figure 3.17. High above the helicopter (at station 0) the flow is slow and the cylinder wide. Close to the helicopter (at station 1, denoted the near wake) flow velocity is v_i and the cylinder is described by the circular tip path plane. Down stream under the helicopter (at station 2, denoted the far wake), momentum theory predicts that the inflow velocity changes from v_i to $2v_i$ as the wake develops and the wake contracts fully. As the helicopter moves through the air, the cylinder stretches behind the helicopter and the mapping of the wake is dependent on the induced inflow and the helicopter forward velocity (see figure 3.18).

We simplify this description by modeling it using two elliptical cylinders, one to describe the near wake and one for the far wake as shown in figure 3.19. As mentioned earlier it is assumed that the load is situated far enough down stream to be in the far wake and therefore we do not to consider the region between the near and far wake. The

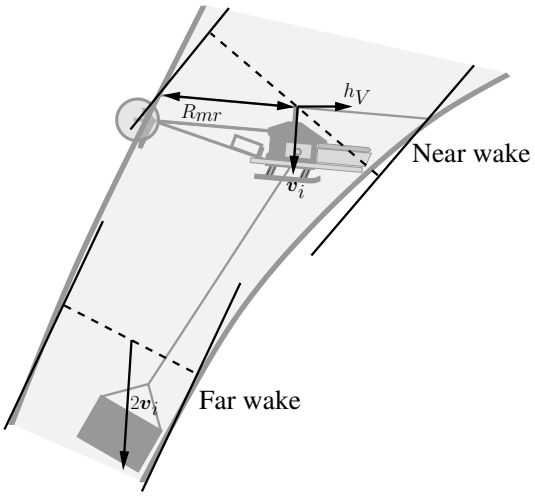

Figure 3.19: The simplified model of the wake using two cylinders for near and far wake.

direction of the near wake is given by the wake-skew angle

$$\chi_s = \arctan\left(\frac{-\lambda_{mr}}{\mu_{mr}}\right) , \tag{3.91}$$

where $\mu_{mr} = \sqrt{\mu_x^2 + \mu_y^2 + \mu_z^2}$. This angle changes further down the wake as the inflow velocity changes from v_i to $2v_i$ in the fully developed wake and by calculating this a prediction of the wake center-line can be made. An important part of this prediction is the distance from the rotor to the far wake, both [Ronen *et al.*, 1986] and [Chen, 1990] mentions a distance of $1.5R_{mr}$ to be a suitable assumption.

In the near wake the cylinder is centered around the velocity vector $^h\boldsymbol{V}'$

$$^h\boldsymbol{V}' = {}^h\boldsymbol{v}_i - {}^h\boldsymbol{V} , \tag{3.92}$$

where $^h\boldsymbol{v}_i$ is a vector perpendicular to the tip path plane with the length v_i. In the far field the wake follows

$$^h\boldsymbol{V}'' = 2^h\boldsymbol{v}_i - {}^h\boldsymbol{V} . \tag{3.93}$$

The position of the far wake starting point is described by the vector $\boldsymbol{R}_{fw}$ is then given by

$$ {}^{h}\boldsymbol{R}_{fw} = 1.5R_{mr}\frac{{}^{h}\boldsymbol{V}^{'}}{|{}^{h}\boldsymbol{V}^{'}|} , \tag{3.94} $$

as illustrated in figure 3.20.

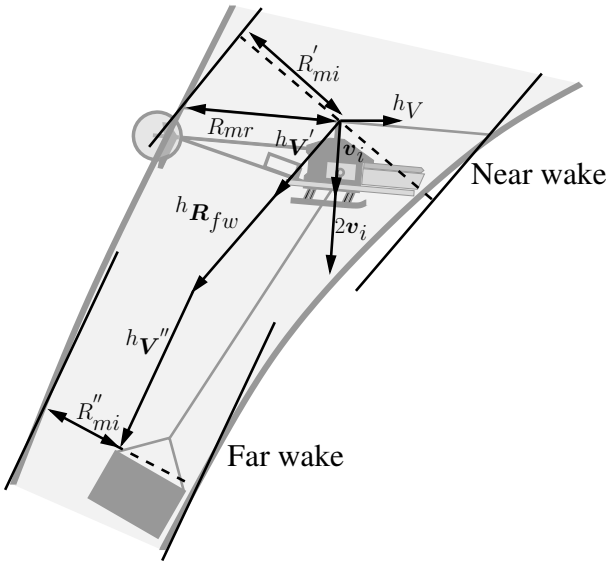

Figure 3.20: Rotor wake geometry.

To calculate the boundaries of the far wake we use the fact that the wake has a circular cross section at the tip path plane. This means that the cross section perpendicular to ${}^{h}\boldsymbol{V}^{'}$ is a ellipse with a major axis radius of

$$ R_{ma}^{'} = R_{mr} , \tag{3.95} $$

and a minor axis radius of

$$ R_{mi}^{'} = R_{mr}\cos(\chi_s) . \tag{3.96} $$

If we assume that the tube contracts an equal amount on both axes, the cross section ellipse perpendicular to ${}^{h}\boldsymbol{V}^{''}$ in the far wake, can be described by

$$ R_{ma}^{''} = K_{con}R_{ma}^{'} , \tag{3.97} $$

$$ R_{mi}^{''} = K_{con}R_{mi}^{'} . \tag{3.98} $$

The continuity equation used in the momentum theory states that the mass flow is constant throughout the wake and if we assume constant pressure both in the near and far wake, it makes the equation only dependent on tube cross section area and velocity. This means that the contraction of the tube can be calculated as

$$\begin{aligned}\pi R_{ma}^{'} R_{mi}^{'} \| {}^{h}\boldsymbol{V}^{'} \| &= \pi R_{ma}^{''} R_{mi}^{''} \| {}^{h}\boldsymbol{V}^{''} \| \Leftrightarrow \\ R_{ma}^{'} R_{mi}^{'} \| {}^{h}\boldsymbol{V}^{'} \| &= K_{con} R_{ma}^{'} K_{con} R_{mi}^{'} \| {}^{h}\boldsymbol{V}^{''} \| \Leftrightarrow \\ K_{con} &= \sqrt{\frac{\| {}^{h}\boldsymbol{V}^{'} \|}{\| {}^{h}\boldsymbol{V}^{''} \|}} \, . \end{aligned} \tag{3.99}$$

Load Wake Interaction

The position of the load relative to the beginning of the far wake can be calculated as

$$\begin{aligned} {}^{h}\boldsymbol{R}_{wl} &= \boldsymbol{T}_{he}({}^{e}\boldsymbol{R}_{l} - {}^{h}\boldsymbol{R}_{h}) - {}^{h}\boldsymbol{R}_{fw} \Leftrightarrow \\ {}^{h}\boldsymbol{R}_{wl} &= {}^{h}\boldsymbol{R}_{Rl} - {}^{h}\boldsymbol{R}_{fw} \, , \end{aligned} \tag{3.100}$$

in the helicopter fixed frame. We now introduce a new frame which is fixed in the wake such that the z-axis points along $\boldsymbol{V}^{''}$ and the x-axis points in the opposite direction of $\boldsymbol{V}$. The Euler angles for the transformation between the wake frame and the helicopter frame is then determined as

$$\begin{aligned} \phi_w &= 0 \, , \\ \theta_w &= \arccos\left(\frac{\sqrt{v_x^2 + v_y^2}}{\sqrt{(2v_i - v_z)^2 + v_x^2 + v_y^2}} \right) \, , \\ \psi_w &= \arccos\left(\frac{v_x}{\sqrt{v_x^2 + v_y^2}} \right) \, , \end{aligned}$$

This can be used to transform the position of the load relative to the wake into this frame

$${}^{w}\boldsymbol{R}_{wl} = \boldsymbol{T}_{wh} {}^{h}\boldsymbol{R}_{wl} \, , \tag{3.101}$$

which makes it possible directly to compare it to the wake boundaries found earlier. Using this, the load is then assumed to be inside the wake when the following condition is true

$$\left(\frac{x_{wl}}{R_{mi}^{''}} \right)^2 + \left(\frac{y_{wl}}{R_{ma}^{''}} \right)^2 < 1 \, , \tag{3.102}$$

and outside when false – under the assumption that the load is more that $1.5R_{mr}$ under the helicopter. The above can be evaluated by substituting in (3.95)-(3.98)

$$\left(\frac{x_{wl}}{K_{con} R_{mr} \cos(\chi_s)} \right)^2 + \left(\frac{y_{wl}}{K_{con} R_{mr}} \right)^2 < 1 \, . \tag{3.103}$$

When the load is inside the wake, the load velocities is augmented the following term

$$ {}^{l}\boldsymbol{V}_{il} = \boldsymbol{T}_{le}\boldsymbol{T}_{eh} \begin{bmatrix} 0 \\ 0 \\ 2v_i \end{bmatrix} , \tag{3.104} $$

which can then be used to calculate the drag on the load. When outside the wake, the load velocities are simply used alone.

3.9 Force and Moment Transformations

The final step of the aerodynamic modeling is to project all the forces and torques onto the CM of the helicopter and load. The final summation and projection of forces for the helicopter can be described as

$$ {}^{h}\boldsymbol{F}_h = m_h g \begin{bmatrix} -\sin(\phi_h) \\ \sin(\phi_h)\cos(\theta_h) \\ \cos(\phi_h)\cos(\theta_h) \end{bmatrix} + {}^{h}\boldsymbol{F}_{mr} + {}^{h}\boldsymbol{F}_{tr} + {}^{h}\boldsymbol{D}_{tf} + {}^{h}\boldsymbol{D}_{tp} + {}^{h}\boldsymbol{D}_{fp} + {}^{h}\boldsymbol{D}_h , $$

$$ {}^{h}\boldsymbol{\tau}_h = {}^{h}\boldsymbol{\tau}_{mr} + {}^{h}\boldsymbol{F}_{mr} \times {}^{h}\boldsymbol{R}_{mr} + {}^{h}\boldsymbol{F}_{tr} \times {}^{h}\boldsymbol{R}_{tr} + {}^{h}\boldsymbol{D}_{tf} \times {}^{h}\boldsymbol{R}_{tf} + {}^{h}\boldsymbol{D}_{tp} \times {}^{h}\boldsymbol{R}_{tp} + {}^{h}\boldsymbol{D}_{fp} \times {}^{h}\boldsymbol{R}_{fp} , $$

and for the load as

$$ {}^{l}\boldsymbol{F}_l = m_l g \begin{bmatrix} -\sin(\phi_l) \\ \sin(\phi_l)\cos(\theta_l) \\ \cos(\phi_l)\cos(\theta_l) \end{bmatrix} + {}^{l}\boldsymbol{D}_l , \qquad {}^{l}\boldsymbol{\tau}_l = \begin{bmatrix} 0 \\ 0 \\ 0 \end{bmatrix} , \tag{3.105} $$

where the gravity effects on the bodies are included.

Chapter 4

Slung Load Modeling

This chapter describes the modeling of the coupled rigid body system of the helicopter and the slung load. An introduction to general slung load systems and a discussion of existing models and results starts this chapter. A modeling approach is then decided upon and the actual model is derived including multi-lift systems and special situations like wire collapse and collisions.

4.1 Slung Load System Description

A slung load system consists of a towing body, a tow system, and a towed body. The tow system is a configuration of one or more wires. In figure 4.1 different slung load configurations are shown – some are commonly found in full scale systems and some are more rare.

The single wire configuration (a) in figure 4.1 is the simplest to implement and it is widely used in full scale applications like firefighting or simply cargo transport as illustrated in figure 1.1 on page 8. If compared to two unconstrained 6 degrees of freedom systems, the single wire suspension between the two generates one constraint which links the vertical motion of helicopter and load. It puts no restrictions on the yaw motion and there is little control on pitch and roll. In total this system has 11 degrees of freedom.

The dual wire suspension (b) is also a quite simple system that yields better yaw control of the load and it links the pitch motion of the helicopter and the load. It constrains the pitch motion and the vertical motion of the helicopter and the load and therefore yields 10 degrees of freedom.

The inverted V (c) restrict the system to 9 degrees of freedom by adding an additional constraint compared to the dual wire suspension. This additional constraint links the load lateral motion with the load roll motion and the systems therefore has three constraints.

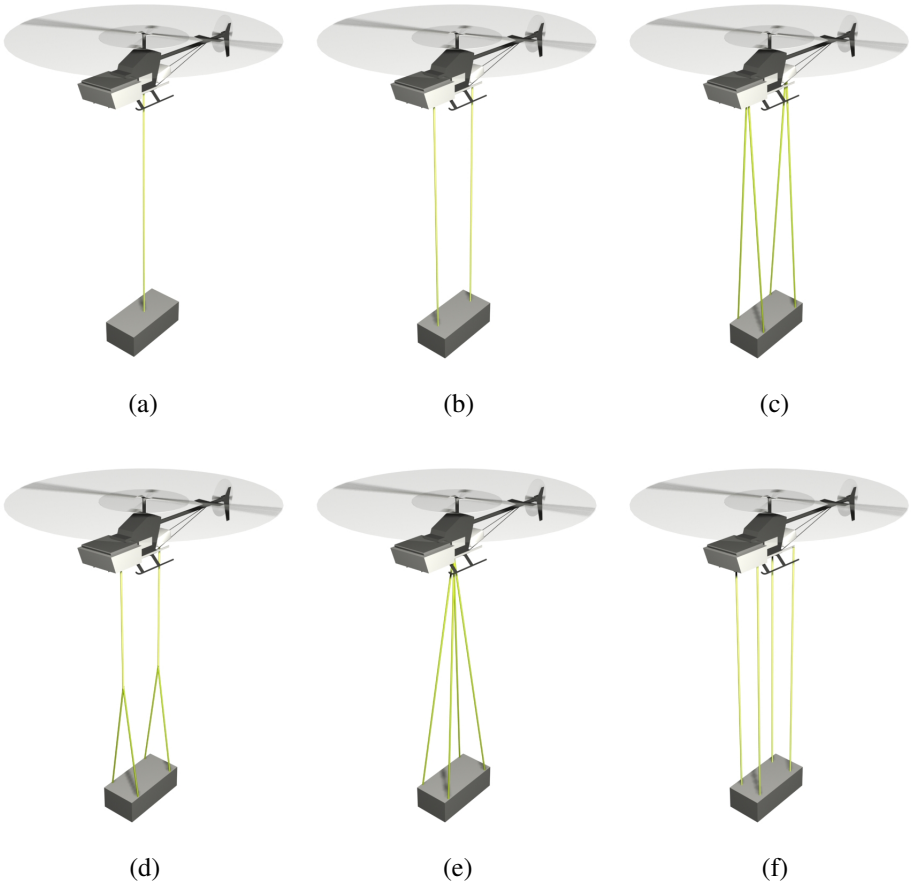

Figure 4.1: Six different slung load configurations. Top: Single wire (a), Dual wire (b), Inverted V (c). Bottom: Inverted Y (d), 4 wire centered (e), 4 wire straight (f).

This scheme has the attribute that during a yaw motion, two of the wires will collapse while the other two remain taut.

The inverted Y (d) is the only suspension system presented that does not consist entirely of body-to-body connections. The number of wires used in this system is six even though it has the same number of degrees of freedom (10) as the dual wire system. Systems like this are often found in full-scale applications. Suspension systems like these can often be approximated by their simpler counterpart, like the dual wire system or the inverted V.

Suspension system (e) constrains the vertical motion as well as subjecting the system

to two constraints by linking the longitudinal and lateral motion with the roll and pitch motion. It does not constrain the yaw motion of the load, but is nevertheless a widely used scheme. For general cargo transport there is no need to control the yaw motion of the slung load and most helicopters only have one suspension point. Therefore system (a) and (e) are very widespread in full scale applications.

The last suspension system (f) links the roll, pitch and the vertical motion of the helicopter and the load which yields a system with 8 degrees of freedom and with good control of the load yaw motion. It is the only one of the systems presented here that is not commonly found in slung load literature and we have not been able to find examples of full-scale applications of it.

From a modeling point of view the system consists of two rigid bodies, which are connected by a number of holonomic constraints given by the wires.

4.2 Choice of Modeling Approach

A natural approach for the modeling would be to adapt one of the models from the different studies that have been described in the literature review (see section 1.4 on page 15), but almost all of the models have been made explicitly for stability analysis and they are unsuitable for simulation and control However, some – like [Sampath, 1980], [Ronen *et al.*, 1986] and [Cicolani and Kanning, 1992] – develop models with simulation in mind and these are potential candidates for the model used in this thesis.

It is a requirement that the model must be able to do realistic transitions between the helicopter picking up and setting down the load during start and landings. These situations are highly critical for both human pilots and for autopilots and we therefore believe that it is important to achieve realistic simulation results for these. This means that the model must be able to detect individual wire collapse and collision and predict the resulting response.

Some of the full scale slung load publications include the option of elastic wires and several present results that indicates that many full scale suspension systems indeed exhibit elastic modes. For the small scale system deployed in this project the elasticity of the system is greatly reduced and thus can be neglected. This is due to the fact that the the wires used are comparatively much stiffer than the ones used in full scale systems.

Finally, it is desirable that the model supports all possible body-to-body suspension schemes such that the simulation model can be used to find an appropriate scheme for this project. For model-based estimation use it is very important that the model is computational efficient to be able to run in real-time together with the helicopter model. It is also desirable that the model is able to predict wire collapse such that these conditions can be incorporated into the control design and be avoided during flight.

4.2.1 Discussion of Existing Models

In order to understand the modeling of slung load systems it is necessary to realize that two different modeling approaches exist: The embedded and the augmented formulation. The embedded formulation formulate the problem in terms of degrees of freedom and generalized coordinates. This leads to a minimum set of equations that does not reveal the constraint forces. The augmented formulation expresses the system in terms of redundant coordinates and the resulting equations are in dependent coordinates as well as constraint forces.

The model in [Sampath, 1980] is developed using Lagrange formulation where Lagrange multipliers are used to include the constraints and it can describe all body-to-body suspension schemes. It also includes wire collapse through calculation of wire constraint forces and describes the wires as elastic, but there are no direct option of describing the wires as inelastic. Finally, the model derivation seems inadequate as there are several shortcomings in the form of errors and missing equations, and thus the model would require considerable reworking to be used in this research.

The derivation of the equations of motion in [Ronen *et al.*, 1986] includes both elastic and inelastic wire models, but it is limited to single-point suspension systems. The Newtonian modeling approach yields an embedded formulation in terms of degrees of freedom and is computationally efficient; however it complicates the prediction of system motion after a wire collapse. Therefore, this model cannot be used directly for this research either.

The third model is presented in [Cicolani and Kanning, 1992] and while it does not present a general model for all body-to-body suspension systems it does present specific models for all commonly used suspension types. It includes elastic and inelastic wires and calculation of wire forces for wire collapse. It uses an embedded formulation which complicates the calculation of motion with a collapsed wire, but the derivation is thorough and extensively documented. While this is the best option of the three models discussed the specific models in [Cicolani and Kanning, 1992] are quite complex and for each suspension type a new model must be implemented.

None of the available models are well suited for use in this research and it is thus decided to derive a new model and the exact modeling approach must therefore be chosen.

4.2.2 Modeling Approach

The modeling of constraint dynamic systems has been the focus of intensive research during several centuries with the first large contributions being the principle of virtual work by D'Alembert in 1743 and the elaboration of it by Lagrange in 1787 and later by Hamilton. The principle states that the total work done by the forces of constraint under virtual displacements are zero. In 1829 came the principle of Least Constraint by Gauss which states that the system motion is governed by the acceleration vector of the system that is closest to the unconstrained acceleration of the system while satisfying the constraints.

Based on these principles a number of different approaches are available for the modeling of the slung load system. The most basic approach is to formulate the problem using an embedded formulation, which can be done using standard Newton-Euler rigid-body dynamics. However, this would be a quite cumbersome approach which is unsuited for a generalized approach as it is necessary to derive a model for each suspension configuration.

A better approach is to use the principle of virtual work by D'Alembert in a Lagrangian formulation. This can be done by an embedded formulation, but again this type of approach requires quite extensive modeling when several configurations must be analyzed. To accommodate an augmented formulation a Lagrange or Hamiltonian approach with multipliers is preferable.

More recently, a different perspective on constraint systems have been developed by Udwadia and Kalaba [Udwadia and Kalaba, 1992] who have derived a new principle of dynamic system. This principle yields an explicit equation for calculation of the dynamics and it seems to be simpler in use than the other approaches discussed. It can be applied with equal ease to embedded and augmented systems and is based on Gauss' principle.

Based on the promising results in [Udwadia and Kalaba, 1992] and [Udwadia and Kalaba, 1995] the Udwadia-Kalaba equation is chosen as basis for the slung load modeling. It should be noted that the equations of Lagrange and Udwadia-Kalaba are equivalent as shown in [Udwadia, 1996].

4.3 Deriving the Udwadia-Kalaba Equation

As a starting point a standard unconstrained Newtonian system

$$\boldsymbol{M}\ddot{\boldsymbol{q}}_u = \boldsymbol{Q}\,, \tag{4.1}$$

is considered. $\boldsymbol{M} \in \mathbb{R}^{n\times n}$ is the positive definite symmetric generalized mass matrix, $\boldsymbol{q}_u \in \mathbb{R}^n$ is the unconstrained generalized coordinates of the system, and $\boldsymbol{Q} \in \mathbb{R}^n$ is the generalized forces acting on the system.

The system is then subjected to m constraints that do not need to be independent and can be either holonomic

$$\boldsymbol{\Theta}(\boldsymbol{q}, t) = 0\,, \tag{4.2}$$

or nonholonomic

$$\boldsymbol{\Theta}(\boldsymbol{q}, \dot{\boldsymbol{q}}, t) = 0\,, \tag{4.3}$$

where $\boldsymbol{q} \in \mathbb{R}^n$ is the generalized coordinates of the constrained system. Under the assumption that the constraints are sufficiently smooth they can then be differentiated either once or twice to yield

$$\boldsymbol{A}(\boldsymbol{q}, \dot{\boldsymbol{q}}, t)\ddot{\boldsymbol{q}} = \boldsymbol{b}(\boldsymbol{q}, \dot{\boldsymbol{q}}, t)\,, \tag{4.4}$$

where $\boldsymbol{A} \in \mathbb{R}^{m\times n}$ is the Jacobian of the constraint function and $\boldsymbol{b} \in \mathbb{R}^m$. It can be noted that (4.4) are equivalent to (4.2) and (4.3) when used together with a set of inertial conditions that satisfy the constraints.

To transform the original Newtonian system into a constrained systems, (4.1) is augmented with a constraint force ($\boldsymbol{Q}_c \in \mathbb{R}^n$)

$$\boldsymbol{M}\ddot{\boldsymbol{q}} = \boldsymbol{Q} + \boldsymbol{Q}_c \,, \tag{4.5}$$

which means that the motion of the constraint system originates both from the external forces as well as the constraints.

4.3.1 Gauss' Principle of Least Constraint

To solve (4.5) the constraint force must be determined and to this end the principle of Least Constraint can be employed (see [Gauss, 1829] or an English translation [Peters, 2005]). The principle states that the system motion is governed by the acceleration vector of the system that is closest to the unconstrained acceleration of the system while satisfying the constraints.

Theorem 4.1. *A constrained system will at each instant of time have an acceleration $\ddot{\boldsymbol{q}}$ that minimizes*

$$\mathcal{G} = (\ddot{\boldsymbol{q}}_\delta - \ddot{\boldsymbol{q}}_u)^T \boldsymbol{M} (\ddot{\boldsymbol{q}}_\delta - \ddot{\boldsymbol{q}}_u) \,, \tag{4.6}$$

over all possible acceleration vectors $\ddot{\boldsymbol{q}}_\delta$ that satisfy the constraint equation (4.4)*.*

Proof. All possible acceleration vectors $\ddot{\boldsymbol{q}}_\delta$ is given by

$$\ddot{\boldsymbol{q}}_\delta = \ddot{\boldsymbol{q}} + \mathcal{W} \,, \tag{4.7}$$

where $\mathcal{W}$ is a virtual displacement of the nominal vector. We can now employ D'Alembert's principle

$$0 = \mathcal{W}^T \boldsymbol{M} (\ddot{\boldsymbol{q}} - \ddot{\boldsymbol{q}}_u) \,, \tag{4.8}$$

and by substituting (4.7) into it we get

$$\begin{aligned} 0 &= (\ddot{\boldsymbol{q}}_\delta - \ddot{\boldsymbol{q}})^T \boldsymbol{M} (\ddot{\boldsymbol{q}} - \ddot{\boldsymbol{q}}_u) \Leftrightarrow \\ 0 &= \ddot{\boldsymbol{q}}_\delta^T \boldsymbol{M} \ddot{\boldsymbol{q}} - \ddot{\boldsymbol{q}}^T \boldsymbol{M} \ddot{\boldsymbol{q}} - \ddot{\boldsymbol{q}}_\delta^T \boldsymbol{M} \ddot{\boldsymbol{q}}_u + \ddot{\boldsymbol{q}}^T \boldsymbol{M} \ddot{\boldsymbol{q}}_u \,, \end{aligned} \tag{4.9}$$

This is then rewritten in the following way

$$\begin{aligned} &0 = 2\ddot{\boldsymbol{q}}_\delta^T \boldsymbol{M} \ddot{\boldsymbol{q}} - 2\ddot{\boldsymbol{q}}^T \boldsymbol{M} \ddot{\boldsymbol{q}} - 2\ddot{\boldsymbol{q}}_\delta^T \boldsymbol{M} \ddot{\boldsymbol{q}}_u + 2\ddot{\boldsymbol{q}}^T \boldsymbol{M} \ddot{\boldsymbol{q}}_u \Leftrightarrow \\ &\ddot{\boldsymbol{q}}_\delta^T \boldsymbol{M} \ddot{\boldsymbol{q}}_\delta + \ddot{\boldsymbol{q}}_u^T \boldsymbol{M} \ddot{\boldsymbol{q}}_u - 2\ddot{\boldsymbol{q}}_u^T \boldsymbol{M} \ddot{\boldsymbol{q}}_\delta = \\ &\ddot{\boldsymbol{q}}^T \boldsymbol{M} \ddot{\boldsymbol{q}} + \ddot{\boldsymbol{q}}_u^T \boldsymbol{M} \ddot{\boldsymbol{q}}_u - 2\ddot{\boldsymbol{q}}_u^T \boldsymbol{M} \ddot{\boldsymbol{q}} + \ddot{\boldsymbol{q}}_\delta^T \boldsymbol{M} \ddot{\boldsymbol{q}}_\delta + \ddot{\boldsymbol{q}}^T \boldsymbol{M} \ddot{\boldsymbol{q}} - 2\ddot{\boldsymbol{q}}^T \boldsymbol{M} \ddot{\boldsymbol{q}}_\delta \,, \end{aligned} \tag{4.10}$$

which can finally be transformed into a to a quadratic form

$$(\ddot{\boldsymbol{q}}_\delta - \ddot{\boldsymbol{q}}_u)^T \boldsymbol{M} (\ddot{\boldsymbol{q}}_\delta - \ddot{\boldsymbol{q}}_u) = (\ddot{\boldsymbol{q}} - \ddot{\boldsymbol{q}}_u)^T \boldsymbol{M} (\ddot{\boldsymbol{q}} - \ddot{\boldsymbol{q}}_u) + (\ddot{\boldsymbol{q}}_\delta - \ddot{\boldsymbol{q}})^T \boldsymbol{M} (\ddot{\boldsymbol{q}}_\delta - \ddot{\boldsymbol{q}}) \,. \tag{4.11}$$

By observing that the last term of (4.11) is strictly positive it is established that $\ddot{\boldsymbol{q}}$ is indeed the minimum of all possible acceleration vectors the system can follow. □

Remark 4.1.1. *The proof of theorem 4.1 follows the approach of the derivation of Hertz's principle of least curvature in [Whittaker, 1964].*

The situation is illustrated by an example in figure 4.2 where a ball is rolling on a curved surface (which yields a constraint force $\boldsymbol{Q}_c$) under the influence of gravity as the external force $\boldsymbol{Q}$. The actual ($\ddot{\boldsymbol{q}}$), the unconstrained ($\ddot{\boldsymbol{q}}_u$), and a possible acceleration ($\ddot{\boldsymbol{q}}_\delta$) are shown and it is illustrated how $\ddot{\boldsymbol{q}}$ is the acceleration vector that is closest to the unconstrained acceleration vector, while satisfying the constraint.

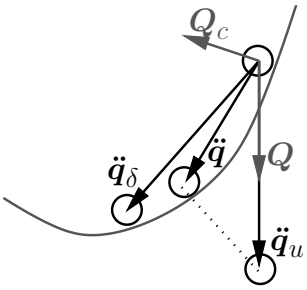

Figure 4.2: A ball rolling on a curved surface under the influence of gravity.

4.3.2 The Udwadia-Kalaba Equation

We have now established that minimizing (4.6)

$$\ddot{\boldsymbol{q}} = \arg\min_{\ddot{\boldsymbol{q}}_\delta} \mathcal{G}(\ddot{\boldsymbol{q}}_\delta)$$
$$\text{subject to}$$
$$\boldsymbol{A}(\boldsymbol{q}_\delta, \dot{\boldsymbol{q}}_\delta, t)\ddot{\boldsymbol{q}}_\delta = \boldsymbol{b}(\boldsymbol{q}_\delta, \dot{\boldsymbol{q}}_\delta, t)\,,$$

will yield the actual system acceleration and the task is then to perform the minimization. To do this first define

$$\boldsymbol{\mathcal{Y}} = \boldsymbol{M}^{1/2}(\ddot{\boldsymbol{q}}_\delta - \ddot{\boldsymbol{q}}_u) \Leftrightarrow \ddot{\boldsymbol{q}}_\delta = \boldsymbol{M}^{-1/2}\boldsymbol{\mathcal{Y}} + \ddot{\boldsymbol{q}}_u\,, \tag{4.12}$$

which reduces the minimization problem to

$$\min_{\boldsymbol{\mathcal{Y}}} \boldsymbol{\mathcal{Y}}^T\boldsymbol{\mathcal{Y}} \Leftrightarrow \min_{\mathcal{Y}} \|\mathcal{Y}\|_2^2\,. \tag{4.13}$$

By substituting (4.12) into (4.4) we get

$$\boldsymbol{A}(\boldsymbol{M}^{-1/2}\boldsymbol{\mathcal{Y}} + \ddot{\boldsymbol{q}}_u) = \boldsymbol{b} \Leftrightarrow \boldsymbol{A}\boldsymbol{M}^{-1/2}\boldsymbol{\mathcal{Y}} = \boldsymbol{b} - \boldsymbol{A}\ddot{\boldsymbol{q}}_u\,, \tag{4.14}$$

and thereby arrive at an expression on the form $\boldsymbol{Dy} = \boldsymbol{v}$. For an overdetermined system this has infinitely many solutions. We are looking for the one that satisfies (4.14), that is, the solution $\boldsymbol{y}$ with smallest 2-norm, which is exactly given by the Moore-Penrose inverse [Rao and Mitra, 1972]. By using the Moore-Penrose generalized inverse we get the following solution to (4.14)

$$\boldsymbol{\mathcal{Y}} = (\boldsymbol{A}\boldsymbol{M}^{-1/2})^{+}(\boldsymbol{b} - \boldsymbol{A}\ddot{\boldsymbol{q}}_u)\,. \tag{4.15}$$

We can now substitute this minimum $\boldsymbol{\mathcal{Y}}$ into (4.12) which gives the minimum $\ddot{\boldsymbol{q}}_\delta$ that exactly is the constraint acceleration of the system

$$\begin{aligned}\boldsymbol{M}^{1/2}(\ddot{\boldsymbol{q}} - \ddot{\boldsymbol{q}}_u) &= (\boldsymbol{A}\boldsymbol{M}^{-1/2})^{+}(\boldsymbol{b} - \boldsymbol{A}\ddot{\boldsymbol{q}}_u) \Leftrightarrow \\ \ddot{\boldsymbol{q}} &= \ddot{\boldsymbol{q}}_u + \boldsymbol{M}^{-1/2}(\boldsymbol{A}\boldsymbol{M}^{-1/2})^{+}(\boldsymbol{b} - \boldsymbol{A}\ddot{\boldsymbol{q}}_u)\,.\end{aligned} \tag{4.16}$$

By comparing (4.16) with (4.5) it is possible to identify the constraint force as

$$\boldsymbol{Q}_c = \boldsymbol{M}^{1/2}(\boldsymbol{A}\boldsymbol{M}^{-1/2})^{+}(\boldsymbol{b} - \boldsymbol{A}\ddot{\boldsymbol{q}}_u)\,. \tag{4.17}$$

4.3.3 Example: Sliding Bead

We will here illustrate the Udwadia-Kalaba equation by using it for modeling a simple constrained dynamical system: A bead sliding frictionless on a bend rod under the influence of gravity. The rod is described by

$$y(l) = 2x(l)^2,\;\; x_0 = -0.5\ \mathrm{m}\,,$$

where l is the position along the rod. The bead is described by its generalized coordinates and mass

$$\boldsymbol{q} = \begin{bmatrix} x \\ y \end{bmatrix},\;\; m = 2\ \mathrm{kg}\,.$$

The constraint equation is found and differentiated to yield

$$\begin{aligned} g(\boldsymbol{q}) &= 2x^2 - y \Rightarrow \\ \dot{g}(\boldsymbol{q}, \dot{\boldsymbol{q}}) &= 4x\dot{x} - \dot{y} \Rightarrow \\ \ddot{g}(\boldsymbol{q}, \dot{\boldsymbol{q}}, \ddot{\boldsymbol{q}}) &= 4\dot{x}^2 + 4x\ddot{x} - \ddot{y}\,, \end{aligned}$$

and then $\boldsymbol{A}$ and b can be determined

$$\boldsymbol{A} = \begin{bmatrix} 4x & -1 \end{bmatrix},\;\; \ddot{\boldsymbol{q}} = \begin{bmatrix} \ddot{x} \\ \ddot{y} \end{bmatrix},\;\; b = -4\dot{x}^2\,.$$

The result of the numerical simulation is show in figure 4.3 where it is clear how the constraints forces the sliding bead to follow the rod.

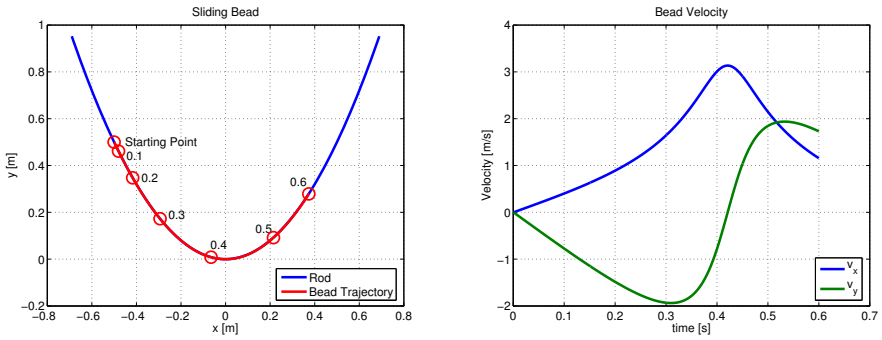

Figure 4.3: Numerical results from sliding bead example.

4.4 Rigid Body Modeling

The rigid body modeling of the entire helicopter/slung load system is will be done in an analog way to the usual approach for single rigid body. This relationship is described by the standard rigid body equations

$$ {}^{b}\dot{\boldsymbol{v}}_b = {}^{b}\boldsymbol{a}_b - {}^{b}\boldsymbol{\omega}_b \times {}^{b}\boldsymbol{v}_b \,, \tag{4.18} $$

$$ {}^{b}\dot{\boldsymbol{\omega}}_b = {}^{b}\boldsymbol{\alpha}_b - \boldsymbol{I}_b^{-1}\, {}^{b}\boldsymbol{\omega}_b \times (\boldsymbol{I}_b\, {}^{b}\boldsymbol{\omega}_b) \,, \tag{4.19} $$

where ${}^{b}\boldsymbol{a}_b$ and ${}^{b}\boldsymbol{v}_b$ are the body fixed translational acceleration and velocity, ${}^{b}\boldsymbol{\alpha}_b$ and ${}^{b}\boldsymbol{\omega}_b$ are the body fixed angular acceleration and velocity, and $\boldsymbol{I}_b$ is the inertia tensor of the body. A dot indicates a time derivative, i.e. ${}^{b}\dot{\boldsymbol{v}}_b = d/dt\, {}^{b}\boldsymbol{v}_b$ and the sub- and superscript b is used to indicate a generic rigid body.

Integration of (4.18) and (4.19) yields the body velocities which then can be transformed into the earth fixed frame to be integrated once more to yield the position and Euler angles

$$ {}^{e}\boldsymbol{v}_b = \boldsymbol{T}_{eb}\, {}^{b}\boldsymbol{v}_b \,, \tag{4.20} $$

$$ {}^{e}\dot{\boldsymbol{\theta}}_b = \boldsymbol{T}_{\theta b}\, {}^{b}\boldsymbol{\omega}_b \,, \tag{4.21} $$

where the transformation matrix $\boldsymbol{T}_{eb} : \mathbb{R}^3 \rightarrow \mathbb{R}^3$ is the orthogonal transformation that maps from the body to the earth frame – in this case the 3-2-1 Euler angle transformation is used. The non-orthogonal singular transformation matrix $\boldsymbol{T}_{\theta b} : \mathbb{R}^3 \rightarrow \mathbb{R}^3$ relates the body angular velocities to the Euler velocities. This approach is illustrated in figure 4.4 using the generalized coordinates.

As an augmented approach to the rigid body modeling is taken here the earth fixed

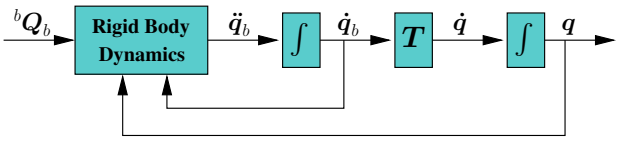

Figure 4.4: Rigid body modeling approach.

generalized coordinates

$$\boldsymbol{q} = \begin{bmatrix} {}^{e}\boldsymbol{R}_{h} \\ {}^{e}\boldsymbol{\theta}_{h} \\ {}^{e}\boldsymbol{R}_{l} \\ {}^{e}\boldsymbol{\theta}_{l} \end{bmatrix}_{12\times 1} \qquad {}^{e}\boldsymbol{R}_{b} = \begin{bmatrix} {}^{e}x_{b} \\ {}^{e}y_{b} \\ {}^{e}z_{b} \end{bmatrix} \qquad {}^{e}\boldsymbol{\theta}_{b} = \begin{bmatrix} {}^{e}\phi_{b} \\ {}^{e}\theta_{b} \\ {}^{e}\psi_{b} \end{bmatrix}, \tag{4.22}$$

is chosen to be the position vector ${}^{e}\boldsymbol{R}_{b}$ and Euler angle vector ${}^{e}\boldsymbol{\theta}_{b}$ of the respective bodies. The body fixed generalized coordinates then becomes

$$\dot{\boldsymbol{q}}_{b} = \begin{bmatrix} {}^{h}\boldsymbol{v}_{h} \\ {}^{h}\boldsymbol{\omega}_{h} \\ {}^{l}\boldsymbol{v}_{l} \\ {}^{l}\boldsymbol{\omega}_{l} \end{bmatrix}_{12\times 1} \qquad {}^{b}\boldsymbol{v}_{b} = \begin{bmatrix} {}^{b}v_{xb} \\ {}^{b}v_{yb} \\ {}^{b}v_{zb} \end{bmatrix} \qquad {}^{b}\boldsymbol{\omega}_{b} = \begin{bmatrix} {}^{b}\omega_{xb} \\ {}^{b}\omega_{yb} \\ {}^{b}\omega_{zb} \end{bmatrix}. \tag{4.23}$$

4.4.1 The Constraint Equation

To be usable for the Udwadia-Kalaba equation the constraints of the suspension system must be transformed into the form of (4.4) if not already in that form. The general configuration of the slung load system is illustrated in figure 4.5 where the ith wire is shown. The ith wire vector ${}^{e}\boldsymbol{L}_{i}$ is given by

$$\begin{aligned} {}^{e}\boldsymbol{L}_{i} &= {}^{e}\boldsymbol{R}_{h} + {}^{e}\boldsymbol{R}_{hai} - {}^{e}\boldsymbol{R}_{l} - {}^{e}\boldsymbol{R}_{lai} \Leftrightarrow \\ {}^{e}\boldsymbol{L}_{i} &= {}^{e}\boldsymbol{R}_{h} + \boldsymbol{T}_{eh}\,{}^{h}\boldsymbol{R}_{hai} - {}^{e}\boldsymbol{R}_{l} - \boldsymbol{T}_{el}\,{}^{l}\boldsymbol{R}_{lai}\,, \end{aligned} \tag{4.24}$$

as a function of the position vectors of the helicopter and the load (${}^{e}\boldsymbol{R}_{h}$ and ${}^{e}\boldsymbol{R}_{l}$) as well as the static position vectors describing the attachment points on the helicopter and the load (${}^{h}\boldsymbol{R}_{hai}$ and ${}^{l}\boldsymbol{R}_{lai}$).

In order to transform this constraint equation into the general form of (4.4) it needs to be differentiated twice. However it is important to note that the wire vector is the unknown it this case and it is therefore desirable to cancel it from the equation. This can

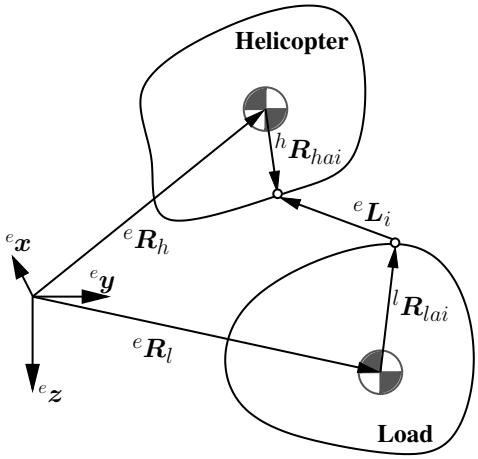

Figure 4.5: General configuration of the slung load system shown for the ith wire.

be achieved by working with the norm of ${}^e\boldsymbol{L}_i$ instead of the vector itself which yields

$$\begin{aligned}
&g_i(\boldsymbol{q}) = \\
&\|{}^e\boldsymbol{L}_i\|^2 - l_i^2 = \\
&({}^e\boldsymbol{L}_i)^T({}^e\boldsymbol{L}_i) - l_i^2 = \\
&({}^e\boldsymbol{R}_h + \boldsymbol{T}_{eh}\,{}^h\boldsymbol{R}_{hai} - {}^e\boldsymbol{R}_l - \boldsymbol{T}_{el}\,{}^l\boldsymbol{R}_{lai})^T({}^e\boldsymbol{R}_h + \boldsymbol{T}_{eh}\,{}^h\boldsymbol{R}_{hai} - {}^e\boldsymbol{R}_l - \boldsymbol{T}_{el}\,{}^l\boldsymbol{R}_{lai}) - l_i^2\,, \quad (4.25)
\end{aligned}$$

where l_i is the nominal undeformed, taut length of the i'th wire.

In the following the notation is eased by dropping the coordinate system indices on the position vectors, i.e. it is implicit that the position vector of the ith attachment on the load is given in the load frame etc. To achieve the standard form of (4.4) it is necessary to differentiate the constraint equation twice using the chain-rule

$$\begin{aligned}
&\frac{d}{dt}g_i(\boldsymbol{q}) = \\
&0 = 2(\dot{\boldsymbol{R}}_h + \dot{\boldsymbol{T}}_{eh}\boldsymbol{R}_{hai} - \dot{\boldsymbol{R}}_l - \dot{\boldsymbol{T}}_{el}\boldsymbol{R}_{lai})^T(\boldsymbol{R}_h + \boldsymbol{T}_{eh}\boldsymbol{R}_{hai} - \boldsymbol{R}_l - \boldsymbol{T}_{el}\boldsymbol{R}_{lai})\,, \quad (4.26)
\end{aligned}$$

$$\begin{aligned}
&\frac{d^2}{dt^2}g_i(\boldsymbol{q}) = \\
&0 = 2(\ddot{\boldsymbol{R}}_h + \ddot{\boldsymbol{T}}_{eh}\boldsymbol{R}_{hai} - \ddot{\boldsymbol{R}}_l - \ddot{\boldsymbol{T}}_{el}\boldsymbol{R}_{lai})^T(\boldsymbol{R}_h + \boldsymbol{T}_{eh}\boldsymbol{R}_{hai} - \boldsymbol{R}_l - \boldsymbol{T}_{el}\boldsymbol{R}_{lai}) \\
&+ 2(\dot{\boldsymbol{R}}_h + \dot{\boldsymbol{T}}_{eh}\boldsymbol{R}_{hai} - \dot{\boldsymbol{R}}_l - \dot{\boldsymbol{T}}_{el}\boldsymbol{R}_{lai})^T(\dot{\boldsymbol{R}}_h + \dot{\boldsymbol{T}}_{eh}\boldsymbol{R}_{hai} - \dot{\boldsymbol{R}}_l - \dot{\boldsymbol{T}}_{el}\boldsymbol{R}_{lai})\,. \quad (4.27)
\end{aligned}$$

By applying the chain-rule the first differentiation of a transformation matrix yields

$$\frac{d}{dt}\boldsymbol{T}_{eb}(\theta(t),\phi(t),\psi(t)) = \frac{d\boldsymbol{T}_{eb}}{d\phi}\dot{\phi} + \frac{d\boldsymbol{T}_{eb}}{d\theta}\dot{\theta} + \frac{d\boldsymbol{T}_{eb}}{d\psi}\dot{\psi}\,, \tag{4.28}$$

where $\dot{\phi}$ denotes the time derivative of ϕ. Carrying out the final differentiation the following is derived

$$\begin{aligned}&\frac{d^2}{dt^2}\boldsymbol{T}_{eb}(\theta(t),\phi(t),\psi(t)) = \\ &\frac{d}{dt}\left(\frac{d\boldsymbol{T}_{eb}}{d\phi}\right)\dot{\phi} + \frac{d\boldsymbol{T}_{eb}}{d\phi}\ddot{\phi} + \frac{d}{dt}\left(\frac{d\boldsymbol{T}_{eb}}{d\theta}\right)\dot{\theta} + \frac{d\boldsymbol{T}_{eb}}{d\theta}\ddot{\theta} + \frac{d}{dt}\left(\frac{d\boldsymbol{T}_{eb}}{d\psi}\right)\dot{\psi} + \frac{d\boldsymbol{T}_{eb}}{d\psi}\ddot{\psi}\,,\end{aligned}$$

and by further expansion we arrive at

$$\begin{aligned}&\frac{d^2}{dt^2}\boldsymbol{T}_{eb}(\theta(t),\phi(t),\psi(t)) = \\ &\left(\frac{d^2\boldsymbol{T}_{eb}}{d\phi d\phi}\dot{\phi} + \frac{d^2\boldsymbol{T}_{eb}}{d\phi d\theta}\dot{\theta} + \frac{d^2\boldsymbol{T}_{eb}}{d\phi d\psi}\dot{\psi}\right)\dot{\phi} + \frac{d\boldsymbol{T}_{eb}}{d\phi}\ddot{\phi} + \\ &\left(\frac{d^2\boldsymbol{T}_{eb}}{d\theta d\phi}\dot{\psi} + \frac{d^2\boldsymbol{T}_{eb}}{d\theta d\theta}\dot{\theta} + \frac{d^2\boldsymbol{T}_{eb}}{d\theta d\psi}\dot{\psi}\right)\dot{\theta} + \frac{d\boldsymbol{T}_{eb}}{d\theta}\ddot{\theta} + \\ &\left(\frac{d^2\boldsymbol{T}_{eb}}{d\psi d\phi}\dot{\psi} + \frac{d^2\boldsymbol{T}_{eb}}{d\psi d\theta}\dot{\theta} + \frac{d^2\boldsymbol{T}_{eb}}{d\psi d\psi}\dot{\psi}\right)\dot{\psi} + \frac{d\boldsymbol{T}_{eb}}{d\psi}\ddot{\psi}\,,\end{aligned} \tag{4.29}$$

where $\ddot{\phi}$ denotes the double time derivative of ϕ. Equation (4.29) can then be substituted

into (4.27) together with (4.24) and its time derivative to achieve the constraint equation

$$
\begin{aligned}
&\frac{d^2}{dt^2} g_i(\boldsymbol{q}) = \\
&2\boldsymbol{L}_i^T \Bigg(\ddot{\boldsymbol{R}}_h + \left(\frac{d\boldsymbol{T}_{eh}}{d\phi_h} \ddot{\phi}_h + \frac{d\boldsymbol{T}_{eh}}{d\theta_h} \ddot{\theta}_h + \frac{d\boldsymbol{T}_{eh}}{d\psi_h} \ddot{\psi}_h \right) \boldsymbol{R}_{hai} - \ddot{\boldsymbol{R}}_l \\
&- \left(\frac{d\boldsymbol{T}el}{d\phi_l} \ddot{\phi}_l + \frac{d\boldsymbol{T}_l}{d\theta_l} \ddot{\theta}_l + \frac{d\boldsymbol{T}_{el}}{d\psi_l} \ddot{\psi}_l \right) \boldsymbol{R}_{lai} \Bigg) + \\
&2\boldsymbol{L}_i^T \Bigg(\Bigg(\left(\frac{d^2\boldsymbol{T}_{eh}}{d\phi_h d\phi_h} \dot{\phi}_h + \frac{d^2\boldsymbol{T}_{eh}}{d\phi_h d\theta_h} \dot{\theta}_h + \frac{d^2\boldsymbol{T}_{eh}}{d\phi_h d\psi_h} \dot{\psi}_h \right) \dot{\phi}_h \\
&+ \left(\frac{d^2\boldsymbol{T}_{eh}}{d\theta_h d\phi_h} \dot{\psi}_h + \frac{d^2\boldsymbol{T}_{eh}}{d\theta_h d\theta_h} \dot{\theta}_h + \frac{d^2\boldsymbol{T}_{eh}}{d\theta_h d\psi_h} \dot{\psi}_h \right) \dot{\theta}_h \\
&+ \left(\frac{d^2\boldsymbol{T}_{eh}}{d\psi_h d\phi_h} \dot{\psi}_h + \frac{d^2\boldsymbol{T}_{eh}}{d\psi_h d\theta_h} \dot{\theta}_h + \frac{d^2\boldsymbol{T}_{eh}}{d\psi_h d\psi_h} \dot{\psi}_h \right) \dot{\psi}_h \Bigg) \boldsymbol{R}_{hai} \\
&- \Bigg(\left(\frac{d^2\boldsymbol{T}_{el}}{d\phi_l d\phi_l} \dot{\phi}_l + \frac{d^2\boldsymbol{T}_{el}}{d\phi_l d\theta_l} \dot{\theta}_l + \frac{d^2\boldsymbol{T}_{el}}{d\phi_l d\psi_l} \dot{\psi}_l \right) \dot{\phi}_l \\
&+ \left(\frac{d^2\boldsymbol{T}_{el}}{d\theta_l d\phi_l} \dot{\psi}_l + \frac{d^2\boldsymbol{T}_{el}}{d\theta_l d\theta_l} \dot{\theta}_l + \frac{d^2\boldsymbol{T}_{el}}{d\theta_l d\psi_l} \dot{\psi}_l \right) \dot{\theta}_l \\
&+ \left(\frac{d^2\boldsymbol{T}_{el}}{d\psi_l d\phi_l} \dot{\psi}_l + \frac{d^2\boldsymbol{T}_{el}}{d\psi_l d\theta_l} \dot{\theta}_l + \frac{d^2\boldsymbol{T}_{el}}{d\psi_l d\psi_l} \dot{\psi}_l \right) \dot{\psi}_l \Bigg) \boldsymbol{R}_{lai} \Bigg) + 2\dot{\boldsymbol{L}}_i^T \dot{\boldsymbol{L}}_i \,. \qquad (4.30)
\end{aligned}
$$

To simplify the notation, (4.30) can be reformulated to the following more compact way

$$
\begin{aligned}
&\frac{d^2}{dt^2} g_i(\boldsymbol{q}) = \\
&2\boldsymbol{L}_i^T \left(\ddot{\boldsymbol{R}}_h + \boldsymbol{G}_h \ddot{\boldsymbol{\theta}}_h - \ddot{\boldsymbol{R}}_l - \boldsymbol{G}_l \ddot{\boldsymbol{\theta}}_l \right) + \\
&2\boldsymbol{L}_i^T \left[\boldsymbol{G}_{\phi_h} \dot{\boldsymbol{\theta}}_h \quad \boldsymbol{G}_{\theta_h} \dot{\boldsymbol{\theta}}_h \quad \boldsymbol{G}_{\psi_h} \dot{\boldsymbol{\theta}}_h \right]_{3\times 3} \dot{\boldsymbol{\theta}}_h + \\
&2\boldsymbol{L}_i^T \left[\boldsymbol{G}_{\phi_l} \dot{\boldsymbol{\theta}}_l \quad \boldsymbol{G}_{\theta_l} \dot{\boldsymbol{\theta}}_l \quad \boldsymbol{G}_{\psi_l} \dot{\boldsymbol{\theta}}_l \right]_{3\times 3} \dot{\boldsymbol{\theta}}_l + 2\dot{\boldsymbol{L}}_i^T \dot{\boldsymbol{L}}_i \,, \qquad (4.31)
\end{aligned}
$$

where

$$\begin{aligned}
\boldsymbol{G}_b &= \left[\frac{d\boldsymbol{T}_{eb}}{d\phi_b}\boldsymbol{R}_{bai} \quad \frac{d\boldsymbol{T}_{eb}}{d\theta_b}\boldsymbol{R}_{bai} \quad \frac{d\boldsymbol{T}_{eb}}{d\psi_b}\boldsymbol{R}_{bai}\right]_{3\times 3} , \\
\boldsymbol{G}_{\phi_b} &= \left[\frac{d^2\boldsymbol{T}_{eb}}{d\phi_b d\phi_b}\boldsymbol{R}_{bai} \quad \frac{d^2\boldsymbol{T}_{eb}}{d\phi_b d\theta_b}\boldsymbol{R}_{bai} \quad \frac{d^2\boldsymbol{T}_{eb}}{d\phi_b d\psi_b}\boldsymbol{R}_{bai}\right]_{3\times 3} , \\
\boldsymbol{G}_{\theta_b} &= \left[\frac{d^2\boldsymbol{T}_{eb}}{d\theta_b d\phi_b}\boldsymbol{R}_{bai} \quad \frac{d^2\boldsymbol{T}_{eb}}{d\theta_b d\theta_b}\boldsymbol{R}_{bai} \quad \frac{d^2\boldsymbol{T}_{eb}}{d\theta_b d\psi_b}\boldsymbol{R}_{bai}\right]_{3\times 3} , \\
\boldsymbol{G}_{\psi_b} &= \left[\frac{d^2\boldsymbol{T}_{eb}}{d\psi_b d\phi_b}\boldsymbol{R}_{bai} \quad \frac{d^2\boldsymbol{T}_{eb}}{d\psi_b d\theta_b}\boldsymbol{R}_{bai} \quad \frac{d^2\boldsymbol{T}_{eb}}{d\psi_b d\psi_b}\boldsymbol{R}_{bai}\right]_{3\times 3} .
\end{aligned}$$

Changing to Body Coordinates

In the previous section the standard constraint equation (4.4) was derived to yield (4.30) using the set of generalized coordinates given in (4.22). This makes the constraint equation a function of

$$\ddot{\boldsymbol{q}} = \begin{bmatrix} \ddot{\boldsymbol{R}}_h \\ \ddot{\boldsymbol{\theta}}_h \\ \ddot{\boldsymbol{R}}_l \\ \ddot{\boldsymbol{\theta}}_l \end{bmatrix}_{12\times 1} , \tag{4.32}$$

which is somewhat inconvenient when using these coordinates in the system equation (4.5) as it is desirable to use the standard body-fixed inertia tensor in the generalized mass matrix. Following the approach given in figure 4.4 the acceleration coordinates will therefore be changed in (4.31) to

$$\ddot{\boldsymbol{q}}_a = \begin{bmatrix} {}^h\boldsymbol{a}_h \\ {}^h\boldsymbol{\alpha}_h \\ {}^l\boldsymbol{a}_l \\ {}^l\boldsymbol{\alpha}_l \end{bmatrix}_{12\times 1} . \tag{4.33}$$

In order to achieve this, a standard equation of a Newtonian system (4.1) is used and the relationship between the body and the earth fixed translational acceleration is found as

$$\begin{aligned}
\ddot{\boldsymbol{R}}_b &= \frac{1}{m}\,{}^e\boldsymbol{F}_b \Leftrightarrow \\
\ddot{\boldsymbol{R}}_b &= \frac{1}{m}\boldsymbol{T}_{eb}\,{}^b\boldsymbol{F}_b \Leftrightarrow \\
\ddot{\boldsymbol{R}}_b &= \boldsymbol{T}_{eb}\,{}^b\boldsymbol{a}_b .
\end{aligned} \tag{4.34}$$

The relationship between body and earth fixed angular acceleration is found by taking the time derivative of (4.21), which yields

$$\ddot{\boldsymbol{\theta}}_b = \boldsymbol{T}_{\theta b}{}^b\dot{\boldsymbol{\omega}}_b + \dot{\boldsymbol{T}}_{\theta b}{}^b\boldsymbol{\omega}_b . \tag{4.35}$$

By defining the skew symmetric matrix

$$ {}^{b}\tilde{\boldsymbol{\omega}}_b = \begin{bmatrix} 0 & -\omega_z & \omega_y \\ \omega_z & 0 & -\omega_x \\ -\omega_y & \omega_x & 0 \end{bmatrix} , \tag{4.36} $$

which can be used instead of the cross product and by using (4.19), (4.34), and (4.35), the final two equations for the coordinate change can be written as

$$ \ddot{\boldsymbol{R}} = \boldsymbol{T}_{eb}{}^{b}\boldsymbol{a}_b , \tag{4.37} $$

$$ \ddot{\boldsymbol{\theta}} = \boldsymbol{T}_{\theta b}{}^{b}\boldsymbol{\alpha}_b \;-\; \boldsymbol{T}_{\theta b}\boldsymbol{I}_b{}^{-1}\,{}^{b}\tilde{\boldsymbol{\omega}}_b\boldsymbol{I}_b{}^{b}\boldsymbol{\omega}_b \;+\; \dot{\boldsymbol{T}}_{\theta b}{}^{b}\boldsymbol{\omega}_b . \tag{4.38} $$

The constraint equation after the coordinate change is then found by substituting (4.37) and (4.38) into (4.31) and isolating the double derivative parts

$$ \begin{aligned} &\frac{d^2}{dt^2}g_i(\boldsymbol{q}) = \\ &2\boldsymbol{L}_i^T\left(\boldsymbol{T}_{eh}{}^{h}\boldsymbol{a}_h + \boldsymbol{G}_h\boldsymbol{T}_{\theta h}{}^{h}\boldsymbol{\alpha}_h - \boldsymbol{T}_{el}{}^{l}\boldsymbol{a}_l - \boldsymbol{G}_l\boldsymbol{T}_{\theta l}\,{}^{l}\boldsymbol{\alpha}_l\right)+ \\ &2\boldsymbol{L}_i^T\left[\boldsymbol{G}_{\phi_h}\dot{\boldsymbol{\theta}}_h \quad \boldsymbol{G}_{\theta_h}\dot{\boldsymbol{\theta}}_h \quad \boldsymbol{G}_{\psi_h}\dot{\boldsymbol{\theta}}_h\right]_{3\times 3}\dot{\boldsymbol{\theta}}_h+ \\ &2\boldsymbol{L}_i^T\left[\boldsymbol{G}_{\phi_l}\dot{\boldsymbol{\theta}}_l \quad \boldsymbol{G}_{\theta_l}\dot{\boldsymbol{\theta}}_l \quad \boldsymbol{G}_{\psi_l}\dot{\boldsymbol{\theta}}_l\right]_{3\times 3}\dot{\boldsymbol{\theta}}_l + 2\dot{\boldsymbol{L}}_i{}^{T}\dot{\boldsymbol{L}}_i+ \\ &2\boldsymbol{L}_i{}^{T}\left(-\boldsymbol{G}_h(\boldsymbol{T}_{\theta h}\boldsymbol{I}_h^{-1}\,{}^{h}\tilde{\boldsymbol{\omega}}_h\boldsymbol{I}_h{}^{h}\boldsymbol{\omega}_h + \dot{\boldsymbol{T}}_{\theta h}{}^{h}\boldsymbol{\omega}_h) + \boldsymbol{G}_l(\boldsymbol{T}_{\theta l}\boldsymbol{I}_l^{-1}\,{}^{l}\tilde{\boldsymbol{\omega}}_l\boldsymbol{I}_l{}^{l}\boldsymbol{\omega}_l - \dot{\boldsymbol{T}}_{\theta l}{}^{l}\boldsymbol{\omega}_l)\right) . \end{aligned} \tag{4.39} $$

4.4.2 The Rigid Body Model

To relate the constraint equation (4.39) to the Udwadia-Kalaba equation (4.16) it is necessary to identify $\boldsymbol{A}$ and $\boldsymbol{b}$ of (4.4). As (4.39) describes the ith constraint it is possible to identify the ith part of $\boldsymbol{A}$ and $\boldsymbol{b}$ from it. b_i is the part of the equation that is independent of $\ddot{\boldsymbol{q}}_a$ which means that (4.39) can be reformulated in the following way

$$ \frac{d^2}{dt^2}g_i = 2\boldsymbol{L}_i^T\left(\boldsymbol{T}_{eh}{}^{h}\boldsymbol{a}_h + \boldsymbol{G}_h\boldsymbol{T}_{\theta h}{}^{h}\boldsymbol{\alpha}_h - \boldsymbol{T}_{el}{}^{l}\boldsymbol{a}_l - \boldsymbol{G}_l\boldsymbol{T}_{\theta l}\,{}^{l}\boldsymbol{\alpha}_l\right) + b_i , \tag{4.40} $$

and thereby identifying b_i. The remaining part of (4.39) can then be formulated as $\boldsymbol{A}_i$

$$ \boldsymbol{A}_i = 2\boldsymbol{L}_i^T\left[\boldsymbol{T}_{eh} \quad \boldsymbol{G}_h\boldsymbol{T}_{\theta h} \quad -\boldsymbol{T}_{el} \quad -\boldsymbol{G}_l\boldsymbol{T}_{\theta l}\right]_{3\times 12} . \tag{4.41} $$

Finally, the full constraint equation of (4.4) can be found

$$\boldsymbol{A} = \begin{bmatrix} \boldsymbol{A}_1 \\ \boldsymbol{A}_2 \\ \vdots \\ \boldsymbol{A}_m \end{bmatrix}_{m\times 12} \qquad \boldsymbol{b} = \begin{bmatrix} b_1 \\ b_2 \\ \vdots \\ b_m \end{bmatrix}_{n\times 1} \qquad \ddot{\boldsymbol{q}}_a = \begin{bmatrix} {}^h\boldsymbol{a}_h \\ {}^h\boldsymbol{\alpha}_h \\ {}^l\boldsymbol{a}_l \\ {}^l\boldsymbol{\alpha}_l \end{bmatrix}_{12\times 1}, \tag{4.42}$$

which can then be inserted into (4.16) to yield $\ddot{\boldsymbol{q}}_a$. Using this in (4.18) to (4.21) the final model is achieved.

4.4.3 Example: Inverted-V Suspension

To illustrate how the model performs, an example with an inverted V-suspension (see figure 4.1 (c)) is carried out. In the example only rigid body dynamics for the helicopter and load is included and all other dynamics and influences are excluded. The equation are propagated using a 4th order Runge-Kutta at 100 Hz and the parameters used are shown in table 4.1. The simulation is run for 10 seconds and gravity is applied to both helicopter

Parameter	Value	Unit
$\boldsymbol{I}_h$ & $\boldsymbol{I}_l$	$\begin{bmatrix} 0.4 & 0 & -0.1 \\ 0 & 0.4 & 0 \\ -0.1 & 0 & 0.4 \end{bmatrix}$	Nm
m_h	14	kg
m_l	4	kg
$\boldsymbol{R}_{ha1}$ & $\boldsymbol{R}_{ha3}$	$\begin{bmatrix} 0.2 & 0 & 0.15 \end{bmatrix}^T$	m
$\boldsymbol{R}_{ha2}$ & $\boldsymbol{R}_{ha4}$	$\begin{bmatrix} -0.2 & 0 & 0.15 \end{bmatrix}^T$	m
$\boldsymbol{R}_{la1}$	$\begin{bmatrix} 0.2 & 0.15 & -0.1 \end{bmatrix}^T$	m
$\boldsymbol{R}_{la2}$	$\begin{bmatrix} -0.2 & 0.15 & -0.1 \end{bmatrix}^T$	m
$\boldsymbol{R}_{la3}$	$\begin{bmatrix} 0.2 & -0.15 & -0.1 \end{bmatrix}^T$	m
$\boldsymbol{R}_{la4}$	$\begin{bmatrix} -0.2 & -0.15 & -0.1 \end{bmatrix}^T$	m

Table 4.1: The parameters used in the Inverted-V suspension example.

and load, both starting with a forward velocity of 1.5 m/s. An earth fixed thrust force large enough to counter the gravitational effect on both bodies are applied to the helicopter. A lateral earth fixed force and a body fixed yaw torque is applied to the helicopter and the result can be seen in figure 4.6, 4.7, and 4.8. If the top view of the system in figure 4.6 is observed it can be seen that the helicopter and load start out with a forward motion. This is then changed into a turn by the forces and torques acting on the helicopter and the load is clearly dragged after the helicopter. To visualize the behavior of the model the graphs of figure 4.8 must be related to the modeling equations. The body velocity and the position/Euler angle graphs is given by (4.20) and (4.21) and the integration of these. The body accelerations are given by (4.18) and (4.19) and the generalized applied

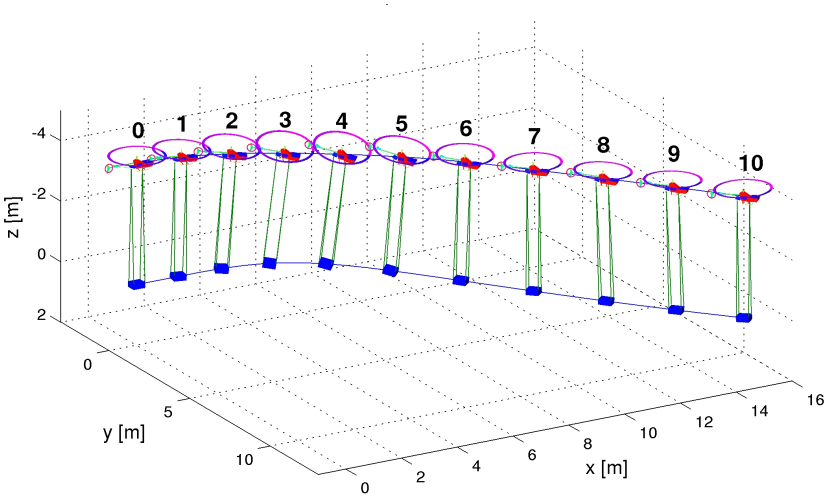

Figure 4.6: 3D plot of the Inverted-V suspension example with timeline.

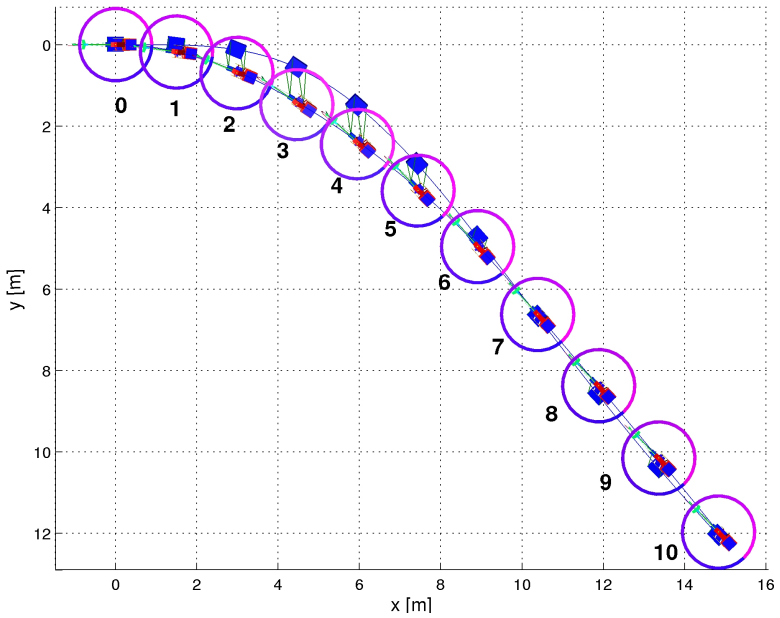

Figure 4.7: Top view plot of the Inverted-V suspension example with timeline.

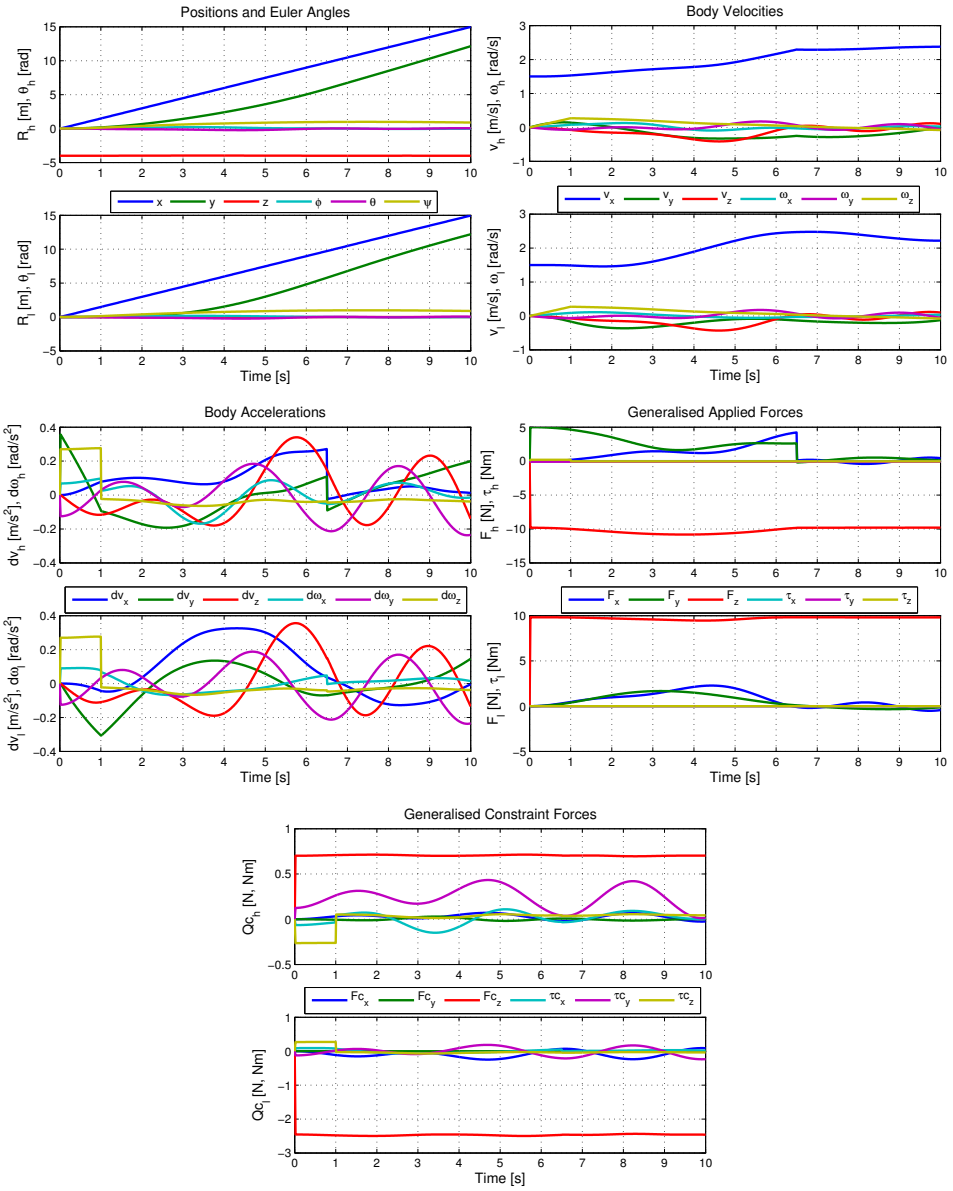

Figure 4.8: Graphs from the Inverted-V suspension example.

forces and constraint forces are given by (4.5). The applied body fixed yaw torque can be observed on the acceleration graph in the time interval [0;1] and at time = 6.5 s, the applied force on the helicopter is set to zero. The same is evident from the applied force and the constraint force graphs. A oscillation period of 3 s can be observed on the lateral acceleration, which was initiated by the applied lateral force.

4.5 Wire Collapse and Collisions

Wire collapse and collisions are a little researched subject in the literature. This is mainly due to the fact that collapse (and the following collision) of wires are situations to avoid with a slung load. However, there are two reasons for incorporating collapse and collision into the model: Firstly, it is very desirable to avoid wire collapse during flight and thus is necessary to be able to determine when this occurs. Secondly, during take off and landing collision and collapse of wires is unavoidable. In the following a way of incorporating the ability to handle wire collapse and collision will be discussed. The situations with a collapsed and a taut wire is illustrated in figure 4.9.

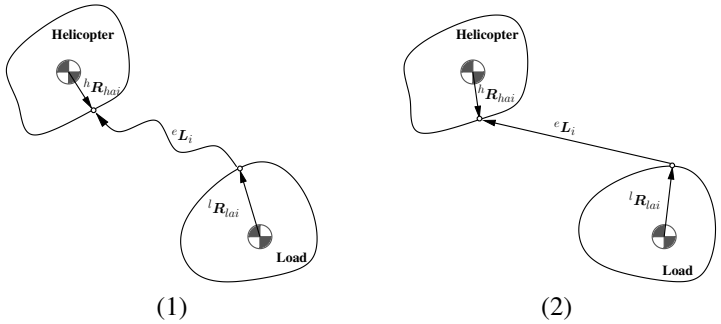

Figure 4.9: (1): Wire collapsed. (2): Wire taut.

4.5.1 Detection of Wire Collapse and Wire Collision

Collapse of wires can be determined simply by projecting the generalized constraint forces onto the wires and looking for compressive forces. This is done by first finding the total constraint force acting in the attachment point, then transforming this into the earth fixed frame and finally projecting the force onto a unit wire vector, which yields

$$Q_{bwi} = \Big(\boldsymbol{T}_{eb} \big(\boldsymbol{\tau}_{bc} \times \boldsymbol{R}_{bai} + \boldsymbol{F}_{bc} \big) \Big) \cdot \boldsymbol{N}_i \,, \tag{4.43}$$

where Q_{bwi} is the constraint force acting on the ith wire from the specific body and $\boldsymbol{N}_i$ is a unit vector along $\boldsymbol{L}_i$. The two contributions from the helicopter and the load are then subtracted

$$Q_{wi} = Q_{hwi} - Q_{lwi} \,, \tag{4.44}$$

which makes it possible to determine if the resulting constraint forces acting on the wire is compressing (negative) or tensioning (positive). A collision of a wire can be determined by observing the norm of the wire and when it becomes equal to or larger than the nominal length of the wire a collision has occurred.

$$\begin{aligned} Q_{wi} < 0: &\quad \text{Collapse} \\ |\boldsymbol{L}_i| > l_i: &\quad \text{Collision} \end{aligned}$$

The collapse/collision state machine is shown in figure 4.10.

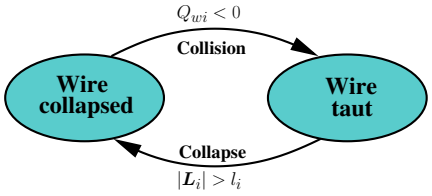

Figure 4.10: The state machine for the wire collapse/collision mechanism.

Wire Collapse and Collision Response

Handling the response of a wire collapse is quite simple, while a collision response is somewhat more complicated. When a collapse has been determined for wire i, this wire is removed from the constraint equation by setting $\boldsymbol{A}_i = \boldsymbol{0}$ and $b_i = 0$. Any given collision – both elastic and inelastic – will be modeled using conservation of momentum. The relationship between translational and angular velocity before and after the impact can be described in the following way using the standard relationship between linear and angular momentum given by the impulse of the collision

$$\begin{aligned} {}^{h}_{2}\boldsymbol{v}_h &= {}^{h}_{1}\boldsymbol{v}_h + m_h^{-1}\, {}^{h}\boldsymbol{N}_i J \,, && (4.45) \\ {}^{l}_{2}\boldsymbol{v}_l &= {}^{l}_{1}\boldsymbol{v}_l - m_l^{-1}\, {}^{l}\boldsymbol{N}_i J \,, && (4.46) \\ {}^{h}_{2}\boldsymbol{\omega}_h &= {}^{h}_{1}\boldsymbol{\omega}_h + \boldsymbol{I}_h^{-1}(\boldsymbol{R}_{hai} \times {}^{h}\boldsymbol{N}_i J) \,, && (4.47) \\ {}^{l}_{2}\boldsymbol{\omega}_l &= {}^{l}_{1}\boldsymbol{\omega}_l - \boldsymbol{I}_l^{-1}(\boldsymbol{R}_{lai} \times {}^{l}\boldsymbol{N}_i J) \,, && (4.48) \end{aligned}$$

where J is the impulse and the situation just before and just after the collision is denoted with pre-subscript 1 and 2 respectively: ${}_1X$ and ${}_2X$.

A perfectly inelastic collision is characterized by the relative velocity between the two attachment points projected onto the wire (${}^{e}\boldsymbol{v}_{\Delta} \cdot {}^{e}\boldsymbol{N}_i$) must be zero after the collision. An elastic collision is characterized by energy conservation and thus allowing the colliding objects to bounce. Thus a collision can be described by

$$-K_e \; {}^{e}_{1}\boldsymbol{v}_{\Delta} \cdot {}^{e}\boldsymbol{N}_i = {}^{e}_{2}\boldsymbol{v}_{\Delta} \cdot {}^{e}\boldsymbol{N}_i \,, \tag{4.49}$$

where the elasticity in a collision is described by a constant K_e. When equal to 0 it describes an inelastic collision, when equal to 1 it describes an elastic collision and when in between it describes a combination of the two.

The relative velocity of the two attachment points can be described by the translational and angular velocity of the two bodies

$$-K_e \; {}^{e}_{1}\boldsymbol{v}_{\Delta} \cdot {}^{e}\boldsymbol{N}_i = (\boldsymbol{T}_{eh}({}^{h}_{2}\boldsymbol{v}_h + {}^{h}_{2}\boldsymbol{\omega}_h \times \boldsymbol{R}_{hai}) - \boldsymbol{T}_{el}({}^{l}_{2}\boldsymbol{v}_l + {}^{l}_{2}\boldsymbol{\omega}_l \times \boldsymbol{R}_{lai})) \cdot {}^{e}\boldsymbol{N}_i \,.$$

It is now possible to substitute the relations between the velocities before and after collision (4.45) into (4.48) such that the equation only depends on velocities before the collision

$$\begin{aligned}
-K_e \, {}^{e}_{1}\boldsymbol{v}_{\Delta} = &\left(\boldsymbol{T}_{eh} \left({}^{h}_{1}\boldsymbol{v}_h + \frac{1}{m_h} {}^{h}\boldsymbol{N}_i J + ({}^{h}_{1}\boldsymbol{\omega}_h + {I_h}^{-1}(\boldsymbol{R}_{hai} \times {}^{h}\boldsymbol{N}_i J)) \times \boldsymbol{R}_{hai} \right) - \right. \\
&\left. \boldsymbol{T}_{el} \left({}^{l}_{1}\boldsymbol{v}_l \; - \frac{1}{m_l} \, {}^{l}\boldsymbol{N}_i J + ({}^{l}_{1}\boldsymbol{\omega}_l \; - {I_l}^{-1}(\boldsymbol{R}_{lai} \times \; {}^{l}\boldsymbol{N}_i J)) \times \boldsymbol{R}_{lai} \right) \right) \cdot {}^{e}\boldsymbol{N}_i \\
\Leftrightarrow \\
-(1+K_e){}^{e}_{1}\boldsymbol{v}_{\Delta} \cdot {}^{e}\boldsymbol{N}_i = &\left(\boldsymbol{T}_{eh} \left(\frac{1}{m_h} {}^{h}\boldsymbol{N}_i J + ({I_h}^{-1}(\boldsymbol{R}_{hai} \times {}^{h}\boldsymbol{N}_i J)) \times \boldsymbol{R}_{hai} \right) - \right. \\
&\left. \boldsymbol{T}_{el} \left(-\frac{1}{m_l} \, {}^{l}\boldsymbol{N}_i J - (+{I_l}^{-1}(\boldsymbol{R}_{lai} \times \; {}^{l}\boldsymbol{N}_i J)) \times \boldsymbol{R}_{lai} \right) \right) \cdot {}^{e}\boldsymbol{N}_i \\
\Leftrightarrow \\
-(1+K_e){}^{e}_{1}\boldsymbol{v}_{\Delta} \cdot {}^{e}\boldsymbol{N}_i = J &\left(\frac{1}{m_h} + \frac{1}{m_l} + \left(\boldsymbol{T}_{eh}({I_h}^{-1}(\boldsymbol{R}_{hai} \times {}^{h}\boldsymbol{N}_i J)) \times \boldsymbol{R}_{hai} \right) \cdot {}^{e}\boldsymbol{N}_i + \right. \\
&\left. \left(\boldsymbol{T}_{el}({I_l}^{-1}(\boldsymbol{R}_{lai} \times \; {}^{l}\boldsymbol{N}_i J)) \times \boldsymbol{R}_{lai} \right) \cdot {}^{e}\boldsymbol{N}_i \right) .
\end{aligned}$$

Solving for J yields

$$J = \frac{-(1+K_e){}^{e}_{1}\boldsymbol{v}_{\Delta} \cdot {}^{e}\boldsymbol{N}_i}{\frac{1}{m_h} + \frac{1}{m_l} + \left(\boldsymbol{T}_{eh}(I_h^{-1}(\boldsymbol{R}_{hai} \times {}^{h}\boldsymbol{N}_i J)) \times \boldsymbol{R}_{hai} + \boldsymbol{T}_{el}(I_l^{-1}(\boldsymbol{R}_{lai} \times \; {}^{l}\boldsymbol{N}_i J)) \times \boldsymbol{R}_{lai} \right) \cdot {}^{e}\boldsymbol{N}_i} \,. \tag{4.50}$$

By using (4.50) to determine the resulting impulse from the collision and using this in (4.45) to (4.48) it is possible to determine the collision response for a wire.

4.5.2 Example: Dual Wire Take-Off

To illustrate the wire collapse/collision system a take-off situation is simulated using a dual wire suspension. Note that the example only includes rigid body dynamics and no other dynamics are included. The equation are propagated using a 4th order Runge-Kutta at 100 Hz and the parameters used are shown in table 4.2. The helicopter is started at

Parameter	Value	Unit
$\boldsymbol{I}_h$ & $\boldsymbol{I}_l$	$\begin{bmatrix} 0.4 & 0 & -0.1 \\ 0 & 0.4 & 0 \\ -0.1 & 0 & 0.4 \end{bmatrix}$	Nm
m_h	10	kg
m_l	10	kg
$\boldsymbol{R}_{ha1}$	$\begin{bmatrix} 0.15 & 0 & 0.15 \end{bmatrix}^T$	m
$\boldsymbol{R}_{ha2}$	$\begin{bmatrix} -0.15 & 0 & 0.15 \end{bmatrix}^T$	m
$\boldsymbol{R}_{la1}$	$\begin{bmatrix} 0.15 & 0 & -0.09 \end{bmatrix}^T$	m
$\boldsymbol{R}_{la2}$	$\begin{bmatrix} -0.15 & 0 & -0.09 \end{bmatrix}^T$	m

Table 4.2: The parameters used in the dual wire take-off example.

an altitude of 2 m, the load is on the ground and the length of the wires are set to 3.76 m which means that they start out collapsed. Forces are then applied to the helicopter, which starts to move forward and upwards. At time 1.45 s and 1.55 s the two wires becomes taut and the load is lifted off ground by the helicopter as shown on figure 4.11. The rear wire collides first due to the pitching of the helicopter as it can be seen from the wire length plot in figure 4.12. It shows the direct distance between the attachment points and when the distance becomes equal to the taut length of the wire it collides. The result from this collision is clear from the body velocity and acceleration plots in figure 4.12, where it can be seen that the collision results in a backwards pitching (positive) and downwards motion for the helicopter and a forward pitching (negative) and upwards motion for the load. Shortly after the second wire becomes taut and the pitching motion of the load and the helicopter is aligned and the load is lifted off ground.

When the load is on ground the gravity is countered by the normal force from the ground and it is therefore not affected by any resulting force. This can be seen from the generalized applied forces plot in figure 4.12, which shows that no force is present on the load until the first collision. From the generalized constraint force plot it is clear that no constraint forces are present when the wires are collapsed. It can be seen that when the first wire collides it results in a small pitching torque as well as forces as the wire is off-centered. However, shortly after when the second wire becomes taut this torque is canceled out.

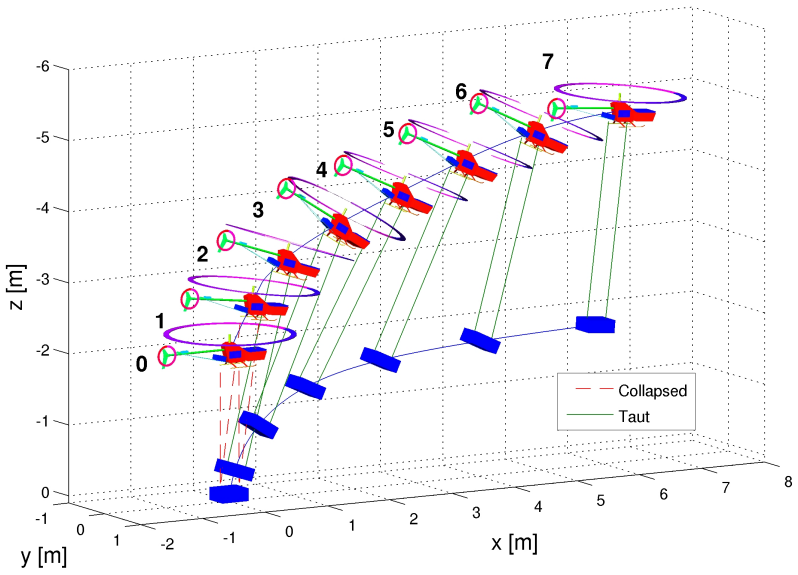

Figure 4.11: 3D plot of the dual wire take-off example with timeline.

4.6 Multi Lift Systems

Multi lift systems – where two or more helicopters are used to lift the load – are of both theoretical and practical interest. From a practical point of view there are many situations where there is an advantage in using two smaller helicopters to lift a load rather than one large one. From a theoretical point of view the challenge of modeling and controlling multi-lift systems have been the focus of some research during the past decades (see for instance [H. C. Curtiss, 1988] and [Cicolani and Kanning, 1992]).

Multi lift systems are traditionally considered highly complex systems and often result in equally complex models. Fortunately, the modeling approach introduced in this chapter can easily be extended to general multi lift systems simply by augmenting the equations with extra bodies.

Figure 4.13 shows three different dual lift systems. The pendant suspension (a) is simply the single wire configuration of figure 4.1 (a) using two helicopters. In the straight dual lift system (b) the attachment points on the load is moved away from each other such that the load on the helicopters becomes less slanted compared to the pendant suspension. The spreader bar system (c) can be seen as a combination of the two previous systems

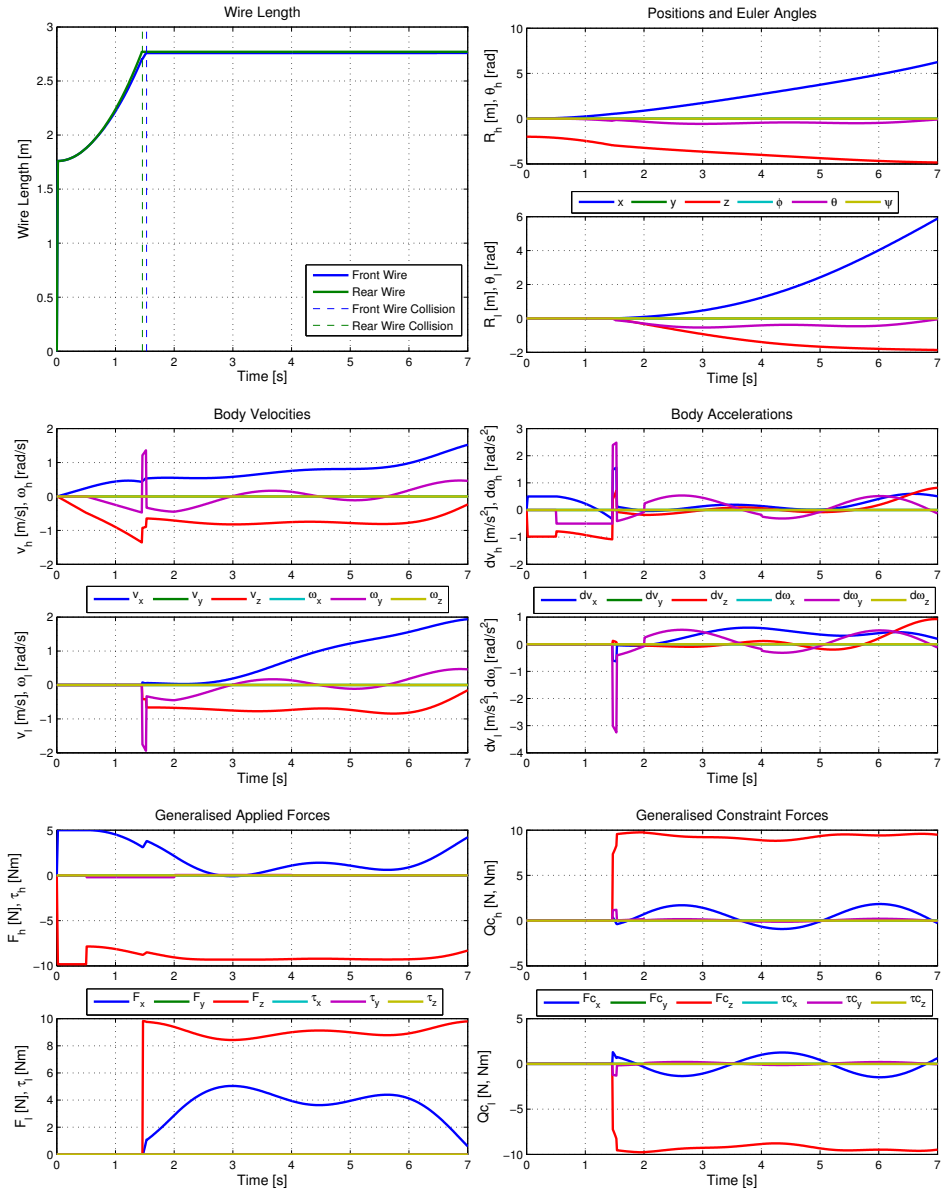

Figure 4.12: Graphs from the dual wire take-off example.

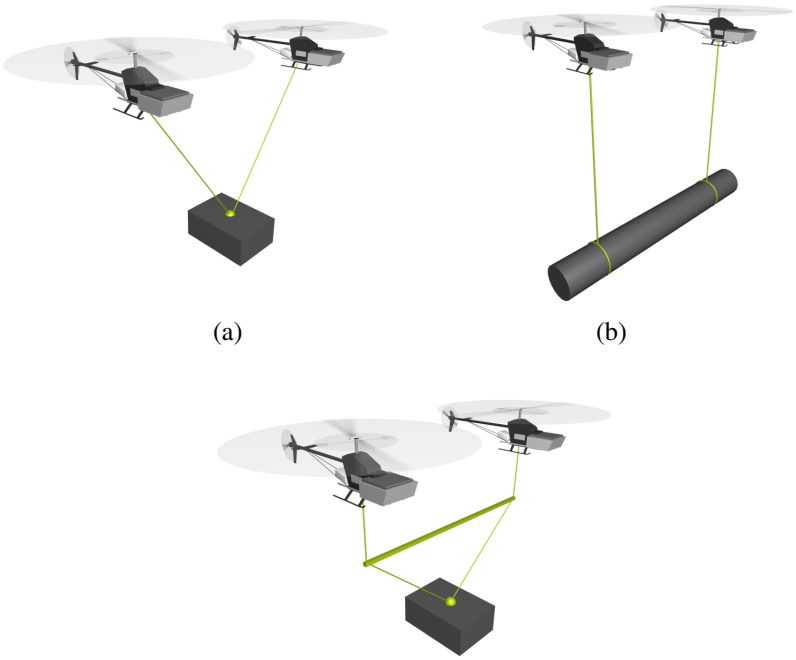

(a) (b)

(c)

Figure 4.13: Three different multi lift configurations. Dual lift pendant system (a), Straight dual lift system (b), Dual lift spreader bar system (c).

where the straight load distribution is achieved by placing a spreader bar between the two wires. It should be noted that while the general equations derived in this section cover l wires for each helicopter and k helicopters, almost all practical multi lift systems only use one wire for each helicopter.

In the following the focus will be on point-to-point dual lift suspension systems like the dual pendant suspension and the straight dual lift suspension, although systems including spreader bars can easily be modeled by including the bar as an extra body using the methods presented in the following. A general point-to-point multi lift suspension system is shown in figure 4.14.

To describe the system shown in figure 4.14, the equations derived in the sections are

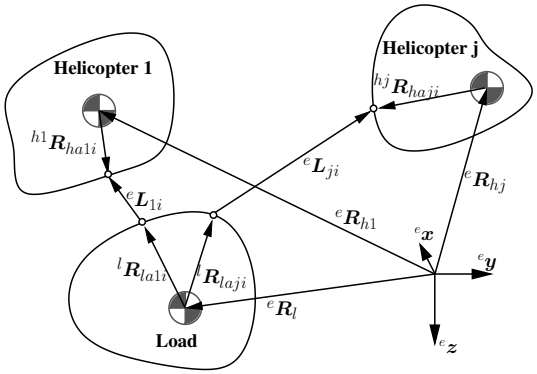

Figure 4.14: Configuration of a multi-lift system with two helicopters shown with the 1st and the jth helicopter.

augmented with the new body in the system

$$\boldsymbol{q} = \begin{bmatrix} \boldsymbol{R}_{h1} \\ \boldsymbol{\theta}_{h1} \\ \vdots \\ \boldsymbol{R}_{hk} \\ \boldsymbol{\theta}_{hk} \\ \boldsymbol{R}_{l} \\ \boldsymbol{\theta}_{l} \end{bmatrix}_{n\times 1} \qquad \ddot{\boldsymbol{q}}_a = \begin{bmatrix} {}^{h1}\boldsymbol{a}_{h1} \\ {}^{h1}\boldsymbol{\alpha}_{h1} \\ \vdots \\ {}^{hk}\boldsymbol{a}_{hk} \\ {}^{hk}\boldsymbol{\alpha}_{hk} \\ {}^{l}\boldsymbol{a}_{l} \\ {}^{l}\boldsymbol{\alpha}_{l} \end{bmatrix}_{n\times 1} . \tag{4.51}$$

The final constraint equation (4.39) can then be reformulated to encompass multiple bodies

$$\begin{aligned}
&\frac{d^2}{dt^2} g_{ji}(\boldsymbol{q}) = \\
&2\boldsymbol{L}_{ji}^T \left(\boldsymbol{T}_{ehj}\, {}^{hj}\boldsymbol{a}_{hj} + \boldsymbol{G}_{hj}\boldsymbol{T}_{\theta hj}\, {}^{hj}\boldsymbol{\alpha}_{hj} - \boldsymbol{T}_{el}\, {}^{l}\boldsymbol{a}_{l} - \boldsymbol{G}_{lj}\boldsymbol{T}_{\theta l}\, {}^{l}\boldsymbol{\alpha}_{l} \right) + \\
&2\boldsymbol{L}_{ji}^T \begin{bmatrix} \boldsymbol{G}_{\phi_{hj}}\dot{\boldsymbol{\theta}}_{hj} & \boldsymbol{G}_{\theta_{hj}}\dot{\boldsymbol{\theta}}_{hj} & \boldsymbol{G}_{\psi_{hj}}\dot{\boldsymbol{\theta}}_{hj} \end{bmatrix}_{3\times 3} \dot{\boldsymbol{\theta}}_{hj} + \\
&2\boldsymbol{L}_{ji}^T \begin{bmatrix} \boldsymbol{G}_{\phi_{jl}}\dot{\boldsymbol{\theta}}_{l} & \boldsymbol{G}_{\theta_{jl}}\dot{\boldsymbol{\theta}}_{l} & \boldsymbol{G}_{\psi_{jl}}\dot{\boldsymbol{\theta}}_{l} \end{bmatrix}_{3\times 3} \dot{\boldsymbol{\theta}}_{l} + 2\dot{\boldsymbol{L}}_{ji}^T \dot{\boldsymbol{L}}_{ji} + \\
&2\boldsymbol{L}_{ji}^T \left(-\boldsymbol{G}_{hj}(\boldsymbol{T}_{\theta hj}\boldsymbol{I}_{hj}^{-1}\, {}^{hj}\tilde{\boldsymbol{\omega}}_{hj}\boldsymbol{I}_{hj}\, {}^{hj}\boldsymbol{\omega}_{hj} + \dot{\boldsymbol{T}}_{\theta hj}\, {}^{hj}\boldsymbol{\omega}_{hj}) + \boldsymbol{G}_{l}(\boldsymbol{T}_{\theta l}\boldsymbol{I}_{l}^{-1}\, {}^{l}\tilde{\boldsymbol{\omega}}_{l}\boldsymbol{I}_{l}\, {}^{l}\boldsymbol{\omega}_{l} - \dot{\boldsymbol{T}}_{\theta l}\, {}^{l}\boldsymbol{\omega}_{l}) \right),
\end{aligned} \tag{4.52}$$

where the constraint equation now describes the ith wire on the jth body. Again, it is

possible to identify $\boldsymbol{A}$ and $\boldsymbol{b}$ from the constraint equation

$$\boldsymbol{A} = \begin{bmatrix} \boldsymbol{A}_{11} \\ \boldsymbol{A}_{12} \\ \vdots \\ \boldsymbol{A}_{ji} \\ \vdots \\ \boldsymbol{A}_{kl} \end{bmatrix}_{km \times n} \qquad \boldsymbol{b} = \begin{bmatrix} b_{11} \\ b_{12} \\ \vdots \\ b_{ji} \\ \vdots \\ b_{kl} \end{bmatrix}_{km \times 1},$$

where

$$\begin{aligned} &b_{ji} = \\ &2\boldsymbol{L}_{ji}^T \begin{bmatrix} \boldsymbol{G}_{\phi_{hj}} \dot{\boldsymbol{\theta}}_{hj} & \boldsymbol{G}_{\theta_{hj}} \dot{\boldsymbol{\theta}}_{hj} & \boldsymbol{G}_{\psi_{hj}} \dot{\boldsymbol{\theta}}_{hj} \end{bmatrix}_{3\times 3} \dot{\boldsymbol{\theta}}_{hj} + \\ &2\boldsymbol{L}_{ji}^T \begin{bmatrix} \boldsymbol{G}_{\phi_{jl}} \dot{\boldsymbol{\theta}}_{l} & \boldsymbol{G}_{\theta_{jl}} \dot{\boldsymbol{\theta}}_{l} & \boldsymbol{G}_{\psi_{jl}} \dot{\boldsymbol{\theta}}_{l} \end{bmatrix}_{3\times 3} \dot{\boldsymbol{\theta}}_{l} + 2\dot{\boldsymbol{L}}_{ji}^T \dot{\boldsymbol{L}}_{ji} + \\ &2\boldsymbol{L}_{ji}^T \Bigg(- \boldsymbol{G}_{hj}(\boldsymbol{T}_{\theta hj} \boldsymbol{I}_{hj}^{-1\ hj} \tilde{\boldsymbol{\omega}}_{hj} \boldsymbol{I}_{hj}{}^{hj} \boldsymbol{\omega}_{hj} + \dot{\boldsymbol{T}}_{\theta hj}{}^{hj} \boldsymbol{\omega}_{hj}) + \boldsymbol{G}_{hj}(\boldsymbol{T}_{\theta l} \boldsymbol{I}_{l}^{-1\ l} \tilde{\boldsymbol{\omega}}_{l} \boldsymbol{I}_{l}{}^{l} \boldsymbol{\omega}_{l} + \dot{\boldsymbol{T}}_{\theta l}{}^{l} \boldsymbol{\omega}_{l}) \Bigg), \end{aligned}$$

and

$$\boldsymbol{A}_{ji} = 2\boldsymbol{L}_{ji}^T \begin{bmatrix} \boldsymbol{0}_{3\times nj} & \boldsymbol{T}_{hj} & \boldsymbol{G}_{hj}\boldsymbol{T}_{\theta hj} & \boldsymbol{0}_{3\times n(k-j-1)} & \boldsymbol{0}_{3\times nk} & -\boldsymbol{T}_{l} & -\boldsymbol{G}_{lj}\boldsymbol{T}_{\theta l} \end{bmatrix}_{3\times n}.$$

The jith part of $\boldsymbol{b}$ is very similar to the single helicopter case and where the jith part of $\boldsymbol{A}$ has zeros on the rows not related to the jth body.

4.6.1 Example: Dual Lift Suspension

To illustrate the multi lift equations a simulation using a dual lift system is presented. Two helicopters of equal mass and a lighter load is used in a suspension system that is a mixture between the pendant and the straight dual suspension system. The equation are propagated using a 4th order Runge-Kutta at 100 Hz and the parameters used are shown in table 4.3. Again it should be noted that the example only includes rigid body dynamics

Parameter	Value	Unit
$\boldsymbol{I}_{h1}$ & $\boldsymbol{I}_{h2}$ & $\boldsymbol{I}_{l}$	$\begin{bmatrix} 0.4 & 0 & -0.1 \\ 0 & 0.4 & 0 \\ -0.1 & 0 & 0.4 \end{bmatrix}$	Nm
m_{h1} & m_{h2}	14	kg
m_l	4	kg
$\boldsymbol{R}_{ha11}$ & $\boldsymbol{R}_{ha21}$	$\begin{bmatrix} 0 & 0 & 0.15 \end{bmatrix}^T$	m
$\boldsymbol{R}_{la11}$ & $\boldsymbol{R}_{la21}$	$\begin{bmatrix} \pm 0.15 & 0 & -0.09 \end{bmatrix}^T$	m

Table 4.3: The parameters used in the dual lift example.

for the helicopter and load and all other dynamics and influences are excluded.

The two helicopters are placed 3 meters apart and 4 meters above the load, which has two slightly offset attachment points. Gravity is applied to all bodies and upward forces to keep the system flying are applied to the helicopters. Furthermore, appropriate forces in the sideways direction are applied to the helicopters to keep them apart as they would otherwise be dragged together by the load. A longitudinal, lateral, and upwards force is then applied to the helicopters (and removed again at time equal to 4 s) and the result can be observed on figure 4.15, 4.16, and 4.17.

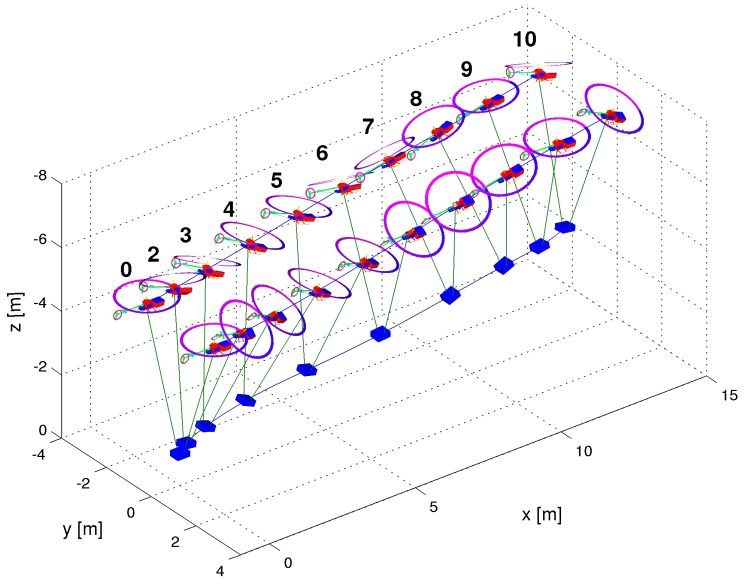

Figure 4.15: 3D plot of helicopters and load with timeline.

As it can be seen from figure in 4.15 the helicopters move as expected with the load hanging between them. From the top view it is clear that the load exhibit a pendulum-like oscillation between the helicopters in the longitudinal direction which is also clear from the velocity plot. The removal of the applied forces is evident from the bottom right figure where after only the gravity and thrust forces are present. The example shows that the equations are indeed capable of simulating a 3-body system in a simple and intuitive way.

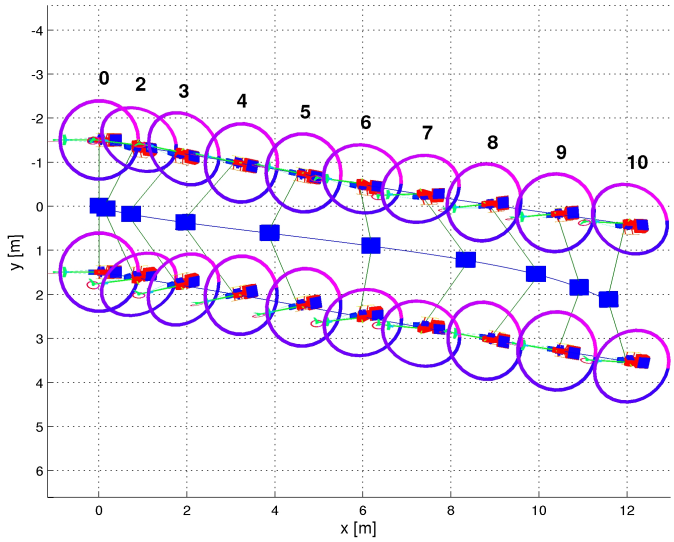

Figure 4.16: Top view of helicopters and load with timeline.

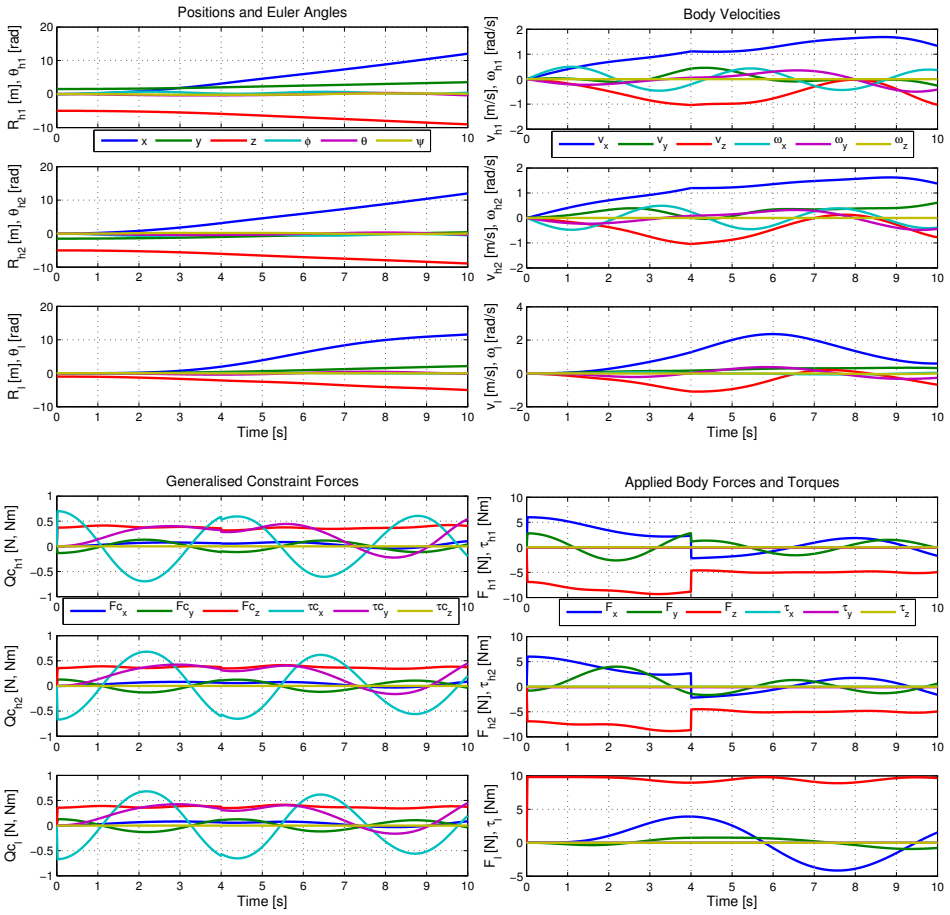

Figure 4.17: Graphs from the dual lift example.

4.7 Numerical Considerations

As mentioned in section 4.2 one of the disadvantages of using a full state model instead of a reduced state model is that numerical integration errors will over time violate the constraints. This means that the length of the wires will start to drift as the simulation progresses. This is due to the fact that the dynamic equations ensures that the system obeys the constraints in an acceleration sense such that

$$\ddot{g}(\ddot{\boldsymbol{q}}_a, \dot{\boldsymbol{q}}_b, \boldsymbol{q}) = 0\,, \tag{4.53}$$

in accordance with (4.4). There are no direct enforcement of the constraints in a velocity and position sense which means that

$$\begin{aligned} \dot{g}(\dot{\boldsymbol{q}}_b, \boldsymbol{q}) &\neq 0\,, \\ g(\boldsymbol{q}) &\neq 0\,, \end{aligned}$$

and the error on the constraints can therefore grow unbounded. The extend of the problem is highly dependent on the chosen integration method and the step size used in the integration, but nevertheless it is a widely recognized problem in the literature (see for instance [Ascher *et al.*, 1994] and [Clien and Pai, 2003]). Several different approaches has been suggested to counter this problem and the most popular is the method suggested in [Baumgarte, 1972]. Here we will discuss the Baumgarte algorithm and suggest an alternative approach which will be denoted the spring-damper approach. We will then compare the two methods.

To motivate the discussion an example of the drifting constraints is given here. In the inverted-V example in section 4.4, a 4th order Runge-Kutta was used to propagate the equations at 100 Hz and errors on the constraints of this is illustrated in figure 4.18 together with the results from the same example when a forward Euler is used.

It can be seen that the variations for the 4th order Runge-Kutta are less that 10^{-8} m and much longer simulations shows that the errors only increase slowly. From this it can be concluded that the 4th order Runge Kutta is clearly capable of propagating the system with a satisfactory precision. However, if the simulations are run with a standard forward Euler at 100 Hz, the constraints drift much faster and there is clearly a need for a method to bound the errors on the constraints.

4.7.1 Baumgarte

The method suggested by Baumgarte is a simple state feedback approach to stabilize the following system

$$\begin{bmatrix} \dot{\boldsymbol{g}} \\ \ddot{\boldsymbol{g}} \end{bmatrix} = \begin{bmatrix} \mathbf{0} & \mathbf{1} \\ \mathbf{0} & \mathbf{0} \end{bmatrix} \begin{bmatrix} \boldsymbol{g} \\ \dot{\boldsymbol{g}} \end{bmatrix}\,.$$

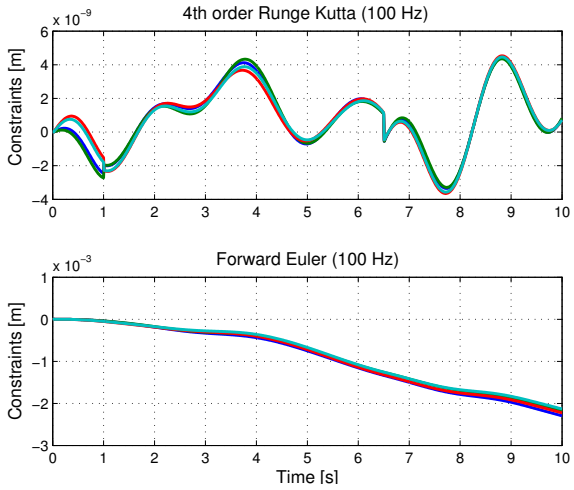

Figure 4.18: Numerical propagation-error on constraints from the Inverted V example. Shown for a 4th order Runge Kutta and forward Euler (100 Hz).

Baumgarte suggest a change of (4.53) to

$$\begin{aligned} \dot{\boldsymbol{g}} &= -2\alpha_b \dot{\boldsymbol{g}} - \beta_b^2 \boldsymbol{g} \Leftrightarrow \\ \boldsymbol{A}\ddot{\boldsymbol{q}} &= \boldsymbol{b} - 2\alpha_b \dot{\boldsymbol{g}} - \beta_b^2 \boldsymbol{g}\,, \end{aligned} \tag{4.54}$$

where α_b and β_b are the feedback gains. Choosing suitable values of the gains that yields a stabilizing feedback is dependent on the propagation method and the time step used in the propagation, consult [Lin, 2002] and [Jeon *et al.*, 2004] for examples on how to choose gains for specific integration methods. By substituting the changed constraint equation (4.54) into (4.16) we arrive at the numerically stabilized dynamics equation

$$\ddot{\boldsymbol{q}} = \ddot{\boldsymbol{q}}_u + \boldsymbol{M}^{-1/2}(\boldsymbol{A}\boldsymbol{M}^{-1/2})^{+}(\boldsymbol{b} - 2\alpha_b \dot{\boldsymbol{g}} - \beta_b^2 \boldsymbol{g} - \boldsymbol{A}\ddot{\boldsymbol{q}}_u)\,. \tag{4.55}$$

It should be noted this equation cannot directly be used for the slung load model as the coordinate change performed in section 4.4 must be take into account.

4.7.2 Spring-Damper Approach

As an alternative approach to the problem another simple feedback approach is suggested here, but whereas the Baumgarte method used feedback into the constraint equation this approach introduces the feedback from the constraints into the dynamics equation. The approach was conceived independently of Baumgarte's method through a physical consideration on how the problem affects the system.

The drifting constraint problem results in the length of the wires drifting. This means that when a wire becomes too long we should apply a force along it to pull it back into shape and vice versa. A simple way of doing this is to introduce a spring-damper system in parallel to each wire as shown in figure 4.19. The spring will then try to keep the wire length constant and thus introducing a penalty on the constraint error, the damper is necessary to reduce oscillations. This is done by appending a term $\boldsymbol{a}_n$ to (4.16) as

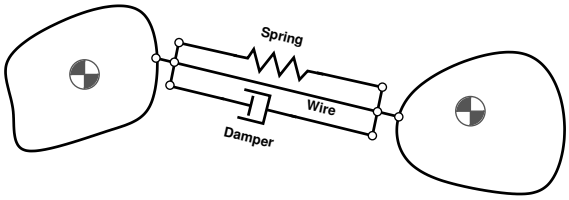

Figure 4.19: Numerical correction of constraints using the developed spring-damper approach.

$$\ddot{\boldsymbol{q}} = \boldsymbol{a} + \boldsymbol{M}^{-1/2}(\boldsymbol{A}\boldsymbol{M}^{-1/2})^{+}(\boldsymbol{b} - \boldsymbol{A}\boldsymbol{a}) + \boldsymbol{a}_n \,, \tag{4.56}$$

where

$$\boldsymbol{a}_n = \begin{bmatrix} \boldsymbol{a}_{nh} \\ \boldsymbol{\alpha}_{nh} \\ \boldsymbol{a}_{nl} \\ \boldsymbol{\alpha}_{nl} \end{bmatrix} \,.$$

This term penalizes numerical errors on the constraints $g_i(\boldsymbol{q})$ given by equation (4.25) and can be calculated using the spring force $\boldsymbol{F}_s$ and damper force $\boldsymbol{F}_d$ as

$$\boldsymbol{a}_{nb} = m_b^{-1} \sum_{i=1}^{m} \boldsymbol{T}_{be}(\boldsymbol{F}_{si} + \boldsymbol{F}_{di}) \,, \tag{4.57}$$

$$\boldsymbol{\alpha}_{nb} = \boldsymbol{I}_b^{-1} \sum_{i=1}^{m} \boldsymbol{R}_{bai} \times \boldsymbol{T}_{be}(\boldsymbol{F}_{si} + \boldsymbol{F}_{di}) \,. \tag{4.58}$$

The spring and damper forces are found as

$$\boldsymbol{F}_{si} = k_s g_i(\boldsymbol{q}) \boldsymbol{N}_i \,, \tag{4.59}$$

$$\boldsymbol{F}_{di} = -c_d \, \dot{g}_i(\boldsymbol{q}) \boldsymbol{N}_i \,, \tag{4.60}$$

where k_s is the spring constant and c_d is the damper constant.

Applying the method to the previously discussed example, the numerical error can be reduced drastically and more importantly it can be kept bounded. The result is shown in figure 4.20 where the error is now less than 10^{-5}.

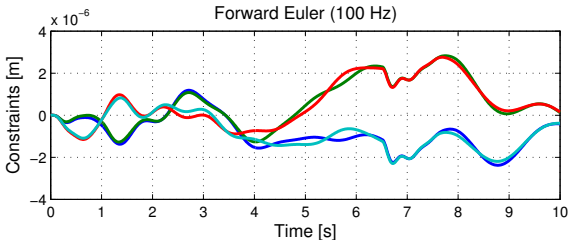

Figure 4.20: Forward Euler (100 Hz) with spring damper numerical correction.

An important part of applying the method is to choose the spring and damper constants. If the spring constant is chosen too high the system becomes stiff and thus becomes more difficult to propagate. In the example $k_s = 200$ and $c_d = 650$ were used. Simulations show a natural frequency of 2 Hz and while this frequency is slightly higher that those of the system it is still far from being necessary to consider the model a stiff system.

Chapter 5

Model Analysis and Verification

In this chapter a verification and discussion of the derived model is presented. First the stand alone helicopter model is verified against flight data and then the full model with both single and dual wire slung load is verified. Then a trimming and linearization scheme is developed and this scheme is used to do a linear analysis of the model.

5.1 Model Verification

In the following we present verification data for both the helicopter model alone and for the helicopter model with slung load. Parameters for the helicopter and slung load model has been identified using a combination of physical measurement and data fitting. Identified parameters are given in appendix B. It should be noted that no external wind measurements was available for these tests and sudden wind changes are therefore not represented in the simulated responses. This means that some discrepancies between simulated and real flight responses can be attribute to external wind. It has not been possible within the time frame of this research to acquire flight data without significant wind disturbances.

5.1.1 Helicopter Model Verification

Verification of the helicopter model is done by observing and comparing the correlation between actuator inputs and system response. If a high level of coherency between the real and the model response is achieved, the model is a good description of the real system. For the helicopter there are four different actuator inputs: Collective main rotor pitch, cyclic lateral and longitudinal main rotor pitch, and tail system yaw rate reference. These inputs affect different states, for the cyclic inputs the direct affectable states are the roll

and pitch rates, for the tail rotor input the relevant output is yaw rate, and for collective the affected output is vertical velocity.

Figure 5.1 shows a comparison between measured flight data and simulated vertical response to a series collective pitch. We can see from the left plot in figure 5.1 that the

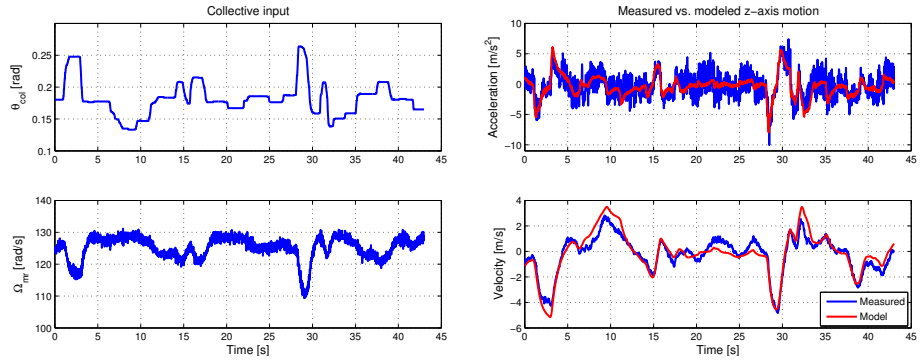

Figure 5.1: Left: Collective pitch and main rotor angular velocity input. Right: Helicopter model vertical response vs. measured response.

governor is capable of keeping the main rotor angular velocity within ± 15 rad/s under large collective pitch changes. The simulated vertical acceleration response has a good agreement with the measured response, especially during big collective pitch changes. The same is evident on the velocity response plot. However, during periods with only small collective pitch changes the external wind disturbances becomes more obvious.

In figure 5.2 and 5.3 horizontal responses to cyclic pitch inputs are shown. As with

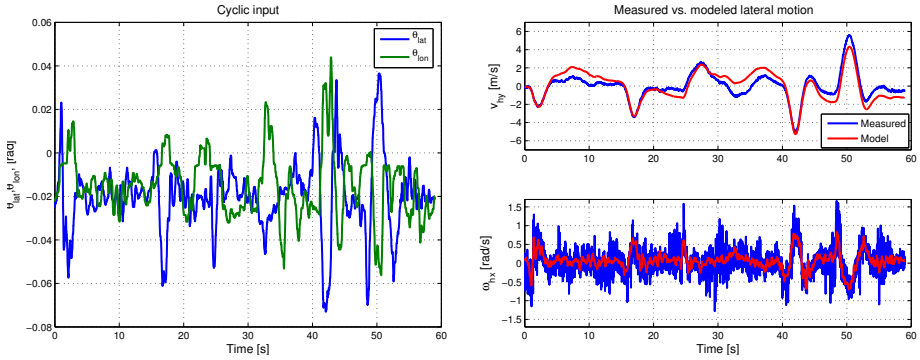

Figure 5.2: Left: Cyclic pitch input. Right: Helicopter model lateral response vs. measured response.

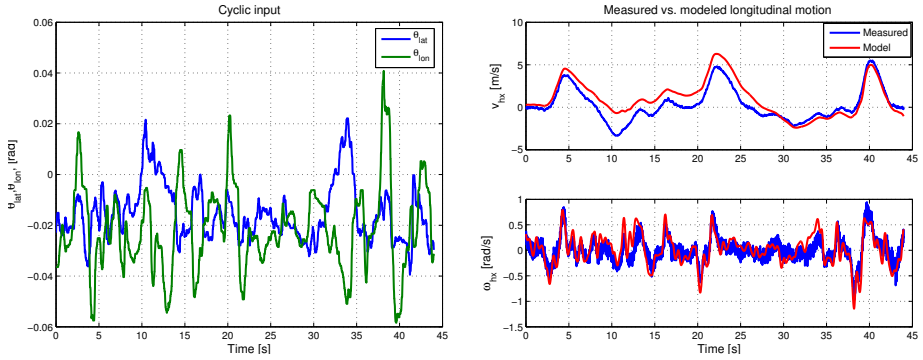

Figure 5.3: Left: Cyclic pitch input. Right: Helicopter model longitudinal response vs. measured response.

the vertical response, an overall good agreement between the simulated and the flight data can be seen. The larger noise level on measured roll rate, compared to measured pitch rate, is due to the smaller helicopter inertia on the x-axis. Both for the roll and pitch rate and for lateral and longitudinal velocity the simulated and recorded data fits very well during periods with large cyclic pitch changes. In the velocity plots, and especially on longitudinal, some deviations most likely due to external wind can be observed.

The good attitude model fit is evident from figure 5.4, where lateral and longitudinal response to saturated cyclic step inputs are shown. Both the fast lateral and the slower

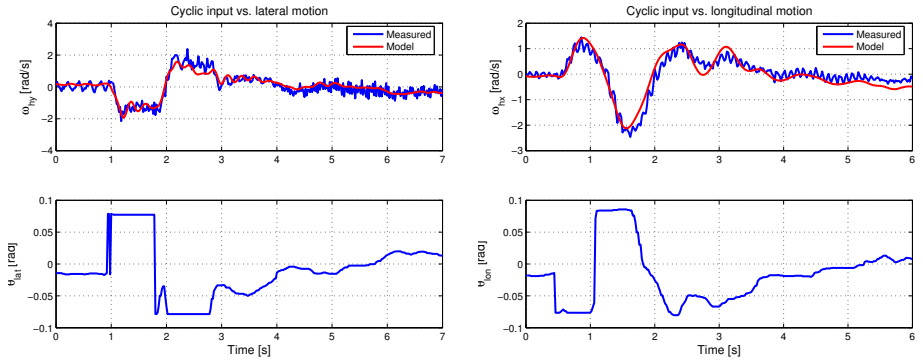

Figure 5.4: Helicopter roll and pitch response to saturated cyclic pitch input.

longitudinal dynamics are captured well by the model.

Response to tail rate input is shown in figure 5.5 and a very good agreement between simulated and recorded data is evident. By comparing the input to the yaw rate data it is

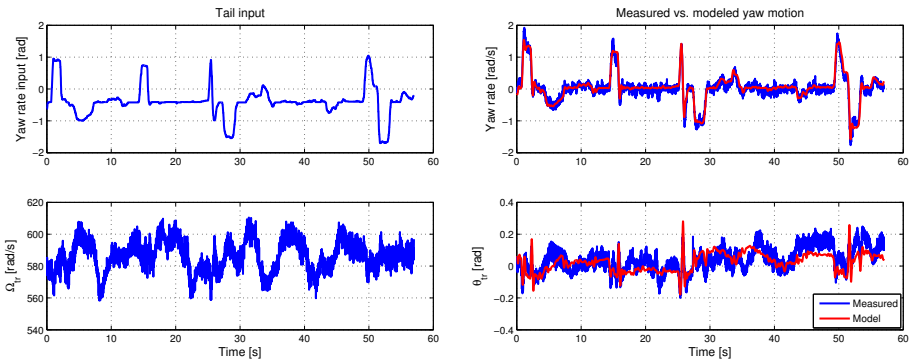

Figure 5.5: Left: Tail rate and angular velocity input. Right: Helicopter model yaw response vs. measured response.

clear that the gyro control system on the tail mentioned in chapter 2 is doing a good job at tracking the desired yaw rate. The good agreement between simulated and measured yaw response is due to the rate controller, which suppress differences between model and the real helicopter and wind disturbances. Larger discrepancies can be seen between the simulated and measured tail rotor pitch, where the data fits well during large yaw rate changes, but deviates at other points due to external wind disturbances.

5.1.2 Slung Load Model Verification

The slung load model derived in chapter 4 on page 69 is somewhat more difficult to verify reliably than the helicopter model alone. This is due to the fact that for the helicopter the system response to input changes are directly visible on the state vector without passing through long integrator chains. For instance, for the lateral cyclic pitch, the response is directly observable on the roll rate.

When looking at slung load response, the input must pass through several rigid body integrators before becoming visible on slung load motion. The flow of the rigid body slung load model is illustrated in figure 4.4 on page 78, where it is shown that the direct input to the rigid body model is a force vector. However, it is not possible to extract this force vector from the measurement data and we are therefore limited to use the helicopter model as a force generator. For a lateral motion, the cyclic input becomes helicopter roll rate, which integrates to helicopter roll. The helicopter attitude works as a actuator to the helicopter translation motion and through this motion we achieve a slung load motion. Through this long integrator chain, small model errors and external wind disturbances can result in very large response discrepancies. It can therefore be difficult to assess whether the model provides a good description of the system.

To help reduce this problem and for the slung load model response to become more

clear, we introduce a setup where the modeled helicopter position and Euler angles are gradually attracted to the estimated position and Euler angles. This means that the model is aided in following helicopter absolute motion, while the slung load is allowed to move freely. In a sense we create a force generator that, similar to the spring-damper approach presented in section 4.7.2 on page 100, continuously, but weakly, will attract the modeled helicopter position to the estimated position. In effect we make sure that the model generates a close to correct unconstrained acceleration for the helicopter – from (4.16)

$$\ddot{\boldsymbol{q}} = \ddot{\boldsymbol{q}}_u + \boldsymbol{M}^{-1/2}(\boldsymbol{A}\boldsymbol{M}^{-1/2})^{+}(\boldsymbol{b} - \boldsymbol{A}\ddot{\boldsymbol{q}}_u)\,. \tag{5.1}$$

This allows us to observe whether the slung load model is capable of filling in the remaining elements of the model, which are the slung load forces like gravity and drag and most importantly the wire constraining forces from (4.17)

$$\boldsymbol{Q}_c = \boldsymbol{M}^{1/2}(\boldsymbol{A}\boldsymbol{M}^{-1/2})^{+}(\boldsymbol{b} - \boldsymbol{A}\ddot{\boldsymbol{q}}_u)\,. \tag{5.2}$$

Single Wire Suspension System

In this test we compare the response of model and real system during two lateral steps with the single wire suspension as illustrated in figure 5.6. The test was performed using a controller in close loop on the helicopter motion. The two steps are performed as smooth

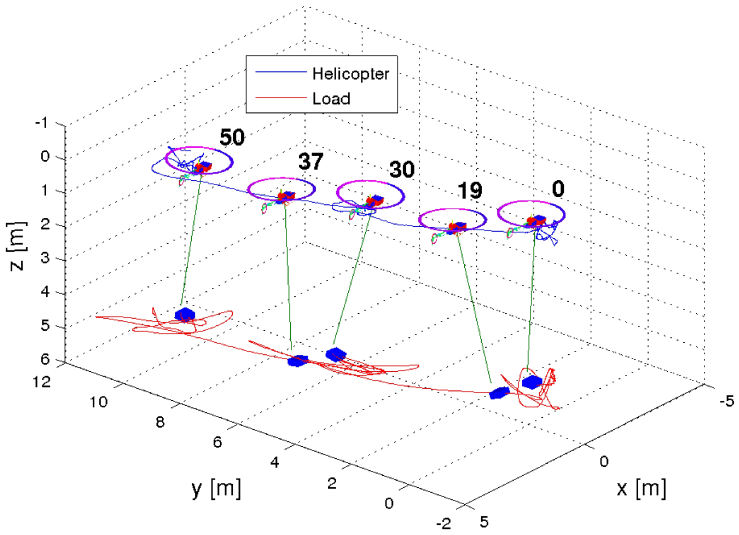

Figure 5.6: 3D plot of the single wire suspension system model verification test (with time line).

transitions from hover to hover with a peak helicopter velocity of 2 m/s. The simulated vs. measured helicopter motion is shown in figure 5.7 and it can be seen that the previously mentioned attractor is making sure that the modeled response is following the broad lines of the measured response for the helicopter. To the right in figure 5.7 we can see the

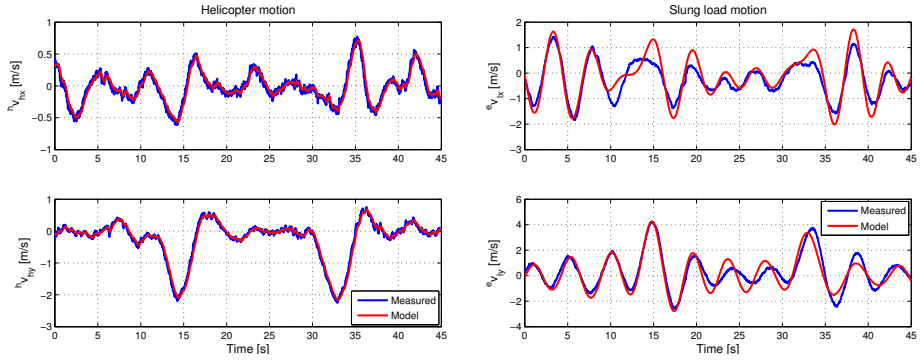

Figure 5.7: Left: Helicopter model horizontal velocity response vs. measured response. Right: Slung load model horizontal velocity response vs. measured response.

comparison between measured and modeled slung load horizontal velocities and it is clear that there is a very good agreement between the two.

Dual Wire Suspension system

Here the model is validated against data from a test flight with the dual wire suspension system. The flight consists of the helicopter flying in a square as illustrated in figure 5.8 with both modeled and measured slung load position plotted. Figure 5.9 shows a comparison between modeled and measured slung load translational and rotation velocities. It can be seen that the model has captured the general motion response of the system well, but naturally the position discrepancies grows with time as the errors are integrated.

Slung Load Release

In this test we verify the ability of the model to change suspension configuration on the fly by releasing the slung load. This is illustrated in figure 5.10 where it can be seen that the wires disappear 4 seconds into the flight and slung load drops to the ground. We have disabled the attractor as not to effect the helicopter motion as the purpose of the test is to verify helicopter response to the release of the slung load. The accelerations sample from the IMU mounted on the slung load is shown to the left in figure 5.11. It can be seen how the slung load drops into free fall before the signal wire is pulled out which freezes the measurement. The response of the model after the slung load release fits very well with the measured response, both when considering accelerations and velocity.

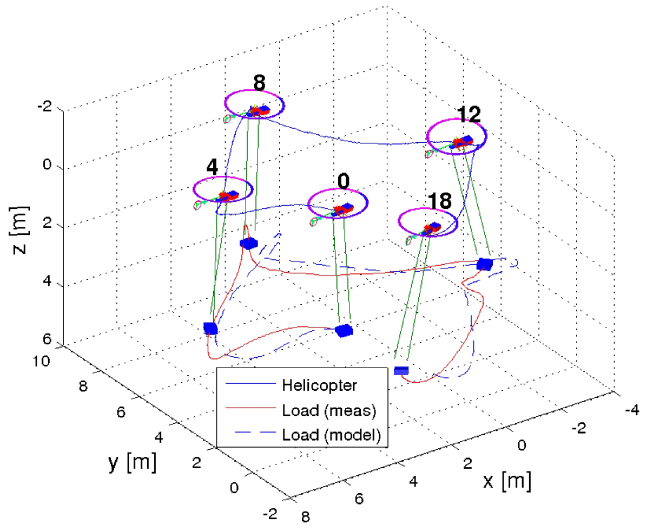

Figure 5.8: 3D plot of dual wire suspension system model verification test (with time line).

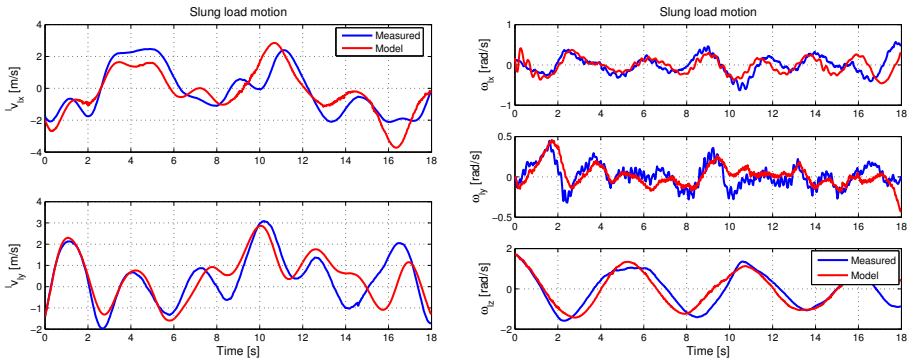

Figure 5.9: Left: Slung load model horizontal velocity response vs. measured response. Right: Slung load attitude rate response vs. measured response.

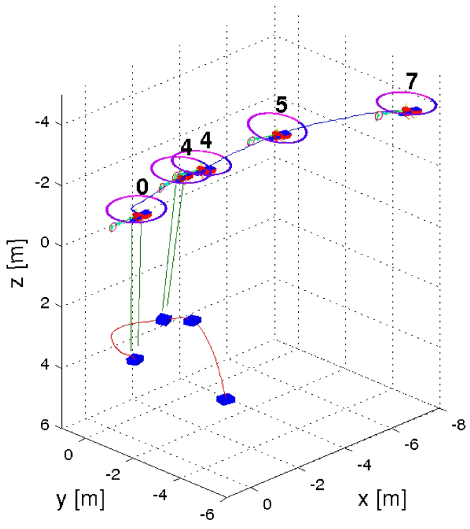

Figure 5.10: 3D plot of slung load release verification test (with timeline).

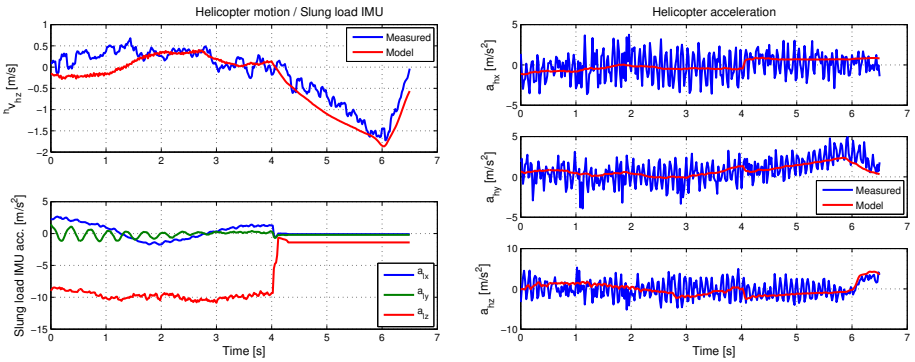

Figure 5.11: Left: Helicopter vertical velocity response and slung load IMU. Right: Helicopter acceleration response.

5.2 Trimming and Linearization

To do linear analysis of the model we need to be able to bring the model into an equilibrium, a procedure that for aircrafts is know as trimming. Trim algorithms for helicopters are well documented in the literature, see for instance [Kim *et al.*, 1993], [Luo *et al.*, 1993], [Peters and Barwey, 1996], and [Civita, 2002] where different solutions are presented ranging from analytical solution of the equations to employing numerical optimization algorithms or even tuning of controllers to "fly" the helicopter into a trim condition. Trim algorithms for helicopters with underslung loads are sparse in the literature, but a few approaches have been presented, see for example [Ronen *et al.*, 1986] and [Fusato *et al.*, 2002]. The trim algorithm developed here is based on the approach presented in [Civita, 2002] for the helicopter only case and it is then extended to handle slung loads.

5.2.1 Helicopter Trim

The general helicopter model is given by

$$\dot{\boldsymbol{X}} = \boldsymbol{f}(\boldsymbol{X}, \dot{\boldsymbol{X}}, \boldsymbol{u}) \,, \tag{5.3}$$

where $\boldsymbol{X} \in \mathbb{R}^n$ is the n element state vector and $\boldsymbol{u} \in \mathbb{R}^m$ is the m element control input vector. The idea of the trim process is to solve (5.3) for

$$\dot{\boldsymbol{X}} = 0 \,, \tag{5.4}$$

which means that (5.3) can be reduced to

$$\begin{aligned} \mathbf{0} &= \boldsymbol{f}(\boldsymbol{X}, \mathbf{0}, \boldsymbol{u}) \Rightarrow \\ \mathbf{0} &= \boldsymbol{f}(\boldsymbol{X}, \boldsymbol{u}) \,. \end{aligned} \tag{5.5}$$

This is formulated as a minimization problem which enables us to solve the nonlinear set of equations with a numerical approach. However, with both the state vector of n elements and the input vector of m elements as the unknowns and only n system equations, the problem not square. For the helicopter we have a input vector of four elements and therefore for the system to be solvable, another four equations must be added to the system. This is done by introducing four equations that represent the actual trim condition. A trim condition $\xi \in \mathbb{R}^4$ is given as

$$\xi = \begin{bmatrix} V \\ \gamma_w \\ \gamma_{\text{fp}} \\ \dot{\psi}_{\text{trim}} \end{bmatrix} \tag{5.6}$$

where V is the length of the velocity vector $\boldsymbol{V}$, γ_w is the sideslip angle, γ_{fp} is the flight plane angle, and $\dot{\psi}_{\text{trim}}$ is the yaw rotation as illustrated in figure 5.12. The sideslip angle

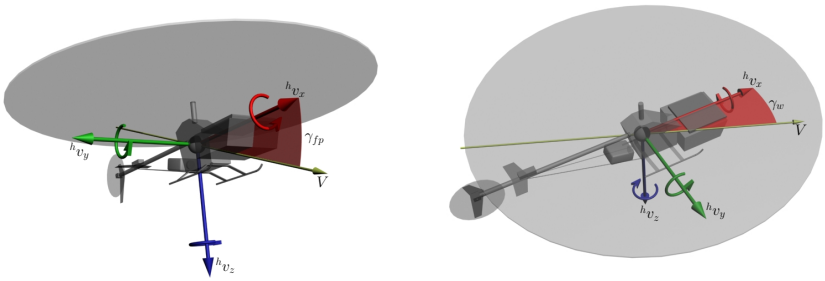

Figure 5.12: The flight plane and sideslip angles with respect to the velocity vector.

represents the direction of the velocity vector $\boldsymbol{V}$ in the x-y plane, side slipangle of $90°$ means sideways flight and $180°$ means backwards flight. The flight plane angle represents the amount of vertical velocity along the velocity vector, a flight plane angle of $90°$ means a vertical descent. The yaw rotation is used for coordinated turns like flying in a circle. Using this representation we can create a set of new equations that can be used to calculate four of the unknowns. This is done by using the speed, the flight plane angle, and the sideslip angle to calculate the earth fixed velocity vector of the helicopter

$$ {}^e\dot{\boldsymbol{R}}_h = \begin{cases} {}^e\dot{x} &= -V\cos(\gamma_{\text{fp}})\cos(\gamma_w) \\ {}^e\dot{y} &= -V\cos(\gamma_{\text{fp}})\sin(\gamma_w) \\ {}^e\dot{z} &= V\sin(\gamma_{\text{fp}}) \end{cases} . \tag{5.7} $$

This can be transformed to yield the body fixed velocity vector

$$ {}^h\boldsymbol{v}_h = \boldsymbol{T}_{be}\,{}^e\dot{\boldsymbol{R}}_h \,, \tag{5.8} $$

that together with

$$ {}^e\dot{\psi}_h = \dot{\psi}_{\text{trim}} \,, \tag{5.9} $$

yields the necessary four equations.

The state vector can be found from (4.22), (4.23), (3.44), (3.47), and (3.3)-(3.6) to be

$$ \begin{aligned} \boldsymbol{X}_{\text{trim}} = [&{}^e\phi \;\; {}^e\theta \;\; {}^h\omega_{x_h} \;\; {}^h\omega_{y_h} \;\; {}^h\omega_{z_h} \;\; a_{\text{con}} \;\; a_{\text{lat}} \;\; a_{\text{lon}} \;\; \dot{a}_{\text{con}} \;\; \dot{a}_{\text{lat}} \;\; \dot{a}_{\text{lon}} \;\; a_{lat,st} \;\; a_{1on,st} \\ &\dot{a}_{lat,st} \;\; \dot{a}_{lon,st} \;\; \theta_{\text{col}} \;\; \theta_{\text{lat}} \;\; \theta_{\text{lon}} \;\; \theta_{\text{tr}} \;\; \dot{\theta}_{\text{col}} \;\; \dot{\theta}_{\text{lat}} \;\; \dot{\theta}_{\text{lon}} \;\; \dot{\theta}_{\text{tr}}]^T_{1\times 23} \,, \end{aligned} \tag{5.10} $$

and the input vector is identified as

$$ \boldsymbol{u} = [S_{\text{col}} \;\; S_{\text{lat}} \;\; S_{\text{lon}} \;\; S_{\text{tr}}]^T_{1\times 4} \,, \tag{5.11} $$

which gives 27 input variables. Note that we neglect the gyro controller in the trim process as there is no yaw rate error for a steady flight condition. The corresponding output vector becomes

$$\dot{\boldsymbol{X}}_{\text{trim}} = [{}^{e}\dot{\phi}\ {}^{e}\dot{\theta}\ {}^{e}\dot{\psi}\ {}^{h}\dot{v}_{x_h}\ {}^{h}\dot{v}_{y_h}\ {}^{h}\dot{v}_{z_h}\ {}^{h}\dot{\omega}_{x_h}\ {}^{h}\dot{\omega}_{y_h}\ {}^{h}\dot{\omega}_{z_h}\ \dot{a}_{\text{con}}\ \dot{a}_{\text{lat}}\ \dot{a}_{\text{lon}}\ \ddot{a}_{\text{con}}\ \ddot{a}_{\text{lat}}\ \ddot{a}_{\text{lon}}\ \dot{a}_{lat,st}\ \dot{a}_{lon,st}\ \ddot{a}_{lat,st}\ \ddot{a}_{lon,st}\ \dot{\theta}_{\text{col}}\ \dot{\theta}_{\text{lat}}\ \dot{\theta}_{\text{lon}}\ \dot{\theta}_{\text{tr}}\ \ddot{\theta}_{\text{col}}\ \ddot{\theta}_{\text{lat}}\ \ddot{\theta}_{\text{lon}}\ \ddot{\theta}_{\text{tr}}]^{T}_{1\times 27}\,. \tag{5.12}$$

The helicopter position and the yaw angle are uncoupled with the rest of the system and can be chose arbitrarily. For the numerical solution Powell's Dogleg method is used in Matlab's *fsolve* implementation.

5.2.2 Example: Helicopter Trim

To illustrate the concept of trim an example is given with the helicopter trimmed in the following flight condition

$$V = 4\ \text{m/s},\ \ \gamma_{\text{fp}} = -0.07\ \text{rad},\ \ \gamma_w = 0\ \text{rad},\ \ \dot{\psi}_{\text{trim}} = 0.6\ \text{rad}\,,$$

which is equivalent to a nose forward flight in a circle with an upwards motion. The result of a 20 second simulation of the helicopter, initialized in the trim condition found by the trimming scheme, is shown in figure 5.13. The helicopter moves in an upwards helix motion and it can be seen in the the acceleration plot that the helicopter starts in good, but not perfect, trim condition. The transients in the beginning comes from the fast flapping dynamics and the subsequent oscillatory behavior originates from the rigid body modes. As time progresses the accelerations begins to exhibit a distinct unstable motion as expected when initialized close to an unstable equilibrium.

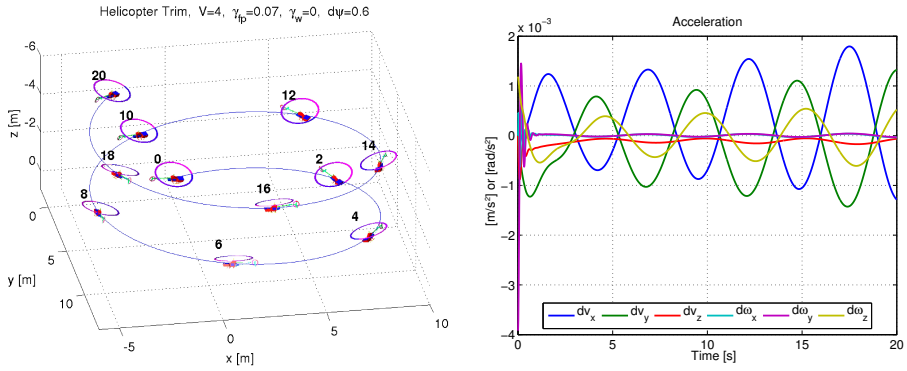

Figure 5.13: 3D plot and accelerations of helicopter trim example.

5.2.3 Helicopter-Slung Load Trim

When the entire helicopter slung load system is considered the state vector is extended to

$$\begin{aligned}\boldsymbol{X}_{\text{trim}} = [&{}^{e}x_h \;\; {}^{e}y_h \;\; {}^{e}z_h \;\; {}^{e}\phi_h \;\; {}^{e}\theta_h \;\; {}^{e}\psi_h \;\; {}^{h}v_{x_h} \;\; {}^{h}v_{y_h} \;\; {}^{h}v_{z_h} \;\; {}^{h}\omega_{x_h} \;\; {}^{h}\omega_{y_h} \;\; {}^{h}\omega_{z_h} \;\; {}^{e}x_l \;\; {}^{e}y_l \;\; {}^{e}z_l \\ &{}^{e}\phi_l \;\; {}^{e}\theta_l \;\; {}^{e}\psi_l \;\; {}^{l}v_{x_l} \;\; {}^{l}v_{y_l} \;\; {}^{l}v_{z_l} \;\; {}^{l}\omega_{x_l} \;\; {}^{l}\omega_{y_l} \;\; {}^{l}\omega_{z_l} \;\; a_{\text{con}} \;\; a_{\text{lat}} \;\; a_{\text{lon}} \;\; \dot{a}_{\text{con}} \;\; \dot{a}_{\text{lat}} \;\; \dot{a}_{\text{lon}} \\ &a_{lat,st} \;\; a_{1on,st} \;\; \dot{a}_{lat,st} \;\; \dot{a}_{lon,st} \;\; \theta_{\text{col}} \;\; \theta_{\text{lat}} \;\; \theta_{\text{lon}} \;\; \theta_{\text{tr}} \;\; \dot{\theta}_{\text{col}} \;\; \dot{\theta}_{\text{lat}} \;\; \dot{\theta}_{\text{lon}} \;\; \dot{\theta}_{\text{tr}}]^{T}_{1\times 42} \;,\end{aligned} \tag{5.13}$$

where the positions can no longer be omitted as the positions of the helicopter and the load are coupled. However, if the slung load position and yaw angle are defined relative to the helicopter, the helicopter positions and yaw angle can still by chosen arbitrarily. Furthermore, (5.8)-(5.9) can still be used for calculating the velocity and yaw rate of the helicopter.

Thereby new unknown states are the slung load position, Euler angles, translational, and angular velocities. However, these states are tightly coupled with the helicopter states and to reduce the number of states to be found by the minimization process the load velocities can be calculated from the helicopter velocities. This can intuitively be found by observing that in a non-turning flight condition, the earth fixed velocity of helicopter and load must be equal. If a turning flight condition is considering then the load will exhibit a larger turning radius than the helicopter due to centrifugal forces, which will result in a larger translational velocity. This additional element can easily be found by the cross product between the arm from the helicopter to the load and the angular velocity of the helicopter which is added to the helicopter velocity as

$${}^{l}\boldsymbol{v}_l = \boldsymbol{T}_{el}\left(\boldsymbol{T}_{he}{}^{h}\boldsymbol{v}_h + \left(\boldsymbol{T}_{he}{}^{h}\boldsymbol{\omega}_h \times ({}^{e}\boldsymbol{R}_l - {}^{e}\boldsymbol{R}_h)\right)\right) \;. \tag{5.14}$$

Furthermore, it is a necessary condition in steady state flight that the angular velocities of both helicopter and load are equal in the earth fixed frame. This means that the load angular velocities can be calculated as

$${}^{l}\boldsymbol{\omega}_l = \boldsymbol{T}_{el}\boldsymbol{T}_{he}{}^{h}\boldsymbol{\omega}_h \;, \tag{5.15}$$

together with

$${}^{e}\dot{\psi}_l = \dot{\psi}_{\text{trim}} \;. \tag{5.16}$$

There are no explicit observance of the constraint equation (4.25) in the rigid body equation (4.16). Instead it is subject to the constraints in an acceleration sense (as given in (4.4) on page 73) and there is therefore no direct coupling between the helicopter and load position and Euler angles. However, such a coupling is implemented by the spring-damper numerical correction suggested in section 4.7.2 on page 100. Thus, by including this in the rigid body equations it is ensured that the solution, found by the minimization process, observe the explicit constraint equation. In other words, if the iterative trim

algorithm suggests a solution where the wire lengths are not correct, the springs coupled in parallel with the wires, as shown in (4.56), will yield a resulting acceleration and thus the solution cannot be a minimum.

All in all this yields the following input vector for the trim algorithm

$$\begin{aligned}\boldsymbol{X}_{\text{trim}} = [&{}^{e}\phi_h \;\; {}^{e}\theta_h \;\; {}^{e}x_l \;\; {}^{e}y_l \;\; {}^{e}z_l \;\; {}^{e}\phi_l \;\; {}^{e}\theta_l \;\; {}^{e}\psi_l \;\; {}^{h}\omega_{x_h} \;\; {}^{h}\omega_{y_h} \;\; {}^{h}\omega_{z_h} \\ &a_{\text{con}} \;\; a_{\text{lat}} \;\; a_{\text{lon}} \;\; \dot{a}_{\text{con}} \;\; \dot{a}_{\text{lat}} \;\; \dot{a}_{\text{lon}} \;\; a_{lat,st} \;\; a_{lon,st} \;\; \dot{a}_{lat,st} \;\; \dot{a}_{lon,st} \\ &\theta_{\text{col}} \;\; \theta_{\text{lat}} \;\; \theta_{\text{lon}} \;\; \theta_{\text{tr}} \;\; \dot{\theta}_{\text{col}} \;\; \dot{\theta}_{\text{lat}} \;\; \dot{\theta}_{\text{lon}} \;\; \dot{\theta}_{\text{tr}}]^T_{1\times 29}\,,\end{aligned} \tag{5.17}$$

and the following output vector

$$\begin{aligned}\dot{\boldsymbol{X}}_{\text{trim}} = [&{}^{e}\dot{\phi}_h \;\; {}^{e}\dot{\theta}_h \;\; {}^{e}\dot{\psi}_h \;\; {}^{h}\dot{v}_{x_h} \;\; {}^{h}\dot{v}_{y_h} \;\; {}^{h}\dot{v}_{z_h} \;\; {}^{h}\dot{\omega}_{x_h} \;\; {}^{h}\dot{\omega}_{y_h} \;\; {}^{h}\dot{\omega}_{z_h} \;\; {}^{l}\dot{v}_{x_l} \;\; {}^{l}\dot{v}_{y_l} \;\; {}^{l}\dot{v}_{z_l} \\ &{}^{l}\dot{\omega}_{x_l} \;\; {}^{l}\dot{\omega}_{y_l} \;\; {}^{l}\dot{\omega}_{z_l} \;\; \dot{a}_{\text{con}} \;\; \dot{a}_{\text{lat}} \;\; \dot{a}_{\text{lon}} \;\; \ddot{a}_{\text{con}} \;\; \ddot{a}_{\text{lat}} \;\; \ddot{a}_{\text{lon}} \;\; \dot{a}_{lat,st} \;\; \dot{a}_{lon,st} \\ &\ddot{a}_{lat,st} \;\; \ddot{a}_{lon,st} \;\; \dot{\theta}_{\text{col}} \;\; \dot{\theta}_{\text{lat}} \;\; \dot{\theta}_{\text{lon}} \;\; \dot{\theta}_{\text{tr}} \;\; \ddot{\theta}_{\text{col}} \;\; \ddot{\theta}_{\text{lat}} \;\; \ddot{\theta}_{\text{lon}} \;\; \ddot{\theta}_{\text{tr}}]^T_{1\times 33}\,.\end{aligned} \tag{5.18}$$

It should be noted that the helicopter trim equations augmented with the slung load equations as shown in (5.13) together with (5.8)-(5.9) forms a square system, which is possible to use for the trim algorithm. However, numerical tests have shown that it is very difficult to make this system converge to a solution. The reduced system we arrived at in (5.17) and (5.18) is much more well behaved and converges easily.

5.2.4 Example: Slung Load Trim

To illustrate the concept of trim an example is given with the helicopter trimmed in the following flight condition

$$V = 4\ \text{m/s},\;\; \gamma_{\text{fp}} = -0.16\ \text{rad},\;\; \gamma_w = 0\ \text{rad},\;\; \dot{\psi}_{\text{trim}} = 0.6\ \text{rad}\,,$$

which is a similar flight condition to the one used in example 5.2.2. The result of the trim is shown in figure 5.14 where the helicopter can be seen following the intended trajectory with the load dragging behind it. The accelerations of both helicopter and load is shown in figure 5.15 and it is evident that the system is indeed very close to an equilibrium.

5.2.5 Linearization

The linearization of the system is done using a standard perturbation method, which is implemented using a central difference scheme

$$\begin{aligned}\boldsymbol{y}_1 &= \boldsymbol{f}(\boldsymbol{x}+h,\boldsymbol{u}) \\ \boldsymbol{y}_2 &= \boldsymbol{f}(\boldsymbol{x}-h,\boldsymbol{u}) \\ \boldsymbol{y} &= \frac{\boldsymbol{y}_2-\boldsymbol{y}_1}{2h}\,.\end{aligned}$$

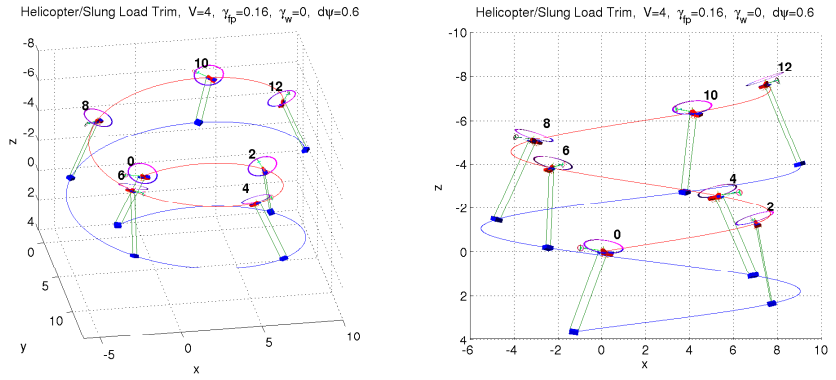

Figure 5.14: 3D plot of slung load trim example with time-line.

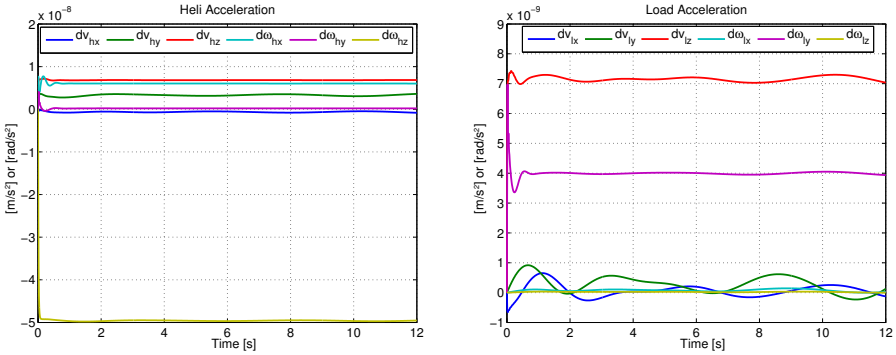

Figure 5.15: Helicopter and slung load accelerations of slung load trim example.

However, for control purposes it is desirable to extract a reduced linear model where only the control relevant states are represented. The remaining states are removed from the model by using steady state solutions. A steady state solution is achieved by zeroing the state derivatives and solving the equations directly. For the main rotor flapping equations the steady state solution is

$$\boldsymbol{a}_{mr} = \boldsymbol{K}_{mr}^{-1}(\boldsymbol{J}_{mr}\boldsymbol{\theta}_{mr} + \boldsymbol{E}_{mr}\lambda + \boldsymbol{G}_{mr}) \,, \tag{5.19}$$

and for the stabilizer bar

$$\boldsymbol{a}_{sb} = \boldsymbol{K}_{sb}^{-1}(\boldsymbol{J}_{sb}\boldsymbol{\theta}_{sb} + \boldsymbol{E}_{sb}\lambda + \boldsymbol{G}_{sb}) \,. \tag{5.20}$$

Similar we can use steady state solutions to the actuator dynamics equations.

5.3 Linear Model Analysis

In this section we present a linear analysis of the model, mainly to identify how different slung load parameters affect the system behavior. First the helicopter alone is analyzed using frequency response and eigenvalue plots. Then the helicopter with the single wire slung load and the dual wire slung load is analyzed. This analysis is focused on hover and slow forward fight ($<$ 10 m/s) as these are the range that the controller design will focus on in this thesis.

As a reference for helicopter handling criteria the US Army Aviation design standard is used [ADS-33E-PRF, 2000], which specify three levels for rotorcraft handling. Level 1 gives the best aircraft characteristics and is specified as ranging between

- *Pilot compensation is not a factor for desired performance*
- *Minimal pilot compensation required for desired performance*

Level 2 ranges between

- *Desired performance requires moderate pilot compensation*
- *Adequate performance requires extensive pilot compensation*

Finally level 3 ranges between

- *Adequate performance not attainable with maximum tolerable pilot compensation*
- *Considerable pilot compensation is required for control*

In [ADS-33E-PRF, 2000] there is very little slung load specific information, but [Hoh *et al.*, 2006] is an elaboration that focuses specifically on slung load handling using the same level specifications, and it mentions that a rotor craft used for slung load operations should be level 1 without load to ensure adequate performance with load.

5.3.1 Helicopter without Slung Load

The following analysis is for the helicopter configured with the parameters given in appendix B on page 243. The primary dynamic modes of the helicopter in hover are shown in table 5.1. The first two eigenvalues (1-2) is the roll short period mode and describes the well damped fast roll dynamics. It originates from a coupling between the main rotor flapping, the stabilizer bar flapping, and the fuselage. The pitch short period (4-5) describes the same coupling, but for the pitch dynamics. It is less damped that the roll mode and is indeed close the the level 1 requirement of a damping of $\zeta > 0.35$.

The damped spiral/yaw mode (3) corresponds to the yaw rate controller that gives a fast response and decouples this mode from the heave mode (6), which is also a damped mode. The unstable phugoid mode (7-8) is mainly a longitudinal mode with couplings to vertical velocity and both pitch and roll rate. The stable dutch roll type mode (9-10) is a coupling between lateral and longitudinal velocities and roll and pitch rate. This means

Mode type	**Pole**	ζ	ω [rad/s]
Roll short period (1-2)	-11.38±19.19i	0.51	22.31
Spiral/Yaw (3)	-13.47	1	13.47
Pitch short period (4-5)	-3.14±7.88i	0.369	8.48
Heave (6)	-0.92	1	0.92
Phugoid (7-8)	0.015 ± 0.305i	-0.0497	0.305
Dutch roll (9-10)	-0.041 ± 0.303i	0.134	0.306

Table 5.1: Eigenvalues of the helicopter in hover.

that it is not truly a dutch roll mode, but can be view as a mix of phugoid and a dutch roll mode.

The helicopter modes in forward flight at 10 m/s is shown in table 5.2 and for most modes the changes from hover are small. Both short period modes become more damped in forward flight and heave mode moves further into the left half plane. Most significant

Mode type	**Pole**	ζ	ω [rad/s]
Roll short period (1-2)	-11.89 ±18.85i	0.53	22.29
Spiral/Yaw (3)	-13.37	1	13.37
Pitch short period (4-5)	-3.19 ± 7.94i	0.373	8.56
Heave (6)	-1.94	1	1.94
Phugoid (7-8)	-0.0218 ±0.253i	0.0859	0.254
Dutch roll (9-10)	-0.223 ± 0.158i	0.820	0.276

Table 5.2: Eigenvalues of the helicopter in forward flight (10 m/s).

are the changes in the phugoid and dutch roll modes. The phugoid mode that was unstable in hover has moved into the left half plane and become stable, but very lightly damped. The dutch roll has become more damped and as a function of forward speed this mode starts to behave like a true lateral dutch roll mode. The modes are shown in figure 5.16 together with level indications from [ADS-33E-PRF, 2000]. The motion of the poles are found by linearizing the system in a range of points between hover (V = 0 m/s) and forward flight (V = 10 m/s). It is clear how the helicopter becomes more stable as forward speed increases, but all modes are classified as level 1, both in hover and in forward flight. The increased stability of the phugoid is due to the tail plane and tail rotor of the helicopter and indeed if a backwards velocity is applied the phugoid becomes more unstable.

Figure 5.17 shows the frequency response of the helicopter in hover from cyclic pitch input to corresponding roll and pitch rate. In other words this is the primary attitude response of the helicopter, i.e. roll rate response for lateral pitch and pitch rate response for longitudinal pitch. Both the short period and long period attitude dynamics can be seen in the frequency response and the lightly damped behavior of the phugoid and dutch roll is visible. It is clear how the roll dynamics is much faster that the pitch dynamics of the helicopter, which is due to the large difference in helicopter inertia on the x- and

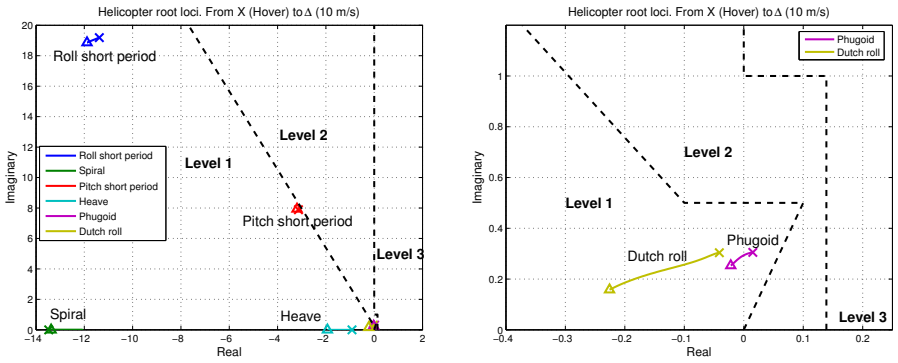

Figure 5.16: Plot of helicopter poles ranging from hover (V = 0 m/s, marked with $\times$) to forward flight (V = 10 m/s, marked with $\triangle$). With ADS-33E limits plotted.

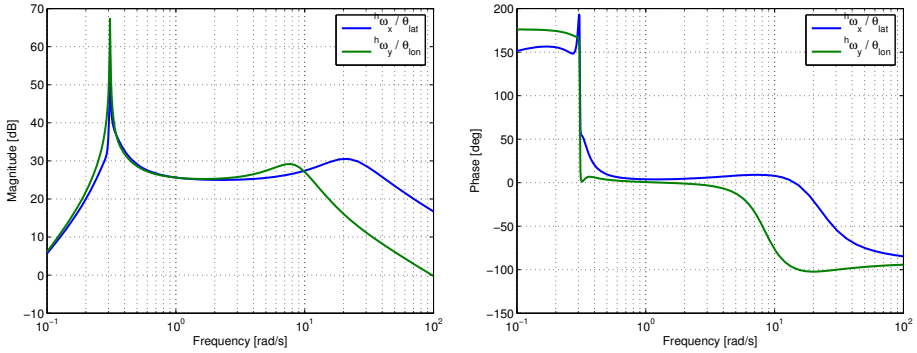

Figure 5.17: Frequency response plot of helicopter roll and pitch rate from corresponding cyclic input (hover).

y-axis. The frequency response of the cross couplings in the attitude dynamics are shown in figure 5.18. It is clear that there is indeed a significant cross coupling between lateral and longitudinal motion, especially around the resonance frequency from both short and long period attitude dynamics.

In figure 5.19 the frequency response of the yaw and heave dynamics are shown and we can see that both exhibit simple first order behavior. Due to the inner loop yaw rate controller there are no significant cross coupling between these two modes.

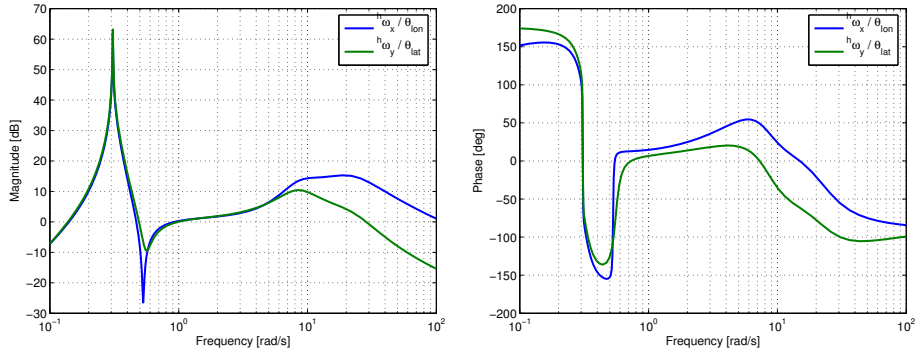

Figure 5.18: Frequency response plot of helicopter attitude cross coupling from cyclic input in hover. Shown are response from lateral cyclic input to pitch rate and from longitudinal cyclic input to roll rate.

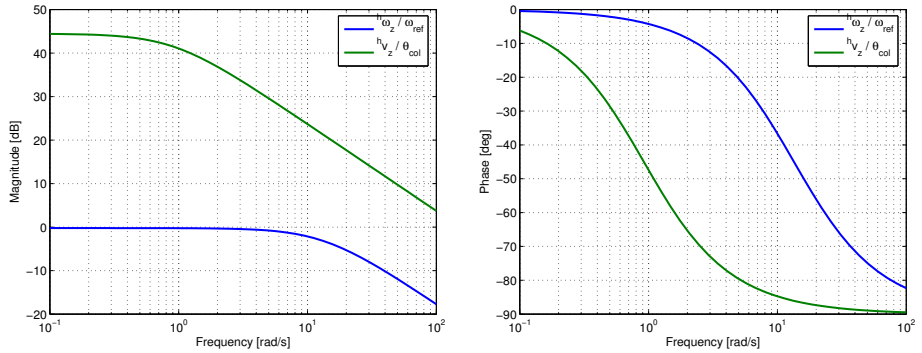

Figure 5.19: Frequency response plot of helicopter vertical velocity and yaw rate from corresponding actuator input (hover).

5.3.2 Helicopter with Single Wire Slung Load

This analysis focuses on the helicopter configured with the single wire slung load with the parameters given in appendix B on page 243 unless otherwise specified. This means a wire length of l = 4 m, a load mass of m_l = 0.95 kg, and a helicopter attachment point of $\boldsymbol{R}_{ha}$= [0 0 0.18] m. The primary modes of the helicopter with the single wire slung load in hover is shown in table 5.3. The slung load primary modes are evident in the lateral and longitudinal pendulum modes (10-11) (12-13). These are stable, but lightly damped and consists mainly of slung load horizontal velocities with a strong coupling to the helicopter horizontal motion, which means the phugoid and dutch roll modes.

Mode type	**Pole**	ζ	ω [rad/s]
Roll short period (1-2)	-11.85±19.03i	0.53	22.42
Spiral/Yaw (3)	-12.53	1	12.53
Pitch short period (4-5)	-3.12±7.96i	0.364	8.55
Slung load roll and pitch (6-9)	-0.003 ± 8.62i	0.0003	8.62
Pendulum longitudinal (10-11)	-0.0187 ± 1.64i	0.0114	1.642
Pendulum lateral (12-13)	-0.0191 ± 1.64i	0.0116	1.638
Heave (14)	-0.85	1	0.85
Phugoid (15-16)	0.00542 ± 0.260i	-0.0208	0.261
Dutch roll (17-18)	-0.032 ± 0.261i	0.120	0.263

Table 5.3: Eigenvalues of the helicopter with single wire slung load in hover.

The slung load attitude modes are all stable, very lightly damped, modes and the roll and pitch are shown in table 5.3 (6-9). These modes have very little coupling to primary motion of the system and they will be neglected further on in the analysis, but we will note that their damping depending on aerodynamic shape of the slung load and their frequency depends on the inertia. The yaw mode is a resonant mode that couples to the helicopter yaw through the wire twisting, but this coupling is very weak and the yaw mode for single wire slung loads can safely be neglected. It should also be noticed that the numerical correction introduced in section 4.7.2 on page 100, in form of a spring-damper in parallel with the suspension wires, results in a wire elasticity mode if included in the model. The damping and frequency of this mode is dependent on the helicopter and slung load mass and on the spring and damper constant of the numerical corrector. This mode is neglected in this analysis as it is insignificant for the primary system motion.

Helicopter short period modes, heave mode, and yaw mode are almost unchanged by the slung load, but a significant coupling between the helicopter long period modes and the slung load horizontal motion has been introduced.

The frequency response of the helicopter attitude dynamics with the slung load are shown in figure 5.20 and 5.21 and we can see that the response is mainly unchanged from figure 5.17 and 5.18. However, the present of the slung load is evident as a notch at the pendulum frequency on both direct and cross coupled response.

The slung load horizontal velocity frequency response from the cyclic input is shown

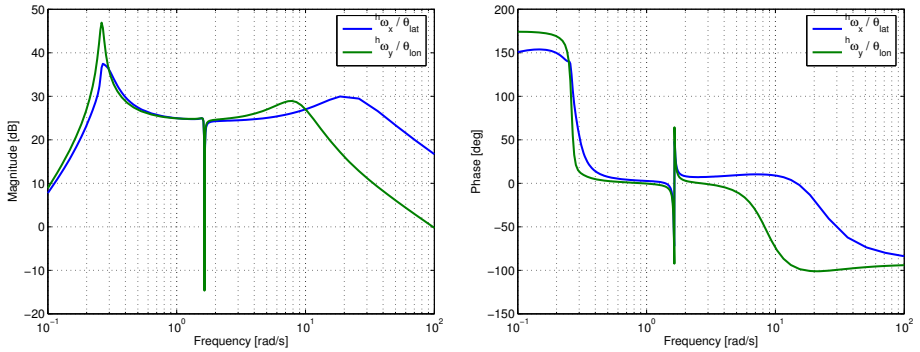

Figure 5.20: Frequency response plot of helicopter roll and pitch rate from corresponding cyclic input (in hover with single wire slung load).

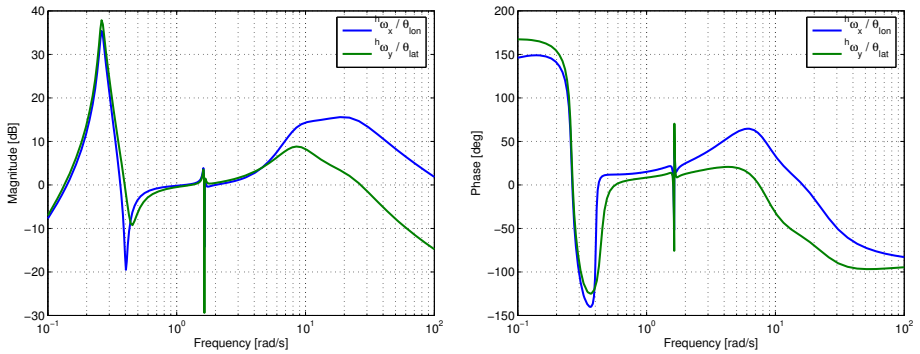

Figure 5.21: Frequency response plot of helicopter attitude cross coupling from cyclic input in hover with single wire slung load. Shown are response from lateral cyclic input to pitch rate and from longitudinal cyclic input to roll rate.

in figure 5.22 and here both the helicopter short period resonance and the slung load pendulum mode resonance are visible.

The position of the helicopter and slung load poles from hover to forward flight with 10 m/s are shown in figure 5.23. We can see that forward flight has a clear damping effect on the pendulum longitudinal mode, while the lateral mode remains almost unchanged. The stabilizing effect on the longitudinal mode comes from the static stable drag on the slung load which also result in a slight rise in frequency. The behavior of the phugoid and dutch roll modes in forward flight is similar to the one observer without slung load.

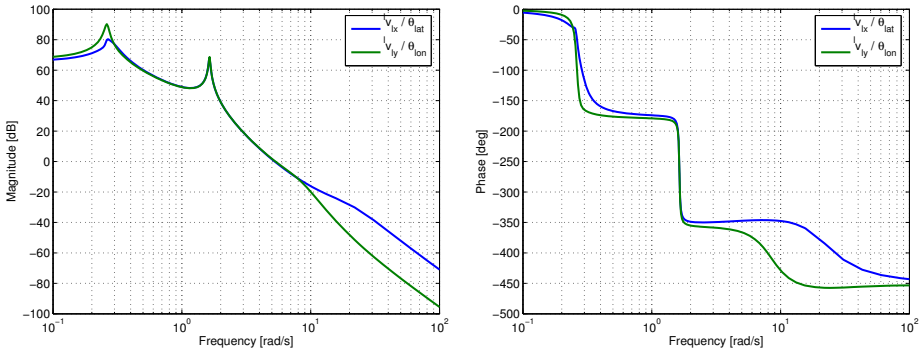

Figure 5.22: Frequency response plot of slung load horizontal velocity from corresponding cyclic input (in hover with single wire slung load).

However, the damping of the dutch roll mode has been amplified slightly and has at 10 m/s become a set of poles on the real axis.

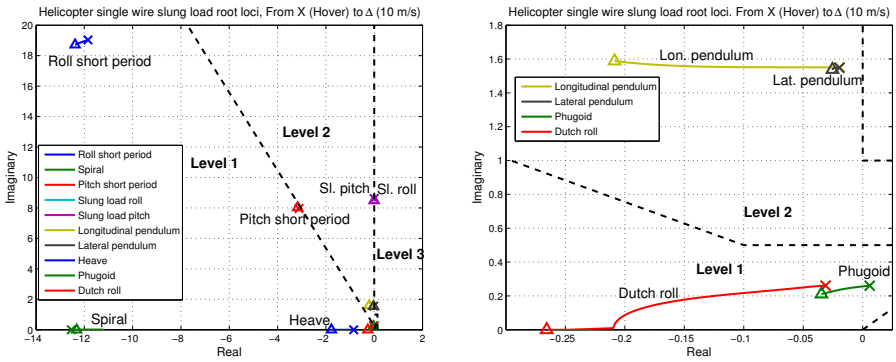

Figure 5.23: Plot of helicopter and slung load poles ranging from hover (V = 0 m/s, marked with $\times$)) to forward flight (V = 10 m/s, marked with $\triangle$). With ADS-33E limits plotted.

If the mass of the slung load is varied from 1 kg to 6 kg (a load to helicopter mass ratio from 0.07 to 0.43) we can see from figure 5.24 that a rising slung load mass has a damping effect on the pendulum modes, but a destabilizing effect on the helicopter long period attitude modes. Pendulum mode damping changes from about 0.012 to 0.051. A change of load helicopter mass ratio also alters the pendulum mode frequency slightly.

By varying the suspension wire length, the pendulum modes change frequency accordingly while the remaining modes remain virtually unchanged as shown in figure 5.25.

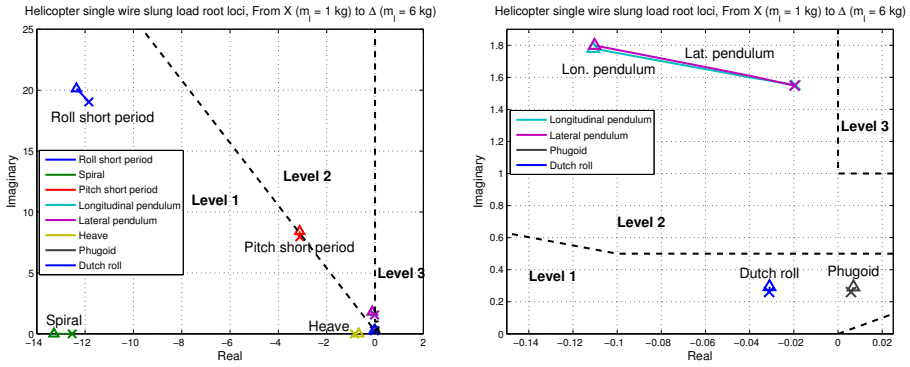

Figure 5.24: Plot of helicopter and slung load hover poles with changing slung load mass from m_l = 1 kg (marked with $\times$) to m_l = 6 kg (marked with $\triangle$). With ADS-33E limits plotted.

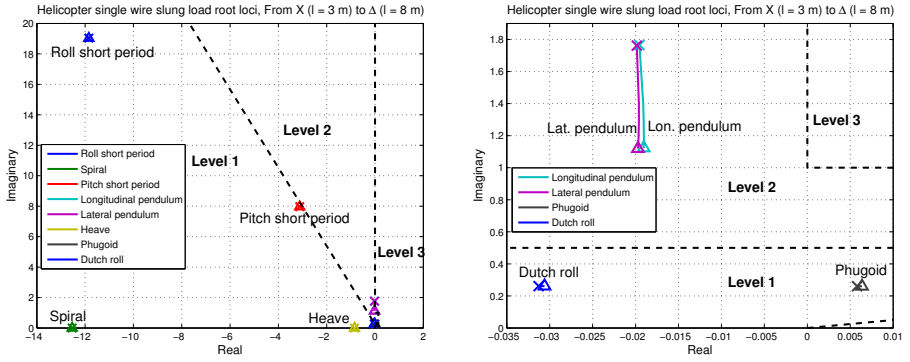

Figure 5.25: Plot of helicopter and slung load hover poles with changing suspension wire length from l = 3 m (marked with $\times$) to l = 8 m (marked with $\triangle$). With ADS-33E limits plotted.

The position of the attachment point on the helicopter has a significant influence on the slung load pendulum modes as we can see from figure 5.26. Here the system poles are plotted with varying helicopter attachment point, changing from being right in center of mass to one meter below the center of mass. As the attachment point distance to center of mass grows larger, the damping of the pendulum modes are increased and the coupling to helicopter attitude dynamics also increase.

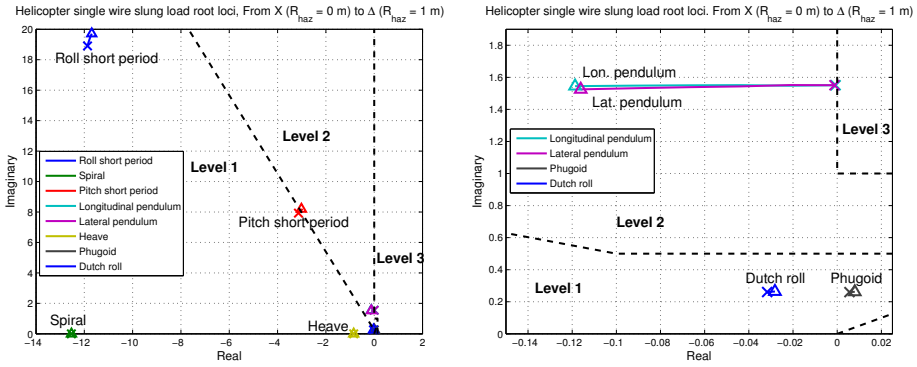

Figure 5.26: Plot of helicopter and slung load poles with changing helicopter suspension point from $\boldsymbol{R}_{ha}$ = [0 0 0] m (marked with $\times$) to $\boldsymbol{R}_{ha}$ = [0 0 1] m (marked with $\triangle$). With ADS-33E limits plotted.

5.3.3 Helicopter with Dual Wire Slung Load

Here the focus is on analysis of the helicopter configured with the dual wire slung load with the parameters given in appendix B on page 243 unless otherwise specified. The standard parameters are l = 4 m, a load mass of m_l = 2.2 kg, and a helicopter attachment point of $\boldsymbol{R}_{ha}$= [$\pm$0.22 0 0.9] m. The dual wire configuration result in a coupling between helicopter and slung load yaw which adds an additional significant resonant mode to system as shown in table 5.3. Again we neglect slung load roll dynamics as it is insignificant for the overall motion of the system. The slung load pitch dynamics couples directly with the helicopter pitch and can be neglected as independent mode. We can observe that the

Mode type	**Pole**	ζ	ω [rad/s]
Roll short period (1-2)	-12.00$\pm$19.18i	0.53	22.63
Spiral/Yaw (3)	-12.74	1	12.74
Pitch short period (4-5)	-2.95$\pm$8.10i	0.34	8.62
Pendulum longitudinal (6-7)	-0.14 $\pm$ 1.72i	0.0812	1.72
Pendulum lateral (8-9)	-0.0236 $\pm$ 1.601i	0.0147	1.601
Pendulum yaw (10-11)	-0.0041 $\pm$ 1.383i	0.0029	1.383
Heave (12)	-0.81	1	0.81
Phugoid (13-14)	0.0073 $\pm$ 0.270i	-0.0269	0.270
Dutch roll (15-16)	-0.031 $\pm$ 0.271i	0.112	0.273

Table 5.4: Eigenvalues of the helicopter with dual wire slung load in hover.

longitudinal pendulum mode has changed frequency slightly, but more importantly it has become somewhat more damped by the suspension change from single to dual wire.

The frequency response of the helicopter attitude dynamics with dual wire slung load is shown in figure 5.27. The notch from the slung load pendulum modes has become wider as the pendulum modes have moved , but otherwise the responses seems unchanged from the single wire setup.

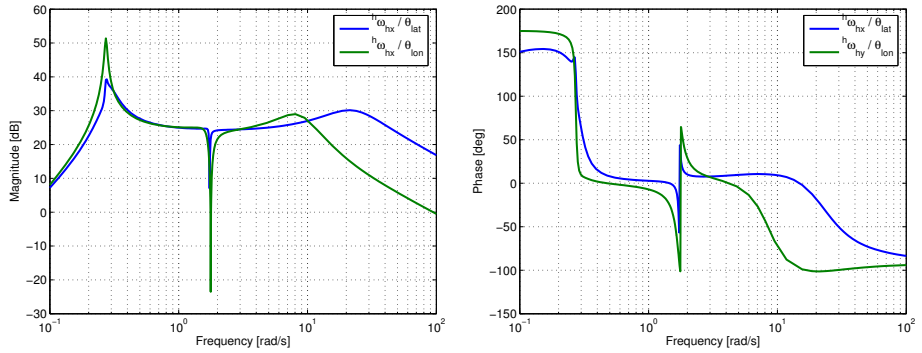

Figure 5.27: Frequency response plot of helicopter roll and pitch rate from corresponding cyclic input (In hover with dual wire slung load).

The response from tail input to both helicopter and load yaw rate is shown in figure 5.28 and we can see how the pendulum yaw mode introduces a notch in the helicopter response. Likewise, the resonance of the pendulum yaw mode is clear in the slung load yaw response to a tail input.

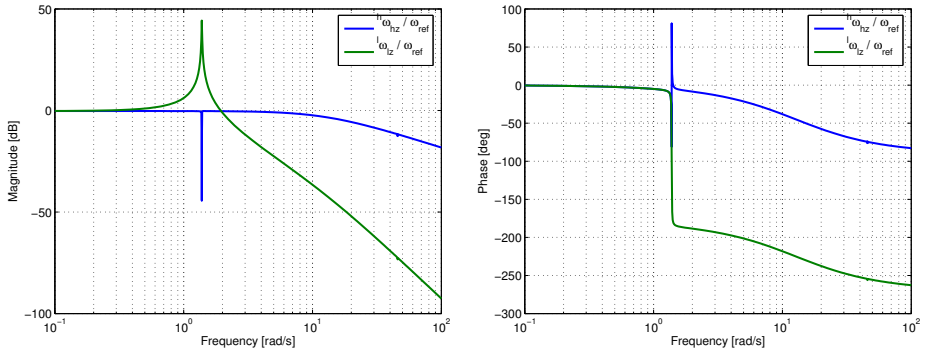

Figure 5.28: Frequency response plot of helicopter and slung load yaw rate from corresponding tail input (In hover with dual wire slung load).

The poles of the helicopter with the dual wire slung load is shown in figure 5.29 for hover to 10 m/s forward flight. We can see how the forward speed has similar effect as was observed with the single wire slung load, i.e. a stabilizing effect on the longitudinal mode. The pendulum yaw mode is virtually unaffected by the forward speed which is expected as the suspension setup aerodynamics surfaces of the slung load are symmetric around the yaw axis. If the aerodynamic surfaces had been larger in the back of the slung load, the forward flight would have resulted in a more stable yaw mode and vice versa.

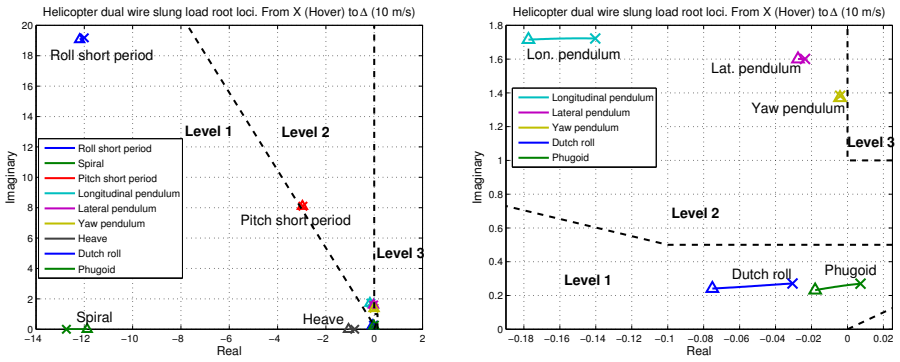

Figure 5.29: Plot of helicopter and slung load hover poles ranging from hover (V = 0 m/s, marked with $\times$) to forward flight (V = 10 m/s, marked with $\triangle$). With ADS-33E limits plotted.

The motion of the system poles as a result of changing distance between the two wires is shown in figure 5.30. As expected the primary, indeed almost the only, effect is on the pendulum yaw mode and we can see how the frequency of the mode rises together with the distance between the wires. Relating this to the tail input response from figure 5.28 it supports the expected result that we achieve a better yaw control of the slung load when there is a large distance between the wires.

5.3.4 Linear Analysis Discussion

Conclusions in the literature, mentioned in section 1.4 on page 15, on how different slung load parameters, flight conditions, and suspension types effect the helicopter and slung load modes are alternating and in many case contradictory. In the following we will not try to account for the different observations made in the literature, but simply sum up the conclusions we have made and draw parallels where it is possible to the previous work in the area.

The behavior that we have identified in the helicopter alone model corresponds well with how the system seems to behave in real flight. For the attitude we see a fast short period roll and a slower pitch. The inner loop yaw controller gives the helicopter a very stable and fast spiral/yaw mode and decouples it from the heave which is slow but also

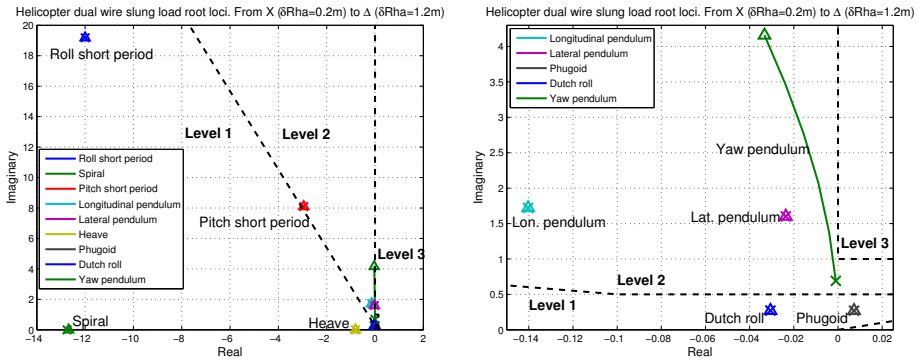

Figure 5.30: Plot of helicopter and slung load hover poles with rising distance between attachment points along x-axis. From R_{hax}=R_{lax}=±0.1 m to ±0.6 m, which means a distance ranging from δR_{ax}=0.2 (marked with $\times$) to 1.2 m (marked with $\triangle$). With ADS-33E limits plotted.

stable. For the long period attitude modes we have identified an unstable phugoid type mode and a stable dutch roll lateral type mode in hover. This corresponds well with the observations made in [Mettler *et al.*, 1999] and [Mettler *et al.*, 2002].

For the slung load we have observed obvious pendulum like modes for lateral and longitudinal swing which affects the helicopter attitude dynamics as a notch at the oscillation frequency. Furthermore, we have determined that a strong coupling between the slung load pendulous modes and the helicopter horizontal motion. These observations corresponds with the conclusions made in the general literature, e.g. in [Raz *et al.*, 1989] and [Fusato *et al.*, 2002]. No significant stability differences has been observed when the load moves in and out of the helicopter wake.

With the dual wire slung load a resonant, but stable, yaw mode was determined and changes in mass, wire separation, and flight speed did not cause any instabilities, which corresponds with the observations in [Sampath, 1980] and [Prabhakar, 1978]. We have found that an increasing mass ratio, i.e. a heavier slung load, has a damping effect on the slung load modes, but at the same time a destabilizing effect on the helicopter long period modes. This makes intuitive sense as a heavier slung load will transfer more of its swing to the helicopter and it corresponds with the conclusions of [Fusato *et al.*, 2002] and [Sampath, 1980].

If we compare to the specifications from [Hoh *et al.*, 2006], the two nominal helicopter slung load configurations that is used in this thesis are no worse that level 2 in the analyzed configurations. A thorough analysis based on the elaborate specifications in [Hoh *et al.*, 2006] is beyond the scope of this thesis.

5.4 Modeling Summary and Discussion

In this and the previous two chapters a full model of the helicopter slung load system was derived, verified, and analyzed. In chapter 3 the helicopter model was derived, including second order actuator dynamics, blade element theory for main and tail rotor forces and torques, second order flapping dynamics for main rotor and stabilizer bar, and momentum theory for the inflow model. Aerodynamic coupling between the helicopter and the load was introduced into the model by calculating the rotor downwash affect on the load.

In chapter 4 a generic slung load model was presented, capable of modeling all body to body suspension types. The model was derived using the Udwaidia-Kalaba equation and a redundant coordinate formulation in which the wires were inserted as acceleration constraints. The model was augmented with the ability to detect and respond to collapsing and tightening of wires in a dynamic way using impulse based collision theory. Furthermore, it was shown how the model could easily be extended to include multi-lift systems in a generic way for multiple helicopters and loads. A numerical correction scheme was developed for use with the redundant coordinate model. In this chapter the model was verified against flight data, trim algorithms for the full helicopter slung load system was developed, and finally a linear analysis of the model was presented.

In conclusion a highly flexible generic model has been developed that can be used for simulations of a wide range of helicopter slung load systems. The parameters of the model was fitted to the AAU Bergen Industrial Twin and successfully verified against flight data for stand alone helicopter and for the helicopter with single and dual wire slung.

Part III

Estimation and Control

This part presents the development of two different estimators for use in helicopter slung load systems. Furthermore, it presents the development of a slung load swing damping controller and of a slung load trajectory tracking controller.

Chapters

Chapter 6

State Estimation and Sensor Fusion

In this chapter sensor fusion and state estimation for helicopter slung load systems are investigated and two different state estimators are developed, one for each application branch. First an introduction to the vision system that delivers sensory input to the estimators is given and then the unscented Kalman filter used in the estimators is discussed briefly. Then the two different estimators are developed and finally simulations and flight verifications of the two are presented.

6.1 Introduction

The helicopter slung load system is equipped with different sensors as described in chapter 2 and in this chapter we take the information from these sensors and fuse it into an estimate of the system state vector. The estimated states can then be used as input to the controller as shown in figure 6.1.

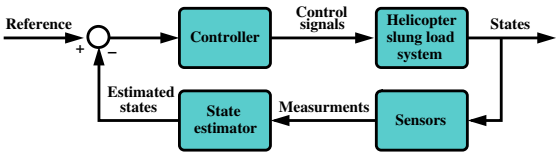

Figure 6.1: Architectural overview of the control scheme.

First a state estimator intended for the general cargo transport application is developed. It is based on a point mass pendulum model and it includes an adaptive element

that enables it to function without knowledge of the wire length or the load mass. Then a full state estimator, which can be used for the mine detection application that requires yaw control, is developed. For this two different approaches are compared: One uses acceleration and rate information for both helicopter and load to drive a dynamic/kinematic model, while the other uses a model based approach and therefore uses the entire helicopter and slung load model.

6.2 Vision System

The vision system uses a digital camera mounted on the helicopter such that it looks down on the load. The resulting image is a top-down view of the load and the ground below. To easily identify the load amongst other objects that might appear in the camera view the load is fitted with a visual marker; in this case a white disk on a dark background with a possible straight line protruding from it. Two pictures of slung loads, from the GTMax and the AAU Bergen helicopter respectively, are shown figure 6.2. The location of the

Figure 6.2: Two different examples of slung load pictures from the vision system. Left from the GTMax and right from the AAU Bergen.

marker in the image is thus an estimate of the position of the load relative to the helicopter. To identify the marker in the image two circular Hough transforms with different radii are used on the same image. A circular Hough transform maps a 2D data set into another 2D data set such that complete circles are mapped to single points. Since points can be found easily by thresholding, it makes the search for circles much simpler. The first of the two transforms uses a radius slightly smaller than the white disc marker and triggers on white. The second transform is applied to the same image and uses a radius slightly bigger than the white disc marker and triggers on black. Correlating the two transforms triggers only those areas where a sufficiently large round white area is present and surrounded by a dark area. In most scenarios this is sufficient to ensure a stable estimate of the marker location.

It is important to keep the delay in the vision system low and this is ensured by using the previous estimate of the location to choose a subset of the image for analysis in the next image frame (only relevant when using a camera with a large field of view) and using

a threshold to simply ignore the pixels that are too far from white to be the marker. The measurement is checked for a false detection by examining the pixel detected as the center of the disk. If it is not sufficiently white, it is assumed that the algorithm has made a false detection and the measurement is discarded. This could happen if the load is outside the field of view (FOV) of the camera. Note that the camera is fixed to the helicopter which means that both load swing and helicopter roll and pitch can result in the load disappearing from the FOV.

When the vision algorithm has estimated the pixel position of the load this measurement must be mapped to a 3D load position. This is done by first transforming the pixel position into two angles – a vertical (θ_p) and a horizontal (ϕ_p) – as shown in figure 6.3. The camera coordinate system is defined to coincide with the helicopter coordinate system when the camera is pointing forward, i.e. the x-axis is pointing in the image direction. This is done by assuming that the angle from the camera to the load (θ_p) is proportional

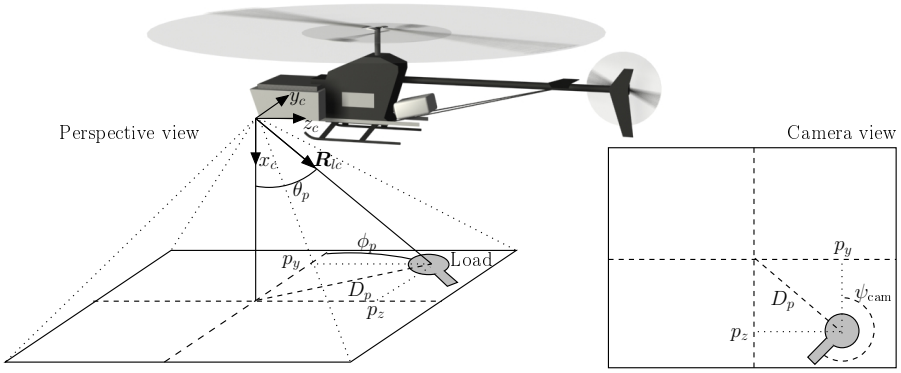

Figure 6.3: The map of 2D image position to the 3D spatial location. Shown is perspective view and camera view.

to the pixel distance from the load to the image center. This is equivalent to a pin-hole lens and neglects optical lens distortion. The distance from the image center to the load is found as

$$D_p = \sqrt{p_y^2 + p_z^2}\,. \tag{6.1}$$

The angle to the load can then be found as

$$\theta_p = \frac{\alpha_{\text{FOV}}}{P_{\text{FOV}}} D_p\,, \tag{6.2}$$

where α_{FOV} is the field of view angle of the camera and P_{FOV} is the number of pixels related to the α_{FOV}. The horizontal angle can be found simply by the relationship between

the x and the y pixel position

$$\phi_p = \arctan(p_z,\ p_y)\ . \tag{6.3}$$

The unit vector from the camera to the load can then be found in the camera coordinate system and rotated into the helicopter coordinate system as

$${}^{h}\boldsymbol{R}_{cl} = \boldsymbol{T}_{hc} \begin{bmatrix} \cos(\theta_p) \\ \sin(\theta_p)\cos(\phi_p) \\ \sin(\theta_p)\sin(\phi_p) \end{bmatrix}\ , \tag{6.4}$$

where $\boldsymbol{T}_{hc}$ is the direct cosine matrix between the camera and the helicopter.

In order to determine the orientation of the slung load (ψ_{cam}) a straight line is added to the circular marker. This line extends from the center of the disc and is longer than radius of the disc, thus giving the disc a little 'pin' as shown in figure 6.3. Once the center of the marker is found, an angular search is performed in the image to find the direction of the pin. Since the marker background is black and the marker and pin is white, a simple pixel search will suffice. This approach is fast and transparent to small changes in roll and pitch of the load. Note that the straight line should be relatively thin, otherwise it will have a noticeable impact on the circular Hough transforms.

An illustration of the Hough transform and line detector at work is shown in figure 6.4, where the pictures from figure 6.2 are processed.

6.3 The Unscented Kalman Filter

An unscented Kalman filter (UKF) is used as the architecture for the estimators developed in this chapter. The UKF is a relative new approach to Kalman filtering and was first proposed in [Julier and Uhlmann, 1997b] and later refined by [Wan and van der Merwe, 2000] and in recent years it has been intensively researched for a wide range of estimation purposes. Its popularity is due to the fact that in theory the UKF yields estimates with higher precision than the conventional extended Kalman filter (EKF), as the UKF does not require the first order linearization of process and sensor models that the EKF needs. However, this advantage is in many cases more theoretical that practical as modeling uncertainties are often more significant than linearization errors [Bisgaard *et al.*, 2005]. Nevertheless, the possibility of using the nonlinear process and sensor models directly in the filter is an advantage in many cases.

The core of the UKF is the Unscented Transform (UT) which makes it possible for the filter to predict means and covariances without linearization. The UT (discussed in detail in [Julier and Uhlmann, 1997a] and [Julier, 2000]) uses a small and deterministic chosen number of specific samples points propagated through the non-linear function to calculate the mean and covariance. The sample points are known as sigma points and consist of sample state vectors with weights assigned. Through this approach it is possible to match

Figure 6.4: Top: Output of the Hough transform. Bottom: The output of the vision system with the located slung loads indicated by red circles.

third order moments for functions that are three times differentiable and even higher order moments in some cases for smoother functions.

In general the $2n+1$ sigma points are selected from the state vector $\hat{\boldsymbol{x}} \in \mathbb{R}^n$ as

$$\boldsymbol{\mathcal{X}}_{0,k-1} = \hat{\boldsymbol{x}}_{k-1} \,, \tag{6.5}$$

$$\boldsymbol{\mathcal{X}}_{i,k-1} = \hat{\boldsymbol{x}}_{k-1} + \left(\sqrt{(n+\lambda_u)\boldsymbol{P}_{k-1}}\right)_i \qquad i = 1,..,n \,, \tag{6.6}$$

$$\boldsymbol{\mathcal{X}}_{i+n,k-1} = \hat{\boldsymbol{x}}_{k-1} - \left(\sqrt{(n+\lambda_u)\boldsymbol{P}_{k-1}}\right)_i \qquad i = n+1,..,2n \,, \tag{6.7}$$

where $\mathcal{X}_i$ (i'th column of $\boldsymbol{\mathcal{X}} \in \mathbb{R}^{n\times 2n+1}$) is the i'th sigma point, $\boldsymbol{P} \in \mathbb{R}^{n\times n}$ is the covariance estimate, $(x)_i$ is the i'th column of x, and λ_u is a scaling parameter. The matrix square root $\boldsymbol{S}$ of $\boldsymbol{P}$ is defined as $\boldsymbol{P} = \boldsymbol{S}\boldsymbol{S}^T$. A number of static weights for the sigma points are calculated by

$$W_0^m = \frac{\lambda_u}{n+\lambda_u} \,, \tag{6.8}$$

$$W_0^c = \frac{\lambda_u}{n+\lambda_u} + (1-\alpha_u^2+\beta_u) \,, \tag{6.9}$$

$$W_i^m = W_i^c = \frac{1}{2(n+\lambda_u)} \qquad i = 1,..,2n \,, \tag{6.10}$$

where $\lambda_u = \alpha_u^2 \cdot (n + \kappa_u) - n$, α_u determines how the sigma points are spread, κ_u is a scaling parameter which can be used to incorporate up to fourth order precision in the transformation - this is however usually set to 0, and β_u is used to incorporate knowledge of the distribution of $\boldsymbol{x}$ (β_u = 2 is optimal for a Gaussian distribution).

The sigma points are then propagated through the nonlinear system and measurement models

$$\boldsymbol{\mathcal{X}}_{k|k-1} = \boldsymbol{f}(\boldsymbol{\mathcal{X}}_{k-1}, \boldsymbol{u}) \,, \tag{6.11}$$

$$\boldsymbol{\mathcal{Z}}_{k|k-1} = \boldsymbol{h}(\boldsymbol{\mathcal{X}}_{k|k-1}) \,, \tag{6.12}$$

where $\boldsymbol{\mathcal{Z}} \in \mathbb{R}^{m \times 2n+1}$ is the sigma point matrix of the estimated measurement vector $\hat{\boldsymbol{z}} \in \mathbb{R}^m$. The prediction of the state and measurement vector as well as the is then performed by using a weighted sum over the sigma points similar to the calculation of standard sample mean and sample covariance calculations

$$\hat{\boldsymbol{x}}_k^- = \sum_{i=0}^{2n} W_i^m \boldsymbol{\mathcal{X}}_{k|k-1} \,, \quad \hat{\boldsymbol{z}}_k = \sum_{i=0}^{2n} W_i^m \boldsymbol{\mathcal{Z}}_{i,k|k-1} \,, \tag{6.13}$$

$$\boldsymbol{P}_k^- = \sum_{i=0}^{2n} W_i^c (\boldsymbol{\mathcal{X}}_{i,k|k-1} - \hat{\boldsymbol{x}}_k^-)(\boldsymbol{\mathcal{X}}_{i,k|k-1} - \hat{\boldsymbol{x}}_k^-)^T + \boldsymbol{P}_p \,, \tag{6.14}$$

where the additive process noise $\boldsymbol{P}_p \in \mathbb{R}^{n \times n}$ is added into the prediction of the covariance. Similarly the measurement covariance and the cross-covariance between the system and measurement can be calculated as

$$\boldsymbol{P}_{\hat{\boldsymbol{z}}_k \hat{\boldsymbol{z}}_k} = \sum_{i=0}^{2n} W_i^c (\boldsymbol{\mathcal{Z}}_{i,k|k-1} - \hat{\boldsymbol{z}}_k)(\boldsymbol{\mathcal{Z}}_{i,k|k-1} - \hat{\boldsymbol{z}}_k)^T + \boldsymbol{P}_m \,, \tag{6.15}$$

$$\boldsymbol{P}_{\hat{\boldsymbol{x}}_k^- \hat{\boldsymbol{z}}_k} = \sum_{i=0}^{2n} W_i^c (\boldsymbol{\mathcal{X}}_{i,k|k-1} - \hat{\boldsymbol{x}}_k^-)(\boldsymbol{\mathcal{Z}}_{i,k|k-1} - \hat{\boldsymbol{z}}_k)^T \,, \tag{6.16}$$

where $\boldsymbol{P}_m \in \mathbb{R}^{n \times n}$ is the measurement noise matrix. Similar to other implementations of the Kalman Filter a Minimum Mean Square Error (MMSE) recursive estimation of the state and covariance can now be made. The MMSE recursive estimator and the optimal gain can be found as

$$\boldsymbol{K}_k = \boldsymbol{P}_{\hat{\boldsymbol{x}}_k^- \hat{\boldsymbol{z}}_k} \boldsymbol{P}_{\hat{\boldsymbol{z}}_k \hat{\boldsymbol{z}}_k}^{-1} \,, \tag{6.17}$$

$$\hat{\boldsymbol{x}}_k^+ = \hat{\boldsymbol{x}}_k^- + \boldsymbol{K}_k(\boldsymbol{z}_k - \hat{\boldsymbol{z}}_k) \tag{6.18}$$

$$\boldsymbol{P}_k^+ = \boldsymbol{P}_k^- - \boldsymbol{K}_k \boldsymbol{P}_{\hat{\boldsymbol{z}}_k \hat{\boldsymbol{z}}_k} \boldsymbol{K}_k^T \,. \tag{6.19}$$

In table 6.1 the entire UKF algorithm is shown.

Predict:

$$\boldsymbol{\mathcal{X}}_{0,k-1} = \hat{\boldsymbol{x}}_{k-1}$$

$$\boldsymbol{\mathcal{X}}_{i,k-1} = \hat{\boldsymbol{x}}_{k-1} + \left(\sqrt{(n+\kappa_u)\boldsymbol{P}_{k-1}}\right)_i \qquad i = 1,..,n$$

$$\boldsymbol{\mathcal{X}}_{i,k-1} = \hat{\boldsymbol{x}}_{k-1} - \left(\sqrt{(n+\kappa_u)\boldsymbol{P}_{k-1}}\right)_i \qquad i = n+1,..,2n$$

$$\boldsymbol{\mathcal{X}}_{k|k-1} = \boldsymbol{f}(\boldsymbol{\mathcal{X}}_{k-1}, \boldsymbol{u})$$

$$\hat{\boldsymbol{x}}_k^- = \sum_{i=0}^{2n} W_i^m \boldsymbol{\mathcal{X}}_{i,k|k-1}$$

$$\boldsymbol{P}_k^- = \sum_{i=0}^{2n} W_i^c (\boldsymbol{\mathcal{X}}_{i,k|k-1} - \hat{\boldsymbol{x}}_k^-)(\boldsymbol{\mathcal{X}}_{i,k|k-1} - \hat{\boldsymbol{x}}_k^-)^T + \boldsymbol{P}_p$$

$$\boldsymbol{\mathcal{Z}}_{k|k-1} = \boldsymbol{h}(\boldsymbol{\mathcal{X}}_{k|k-1})$$

$$\hat{\boldsymbol{z}}_k = \sum_{i=0}^{2n} W_i^m \boldsymbol{\mathcal{Z}}_{i,k|k-1}$$

Update:

$$\boldsymbol{P}_{\hat{\boldsymbol{z}}_k \hat{\boldsymbol{z}}_k} = \sum_{i=0}^{2n} W_i^c (\boldsymbol{\mathcal{Z}}_{i,k|k-1} - \hat{\boldsymbol{z}}_k)(\boldsymbol{\mathcal{Z}}_{i,k|k-1} - \hat{\boldsymbol{z}}_k)^T + \boldsymbol{P}_m$$

$$\boldsymbol{P}_{\hat{\boldsymbol{x}}_k^- \hat{\boldsymbol{z}}_k} = \sum_{i=0}^{2n} W_i^c (\boldsymbol{\mathcal{X}}_{i,k|k-1} - \hat{\boldsymbol{x}}_k^-)(\boldsymbol{\mathcal{Z}}_{i,k|k-1} - \hat{\boldsymbol{z}}_k)^T$$

$$\boldsymbol{K}_k = \boldsymbol{P}_{\hat{\boldsymbol{x}}_k^- \hat{\boldsymbol{z}}_k} \boldsymbol{P}_{\hat{\boldsymbol{z}}_k \hat{\boldsymbol{z}}_k}^{-1}$$

$$\hat{\boldsymbol{x}}_k^+ = \hat{\boldsymbol{x}}_k^- + \boldsymbol{K}_k(\boldsymbol{z}_k - \hat{\boldsymbol{z}}_k)$$

$$\boldsymbol{P}_k^+ = \boldsymbol{P}_k^- - \boldsymbol{K}_k \boldsymbol{P}_{\hat{\boldsymbol{z}}_k \hat{\boldsymbol{z}}_k} \boldsymbol{K}_k^T$$

Table 6.1: UKF algorithm.

6.4 Full State Unscented Kalman Filter

The purpose of the full state estimator is to deliver estimates of the full helicopter and load state vector including position ($\hat{\boldsymbol{R}}_h, \hat{\boldsymbol{R}}_l \in \mathbb{R}^3$), attitude ($\hat{\boldsymbol{\theta}}_h, \hat{\boldsymbol{\theta}}_l \in \mathbb{S}^3$), velocity ($\hat{\boldsymbol{v}}_h, \hat{\boldsymbol{v}}_l \in \mathbb{R}^3$), and rates ($\hat{\boldsymbol{\omega}}_h, \hat{\boldsymbol{\omega}}_l \in \mathbb{S}^3$) and for this two different approaches are investigated: One uses a IMU driven process model and the other uses a full dynamic process model.

6.4.1 IMU Driven Process Model Estimator

This estimator is inspired by the IMU driven Kalman filter approach taken in much of the previous work described in section 1.4.3 on page 18. The general idea is to use the acceleration and rate input from two IMUs, one mounted on the helicopter and one mounted on the load, to drive the process model. To make sure that the constraints imposed by the wires are maintained, a simple technique is devised. A virtual sensor is introduced, which always measures the correct (not the actual) wire length and the sensor noise level in the filter for this sensor is set to a very low value. This ensures that the estimated states always obey the wire constraints. The filter includes estimation of biases on rates and accelerations for both IMUs. The IMU driven unscented Kalman filter is illustrated in figure 6.5.

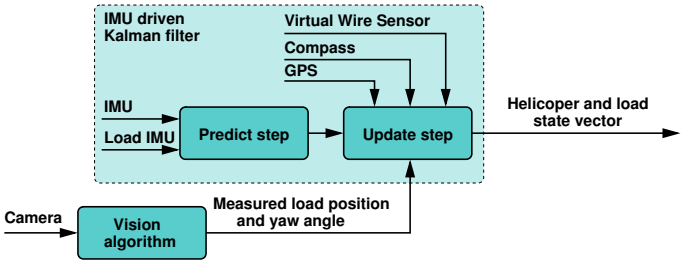

Figure 6.5: The architecture of the IMU driven unscented Kalman filter.

The state vector of the filter is specified as

$$\hat{\boldsymbol{x}} = \begin{bmatrix} {}^{e}\hat{\boldsymbol{R}}_h \\ {}^{e}\hat{\boldsymbol{\theta}}_h \\ {}^{e}\hat{\boldsymbol{R}}_l \\ {}^{e}\hat{\boldsymbol{\theta}}_l \\ {}^{h}\hat{\boldsymbol{v}}_h \\ {}^{l}\hat{\boldsymbol{v}}_l \\ {}^{h}\hat{\boldsymbol{B}}_h \\ {}^{l}\hat{\boldsymbol{B}}_l \end{bmatrix}_{30\times 1} \qquad {}^{b}\hat{\boldsymbol{B}}_b = \begin{bmatrix} {}^{b}\hat{\boldsymbol{a}}_{\text{bias}b} \\ {}^{b}\hat{\boldsymbol{\omega}}_{\text{bias}b} \end{bmatrix}_{6\times 1} \tag{6.20}$$

where $\hat{\boldsymbol{a}}_{\text{bias}b}$ and $\hat{\boldsymbol{\omega}}_{\text{bias}b}$ are the estimated acceleration and rate bias for the IMU mounted on body b. The measurement vector is defined as

$$\boldsymbol{z} = \begin{bmatrix} {}^{e}\tilde{\boldsymbol{R}}_{\text{gps}} \\ {}^{e}\tilde{\boldsymbol{v}}_{\text{gps}} \\ {}^{h}\tilde{\boldsymbol{M}}_{\text{mag}} \\ {}^{h}\tilde{\boldsymbol{R}}_{\text{cam}} \\ {}^{h}\tilde{\psi}_{\text{cam}} \\ \tilde{\boldsymbol{W}}_{\text{virt}} \end{bmatrix}_{(13+m)\times 1} \tag{6.21}$$

where ${}^{e}\tilde{\boldsymbol{R}}_{\text{gps}}$ is the helicopter position measurement from the GPS, ${}^{e}\tilde{\boldsymbol{v}}_{\text{gps}}$ is the helicopter velocity measurement from the GPS, ${}^{h}\tilde{\boldsymbol{M}}_{\text{mag}}$ is the magnetic field measurement by the magnetometer, ${}^{h}\tilde{\boldsymbol{R}}_{\text{cam}}$ is the load position measurement relative the helicopter from the vision system, and ${}^{h}\psi_{\text{cam}}$ is the load yaw angle relative to the helicopter from the vision system. Finally, $\tilde{\boldsymbol{W}}_{\text{virt}}$ is a vector consisting of the virtual measurements of the wire lengths, where m is the number of wires in the system.

Process Model

The input to the process model is the accelerations and rates measured by the IMUs mounted on the helicopter and load. Before being used in the process model the raw measurements are corrected as

$$\tilde{\boldsymbol{a}}_{b,k} = \tilde{\boldsymbol{a}}_{\text{IMU}b,k} - {}^{b}\hat{\boldsymbol{a}}_{\text{bias}b,k-1} - \hat{\boldsymbol{T}}_{be,k-1}{}^{e}\boldsymbol{G}_{ref} \tag{6.22}$$

$$\tilde{\boldsymbol{\omega}}_{b,k} = \tilde{\boldsymbol{\omega}}_{\text{IMU}b,k} - {}^{b}\hat{\boldsymbol{\omega}}_{\text{bias}b,k-1} \tag{6.23}$$

for bias errors and for the acceleration also for the gravitational component. ${}^{e}\boldsymbol{G}_{ref}$ is the gravitational acceleration vector given in the earth fixed frame. The corrected measurements can then be used to calculate the elements of the derivative state vector as

$${}^{e}\dot{\hat{\boldsymbol{R}}}_{b,k} = \hat{\boldsymbol{T}}_{eb,k-1}{}^{b}\hat{\boldsymbol{v}}_{b,k-1} \tag{6.24}$$

$${}^{e}\dot{\hat{\boldsymbol{\theta}}}_{b,k} = \hat{\boldsymbol{T}}_{\theta b,k-1}\tilde{\boldsymbol{\omega}}_{b,k} \tag{6.25}$$

$${}^{b}\dot{\hat{\boldsymbol{v}}}_{b,k} = \tilde{\boldsymbol{a}}_{b,k} - \tilde{\boldsymbol{\omega}}_{b,k} \times {}^{b}\hat{\boldsymbol{v}}_{b,k-1}\,. \tag{6.26}$$

The bias of MEMS sensors like those used in this application exhibit non-zero mean and non-stationary behavior, which can be modeled as a random walk [van der Merwe *et al.*, 2004]. However, to track a random walk it suffices to use a constant process model

$${}^{b}\dot{\hat{\boldsymbol{B}}}_{b,k} = 0\,. \tag{6.27}$$

The state vector defined in (6.20) is missing the angular velocity elements ${}^{h}\hat{\boldsymbol{\omega}}_{h}$ and ${}^{l}\hat{\boldsymbol{\omega}}_{l}$, but non-filtered estimates of these can be found from (6.23). It should be noted that any lever effect on the IMUs are neglected, as they are placed close to the center of mass on both the helicopter and the load used in this study.

Observation Models

The GPS outputs a measurement of the position of the helicopter in earth fixed frame using UTM coordinates. However, the GPS measurement on the helicopter position is not only dependent on the helicopter position, but also on the attitude of the helicopter as the GPS antenna is displaced from the CM as shown in figure 6.6. Furthermore, GPS measure-

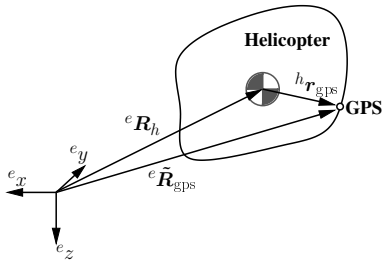

Figure 6.6: The displacement of the GPS from the CM.

ments often exhibit quite high latencies, which can be compensated for by incorporating a similar delay in the observation model. The GPS observation model is formulated as

$$^{e}\hat{\boldsymbol{R}}_{\text{gps},k+\Delta gps} = {}^{e}\hat{\boldsymbol{R}}_{h,k} + \hat{\boldsymbol{T}}_{eh,k}\boldsymbol{r}_{\text{gps}} \,, \tag{6.28}$$

where Δgps is the latency of the GPS measurement. The GPS velocity measurement is modeled as the body fixed velocity compensated for the GPS offset using the bias corrected rate measurements and finally transformed into the earth fixed frame

$$^{e}\hat{\boldsymbol{v}}_{\text{gps},k+\Delta gps} = \hat{\boldsymbol{T}}_{eh,k}({}^{b}\hat{\boldsymbol{v}}_{b,k} + \tilde{\boldsymbol{\omega}}_{b,k} \times \boldsymbol{r}_{\text{gps}}) \,. \tag{6.29}$$

The magnetometer output measurements of the magnetic field surrounding the helicopter, which is modeled simply as the earth fixed magnetic field reference ($^{e}\boldsymbol{M}_{ref}$) rotated into the body frame

$$^{h}\hat{\boldsymbol{M}}_{\text{mag},k} = \hat{\boldsymbol{T}}_{eh,k}{}^{e}\boldsymbol{M}_{ref} \,. \tag{6.30}$$

Part of the output of the vision system – as described in section 6.2 – is a unit vector ($^{h}\tilde{\boldsymbol{R}}_{cam}$) pointing from the camera towards the marker on the load as shown on figure 6.7. This vector is dependent on the position of the helicopter and the load as well as the position of the camera on the helicopter ($^{h}\boldsymbol{R}_{hc}$) and the position of the marker on the load ($^{l}\boldsymbol{R}_{lm}$). The observation model, normalized to yield a unit vector, is formulated as

$$^{h}\hat{\boldsymbol{R}}_{\text{cam},k+\Delta cam} = \frac{\hat{\boldsymbol{T}}_{he,k}({}^{e}\hat{\boldsymbol{R}}_{l,k} - {}^{e}\hat{\boldsymbol{R}}_{h,k} - \hat{\boldsymbol{T}}_{el,k}{}^{l}\boldsymbol{R}_{lm}) - {}^{h}\boldsymbol{R}_{hc}}{|\hat{\boldsymbol{T}}_{he,k}({}^{e}\hat{\boldsymbol{R}}_{l,k} - {}^{e}\hat{\boldsymbol{R}}_{h,k} - \hat{\boldsymbol{T}}_{el,k}{}^{l}\boldsymbol{R}_{lm}) - {}^{h}\boldsymbol{R}_{hc}|} \,, \tag{6.31}$$

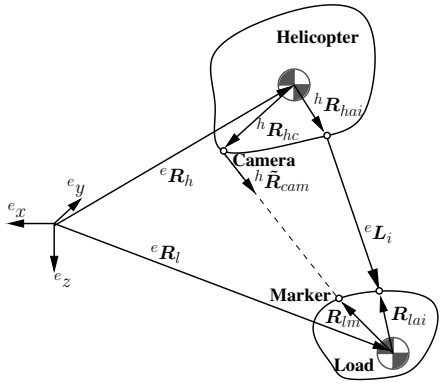

Figure 6.7: The geometric setup of position vision system model.

where Δcam is the latency of the vision system.

The second part of the output from the vision system is a measurement of the yaw angle between the helicopter and the load. This is the angle between the straight line in the marker (denoted $^l\boldsymbol{r}_m$) and the z-axis of the camera. If considered in a small area around the round marker the visual output of the camera can be modeled as a plane with $^h\boldsymbol{R}_{cm}$ as normal. What the camera sees is then $^l\boldsymbol{r}_m$ projected onto this plane as shown in figure 6.8 where the projection is denoted $^l\boldsymbol{r}'_m$ The projection can be found as

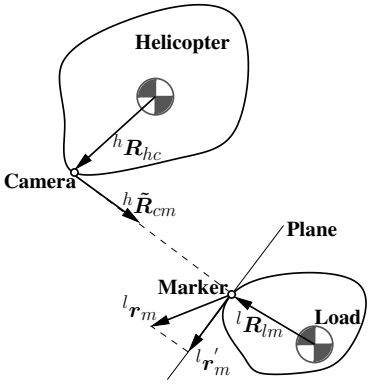

Figure 6.8: The setup of the yaw angle vision system angle.

$$^h\boldsymbol{r}'_m = \hat{\boldsymbol{T}}_{he,k}\hat{\boldsymbol{T}}_{el,k}{}^l\boldsymbol{r}_m - ((\hat{\boldsymbol{T}}_{he,k}\hat{\boldsymbol{T}}_{el,k}{}^l\boldsymbol{r}_m)\cdot{}^l\boldsymbol{R}_{cm})^l\boldsymbol{R}_{cm}\,, \tag{6.32}$$

which is calculated in helicopter frame as the camera is fixed to this frame. A new frame is defined, which coincides with the plane and has its third axis pointing along ${}^{h}\boldsymbol{R}_{cm}$ and its first axis aligned with the first axis of the helicopter frame. The Euler angles defining the rotation between the helicopter and the plane frame can be found as

$$\phi_m = \arcsin({}^{h}R_{cm}(2)) \,, \qquad \theta_m = \arccos\left(\frac{{}^{h}R_{cm}(3)}{\cos(\phi_m)}\right) \,, \qquad \psi_m = 0$$

where ${}^{h}R_{cm}(2)$ and ${}^{h}R_{cm}(3)$ denotes the second and third element of ${}^{h}\boldsymbol{R}_{cm}$. Using these Euler angles the rotation matrix $\boldsymbol{T}_{ph}$ can be formed and ${}^{p}\hat{\boldsymbol{r}}_{mp}$ can be calculated. Using the inner product the yaw angle vision system model can then be found as

$${}^{h}\hat{\psi}_{\text{cam},k+\Delta cam} = \arccos\left(\frac{{}^{p}\hat{r}_{mp,k}(1)}{|{}^{p}\hat{\boldsymbol{r}}_{mp,k}|}\right) . \tag{6.33}$$

where ${}^{p}\hat{r}_{mp,k}(1)$ is the first element of the vector ${}^{p}\hat{\boldsymbol{r}}_{mp,k}$.

The output of the virtual wire sensor is the nominal length of each of the m wires. By considering figure 6.7 where the i'th wire is shown it can be seen that the wire sensor can be modeled as

$$\hat{\boldsymbol{W}}_{\text{virt},k} = \begin{bmatrix} |{}^{e}\hat{\boldsymbol{R}}_{h,k} + \hat{\boldsymbol{T}}_{eh,k}{}^{h}\boldsymbol{R}_{ha1} - {}^{e}\hat{\boldsymbol{R}}_{l,k} - \hat{\boldsymbol{T}}_{el,k}{}^{l}\boldsymbol{R}_{la1}| \\ \vdots \\ |{}^{e}\hat{\boldsymbol{R}}_{h,k} + \hat{\boldsymbol{T}}_{eh,k}{}^{h}\boldsymbol{R}_{ham} - {}^{e}\hat{\boldsymbol{R}}_{l,k} - \hat{\boldsymbol{T}}_{el,k}{}^{l}\boldsymbol{R}_{lam}| \end{bmatrix} , \tag{6.34}$$

where ${}^{h}\boldsymbol{R}_{hai}$ and ${}^{l}\boldsymbol{R}_{lai}$ points to the i'th attachment point on the helicopter and the load.

6.4.2 Dynamic Process Model Estimator

This approach uses a full dynamic aerodynamic and rigid body process model driven by control signals from the controller. As the filter uses the full slung load rigid body model is not mandatory to used the load IMU like it is in the IMU driven approach. It can be enabled or disabled depending on availability, but it should be noted that the roll and pitch dynamics of the load becomes weakly observable without the load IMU. Like with the IMU driven approach the filter includes estimates of biases on rates and accelerations and it furthermore includes estimation of external wind influences which acts as bias in the dynamical model. The model based approach is illustrated in figure 6.9

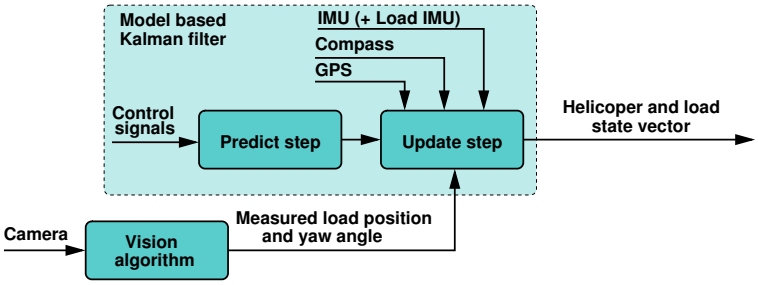

Figure 6.9: The architecture of the dynamic model based unscented Kalman filter.

The state and measurement vectors for the model based approach are specified as

$$\hat{\boldsymbol{x}} = \begin{bmatrix} {}^{e}\hat{\boldsymbol{R}}_{h} \\ {}^{e}\hat{\boldsymbol{\theta}}_{h} \\ {}^{e}\hat{\boldsymbol{R}}_{l} \\ {}^{e}\hat{\boldsymbol{\theta}}_{l} \\ {}^{h}\hat{\boldsymbol{v}}_{h} \\ {}^{h}\hat{\boldsymbol{\omega}}_{h} \\ {}^{l}\hat{\boldsymbol{v}}_{l} \\ {}^{l}\hat{\boldsymbol{\omega}}_{l} \\ {}^{e}\hat{\boldsymbol{v}}_{w} \\ {}^{h}\hat{\boldsymbol{B}}_{h} \\ {}^{l}\hat{\boldsymbol{B}}_{l} \end{bmatrix}_{39\times 1} \qquad \boldsymbol{z} = \begin{bmatrix} {}^{e}\tilde{\boldsymbol{R}}_{\text{gps}} \\ {}^{e}\tilde{\boldsymbol{v}}_{\text{gps}} \\ {}^{h}\tilde{\boldsymbol{M}}_{\text{mag}} \\ {}^{h}\tilde{\boldsymbol{\omega}}_{\text{IMU}h} \\ {}^{h}\tilde{\boldsymbol{a}}_{\text{IMU}h} \\ {}^{l}\tilde{\boldsymbol{\omega}}_{\text{IMU}l} \\ {}^{l}\tilde{\boldsymbol{a}}_{\text{IMU}l} \\ {}^{h}\tilde{\boldsymbol{R}}_{\text{cam}} \\ {}^{h}\tilde{\psi}_{\text{cam}} \\ \tilde{\boldsymbol{W}}_{\text{virt}} \end{bmatrix}_{(25+m)\times 1} \tag{6.35}$$

where ${}^{e}\hat{\boldsymbol{v}}_{w}$ is the external wind in earth fixed frame.

As mentioned earlier it is possible to reduce the state vector to 33 elements as the 6 bias states for the load IMU can be eliminated when this sensor is not available. This also reduces the measurement vector with the associated 6 states, but by removing the IMU, the load attitude observability is affected. If the IMU on the load is used, it provides roll and pitch rate information and the accelerometers provide some information on the the load roll and pitch attitude through the gravity. However, it is possible to achieve full observability through the choice of suspension type. If suspension type (b) from figure 4.1 is used the pitch of the load is directly coupled with the pitch of the helicopter, but the roll is uncoupled. If type (c) or (d) is chosen both roll and pitch of the load is linked to the helicopter and these becomes observable though the the helicopter attitude and the load position.

Process Model

The process model for the model based estimator uses the full dynamic model derived in chapter 3 and 4 with steady state flapping and actuators. This is due to the fact that actuator dynamics, inflow dynamics, and flapping dynamics are difficult to estimate as they are rather weakly observable with the available sensors. The bias model is the same as the one presented under the IMU driven process model in (6.27) and the wind is likewise modeled as a stationary process

$$ {}^{e}\dot{\hat{\boldsymbol{v}}}_{w,k} = 0 \,. \tag{6.36} $$

Observation Models

The observation models for the GPS, the magnetometer, the virtual wire sensor, and the vision system are the same as the ones presented under the IMU driven filter. However, the IMUs are now present as sensors and therefore needs observation models, which are simply rewrites of (6.22) and (6.23) as

$$ \hat{\boldsymbol{a}}_{\text{IMU}b,k} = \hat{\boldsymbol{a}}_{b,k} + {}^{b}\hat{\boldsymbol{a}}_{\text{bias}b,k} + \hat{\boldsymbol{T}}_{be,k}\,{}^{e}\boldsymbol{G}_{ref} \,, \tag{6.37} $$

$$ \hat{\boldsymbol{\omega}}_{\text{IMU}b,k} = \hat{\boldsymbol{\omega}}_{b,k} + {}^{b}\hat{\boldsymbol{\omega}}_{\text{bias}b,k} \,. \tag{6.38} $$

$\hat{\boldsymbol{a}}_{b,k}$ is not part of the state vector of the system, but is instead extracted from the process model prediction step during the propagation of the first sigma point.

6.5 Reduced State Unscented Kalman Filter

This estimator is intended for the general cargo transport development branch and must therefore proved estimates of the slung load translational states ($\hat{\boldsymbol{R}}_l, \hat{\dot{\boldsymbol{v}}}_l \in \mathbb{R}^3$). It is designed to augment an IMU driven helicopter state estimator and it uses the estimated helicopter states as well as the bias and gravity corrected acceleration measurements from the IMU ($\boldsymbol{a}_h$) as shown in figure 6.10. The design of the helicopter sensor fusion will not

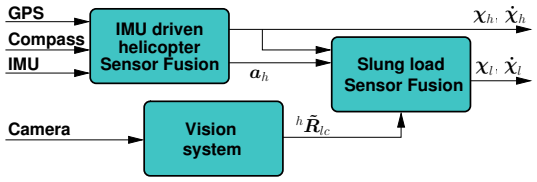

Figure 6.10: The architecture of the slung load state estimator.

be discussed in this thesis, but examples of such can be found in [van der Merwe *et al.*, 2004] and [Jun *et al.*, 1999]. The estimator uses the vision system as the only sensor input and therefore it does not require any mounting of sensors on the load.

6.5.1 Process Model

The system is modeled as a 3-dimensional point mass pendulum as shown in figure 6.11. The position of the load is described by the generalized coordinates $({}^e\theta_w,\ {}^e\phi_w)$, which can be considered as a 2-1 Euler angle rotation around the attachment point. The load position is described using earth fixed coordinates as this means that they are independent of the helicopter attitude changes. The double pendulum motion, created by the attitude

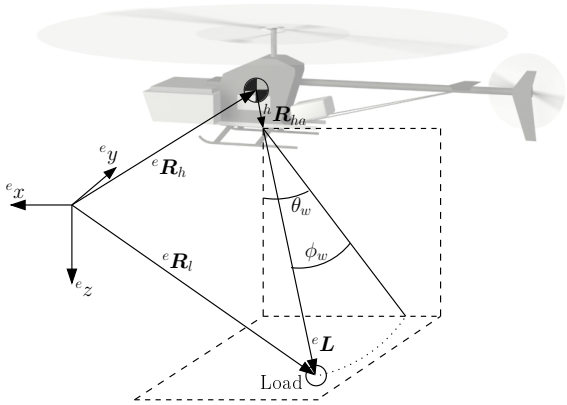

Figure 6.11: The point mass slung load model.

of the load with respect to the wire, is neglected, i.e. the load is considered always to be aligned with the wire. Furthermore, the translational accelerations of the helicopter attachment point generated by angular motions are neglected.

The point mass slung load model can be found by considering the helicopter accelerations and rotating them into the wire frame which yields

$$\begin{aligned} {}^e\ddot{\theta}_w =& (-\cos(\theta_w)\cos(\phi_w){}^e\ddot{x}_h + \\ & \sin(\theta_w)\cos(\phi_w)({}^e\ddot{z}_h - g))/l\,, \end{aligned} \tag{6.39}$$

$$\begin{aligned} {}^e\ddot{\phi}_w =& (\sin(\theta_w)\sin(\phi_w){}^e\ddot{x}_h - \cos(\phi_w){}^e\ddot{y}_h + \\ & \cos(\theta_w)\sin(\phi_w)({}^e\ddot{z}_h - g))/l\,, \end{aligned} \tag{6.40}$$

where $[\ddot{x}_h\ \ddot{y}_h\ \ddot{z}_h]^T$ is the helicopter translational acceleration vector, $l = |{}^e\boldsymbol{L}|$ is the length of the pendulum. The position of the load in the earth fixed frame can be found as

$$\begin{aligned} {}^e\boldsymbol{R}_l =& \begin{bmatrix} \sin(\theta_w)\cos(\phi_w) \\ \sin(\phi_w) \\ \cos(\theta_w)\cos(\phi_w) \end{bmatrix} l + {}^e\boldsymbol{R}_h \\ & + \boldsymbol{T}_{eh}{}^h\boldsymbol{R}_{ha} = {}^e\boldsymbol{L} + {}^e\boldsymbol{R}_h + \boldsymbol{T}_{eh}{}^h\boldsymbol{R}_{ha}\,. \end{aligned} \tag{6.41}$$

The load velocity can be found from figure 6.11 as the angular velocities multiplied with the pendulum length, projected onto the earth fixed frame axis and added to the helicopter velocities

$$ {}^{e}\dot{\boldsymbol{R}}_{l} = \begin{bmatrix} \cos(\theta_w)\cos(\phi_w) & 0 \\ 0 & \cos(\phi_w) \\ -\sin(\theta_w) & -\sin(\phi_w) \end{bmatrix} \begin{bmatrix} \dot{\theta}_w \\ \dot{\phi}_w \end{bmatrix} l + {}^{e}\dot{\boldsymbol{R}}_{h} \, . $$

6.5.2 Sensor Model

The output of the vision system is a unit vector (${}^{h}\tilde{\boldsymbol{R}}_{lc}$) pointing towards the load from the camera as shown on figure 6.12. The estimated position of the load relative to the

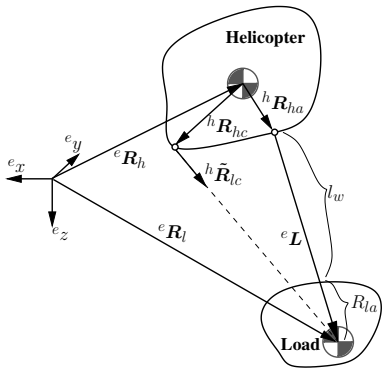

Figure 6.12: The geometric setup of the sensor model.

helicopter attachment point (${}^{e}\hat{\boldsymbol{L}}$) can be found as

$$ {}^{e}\hat{\boldsymbol{L}} = \begin{bmatrix} \sin(\hat{\theta}_w)\cos(\hat{\phi}_w) \\ \sin(\hat{\phi}_w) \\ \cos(\hat{\theta}_w)\cos(\hat{\phi}_w) \end{bmatrix} l \, , \tag{6.42} $$

and the predicted measurement can then be found by offsetting this vector to the camera position and normalizing

$$ {}^{h}\hat{\boldsymbol{R}}_{lc} = \frac{\boldsymbol{T}_{he}\,{}^{e}\hat{\boldsymbol{L}} + {}^{h}\boldsymbol{R}_{ha} - {}^{h}\boldsymbol{R}_{hc}}{|\boldsymbol{T}_{he}\,{}^{e}\hat{\boldsymbol{L}} + {}^{h}\boldsymbol{R}_{ha} - {}^{h}\boldsymbol{R}_{hc}|} \, . \tag{6.43} $$

6.6 Wire Length Estimation

The pendulous mode frequency of the dual mass helicopter slung load system can be determined as

$$\omega_n = -\sqrt{\frac{g(m_h + m_l)}{l m_h}} \,. \tag{6.44}$$

However, if feedback control is applied to the helicopter, the dual mass system behavior is altered as the effect of slung load swing on the helicopter is suppressed. The system can then be approximated by a standard pendulum description, which means that the wire length can then be calculated as

$$l = \frac{\omega_n^2}{g} \,. \tag{6.45}$$

This frequency is present as a slow sine wave in the measured load angles ($\tilde{\theta}_w$ and $\tilde{\phi}_w$), and could be estimated using standard FFT (note that it is important to use the measurements transformed into the earth fixed frame to remove helicopter motion from the signals). However, since we know that the frequency is quite low and as we want to estimate the frequency fairly quickly (i.e. using relatively few samples), a dedicated sine estimator is used. This estimator is a steepest ascent search on (a discretized version of)

$$f(\omega, \theta) = \frac{\int_0^{2\pi} s(t)\cos(\omega t + \theta)dt}{\int_0^{2\pi} \cos^2(\omega t + \theta)dt} \,, \tag{6.46}$$

where $s(t)$ is the input signal. This function is the normalized inner product between the signal and a linearly independent (but non-orthogonal) cosine frame, and thus peaks when ω matches the main frequency of the signal. This method is superior to the oversampled FFT when searching for one, approximately known frequency, partly because it involves significantly fewer computations and partly because the oversampled FFT does not include normalization at 'non-integer' frequencies.

However, it is important to use the wire length estimator with care: Around hover the oscillations may be so small that it is difficult to detect the correct frequency and when used in a closed loop system the frequency of the oscillation can be shifted depending on the controller. Therefore, the strategy for using the estimator is to make a gentle step with the helicopter shortly after take off which generates free swing of the slung load. When the sine estimator has converged after a short period of time, the wire length is locked to the found value and the state estimates are ready for use in close loop.

Example: Frequency Estimation of Noisy Signal

To illustrate the operation of the wire length estimator an example is given here with a 0.2 Hz signal measured by a noisy sensor at 50 Hz as shown in figure 6.13. The estimator is run every second and is initialized at 0.35 Hz and as shown on figure 6.13 it converges to the correct frequency after 4 seconds. In a pendulum application 0.2 Hz is equivalent

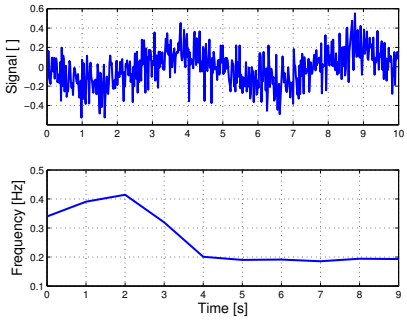

Figure 6.13: Top: The noisy signal. Bottom: The estimated frequency.

to 6.2 m and 0.35 Hz to 2 m. The convergence of the estimator every update step is shown on figure 6.14. At every time step the steepest ascent finds the peak of the fre-

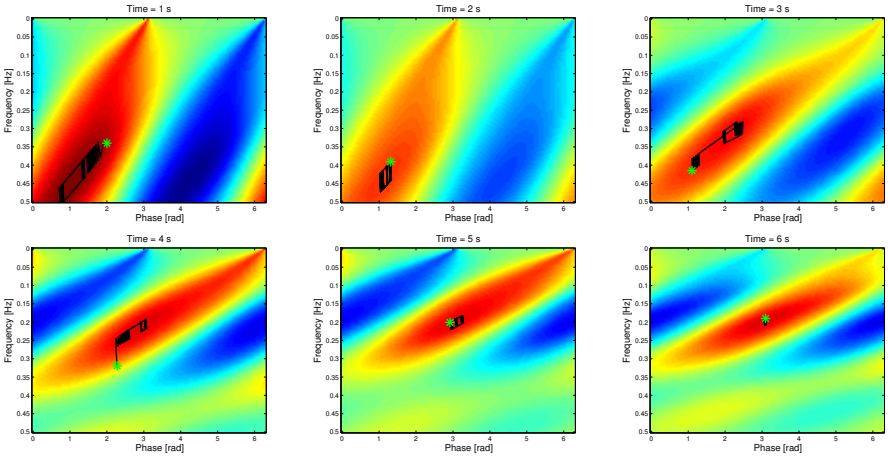

Figure 6.14: The estimator steps for the first 6 seconds plotted on a background of the frequency content of the signal. Green dot shows the final position of the estimator and red area indicate highest energy.

quency/phase map of the signal, but the actual frequency/phase map generated by using inner product is not accurate until around 4 seconds. As it can be seen from figure 6.14 the frequency/phase map is non-convex which means that there is a risk of the optimization algorithm finding a local peak in the map. However, this is not a problem in the slung load application where the initial guess on the frequency, i.e. the wire length, is quite accurate.

6.7 Implementation Considerations

In the IMU driven filter the process model is propagated using a standard forward Euler approach, whereas in the model based filter it is propagated using a second order Runge-Kutta approach. This is because the solution of the redundant coordinate rigid body model benefits greatly from the added numerical precision of the second order Runge-Kutta as compared to the forward Euler. Both filters are run at 50 Hz, which is adequate for estimation of the rigid body dynamics.

Some of the sensors available in the system are unable to deliver output at the filter execution frequency. The GPS, for instance, is capable of an output rate of 20 Hz and the vision system can deliver new measurements at a rate of about 15 Hz. In order to deal with this a simple solution is used – when a measurement is not available, the column in the Kalman gain corresponding to the missing measurement is simply set equal to 0. Thereby, the missing data is not allowed to influence on the prediction of the state vector. This is in practice done by comparing one-sample-time old sensor measurements with the new ones and if there is no difference, the sensor is disabled. This is a simple approach, which relies on a certain noise level on all sensors and it automatically deals with temporary sensor drop out.

6.7.1 State Dependent Separation

When using the unscented Kalman filter an important issue is the computational demands of the prediction step – the UKF can be come very computational demanding when used in connection with a complex model with many states like the one used in the model based filter here. As mentioned earlier the UKF actually requires $2n+1$ calls of the model which in the IMU driven case yields 61 calls of the model. However, in the model based case this becomes 79 calls from the UKF and for each call the model is executed twice in the second order Runge-Kutta with yields a total of 158 model calls for each time step. As the filter is run at 50 Hz and as the model is quite complex, the computational burden is high. Therefore, a method for speeding up the model propagation is devised.

For the dynamical helicopter slung load model used in this research it is possible to make a separation into a sequential set of parts that can be calculated one after another. Indeed this is possible for a wide range of dynamical models. This is interesting when the model is used in the unscented Kalman filter where the sigma points that are propagated contains perturbations on one state at a time with respect to the mean state vector (which is equal to the first sigma point).

Assume that a n'th state in the state vector is only used in the last part of the model.

It is propagated with sigma point $n+1$ and $2n+1$ as

$$\boldsymbol{\chi}_0 = \begin{bmatrix} x_1 \\ x_2 \\ \vdots \\ x_n \end{bmatrix}, \quad \boldsymbol{\chi}_{n+1} = \begin{bmatrix} x_1 \\ x_2 \\ \vdots \\ x_n + \delta_s \end{bmatrix}, \quad \boldsymbol{\chi}_{2n+1} = \begin{bmatrix} x_1 \\ x_2 \\ \vdots \\ x_n - \delta_s \end{bmatrix},$$

where δ_s is the sigma point perturbation term. This means that the model can be separated into two parts, one that is independent of x_n

$$\boldsymbol{y}_1 = \boldsymbol{f}_1(\boldsymbol{u}, x_1, x_2, \ldots, x_{n-1}),$$

and one that is dependent on x_n, the output of the first part and possibly the other states as well

$$\boldsymbol{y}_2 = \boldsymbol{f}_2(\boldsymbol{y}_1, \boldsymbol{u}, x_1, x_2, \ldots, x_n),$$

where $\boldsymbol{y}_2$ is the final output of the model. This separation can then be used in the unscented Kalman filter where the output of $\boldsymbol{f}_1$ from the first sigma point ($\boldsymbol{y}_{1,1}$) is reused in the calculation of $\boldsymbol{f}_2$ for sigma point $n+1$ and $2n+1$ and thereby saving two calculations of $\boldsymbol{f}_1$. This is illustrated in figure 6.15.

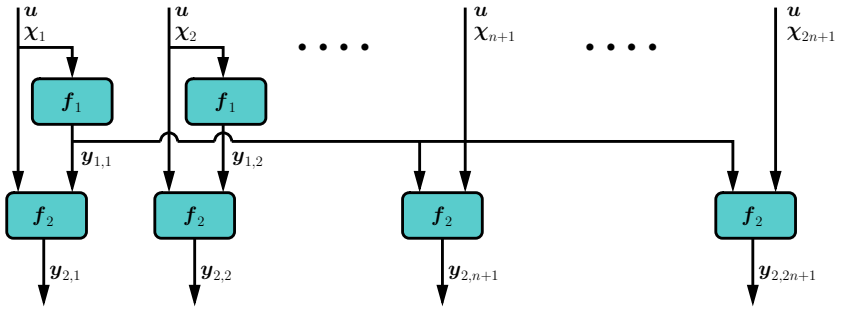

Figure 6.15: The state dependent separation principle used in the propagation of the sigma points.

This principle can be used with great success on the helicopter and slung load dynamical model where the entire aerodynamic helicopter model only depends on the helicopter velocities and therefore only needs to be calculated for 6 out of 24 rigid body states. Furthermore, the helicopter and slung load model is completely independent of the IMU bias states. This means that out of the 158 total calls to the model only 62 full calls are needed using this principle. Another 48 partial calls of the model, where only the rigid body part of the model is call, are needed. Finally, 48 calls where it is unnecessary to call the helicopter slung load model at all and only the simple bias model is used.

6.8 Simulation of Estimators

Verification through simulation provides an opportunity to compare the performance of the estimators against the true values and thus gives insight into the operation of the filters. The sensors are modeled using realistic noise, quantization, and delays. In the case of the IMU on the helicopter, the noise levels are quite high due to vibrations induced by the engine and rotors. The GPS using EGNOS has a horizontal accuracy of approximately 1 m, which is modeled as white noise together with random walk and random jumps that simulate satellite changes. The vision system is simulated using screen capture through the 3D graphical interface. External wind is modeled as a constant vector overlayed with sinusoids and random walks. Biases are modeled as constants overlayed with random walks.

6.8.1 Simulation of Full State Estimators

The two full state estimators are tested on a simple trajectory in close loop using a linear state feedback controller and the dynamic model based filter is used with a slung load IMU. A 4 m dual wire suspension is chosen for the test. The trajectory is a S-like pattern starting and stopping in hover. In figure 6.16 and 6.17 the flight using the IMU driven filter and the model based filter is shown. The estimation errors for the IMU driven filter

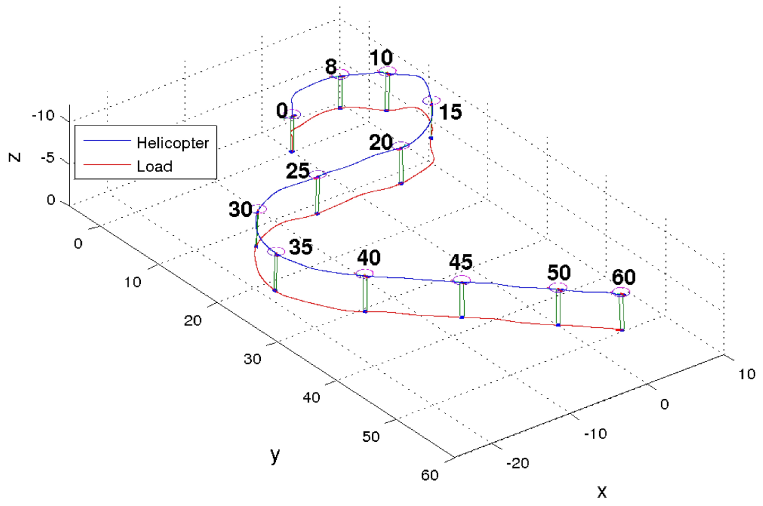

Figure 6.16: (Simulation) 3D plot of the trajectory flown with the IMU driven filter shown in perspective with timeline.

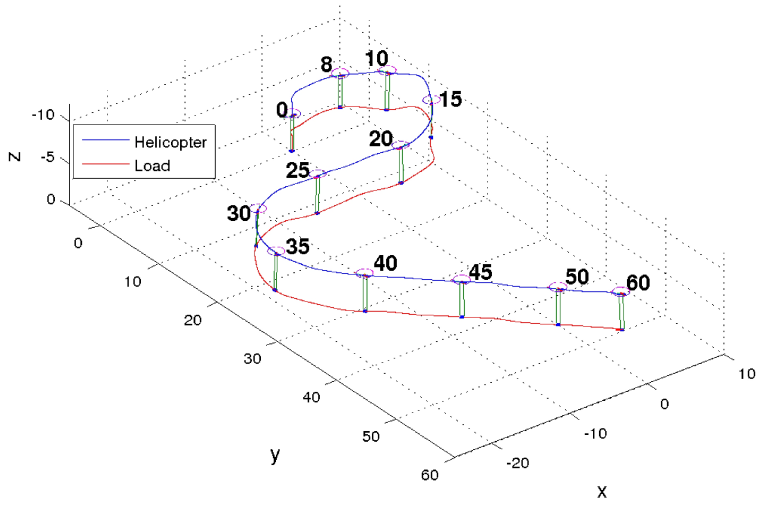

Figure 6.17: (Simulation) 3D plot of the trajectory flown with the dynamics model based filter shown in perspective with timeline.

is shown in figure 6.18. It is capable of tracking the position of the helicopter and the load within 0.2 m, the attitude within 0.05 rad, and velocity within 0.5 m/s after the filter converges. From the error on the biases it is evident that the filter converges, the biases on the gyros converges after only a few seconds, while the biases on the accelerometers takes slightly longer to converge. As mentioned earlier the rate estimates are simply bias compensated gyro measurements and the vibration noise from the helicopter is evident on the rate estimation error. The wire length error is less that 1 mm.

When comparing the estimation errors for the model based filter in figure 6.19 with errors for the IMU driven filter, the results are similar, if slightly better for the model based filter. However, some differences stand out. The vibrational noise, that was very evident on the helicopter rate estimate with the IMU driven filter, is reduced significantly. The bias estimation for the load exhibits a large deviation on the z-axis due to numerical imprecision in the initialization of the rigid body model, but it converges quickly. The wind estimates, which are available in the model based filter, is shown and follows the real wind well.

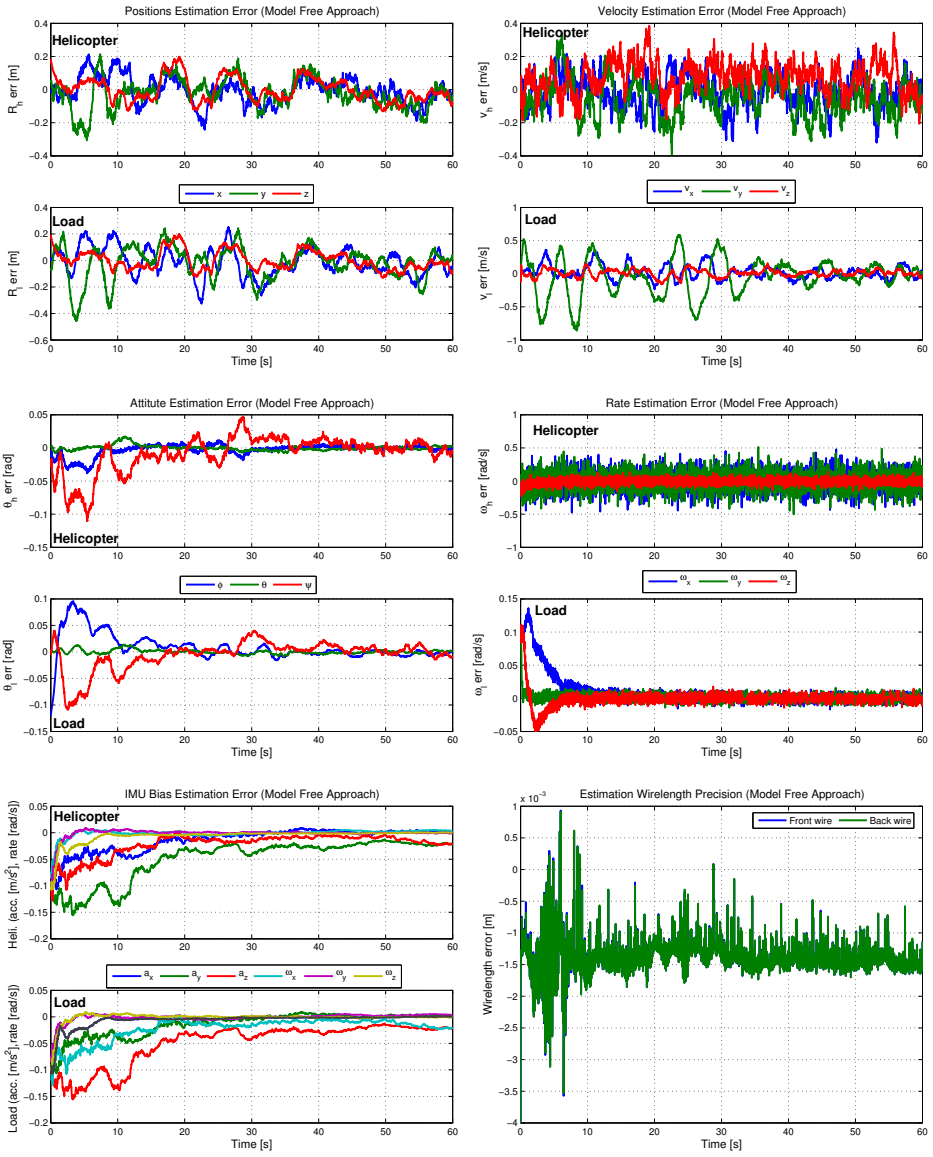

Figure 6.18: (Simulation) Estimation errors using the IMU driven filter.

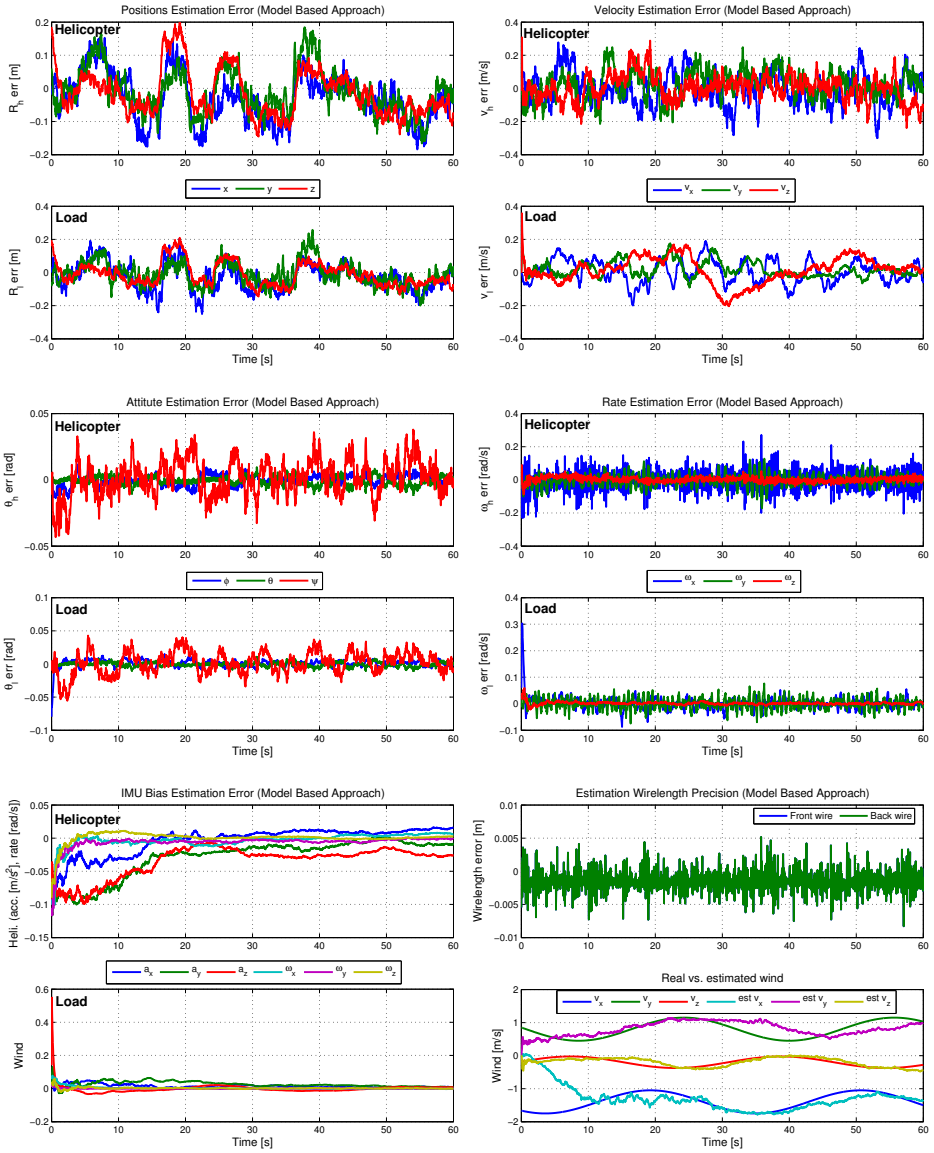

Figure 6.19: (Simulation) Estimation errors using the model based filter.

If the dynamics model based filter is run without slung load IMU input the performance deteriorates and actually comes slightly worse that the IMU driven filter.

The execution time for the filters is shown in table 6.2, which compares the model free with the model based solution. For the model based solution the result with and without using the state dependent separation is shown.

Estimator	Execution time, % of avilable time
IMU driven filter	5.1
Model based filter (optimized)	30.5
Model based filter	46.4

Table 6.2: Execution time comparison for the IMU driven filter, the optimized model based filter and the standard model based filter.

The execution time is measured in % of the avilable computational time when running the system at 50 Hz on the 1.8 GHz onboard computer. In other words, when the IMU driven filter uses 5.1% of the computational resources there is 94.9% time left for controllers, supervisiors etc. As it can be seen the model based filter uses a substantial percentage of the available resources, but this can be reduced by approximately 1/3 by using the state separation principle presented earlier.

6.8.2 Simulation of Reduced State Estimator

The reduced state estimator is tested together with a IMU driven estimator for the helicopter in close loop with a linear state feedback controller. The suspension system is a 5 m single wire setup. The test course is an S-like trajectory, which starts and stops in hover (see figure 6.20).

Estimations errors are shown in figure 6.21 and it can be seen that the positions for both helicopter and load are tracked withing 0.1 m and velocity is tracked withing 0.2 m/s. The actual and estimated wire angle and wire angular velocities are shown on the middle graphs and it can be seen that the estimator tracks the actual slung load angles well. At the bottom the input to the estimator is shown; the helicopter accelerations and the load camera measurement in the x and y picture coordinates. The load position measurements have a low noise level, but as the measurements are dependent on the helicopter rotation, the noise from the attitude estimates effect the measurements. Furthermore, noise is introduced into the estimates by the very noisy acceleration measurements that drives the prediction step.

6.9 Verification of Estimators

To verify the design of the estimator and test the performance, a number of flight tests has been carried out. Both platforms described in 2 on page 27 have been used for these tests.

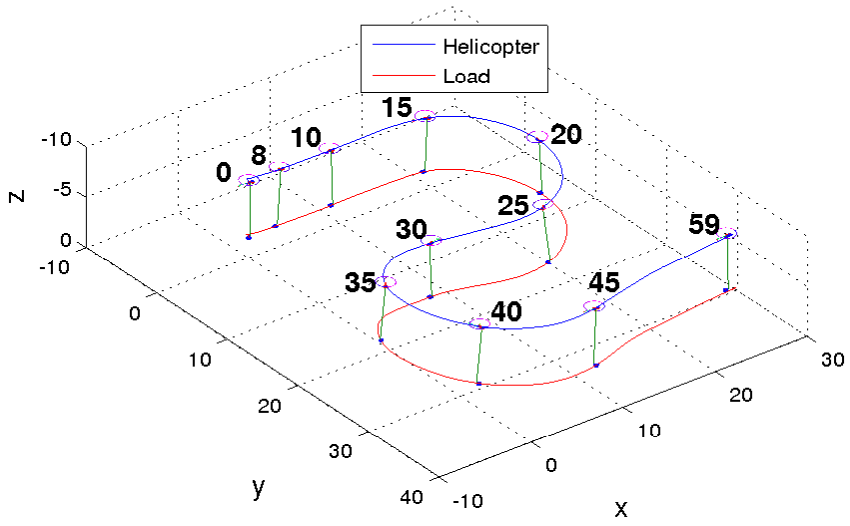

Figure 6.20: (Simulation) 3D plot of the trajectory flown with a IMU driven estimator for the helicopter and the reduced state estimator for the slung load.

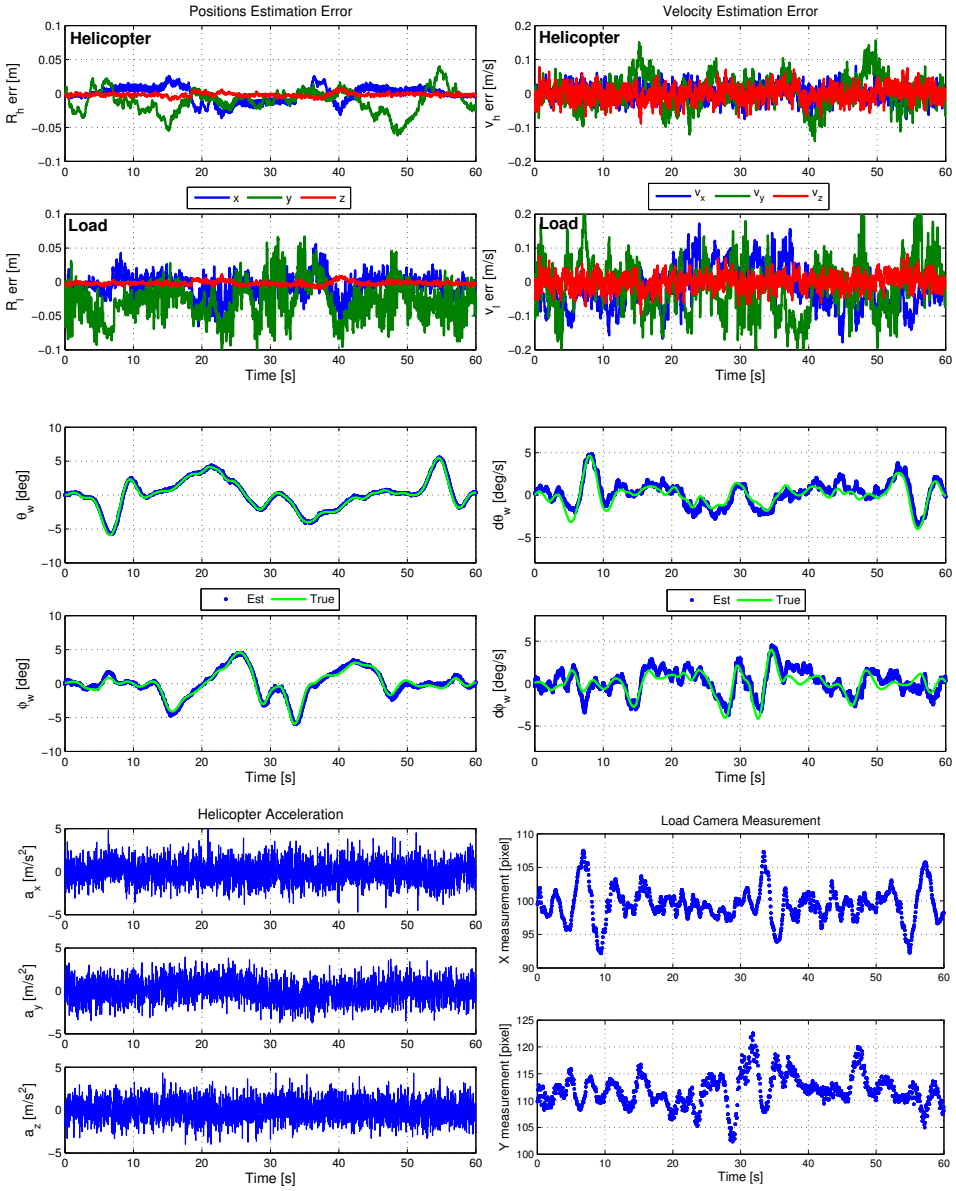

Figure 6.21: (Simulation) Estimation results using the reduced state estimator.

6.9.1 Verification of Reduced State Estimator

In the following two tests using the GTMax are presented; one with gentle motions to see how the filter converges and tracks, and one with an aggressive step where the load swings outside the FOV of the camera to test how well the filter can propagate without measurements. The test slung load has a mass of 5.5 kg and is suspended in a 7 m wire.

Gentle Steps

The estimator is started with the helicopter in hover and the load hanging without significant swing. The sequence of motion is then that the helicopter is rotated 90^o and takes two gentle 6 m steps, first left and then forward as shown in figure 6.22 (note that the plotted positions are estimates).

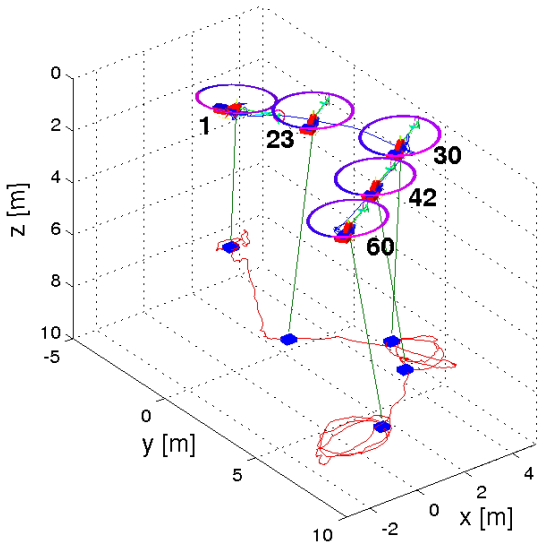

Figure 6.22: (Flight) 3D view of “gentle steps” test with time line plotted.

As mentioned in section 6.6 the wire length estimator needs free oscillation of the system to reliably lock on to the correct frequency. Therefore the wire length estimator is started just before the first step. The estimator is started with the initial angles and angular velocities set to zero and a initial wire length of 4 m – the erroneous initial wire length is seen as a shorter green line at time 1 in figure 6.22.

The input to the filter in form of helicopter accelerations is shown in figure 6.23 where the steps can be observed around 20 s in y and 40 s in x. In figure 6.24 the estimated and

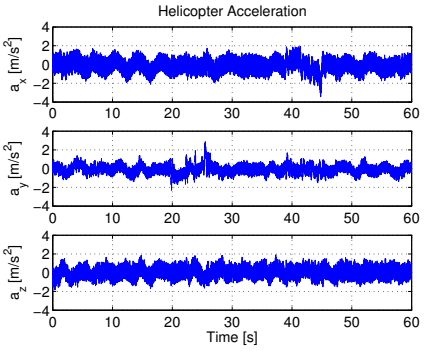

Figure 6.23: (Flight) Helicopter accelerations for “gentle steps”.

measured states are shown and it can be seen that the filter is having problems during the initial 20 s where it uses a wrong wire length. When the wire length estimator is enabled it rapidly converges to the correct wire length of 7 m as shown on figure 6.24, which results in a much better performance on the estimates of the load states.

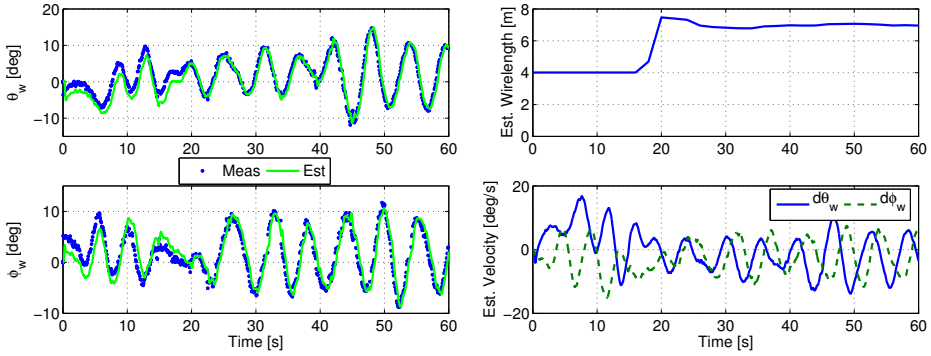

Figure 6.24: (Flight) Left: Estimator output vs. measurements for “gentle steps”. Right: Estimated wire length and estimated velocity.

Aggressive Step

This test is run with an already converged estimator and consists of an aggressive 6 m right step with the helicopter as shown on figure 6.25. The step can also be observed on

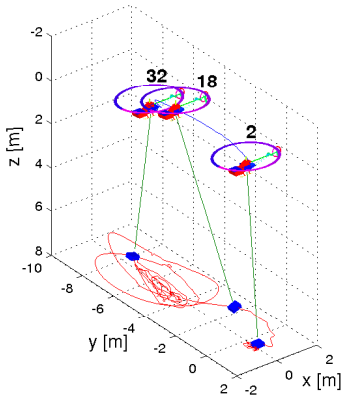

Figure 6.25: (Flight) 3D view of “aggressive step” test with time line plotted.

the helicopter accelerations on figure 6.26. The purpose of this is to create a large enough

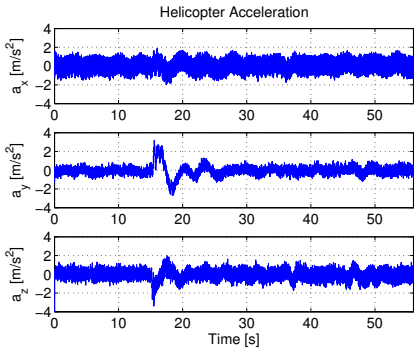

Figure 6.26: (Flight) Helicopter accelerations for “aggressive step”.

swing and/or a large enough tilt of the helicopter for the load to disappear out of FOV. The estimated load angles and measured angles are shown in figure 6.27 and it shows how the estimator propagates correctly during periods without measurements.

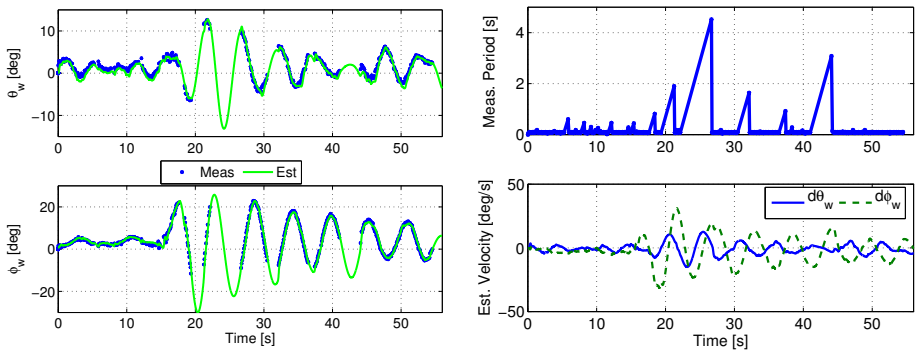

Figure 6.27: (Flight) Left: Estimator output vs. measurement for "aggressive step". Right: Measurement period and estimated velocity.

The missing measurements are evident in the plot of the time-period between measurements in figure 6.27. At one point more that 4 s elapses without new measurements where the load is either outside FOV or passes so quickly through the image that the resulting distortion prevents correct detection of the load. The smaller peaks in the beginning are either due to distortion from vibrations or due to the fact that the vision system is running as an asynchronous thread. This means that measurements do not necessarily arrive with a constant frequency.

6.9.2 Verification of Full State Estimator

The testing is performed using the AAU Bergen Twin and the dual wire slung load. During flight testing of the full state estimators it has become clear that, while it is possible to get good result with both the IMU driven and the full dynamic model estimator, a problem persist with the latter. It has proven to be somewhat difficult to tune the dynamic process model estimator in real flight conditions and even a tuned filter that converges shows rather poor robustness qualities. For changing flight conditions or small changes of helicopter parameters, the filter performance quickly deteriorates. The problem is worse in a filter configuration without slung load IMU. Given these problems and the added computations complexity of the dynamic model based estimator there are no real advantages to this filter compared to the IMU driven filter. Therefore, no flight test verification data will be presented for the dynamic process model estimator and the IMU driven estimator will be used for controller flight tests

In figure 6.28 a 3D plot of a manual controlled test flight with the IMU driven filter is shown. The estimator is started with the helicopter flying around hover and a couple of maneuvers are then made to excite oscillations in the slung load. The output of the vision system, which consists of lateral and longitudinal pixel position and measured relative

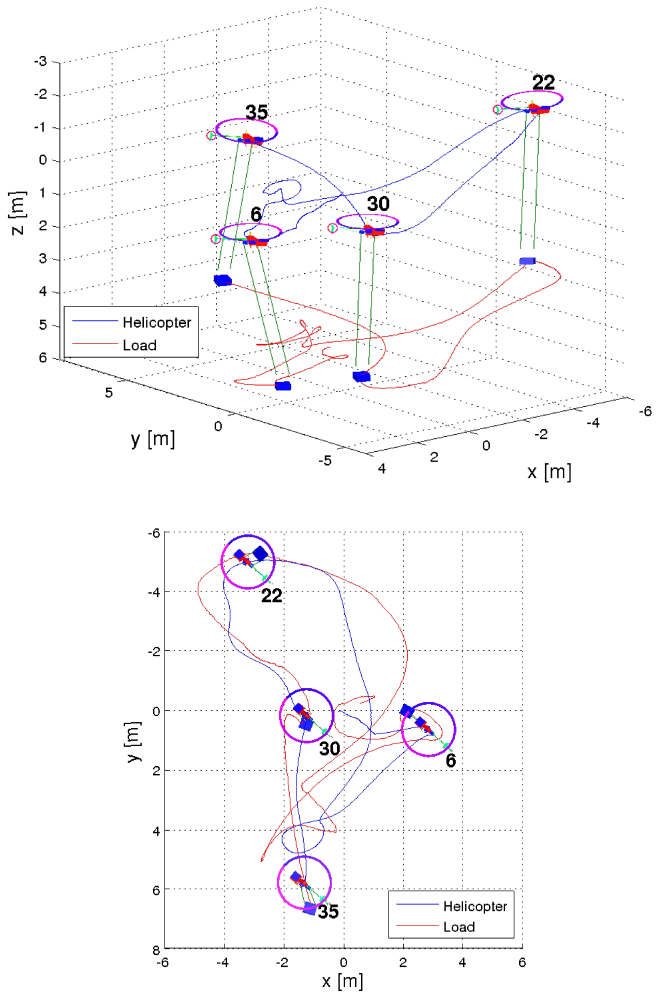

Figure 6.28: (Flight) 3D view of flight test with IMU driven full state filter.

yaw, during the flight is shown in figure 6.29. The estimated states have been mapped backwards through the vision system sensor model which gives what the estimated state vector corresponds to in picture position and yaw of the slung load. These estimated pixel positions and yaw are show together with the actual measurements. We can see how the slung load swings out of camera view four times during the flight which results in missing measurements in up to 0.8 seconds. Looking at figure 6.29 we can how the estimator is

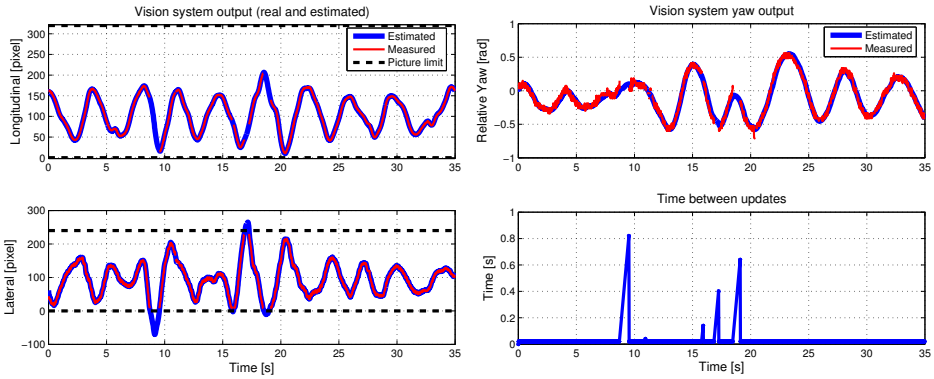

Figure 6.29: (Flight) Measured and estimated vision system output.

capable of propagating smoothly between the measurement updates.

The full estimated state vector is shown in figure 6.30 with helicopter and slung load positions, velocities, Euler angles, and rates. The estimated helicopter position is plotted together with GPS position measurements mapped to helicopter center of mass using the estimated Euler angles. Estimated biases for the helicopter and slung load IMUs are also shown, and we can observe how they seem to converge to steady values during the flight. Given the estimated position and Euler angles for helicopter and slung load we can calculate the estimation error in lengths for both wires, which is shown in the lower right corner of figure 6.30. The virtual wire sensor is capable of keeping the error for the wires almost identical and below 1 mm. The high frequency noise on the error originates mainly from the rather noisy helicopter IMU output.

6.10 Estimation Summary and Discussion

In this chapter the sensor fusion and state estimation for the helicopter slung load system was presented. The main purpose was development of two different estimators: One intended for suspension systems which couples helicopter and slung load yaw and one for suspension systems without yaw couping. Both uses a vision system to measure slung load motion and both are based on the unscented Kalman filter.

The reduced state estimator for non-yaw coupling suspensions was designed specifically to augment autonomous helicopter state estimators; it can therefore be used to add slung load capability to already operating autonomous helicopters. The update step is based entirely on vision based measurements which eliminates the need for sensors on the load. The estimator further includes the ability to estimate the wire length of the slung load and thus requires only basic knowledge of the load and suspension system, which

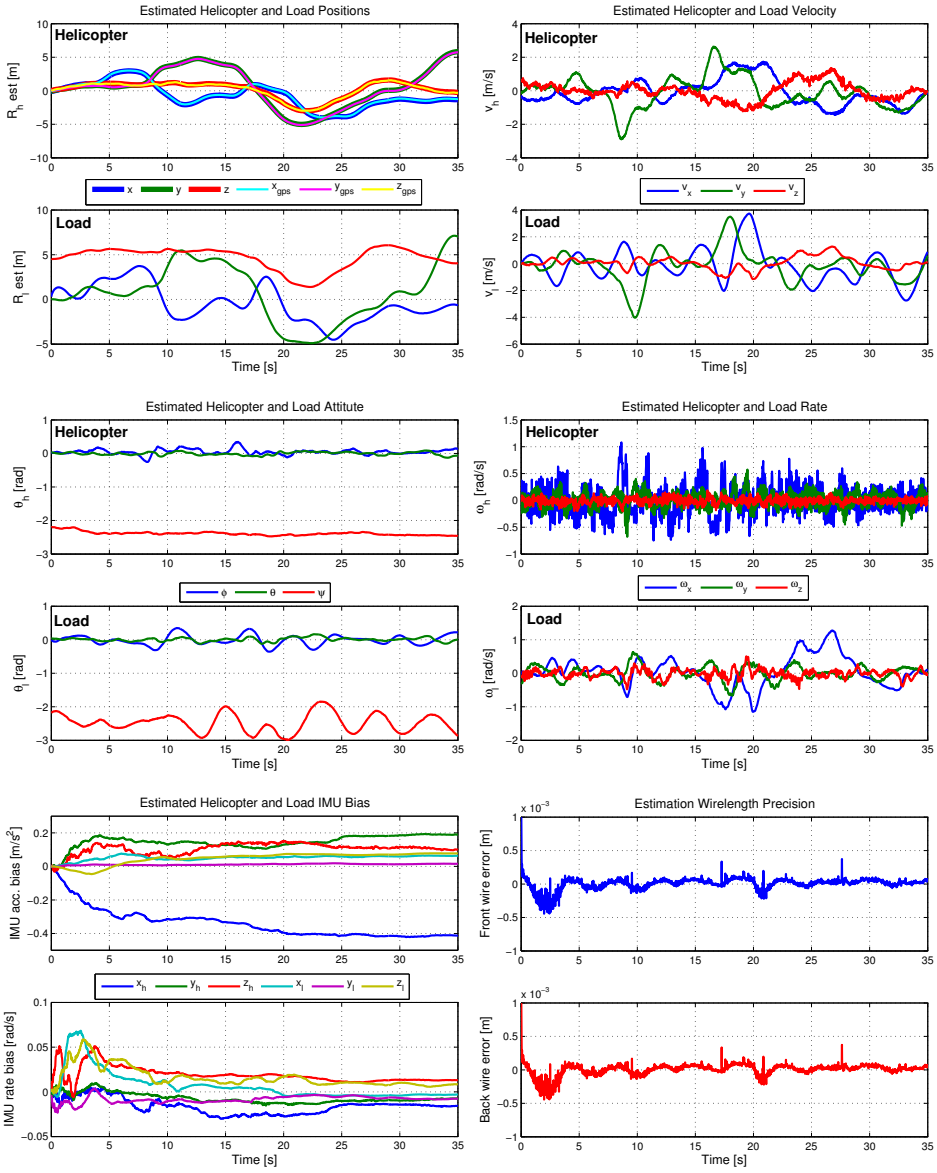

Figure 6.30: (Flight) Estimated states using IMU driven full state filter.

makes it ideal for a general cargo transport application.

The full state estimator was designed as a stand-alone filter capable of delivering full state information for both helicopter and slung load. This was accomplished through two different approaches: A kinematic model and a full model based filter. The kinematic model filter is based on a simple IMU driven model, while the full model based filter uses the full dynamic model. The vision system is used to measure heading and position of the load and an IMU is mounted on the load for acceleration and rate measurement.

The performance of the estimators was demonstrated through simulation as well as in real flight. For the reduced state estimator two flight tests were presented. The first flight test showed the ability to successfully converge to the correct wire length and subsequently to track the load states. The second flight test showed the ability to successfully propagate the estimates during periods without sensor measurements. During flight testing of the full state estimator, the IMU driven process model approach was found superior to the dynamics process model approach with respect to estimation performance and computational burden.

A disadvantage of using the IMU driven full state estimator is that it requires a IMU on the slung load and in many cases it would be advantageous to be independent on any sensor equipment on the slung load. A next step could therefore be to extend the reduced state estimator for estimation of slung load heading. This could be achieved by using a bifilar pendulum model instead of the single wire pendulum model used presently.

Chapter 7

Swing Damping Slung Load Control

This chapter presents a swing reducing control system for augmenting already existing helicopter controllers and enables slung load flight for any autonomous helicopter. This begins with an analysis of the task, including identification of the vibrational modes for the system. A feedforward controller is designed to avoid excitation for of the lightly damped modes of the system by shaping the input reference trajectory. Then a feedback control system is added to actively dampen oscillations of the slung load. Finally, simulations and flight test verifications of the control system are presented.

7.1 Introduction

The purpose of this chapter is to design a control system that can be put on an existing autonomous helicopter and make it capable of flying with a slung load without large oscillations. As mentioned earlier, the main challenge in flying with a slung load is the pendulum like oscillations of the load and the control system is therefore focused on damping load swing.

To dampen swing of a slung load is similar to vibration damping in many other applications and while actual examples of slung load antiswing control are rare in the literature, inspiration can be found in other applications. One of the most obvious applications to draw inspiration from is overhead gantry cranes, which exhibit the same pendulum like behavior, albeit with much simpler actuator dynamics.

A very common approach to reduce swing of gantry cranes is known as input shaping. Input shaping is a feedforward control technique for vibrations damping which works by

shaping the reference signal such that it avoids exciting system vibrational modes. However, as a feedforward controller is not sufficient to deal with initial swing and externally imposed excitations, a feedback controller is introduced. For this purpose a delayed feedback strategy is used to actively absorb oscillations in the system. The architecture of the swing damping control scheme is shown in figure 7.1.

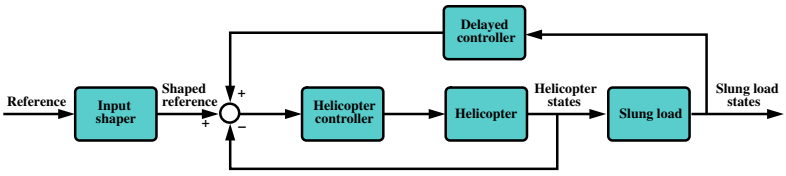

Figure 7.1: Architectural overview of the swing damping control scheme.

7.2 The Helicopter Slung Load Problem

The dominant resonant behavior of the slung load system is given by the pendulum modes of the slung load. As mentioned in chapter 5 these poles are typically very lightly damped and have frequencies that is dependent on the suspension length (typically in the range from 0.35 Hz for 2 m to 0.16 Hz for 10 m wires). In many ways the task of controlling a slung load system is similar to controlling a gantry crane. However, for a helicopter slung load system the control task is complicated by the nonlinear and unstable nature of the helicopter. While the helicopter has excellent actuation on the yaw and z axis, it has somewhat less controllability on the lateral and longitudinal axis, which are the best inputs for controlling the slung load system. For suspension systems where the yaw of the load is coupled to the yaw of the helicopter, like the pendant system, another resonant mode is introduced into the system. However, if the coupling is kept strong the mode is reasonably easy to control as the helicopter features very good actuation on yaw.

The basic helicopter slung load control problem can be described as stabilizing the helicopter and using it as actuator to damping the resonant slung load poles. For a human helicopter pilot this can be a difficult and strenuous task [Hoh *et al.*, 2006]. Indeed, instabilities known as pilot induced oscillations can be the result if the pilot handles the situation incorrectly. An example is seen in figure 7.2 where the pilot tries to keep the helicopter in a fixed position regardless of the swinging load. When the load swings out, the pilot will try to counteract the load influence on the helicopter and thereby risking an amplification of the load swing. Figure 7.3 illustrates the correct way of handling a slung load where the helicopter follows the slung load motion and thereby dampens the oscillations. In other words, negative feedback from the load motion will amplify load swing while positive feedback will dampen the swing.

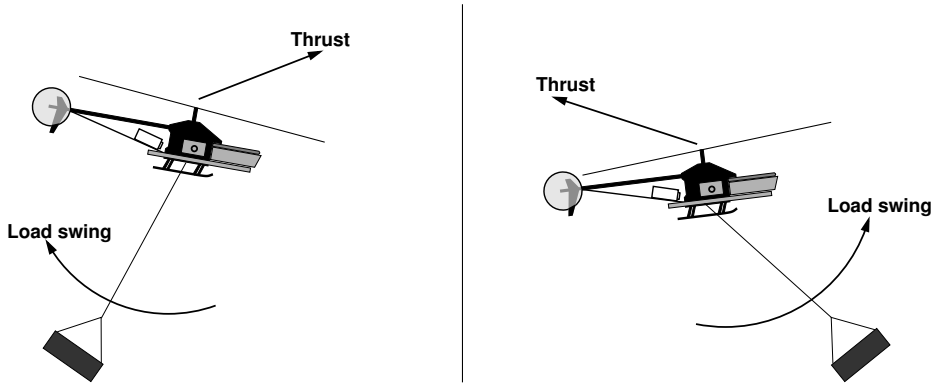

Figure 7.2: An example of pilot induced oscillations, the helicopter pilot attempts to counteract the influence from the slung load by actuating in the opposite direction of the load swing. The consequence of this response is amplified load swing.

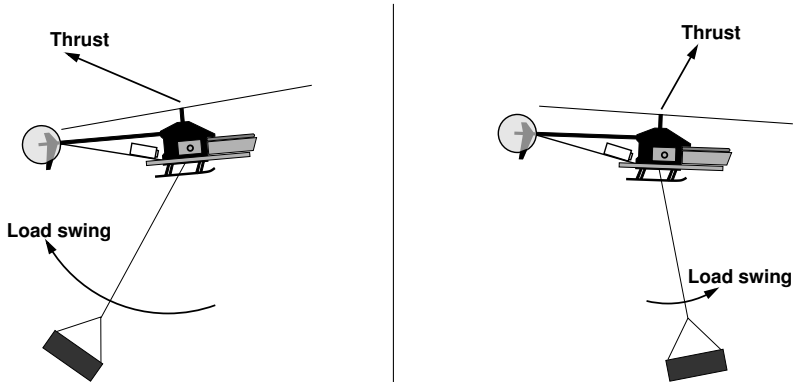

Figure 7.3: An example of slung load flight where the helicopter pilot follows the slung load motion and thereby counteracting the load swing.

The above has only discussed the slung load influence on the lateral and longitudinal behavior of the helicopter and while this is the primary influence [Hoh *et al.*, 2006], the slung load also affect the vertical helicopter dynamics. This was analyzed in section 5.3 with the result shown in figure 5.24 on page 124 and the conclusion was that load to helicopter mass ratio from 0.07 to 0.43 had only little influence on the heave mode of the system. The influence of the slung load on this mode can seen simply as an addition to the helicopter mass m_h and thereby the effect on the damped heave mode frequency can

be described as

$$\omega_n = \frac{D}{m_h + m_l} \tag{7.1}$$

where D is a damping term. This means as the load to helicopter mass ratio rises, the heave mode becomes slower. The augmenting controller scheme designed in this chapter only handles the horizontal slung load influences and thereby we assume that the helicopter controller is capable of handling the change of heave mode bandwidth and includes an integration term that can handle the change in collective trim.

7.2.1 Cart/Pendulum Example: PD Feedback

To illustrate the slung load problem we use a cart/pendulum example which closely resembles a one dimensional slung load system. The system is shown in figure 7.4; a cart with the mass $M = 2$ can be moved a distance x along a surface by the control force F and a pendulum of length $l = 5$ is attached onto the cart. The swing angle is denoted θ and the pendulum mass is $m = 2$. The nonlinear model for the cart/pendulum system can

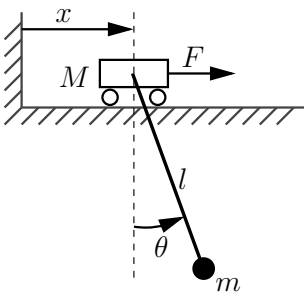

Figure 7.4: The cart/pendulum system.

be found as

$$(M + m)\ddot{x} = -ml\cos(\theta)\ddot{\theta} + ml\sin(\theta)\dot{\theta}^2 + F\,, \tag{7.2}$$

$$ml^2\ddot{\theta} = -ml\cos(\theta)\ddot{x} - ml\sin(\theta)g\,. \tag{7.3}$$

Further, the model can be linearized to

$$\dot{\boldsymbol{x}} = \boldsymbol{A}\boldsymbol{x} + \boldsymbol{B}u\,, \tag{7.4}$$

where

$$\boldsymbol{A} = \begin{bmatrix} 0 & 1 & 0 & 0 \\ 0 & 0 & \frac{mg}{M} & 0 \\ 0 & 0 & 0 & 1 \\ 0 & 0 & -\frac{g(M+m)}{lM} & 0 \end{bmatrix}\,, \quad \boldsymbol{B} = \begin{bmatrix} 0 \\ \frac{1}{M} \\ 0 \\ -\frac{1}{lM} \end{bmatrix}\,, \quad \boldsymbol{x} = \begin{bmatrix} x \\ \dot{x} \\ \theta \\ \dot{\theta} \end{bmatrix}\,, \quad u = F\,. \tag{7.5}$$

If we attempt feedback from the pendulum motion, here defined by the angular rate $\dot{\theta}$, it is possible to show how positive and negative feedback affects the system. In figure 7.5 the position of the cart/pendulum system poles are shown for different values of feedback gain. A positive feedback from $\dot{\theta}$ will in this case mean that when the pendulum

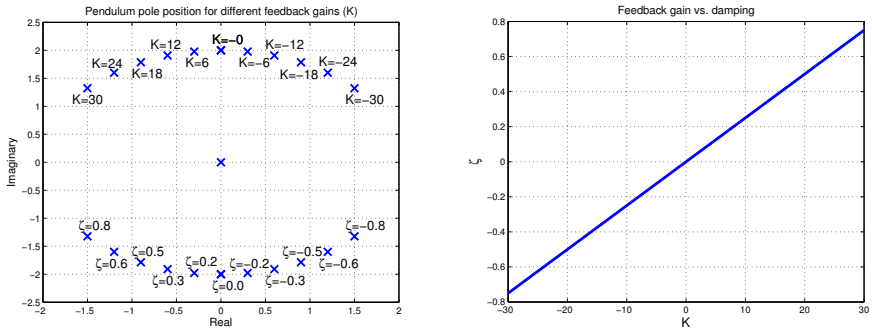

Figure 7.5: (Cart/Pendulum example) Left: The position of the pendulum poles as a function of the feedback gain. Right: Feedback gain vs. pole damping.

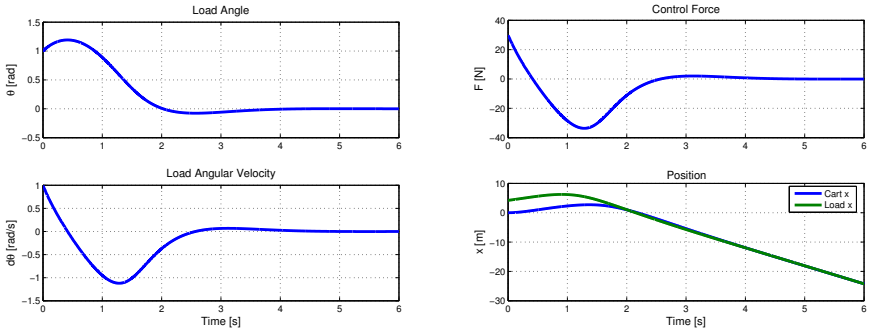

Figure 7.6: (Cart/Pendulum example) Left: Pendulum angle and angular rate. Right: Control force and positions

swings out, the feedback law will make the cart follow the pendulum and thus dampen the oscillation. A simulation of the nonlinear system with a rate feedback of 30 and an initial condition of $\boldsymbol{x}_0 = [0\ 0\ 1\ 1]^T$ is shown in figure 7.6 where it can be seen that the feedback law dampens the pendulum swing very quickly. However, it is also clear that this controller does not restrict cart and pendulum position which grows unbounded after damping out the pendulum swing.

7.3 Feedforward Swing Damping Control: Input Shaper

The concept of input shaping was first suggested in [Smith, 1957]. The method was dubbed the Posicast technique and was based on the idea of exciting two transient oscillations in a underdamped system such that they cancel each other and thereby achieving an oscillation free response. The method was described as

> *The final value is reached just when the velocity goes to zero. This is what happens when a fisherman drops his fly in the water at the maximum-position and zero-velocity instant.*

The concept is illustrated in figure 7.7 for the helicopter slung load system with a transition from hover to forward flight. First the helicopter starts to move forward which then results in a forward velocity of the load. When the load catches up with the helicopter the velocities of the two are matched and they continue forward together.

Some of the first experimental results using input shaping was presented in [Starr, 1985] where rest to rest maneuvers was demonstrated with a crane. Since then input shaping has been applied to a range of applications apart from cranes, including flexible robotic manipulators ([Hillsley and Yurkovich, 1993], [Jones, 1994]) and space crafts ([Singhose *et al.*, 1997], [Banerjee *et al.*, 2001]) with flexible solar arrays and fuel sloshing. A good introduction to input shaping techniques is given in [Singh and Singhose, 2002], where a review of input shaping literature is given together with a tutorial to practical input shaping design. An comprehensive treatment of input shaping is found in [Singhose, 1997] where synthesis of a wide range of command shaping feedforward controllers are discussed.

7.3.1 Zero Vibration Command Generation

The simplest way of driving a system with vibration is by using impulses: An impulse A_1 is first applied to the system which will not only start a motion, but also cause a vibration. However, instead of allowing the system to vibrate, we apply another impulse at an appropriate time which then cancel the vibration. The concept is illustrated in figure 7.8 with a undamped second order system with $\omega_n = 1$ rad/s.

For an under-damped linear second order system with the natural frequency ω_n and the damping ratio ζ, the response to a series of N impulses of amplitude A_i at time t_i for $i = 1 \ldots N$ can be described as a combination of a exponential decay term and a periodic term

$$y(t) = \sum_{i=1}^{N} B_i e^{-\zeta\omega_n t} \sin\left(\omega_d t + \varphi_i\right) \ , \tag{7.6}$$

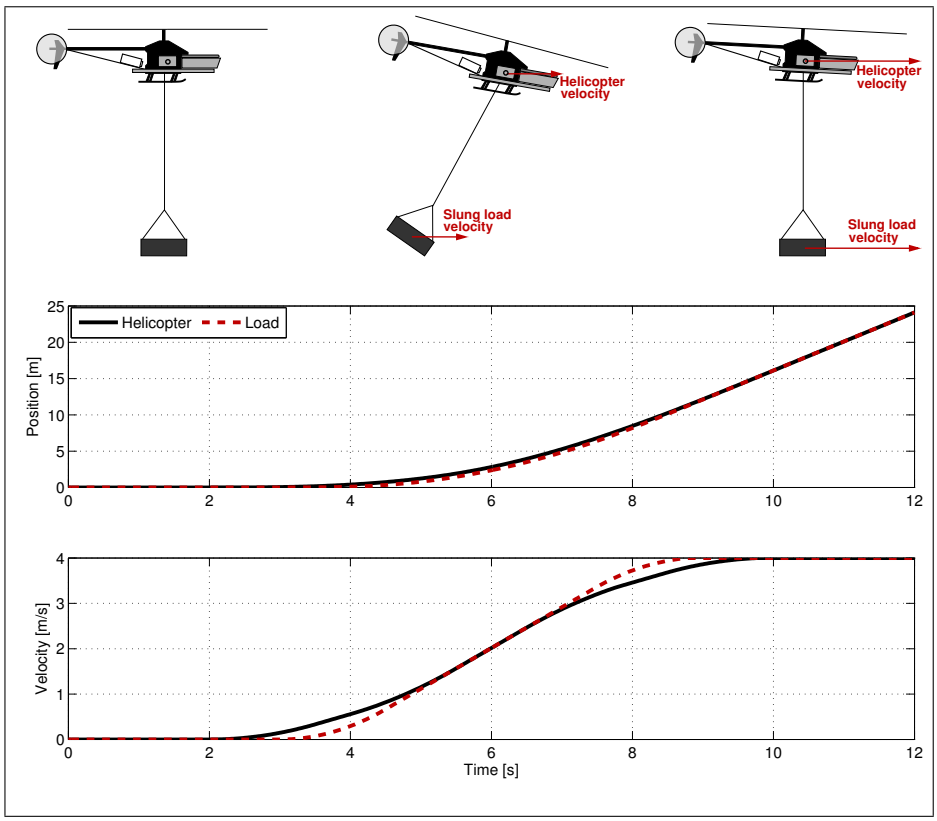

Figure 7.7: The concept of input shaping illustrated with helicopter slung load system oscillation free transition from hover to forward flight.

where

$$B_i = \frac{A_i \omega_n}{\sqrt{1-\zeta^2}} e^{-\zeta \omega_n t_i} \,, \tag{7.7}$$

$$\omega_d = \omega_n \sqrt{1-\zeta^2} \,, \tag{7.8}$$

$$\varphi_i = -\omega_n \sqrt{1-\zeta^2} t_i \,. \tag{7.9}$$

By using the trigonometric law of combining terms of equal frequency (from [Gieck and Gieck, 2006]), (7.6) can be written as

$$y(t) = B e^{-\zeta \omega_n t} \sin\left(\omega_d t + \varphi\right) \,, \tag{7.10}$$

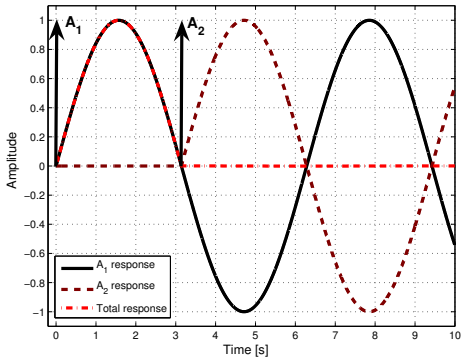

Figure 7.8: An undamped second order system driven by two impulses to achieve a zero vibration response.

where

$$B = \sqrt{\left(\sum_{i=1}^{N} B_i \cos(\varphi_i)\right)^2 + \left(\sum_{i=1}^{N} B_i \sin(\varphi_i)\right)^2}\,, \tag{7.11}$$

$$\varphi = \arctan\left(\frac{\sum_{i=1}^{N} B_i \cos(\varphi_i)}{\sum_{i=1}^{N} B_i \sin(\varphi_i)}\right)\,. \tag{7.12}$$

To evaluate the performance of applying a sequence of impulses to cancel vibration we define a non-dimensional residual vibration term as

$$\mathcal{V} = \frac{\text{Vibration amplitude cause by impulse sequence}}{\text{Vibration amplitude cause by unit impulse}} \tag{7.13}$$

and evaluate it at the time of last impulse in the sequence, which yields

$$\mathcal{V}(\omega_n, \zeta) = e^{\zeta\omega_n t_N}\sqrt{C(\omega_n,\zeta)^2 + S(\omega_n,\zeta)^2}\,, \tag{7.14}$$

where

$$C(\omega_n, \zeta) = \sum_{i=1}^{N} A_i e^{\zeta\omega_n t_i}\cos(\omega_d t_i)\,, \tag{7.15}$$

$$S(\omega_n, \zeta) = \sum_{i=1}^{N} A_i e^{\zeta\omega_n t_i}\sin(\omega_d t_i)\,. \tag{7.16}$$

To achieve a system response without residual vibration we must find the impulse series that satisfies $\mathcal{V} = 0$ in (7.14). A trivial solution is to use zero height impulses with will result in no residual vibration, but as this obviously does not enable us to drive the system, this solution must be avoided by constraining the solution with

$$\sum_{i=1}^{N} A_i = 1 \,. \tag{7.17}$$

This constraint also makes sure that a normalized output response is achieved, but a solution that satisfies (7.17) could very well contain large positive and negative impulses and still sum to one. In general it is desirable to keep the absolute values of the impulses as small as possible and therefore we chose to limit the solution to only positive impulses with the constraint

$$A_i > 0, \quad i = 1 \ldots N \,. \tag{7.18}$$

Different solutions with negative impulses are possible and are discussed in [Singhose, 1997], but for simplicity we restrict ourself to positive-only shapers. The problem is now to find the amplitudes and times of the impulse sequence by solving

$$\mathcal{V} = 0 \quad \text{subject to} \quad A_i > 0, \ \sum_{i=1}^{N} A_i = 1 \,. \tag{7.19}$$

The shortest possible shaper consists of two impulses which yields four unknowns: A_1, A_2, t_1, and t_2. However, it is not necessary to determine the specific time of both impulses, only the time difference between the two which can be achieved by using

$$t_1 = 0 \,, \tag{7.20}$$

and then finding t_2. To solve (7.19) means that (7.15) and (7.16) must be equal to zero independently which given (7.20) yields

$$0 = A_1 + A_2 e^{\zeta \omega_n t_2} \cos(\omega_d t_2) \,, \tag{7.21}$$

$$0 = A_2 e^{\zeta \omega_n t_2} \sin(\omega_d t_2) \,. \tag{7.22}$$

The solution to (7.22) with the shortest t_2 is

$$t_2 = \frac{\pi}{\omega_d} = \frac{T_d}{2} \,, \tag{7.23}$$

where T_d is the period of the damped oscillation. By substituting (7.17) and (7.23) into (7.21) we can arrive at

$$A_1 = \frac{1}{1+K} \,, \qquad K = \exp\left(\frac{-\zeta\pi}{\sqrt{1-\zeta^2}}\right) \,, \tag{7.24}$$

and by further substitution into (7.22) we get

$$A_2 = \frac{K}{1+K} \,. \tag{7.25}$$

By using (7.23), (7.24), and (7.25) the input shaper for the example system of figure 7.8 with $\omega_n = 1$ and $\zeta = 0$ is derived to

$$A_1 = 0.5 \,, \quad A_2 = 0.5 \,, \quad t_2 = \pi \,. \tag{7.26}$$

7.3.2 Robust Zero Vibration Command Generation

As illustrated earlier, the ZV shaper is capable of successfully avoiding any oscillation when the natural frequency and damping of the system oscillatory modes are known. However, in reality we never never have exact system knowledge which means that there will often be a discrepancy between the actual system and the system used for the shaper design. Such a case is illustrated in figure 7.9 where the system from figure 7.8 how has a 5% error in the frequency. It is clear that while the residual vibration is somewhat reduced

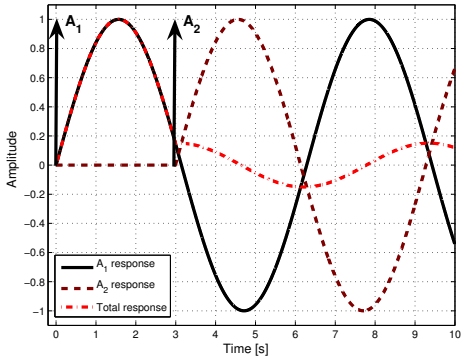

Figure 7.9: Response to ZV shaper with 5% frequency error.

there is still a significant amount of vibration left. One of the first to attend to this problem was [Singer, 1983] who proposed a method to add a robustness to the ZV shaper. This is done by adding the requirement that the derivative of the residual vibration with respect to the natural frequency and damping must be equal to zero

$$0 = \frac{d}{d\omega_n} \mathcal{V}(\omega_n, \zeta) \,, \tag{7.27}$$

$$0 = \frac{d}{d\zeta} \mathcal{V}(\omega_n, \zeta) \,. \tag{7.28}$$

In [Singer, 1983] it is shown that (7.27) and (7.28) combined can be reduced to

$$0 = \sum_{i=1}^{N} A_i t_i e^{\zeta \omega_n t_i} \cos(\omega_d t_i) \,, \tag{7.29}$$

$$0 = \sum_{i=1}^{N} A_i t_i e^{\zeta \omega_n t_i} \sin(\omega_d t_i) \,, \tag{7.30}$$

and by adding these two further constraints, another two variables are needed to find a solution. This is achieved by adding an additional impulse to the two impulse ZV input shaper, which yields the three impulse ZVD input shaper. This gives the 5 unknowns A_1, A_2, A_3, t_2, and t_3. t_1 can still be set to zero. For this three impulse case the following equations can be identified from (7.14) and (7.17)

$$0 = A_1 + A_2 e^{\zeta \omega_n t_2} \cos(\omega_d t_2) + A_3 e^{\zeta \omega_n t_3} \cos(\omega_d t_3) \,, \tag{7.31}$$

$$0 = A_2 e^{\zeta \omega_n t_2} \sin(\omega_d t_2) + A_3 e^{\zeta \omega_n t_3} \sin(\omega_d t_3) \,, \tag{7.32}$$

$$0 = A_2 t_2 e^{\zeta \omega_n t_2} \cos(\omega_d t_2) + A_3 t_3 e^{\zeta \omega_n t_3} \cos(\omega_d t_3) \,, \tag{7.33}$$

$$0 = A_2 t_2 e^{\zeta \omega_n t_2} \sin(\omega_d t_2) + A_3 t_3 e^{\zeta \omega_n t_3} \sin(\omega_d t_3) \,. \tag{7.34}$$

Given (7.18), the only solution to (7.32) is when the two sin terms are zero independently. This yields the following shortest time solution to the timing of the impulses

$$t_2 = \frac{T_d}{2} \,, \tag{7.35}$$

$$t_3 = T_d \,. \tag{7.36}$$

Given that the amplitude of the impulses can be found as

$$A_1 = \frac{1}{1 + 2K + K^2} \,, \tag{7.37}$$

$$A_2 = \frac{2K}{1 + 2K + K^2} \,, \tag{7.38}$$

$$A_3 = \frac{K^2}{1 + 2K + K^2} \,. \tag{7.39}$$

The ZVD input shaper for the example system of figure 7.8 can then be calculated as

$$A_1 = 0.25 \,, \quad A_2 = 0.5 \,, \quad A_3 = 0.25 \,, \quad t_2 = \pi \,, \quad t_3 = 2\pi \,, \tag{7.40}$$

and the result from using the ZVD shaper on the example, again with a model error, is shown in figure 7.10 The robustness of this shaper can be seen from figure 7.11 where the sensitivity curve for the ZV and ZVD shaper can be compared. The zero derivative constraint makes the slope of the ZVD shaper zero around the natural frequency and

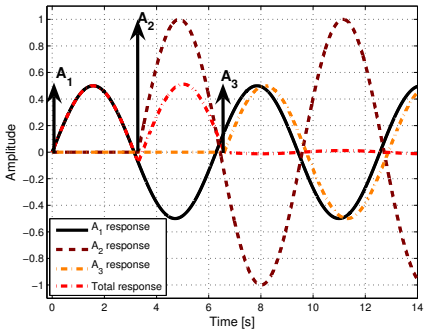

Figure 7.10: Response to ZVD shaper with 5% frequency error.

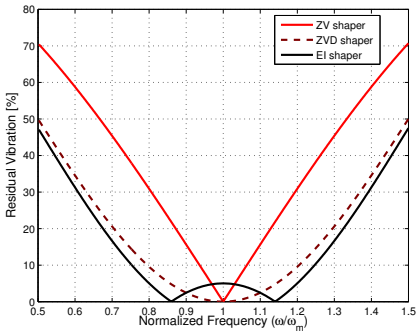

Figure 7.11: The sensitivity curves for the ZV, ZVD and EI input shapers.

thereby improving the robustness of the shaper to modeling errors. For further robustness the extra insensitive (EI) shaper was proposed by [Singhose and Seering, 1991] which is a ZVD shaper where the zero vibration constraint is relaxed. This means that instead of equating (7.14) to zero it is instead equated to a low, but non-zero value. The EI shaper shown in figure 7.11 is designed for 5% residual vibration. In [Singhose *et al.*, 1994] the analytical solution to the EI shaper is given as

$$A_1 = \frac{1+\mathcal{V}}{4}\,, \quad A_2 = \frac{1-\mathcal{V}}{2}\,, \quad A_3 = \frac{1+\mathcal{V}}{4}\,, \tag{7.41}$$

$$t_2 = \frac{T_d}{2}\,, \quad t_3 = T_d\,, \tag{7.42}$$

where $\mathcal{V}$ is the residual vibration limit. In figure 7.12 it is illustrated how robust the different shapers are to errors in damping and frequency.

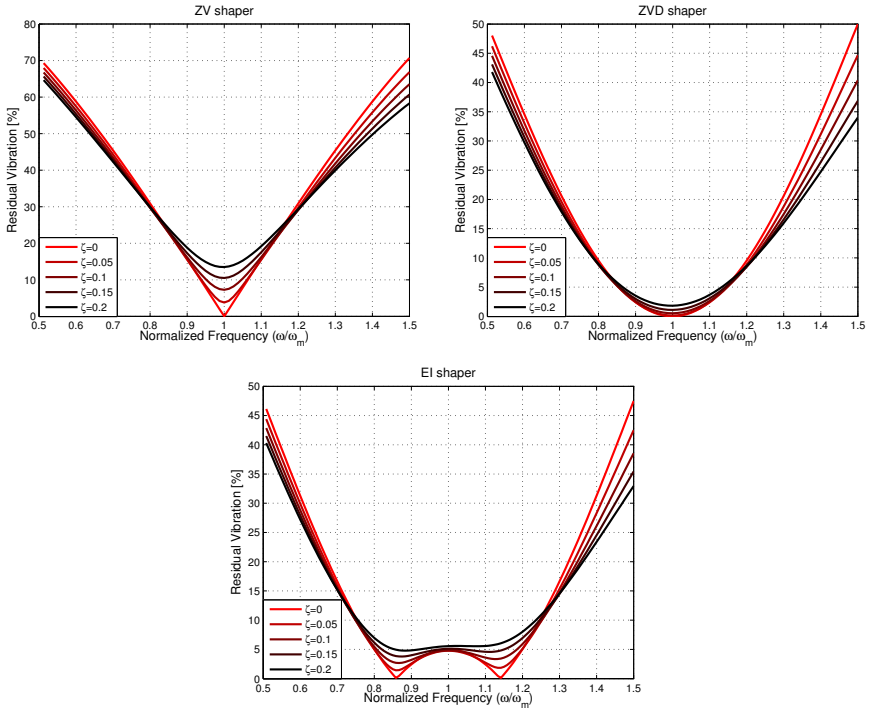

Figure 7.12: Robustness comparison for the ZV, ZVD, and EI shaper.

In [Bhat and Miu, 1991] and [Singhose, 1997] the input shapers are analyzed in the s-plane and it is found that the ZV shaper is equivalent to canceling the resonant poles with a zero for each. The more robust ZVD shaper is equivalent to canceling the poles with two zeros for each pole and thereby creating better damping around the location of zeros. The EI shaper places the two zeros close to the pole on each side of it and thereby trades damping with a perfect model fit for robustness.

Other approaches than impulse based input shapers like IIR and FIR filters have been tested in the literature, but in [Singhose *et al.*, 1995] a comparison between different input shapers conclude that for the same damping the impulse based shapers are the shortest and thereby give the fastest response time.

7.3.3 Real-Time Input Shaping

Input shaping is implemented by convolving a sequence of impulses with any desired command as

$$\overset{*}{\bar{C}}(t) = \mathcal{I} * \bar{C}(t)\,, \tag{7.43}$$

where $\bar{C}$ is the initial command, $\mathcal{I}$ is the input shaper, and $\overset{*}{\bar{C}}$ is the shaped command. By using a well designed input shaper, the system will respond to the shaped reference signal without vibration. An input shaper can therefore be used to filter the reference commands to the system such that, ideally, swing free motion of the slung load can be achieved.

However, there is a price to be paid for the reduced vibration that can be achieved by using the input shapers and especially the robust input shapers. When a command convolved with an input shaper, the duration of the command is extended with the length of the shaper as illustrated in figure 7.13. Therefore, we can generally say that a longer shaper yields a slower system response. However, this prolonged response time is most

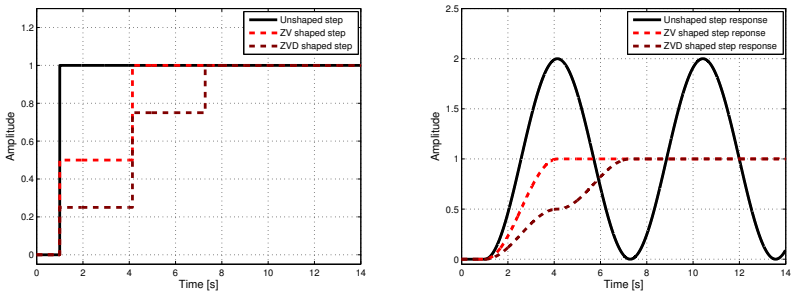

Figure 7.13: Left: A step input without shaping, with ZV and with ZVD shaping. Right: System response to the inputs.

significant for very short maneuver commands like a step. For a longer maneuvers like a flight trajectory for the helicopter slung load system, the additional response time added by the input shaper is insignificant.

7.3.4 Input Shaping for the Helicopter Slung Load

When using the input shaper technique to reduce excitation of this mode, we have the distinct advantage that we do not need to make any preflight tuning of the controller. In section 6.6 on page 149 we demonstrated how it is possible to get fast and accurate estimates of the natural frequency of the pendulum mode. This estimate can be used directly in the input shaper, but is important to remember that the estimate represent the

damped frequency of the system ω_d and provides no information on the damping ζ. The damping of the slung load motion will vary depending on the aerodynamic drag of the load and on the interaction with the helicopter. The latter depends both on suspension system parameters and helicopter parameters.

Given these uncertainties, a robust shaper seems like the better choice and from figure 7.12 we see that the ZVD shaper seems quite robust to uncertainties especially in the damping and we therefore chose to use this shaper.

For small slung load swing angles we can assume that the slung load is almost solely effected by horizontal helicopter motion. Therefore is is only necessary to apply the shaper to part of the reference trajectory. We define a reference trajectory for a helicopter controller to consist of

$$\bar{\boldsymbol{X}} = \begin{bmatrix} {}^{e}\bar{x} & {}^{e}\bar{y} & {}^{e}\bar{z} & {}^{e}\bar{\psi} & {}^{b}\bar{v}_x & {}^{b}\bar{v}_y & {}^{b}\bar{v}_z & {}^{b}\bar{\omega}_z \end{bmatrix}^T , \tag{7.44}$$

which is a full state vector for the helicopter with the roll and pitch motion neglected. This type of reference trajectory is consistent with the control setup used in [Johnson and Kannan, 2005]. However, depending on how the trajectory is calculated it can be necessary to apply the input shaper to the entire trajectory. For coordinated maneuvers it is necessary to apply the shaper to the entire trajectory vector to keep the synchronization between the different elements. If the input shaper is only applied to parts of the reference vector, these will be delayed compared to the remaining elements. Using (7.43) on (7.44) the shaped trajectory is calculated as

$$\overset{*}{\bar{\boldsymbol{X}}} = \mathcal{I}_{\text{ZVD}} * \bar{\boldsymbol{X}} . \tag{7.45}$$

Simulation: Rest-to-Rest Maneuver With and Without Input Shaper

To illustrate that the input shaper technique indeed works on the helicopter slung load system we first present a simulation of a rest to rest maneuver using a trajectory tracking helicopter controller. The maneuver is an aggressive step about 10 m forward done both without shaper and with a ZVD shaper. The shaper is placed between the trajectory planner and the actual controller and in this example the estimated wire length has already converged before the maneuver.

A view of the maneuver sequence with and without shaper is shown in figure 7.14 and we can observe how the shaper helps to remove almost all residual swing of the slung load after the step. On figure 7.15 the position and velocity of the helicopter and slung load are plotted together with the reference trajectory. There is no doubt that the ZVD shaper is capable of shaping the reference trajectory such that residual swing of the load is avoided almost completely. However, the cost of an additional maneuver time is also seen – for this short maneuver the rest to rest time is almost twice as long with the shaper compared to without.

When looking at figure 7.15 it would be natural to draw the conclusion that the better damping comes simply from the slower helicopter response. However, while slower

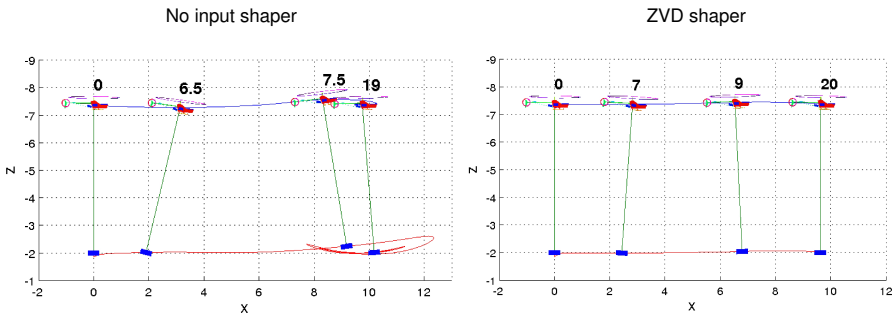

Figure 7.14: (Simulation) Comparison of helicopter slung load step maneuver, without and with input shaper. Sideview with time line plotted.

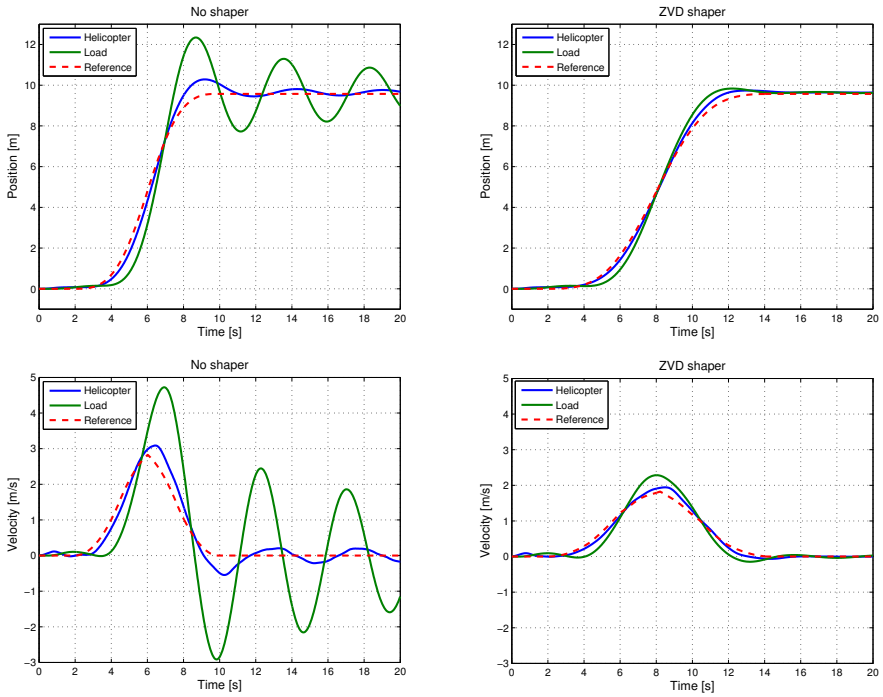

Figure 7.15: (Simulation) Position and velocity of helicopter and load plotted together with reference signal for step. Left: Without shaper. Right: With ZVD shaper.

helicopter motion potentially can result in oscillations with smaller amplitude, the input shaper ensures that almost all residual oscillations are removed. Furthermore, the input shaper works for all inputs, slow and fast, and the added maneuver time is the same for all inputs.

Simulation: Trajectory Flight With and Without Input Shaper

A longer maneuver is shown in figure 7.16 and 7.17 and it is clear that the input shaper is capable of reducing load swing for a more complicated maneuver than just a step. We

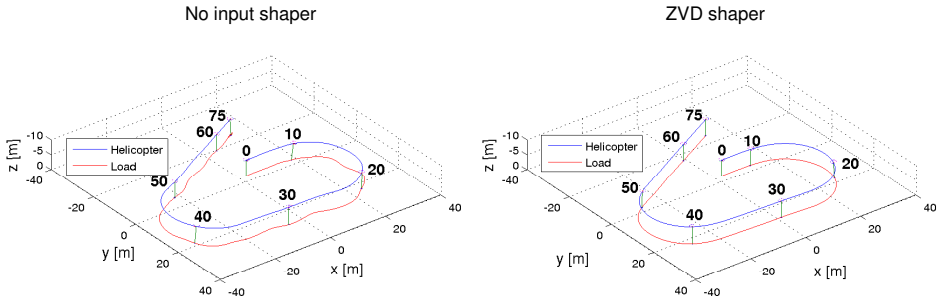

Figure 7.16: (Simulation) 3D plot of helicopter slung load for long maneuver, with and without input shaper.

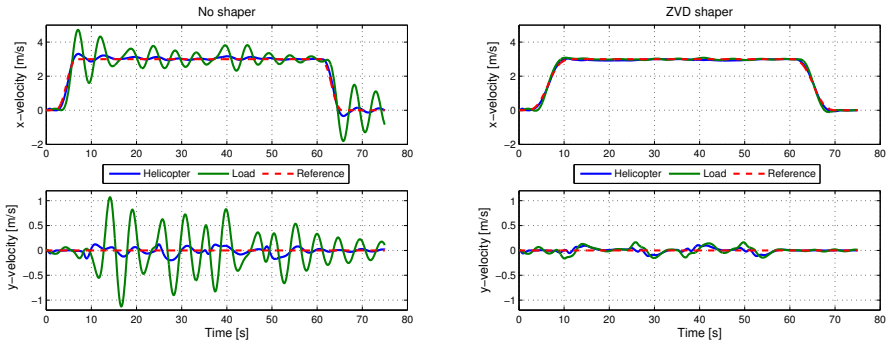

Figure 7.17: (Simulation) Velocity of helicopter and load plotted together with reference signal for long trajectory. Left: Without shaper. Right: With ZVD shaper. Note that velocity is given in helicopter body frame.

can also see that the input shaper results in a longer response time, but compared to the

unshaped maneuver the increase is small compared to the total maneuver time.

7.4 Feedback Swing Damping Control: Delayed Control

The idea behind the delayed controller is that by using intentionally delayed feedback it is possible to absorb vibrations in a oscillating system. Traditionally delay in feedback systems is considered problematic and causes deteriorating performance and even instability, but in this approach we use the delay to our advantage.

It was first suggested in [Olgac and Holm-Hansen, 1994] which consider vibration damping in structures where it was denoted "Delayed Resonator". The delayed resonator is designed as an oscillator with a natural frequency equal to that of the system and with an appropriate delay this can be fed to the system and cancel the system vibrations. In [Olgac *et al.*, 1996] the concept is extended to handle dual mode resonant systems. A comparison of the delayed resonator with a standard PD controller is made in [Elmali *et al.*, 2000] and it is concluded that a comparable performance can be achieved with the two. In [Masoud and Nayfeh, 2003] and [Masoud *et al.*, 2004] the delayed resonator is used to dampen swing in ship cranes. [Udwadia and Phohomsiri, 2005] extends the concept to consider both negative and positive feedback and applies it to vibration damping in structures.

A standard linear second order system is given by

$$\ddot{x}(t) + 2\omega_n\zeta\dot{x}(t) + \omega_n^2 x(t) = u(t)\,, \tag{7.46}$$

where ω_n is the natural frequency and ζ is the damping. We then use a proportional feedback of the time delayed state value

$$\ddot{x}(t) + 2\omega_n\zeta\dot{x}(t) + \omega_n^2 x(t) = G_d x(t-\tau_d)\,, \tag{7.47}$$

where design parameters of the controller are the gain G_d and the time delay τ_d. In the Laplace domain (7.47) becomes

$$x(s^2 + 2\omega_n\zeta s + \omega_n^2) = G_d e^{-\tau_d s}\,. \tag{7.48}$$

More or less complicated approaches have been suggested in the literature for analyzing the system and designing the controller, see e.g. [Masoud and Nayfeh, 2003]. However, we will here propose a simple approach and model the delay using a Padé approximant. A second order Padé approximant is given by

$$e^{-\tau_d s} = \frac{1 - \tau_d/2s + \tau_d^2/12s^2}{1 + \tau_d/2s + \tau_d^2/12s^2}\,, \tag{7.49}$$

and by using this approximation we can simply apply known linear system theory. The delayed feedback controller can then be modeled is state space form as

$$\boldsymbol{A}_C = \begin{bmatrix} -6/\tau_d & -12/\tau_d^2 \\ 1 & 0 \end{bmatrix}, \boldsymbol{B}_C = \begin{bmatrix} G_d \\ 0 \end{bmatrix}, \boldsymbol{C}_C = \begin{bmatrix} -12/\tau_d & 0 \end{bmatrix}, \boldsymbol{D}_C = 1\,.$$

7.4.1 Designing the Delayed Feedback Controller

The purpose of the controller is to damp the pendulous modes of the slung load within the limits of the helicopter performance. The design of the controller can then be formulated as finding the controller parameter set (G_d, τ_d) that achieves the maximum damping of the pendulous modes while maintaining satisfactory helicopter behavior.

The linear system

$$\boldsymbol{H} = \begin{cases} \dot{\boldsymbol{x}} & = \boldsymbol{A}\boldsymbol{x} + \boldsymbol{B}\boldsymbol{u} \\ \boldsymbol{y} & = \boldsymbol{C}\boldsymbol{x} + \boldsymbol{D}\boldsymbol{u} \end{cases}, \tag{7.50}$$

where $\boldsymbol{x} \in \mathbb{R}^n$ is the state vector, $\boldsymbol{u} \in \mathbb{R}^m$ is the input vector, and $\boldsymbol{y} \in \mathbb{R}^p$ is the output vector, is the positive feedback close loop system

$$\boldsymbol{H} = \frac{\boldsymbol{P}}{1 - \boldsymbol{P}\boldsymbol{C}}, \tag{7.51}$$

of the plant ($\boldsymbol{P}$) and the delayed feedback controller ($\boldsymbol{C}$) as shown in figure 7.18. For this

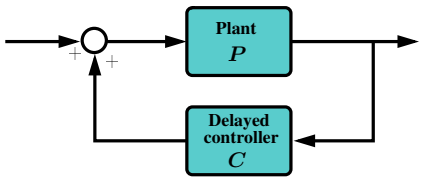

Figure 7.18: Delayed feedback control scheme.

system the eigenvalues are give by

$$(\boldsymbol{A} - \boldsymbol{\lambda}\boldsymbol{I})\boldsymbol{x} = 0\,, \tag{7.52}$$

where $\boldsymbol{\lambda} \in \mathbb{C}^n$ is the vector of eigenvalues with a corresponding vector $\boldsymbol{\zeta} \in \mathbb{R}^n$ of dampings. The damping $\zeta_i \in \boldsymbol{\zeta}$ of the i'th eigenvalue $\lambda_i \in \boldsymbol{\lambda}$ can be found as

$$\zeta_i = \frac{\mathrm{Re}(\lambda_i)}{\omega_{ni}}, \tag{7.53}$$

where

$$\omega_{ni} = |\lambda_i|\,. \tag{7.54}$$

We then define the controller design as by finding the set of control parameters that yields the minimum of the largest eigenvalue damping

$$\underset{(G_d,\tau_d)}{\arg\min} \; \max_i \zeta_i\,. \tag{7.55}$$

Given this formulation the process of designing the controller can be completely automated using optimizations tools.

7.4.2 Cart/Pendulum Example: Delayed Feedback

To exemplify the controller strategy we design a delayed feedback controller to dampen oscillation in the cart/pendulum system described in example 7.2.1 on page 172. A PD-type controller

$$F = P_c(x_r - x) + D_c(\dot{x}_r - \dot{x}) \,, \tag{7.56}$$

is used to control the cart and we assume that the controller is sufficiently good at tracking the references such that the cart dynamics can be neglected. Parameters are selected to P_c = 180 and D_c = 30. Thereby the pendulum model can be described by a linear second order system from cart position to pendulum angle

$$\frac{\theta}{x} = \frac{-\frac{1}{g}s^2}{s^2 + \frac{g}{l}} \,. \tag{7.57}$$

We define the delayed feedback controller as

$$x_r(t) = G_d l \sin(\theta(t - \tau_d)) \,, \tag{7.58}$$

which is equivalent to feedback from the relative position between cart and pendulum given by $l\sin(\theta)$. This actually means that the controller gain G_d can be seen as normalized with respect to the pendulum length. Differentiating (7.58) yields

$$\dot{x}_r(t) = G_d l \cos(\theta(t - \tau_d))\dot{\theta}(t - \tau_d) \,, \tag{7.59}$$

which is necessary as (7.56) requires both position and velocity reference input. Furthermore, we define the controller delay as normalized with respect to the pendulum oscillation period T_n

$$\tau_d = T_n \tau_n \,, \tag{7.60}$$

where

$$T_n = 2\pi\sqrt{\frac{l}{g}} \,. \tag{7.61}$$

That both controller parameters are defined as normalized to the pendulum length means that we can design the controller for one pendulum length and when the length is changed, the controller is redesigned accordingly in a automated way. Thereby, the same oscillation damping is achieved for any pendulum length.

The control parameters are found by solving (7.55), which corresponds to finding the maximum in figure 7.19. This figure shows a map of the system most resonant pole damping as a function of controller parameters. The design process returns the following

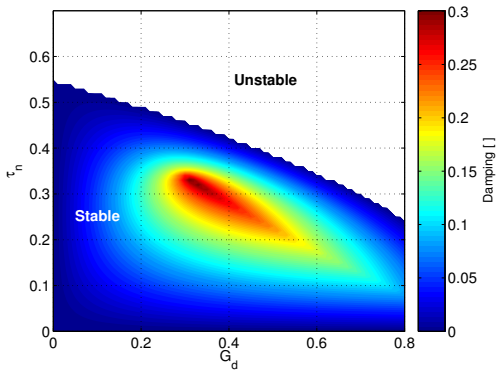

Figure 7.19: Cart/pendulum example. Damping of the system as a function of delayed feedback controller parameters.

control parameters

$$G_d = 0.325\,, \qquad \tau_n = 0.325\,. \tag{7.62}$$

A simulation of the system is shown in figure 7.20 where the pendulum is started at 0.1 rad. The delayed feedback controller is enabled at t=10 s and quickly dampens out the pendulum swing. We can see how the PD controller suppresses the influence of the

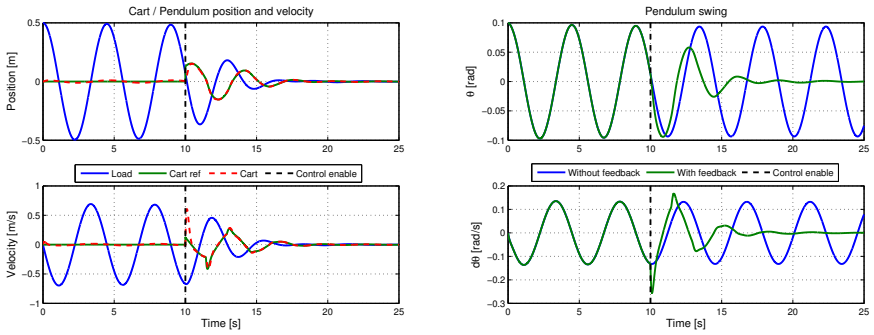

Figure 7.20: Cart/pendulum example. Left: Cart and pendulum load position and velocity plotted with delayed feedback controller output. Right: Pendulum swing angles with and without feedback controller.

pendulum swing on the cart and is doing a good job at tracking the cart references commanded by the delayed feedback controller. The poles of the system are shown in figure

7.21 and for the nominal setup (l =5 m) we can see how the design approach has placed the both close loop poles on the same damping line. We can also see that if the pendulum

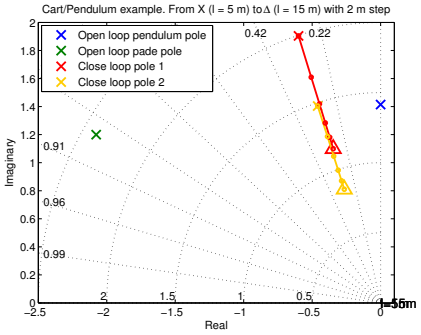

Figure 7.21: Cart/pendulum example. Pole map of open and close system. Shown is open loop Padé approximate pole, open loop pendulum system pole, and close loop poles plotted as a function of changing pendulum length (from X where $l = 5$ m to $\triangle$ where $l = 15$ m with 2 m steps).

length is changed, the controller is automatically scaled accordingly, damping is maintain, and only the frequency of the poles change. However, this only works when the actuator system, in this case the cart, is sufficiently fast to be neglected. If the actuator dynamics are too slow it will interfere with the pendulum and Padé dynamics. This means that the actuator must be included in the design of the controller and the actuator poles will interfere with how the poles move along the damping lines as the pendulum length is changed.

7.4.3 Delayed Feedback for Helicopter Slung Load System

The delayed feedback control is well suited for oscillation damping in complex systems like the helicopter slung load system as it allows to account directly for possible delays in the signal loop. It is important to realize that this control scheme can not be used for stabilizing the helicopter or to track trajectories, but simply to dampen load swing. Therefore an inner loop controller for the helicopter is assumed as illustrated in figure 7.1.

The helicopter slung load system is very similar in structure to the cart/pendulum example from section 7.2.1 and 7.4.2 and we can indeed use the same approach to construct the controller. The feedback variables in the helicopter slung load system is the relative position of the helicopter and the slung load x_δ and y_δ (see figure 7.22). The output of the controller is added to the existing reference to the inner loop helicopter controller as

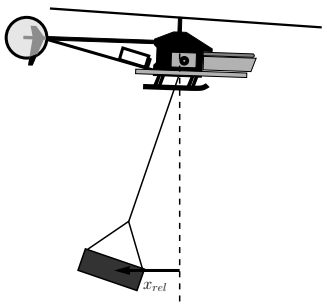

Figure 7.22: Relative position between helicopter and slung load.

illustrated in figure 7.1

$$\tilde{x}_r = x_r + G_d x_\delta(t-\tau)\,, \tag{7.63}$$
$$\tilde{y}_r = y_r + G_d y_\delta(t-\tau)\,. \tag{7.64}$$

The relative position of the load can be found given (6.41) and through a simple approximation (7.63) and (7.64) becomes

$$\tilde{x}_r = x_r + G_d l \sin(\theta_w(t-\tau))\,, \tag{7.65}$$
$$\tilde{y}_r = y_r + G_d l \sin(\phi_w(t-\tau))\,. \tag{7.66}$$

Given a full reference trajectory like (7.44) the velocity reference elements are found as time derivatives of (7.65) and (7.66)

$$\dot{\tilde{x}}_r = \dot{x}_r + G_d l \cos(\theta_w(t-\tau_d))\dot{\theta}_w(t-\tau)\,, \tag{7.67}$$
$$\dot{\tilde{y}}_r = \dot{y}_r + G_d l \cos(\phi_w(t-\tau_d))\dot{\phi}_w(t-\tau)\,. \tag{7.68}$$

For a system as a slung load it should be possible to take advantage of the previously mentioned fact that the controller can be automatically redesigned given the plant natural frequency, which for the slung load system means the suspension wire length. This information is given by the estimator as mentioned in section 6.6 on page 149. However, in contrast to the cart/pendulum example, the actuator dynamics (the helicopter) are so slow that they needs to be incorporated in the controller design. This disturbs the effect of the pendulum poles moving along a damping line with changing wire length. Depending on the exact interaction between the poles this means that the achieved damping deteriorates as the system moves away from the design point. However, given that we know the parameter that changes we can easily achieve a similar effect with a gain scheduling approach.

Design for AAU Bergen Twin

Using the methods of chapter 5 on page 103 we extract a linear model of the helicopter and by applying the helicopter controller we arrive at the actuator dynamics that can be included in the design method described in section 7.4.1. Design is done using the nominal single wire slung load setup with wire length of l = 4 m. The damping for the longitudinal and lateral systems are shown in figure 7.23 It can be seen how the interaction

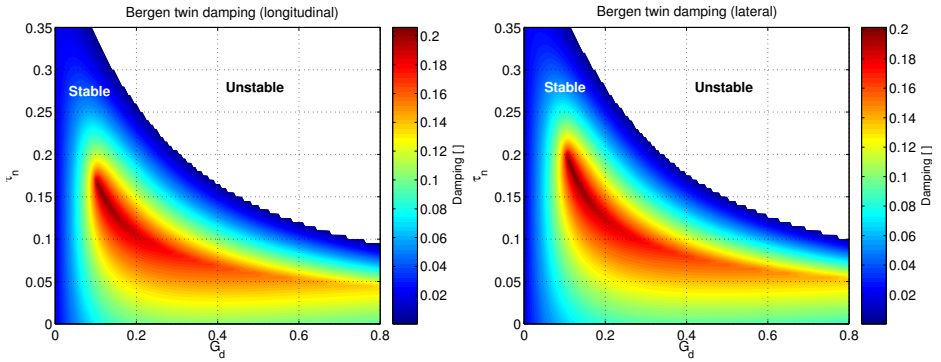

Figure 7.23: AAU Bergen Twin design. Damping of the lateral and longitudinal helicopter slung load system as a function of delayed feedback controller parameters.

of helicopter dynamics significantly have altered the damping map compared to the clean pendulum system shown in figure 7.19. The controller parameters can be identified as

$$G_{d,lon} = 0.10\,, \tau_{n,lon} = 0.17\,,$$
$$G_{d,lat} = 0.11\,, \tau_{n,lat} = 0.19\,.$$

Here a potential robustness problem of the design method shows up. The method arrives at the set of control parameters that yields the maximum damping and for the cart/pendulum example shown in figure 7.19 this seems like a good choice as damping map is reasonably flat around the maximum damping. However, for helicopter design we can see from figure 7.23 that the interplay of the helicopter dynamics has resulted in a more steep damping map and that small changes for example in controller parameters can degrade the achieved damping significantly. The issue is illustrated in figure 7.24 where the achieved damping is shown as a function of errors in the pendulum frequency and damping used for the design. The problem can be attended to by adding a constraint to the minimization of (7.55) that enforces a certain flatness around the selected point by looking at the gradient of the damping map. The desired value of flatness would then become a tuning parameter.

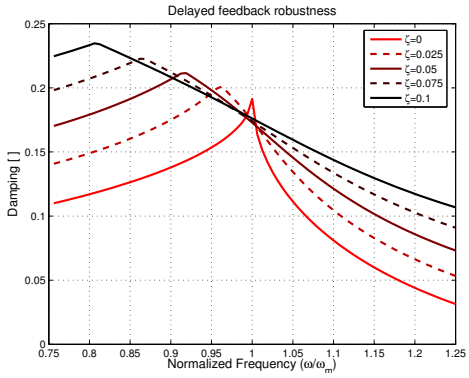

Figure 7.24: Robustness of the designed delayed feedback controller. Shown is achieved damping as a function of error in modeled damping and frequency.

Design for Georgia Tech GTMax

The GTMax features an adaptive loop shaping controller as described in [Johnson and Kannan, 2005] which yields the following translational responses

$$\begin{aligned} \frac{x}{x_r} &= \frac{K_{xp}s^2 + K_{xp}R_{xd}s + K_{xp}R_{xp}}{s^4 + K_{xd}s^3 + K_{xp}s^2 + K_{xp}R_{xd}s + K_{xp}R_{xp}} \,, \\ \frac{y}{y_r} &= \frac{K_{yp}s^2 + K_{yp}R_{yd}s + K_{yp}R_{yp}}{s^4 + K_{yd}s^3 + K_{yp}s^2 + K_{yp}R_{yd}s + K_{yp}R_{yp}} \,, \end{aligned} \tag{7.69}$$

where $K_{xp} = 37.5$, $K_{xd} = 10$, $R_{xp} = 1.04$, $R_{xd} = 1.66$, $K_{yp} = 24$, $K_{yd} = 8$, $R_{yd} = 0.66$, and $R_{yd} = 1.33$ are helicopter controller parameters. The damping map is shown in figure 7.25 and the delayed controller parameters can be identified as

$$\begin{aligned} G_{d,lon} &= 0.16 \,, \tau_{n,lon} = 0.22 \,, \\ G_{d,lat} &= 0.17 \,, \tau_{n,lat} = 0.16 \,. \end{aligned} \tag{7.70}$$

7.5 Simulation of Swing Damping Control

Here we combine the feedforward and feedback slung load controller to avoid introducing while also actively removing slung load oscillations and thereby forms the swing damping control scheme. The AAU Bergen Twin with the single wire slung load is used and the test starts in hover with significant initial load swing. The maneuver is defined as a set of flight conditions with aggressive changes between them. The resulting trajectories with

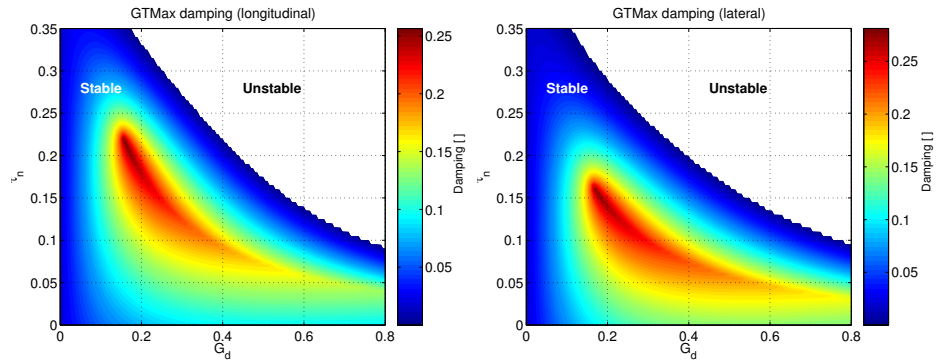

Figure 7.25: GTMax design. Damping of the lateral and longitudinal helicopter slung load system as a function of delayed feedback controller parameters.

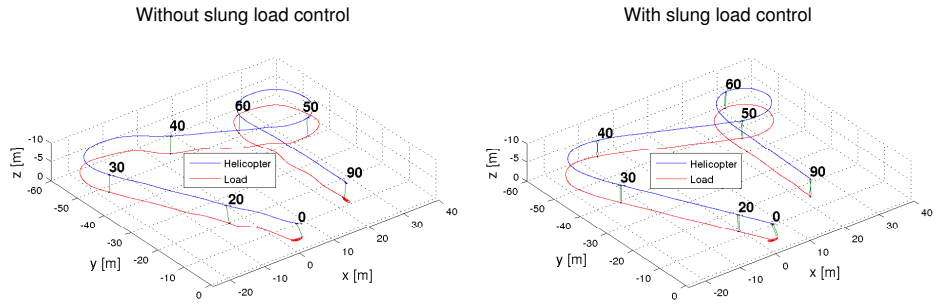

Figure 7.26: (Simulation) 3D plot of helicopter slung load flight with and without swing damping control system.

and without slung load controllers are shown in figure 7.26 and 7.27. We can observe how the slung load trajectory is much more smooth with the swing damping control scheme enable, but we can also see how the use of the slung load controller has changed the actual trajectory somewhat. The reason for this is twofold: As the trajectory is specified as velocities the use of the input shaper will change the actual trajectory slightly, but the feedback controller also changes the helicopter trajectory. When flying in a circle, the slung load swings out due to centrifugal effects which gives a constant lateral slung load angle. The controller defined by (7.66) will then yield a constant lateral displacement in the helicopter trajectory. The same can be observed in figure 7.28 where the helicopter and slung load positions are shown and we can see how the helicopter tracks a trajectory slightly offset from the reference trajectory. This problem will be discussed in further

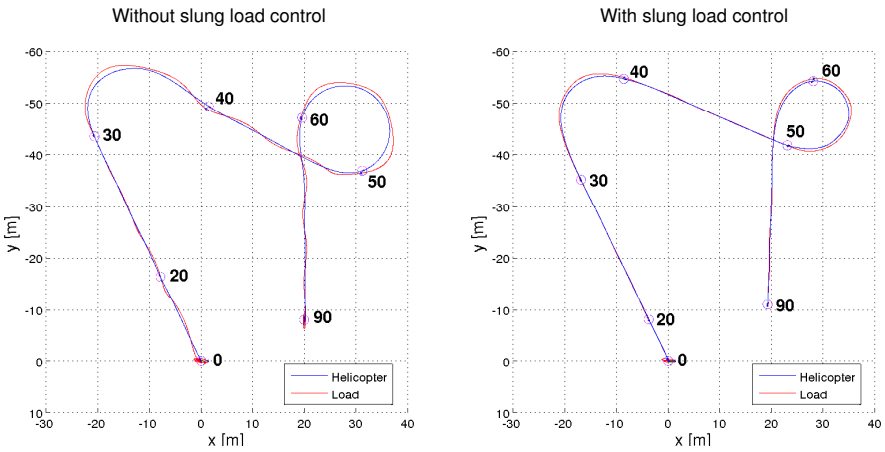

Figure 7.27: (Simulation) Top view of helicopter slung load flight with and without swing damping control system.

detail in chapter 8 in connection with trajectory generation for slung load systems. The

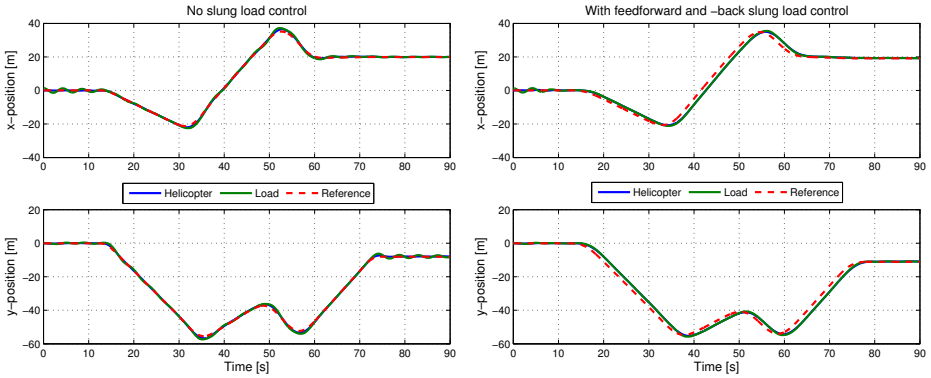

Figure 7.28: (Simulation) Positions of helicopter and load plotted together with reference signal. Left: Without swing damping control. Right: With swing damping control.

delayed feedback controller is enabled after 4 s and as can be seen from the velocities in figure 7.29 it quickly dampens out the initial swing. After that no significant load swing can be observed when using the swing damping control scheme, which is in sharp contrast to the results without.

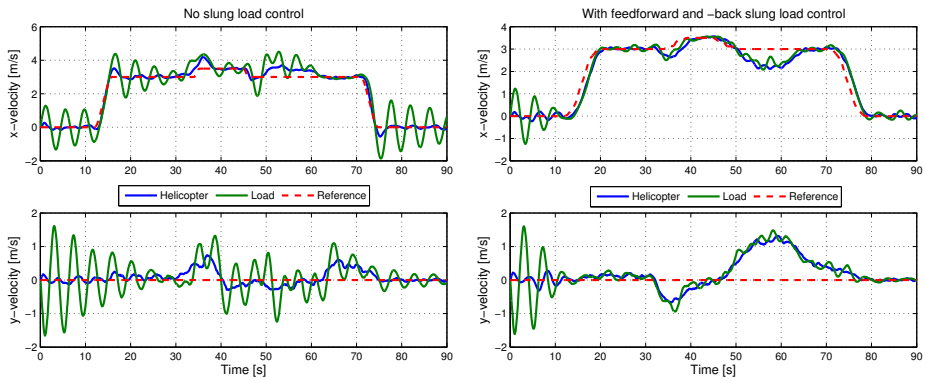

Figure 7.29: (Simulation) Velocity of helicopter and load plotted together with reference signal. Left: Without swing damping control. Right: With swing damping control. Note that velocities are given in helicopter body frame.

7.6 Verification of Swing Damping Control

To verify the design and performance of the swing damping control scheme, flight tests has been carried out with the input shaper and with the delayed feedback controller. It has not been possible within the time frame of this research to acquire data from a flight using both the feedforward and feedback controller. Both test platforms described in chapter 2 are used for these tests.

7.6.1 Verification of Input Shaper

To verify the input shaping concept, two different flight test has been carried out using the AAU Bergen Twin with the single wire slung load: One without and one with a ZVD input shaper. In figure 7.30 a left and right 10 m lateral step without any input shaping is shown and we can see how the helicopter motion causes the slung load to swing significantly. Positions and velocities are shown in figure 7.31 where the residual slung load swing can also clearly be observed.

In figure 7.32 two similar 10 m steps are shown, but this time with a ZVD input shaper applied to the reference before feeding it to the helicopter controller. We can see how there is a significant reduction in the residual slung load swing compared to the steps without the input shaper. In fact, due to the input shaper, the step maneuvers causes no additional oscillation in the slung load which can be seen from figure 7.33 where helicopter and slung load position and velocity are shown. Both the shaped and unshaped reference command are shown and by comparing the two we can see the additional maneuver time introduced by the input shaper.

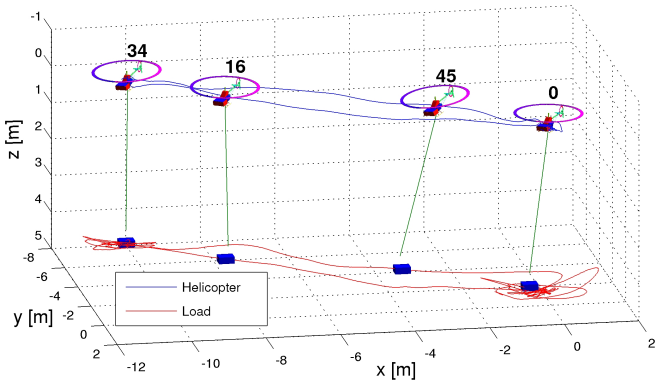

Figure 7.30: (Flight) 3D plot of left and right 10 m lateral step without input shaping.

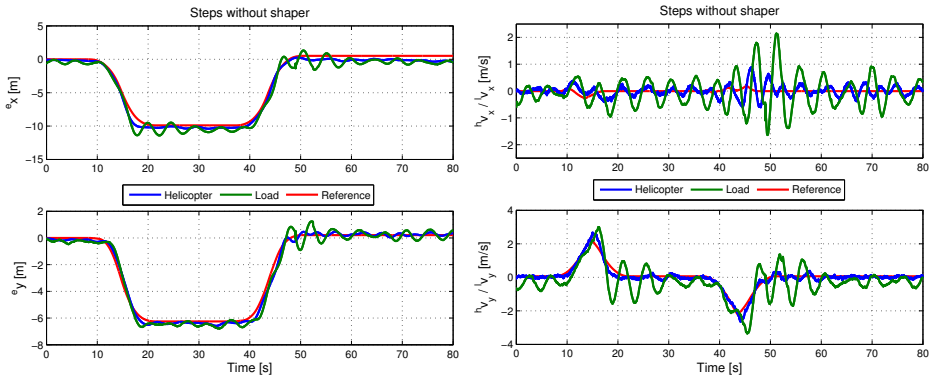

Figure 7.31: (Flight) Steps without input shaping. Left: Helicopter and slung load position and controller position reference. Right: Helicopter and slung load velocity and controller velocity reference.

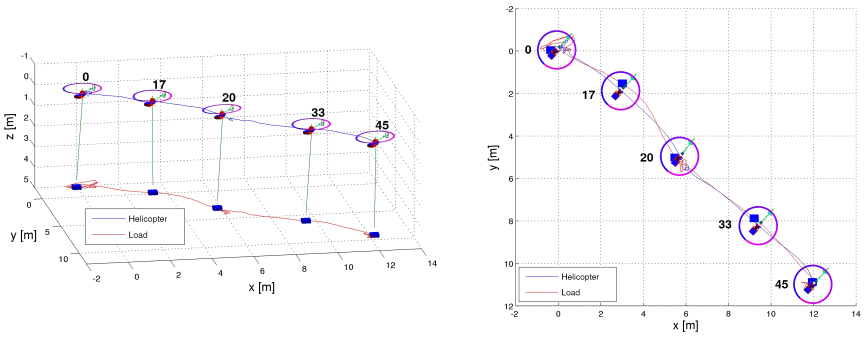

Figure 7.32: (Flight) 3D plot of two right 10 m lateral steps with ZVD input shaper.

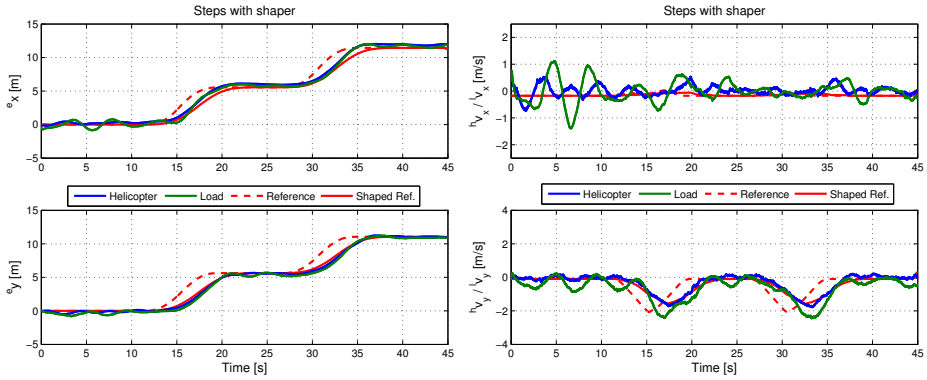

Figure 7.33: (Flight) Steps with ZVD input shaper. Left: Helicopter and slung load position and controller position reference. Right: Helicopter and slung load velocity and controller velocity reference.

7.6.2 Verification of Delayed Feedback

The verification flights for the delayed feedback concept has been carried out using the GTMax and slung load described in section 2.2 on page 33. The delayed feedback controller used for these tests is a detuned version of the design presented earlier in this chapter. The test controller parameters yields a theoretical ζ of 0.19 in both lateral and longitudinal.

A 30 ft ($\simeq$ 9 m) aggressive lateral step without slung load control is shown in figure 7.34 and again it is clear that such a maneuver causes significant slung load swing. The same can be seen on the position and velocity plots in figure 7.35.

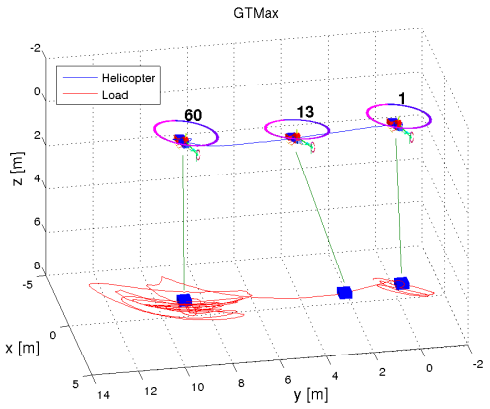

Figure 7.34: (Flight) GTMax without slung load control. 3D plot of aggressive 9 m lateral step.

Figure 7.36 shows two steps similar to the step shown in figure 7.34, but this time with the delayed feedback slung load controller enabled. In figure 7.37 positions and velocities of the maneuver are shown. We can see that the step maneuvers still excite the pendulous modes which result in an overshot of the slung load. As the slung load controller attempts to dampen out these oscillations, this results in an overshot of the helicopter as it tries to move with the slung load motion as described in section 7.2. After a couple of full slung load oscillations, the controller has successfully dampened out the swing. A comparison of slung load angles during the two right steps, with and without slung load controller is shown in figure 7.38 and we can see a significant swing reduction with the slung load controller enabled.

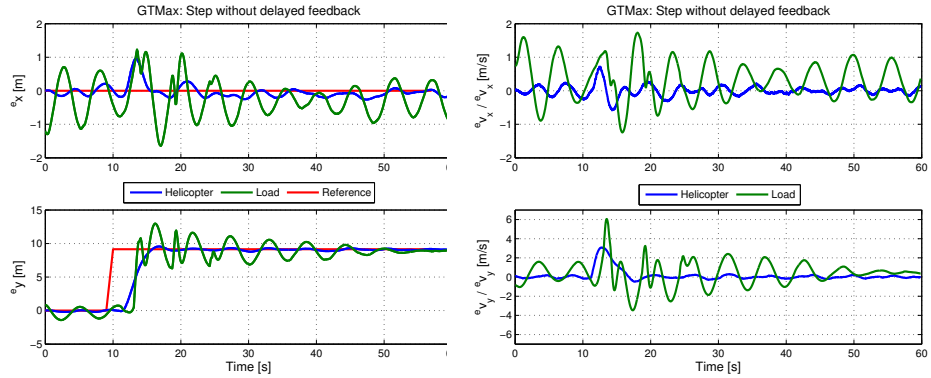

Figure 7.35: (Flight) GTMax without slung load control. Left: Helicopter and slung load position and controller position reference. Right: Helicopter and slung load velocity and controller velocity reference.

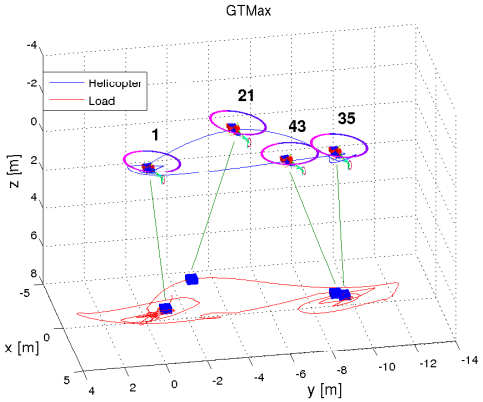

Figure 7.36: (Flight) GTMax with delayed feedback slung load control. 3D plot of two aggressive 9 m lateral steps.

7.7 Swing Damping Control Summary and Discussion

In this chapter a swing damping control scheme was developed to improve slung load flight in autonomous helicopters. It is designed to operate with the reduced state estimator developed in chapter 6 and to augment helicopter stand alone controllers. A feedforward control scheme based on input shaping was design to shape trajectories to the system in such a way that ideally excitation of slung load swing through maneuvering is avoided.

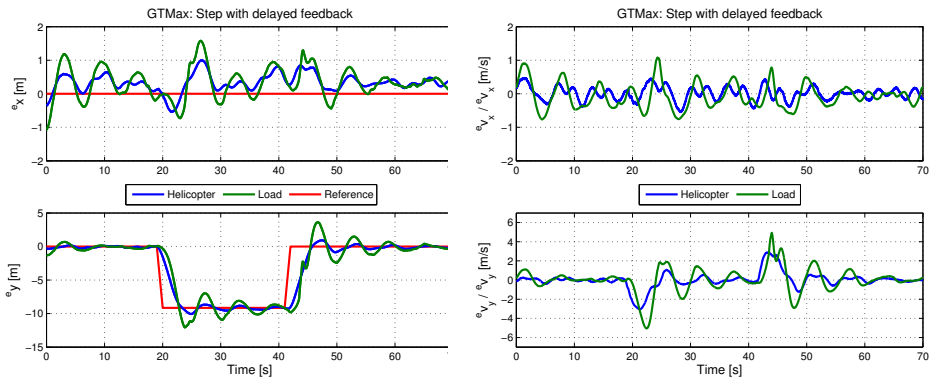

Figure 7.37: (Flight) GTMax with delayed feedback slung load control. Left: Helicopter and slung load position and controller position reference. Right: Helicopter and slung load velocity and controller velocity reference.

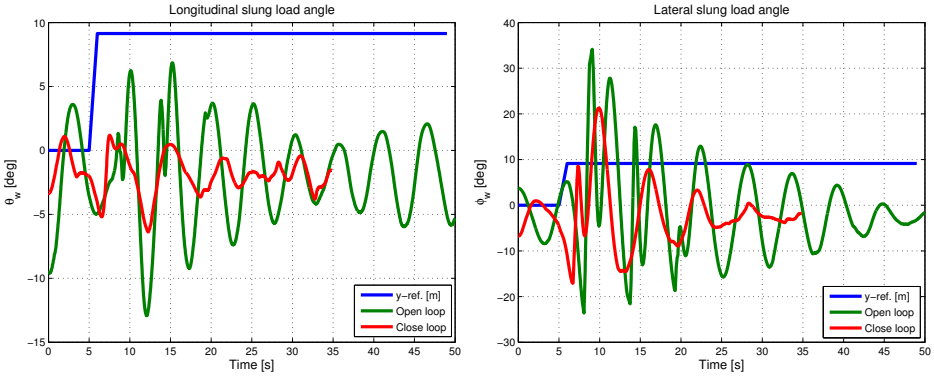

Figure 7.38: (Flight) Comparison of lateral step with and without delayed feedback slung load controller. Left: Longitudinal slung load angle. Right: Lateral slung load angle.

A feedback control scheme based on delayed feedback was designed to actively dampen out slung swing and when using both simultaneously, virtually swing free slung load flight can be achieved. The performance of the control scheme was evaluated through simulation and flight testing and it was found that the control scheme is capable of yielding a significant reduction in slung load swing over flight without the controller scheme.

The input shaping can be robustified against errors in system damping and oscillation frequency through sacrifice of system response time. For the delayed feedback controller

the robustness qualities are more modest and while a robustifying modification to the design method is proposed in this chapter, further attention to this issue is recommended. Furthermore, while the input shaper can be redesigned automatically with changing wire lengths, the slow helicopter dynamics interfere with the scaling of the delayed feedback controller. It was suggested to use a set of controllers and schedule them as a function of the wire length, and while this is a simple and effective approach, a more rigorous treatment of this issues would be beneficial. A different approach could be to do an online design of the delayed feedback controller by a gradient based optimization of the controller parameter map which will ensure an optimum damping at all time.

Both the feedforward and the feedback ultimately alters the trajectory of the helicopter to avoid and dampen load swing and depending on the application these changes could in some cases be unacceptable. A possibility for improvement on the design method could therefore be to integrate a design factor that directly allows a weighting between trajectory changes and slung load swing level.

Chapter 8

Trajectory Tracking Slung Load Control

In this chapter a trajectory tracking control system for the helicopter slung load system is designed. First an optimal state feedback controller is designed and it is shown how the controller can stabilize the system. Next a trajectory mapping scheme is developed that is capable of expanding desired slung load trajectories to the entire system. Finally the performance of the controller is tested through simulation.

8.1 Introduction

The purpose of this chapter is to design a control system capable of trajectory tracking for the full helicopter slung load system with the mine detection application introduced in chapter 1 specifically in mind. This means stabilization and tracking of spatial trajectories at low speeds primarily with yaw-coupled suspension systems using the output of the full state estimator presented in chapter 6. The control design is divided into two parts: A linear controller is designed that allows the system to track trajectories and a trajectory mapping scheme is introduced that for a given desired slung load trajectory can generate a full system trajectory. The control architecture is shown in figure 8.1.

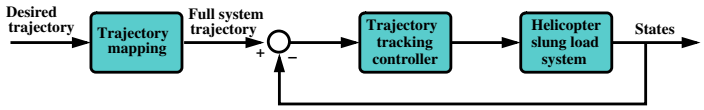

Figure 8.1: Architectural overview of the trajectory tracking slung load control scheme.

8.2 Optimal State Feedback Helicopter Slung Load Control

Given that the requirements specify slow close to hover flight, a linear hover control scheme should suffice for the desired flight envelope and we will here apply linear quadratic regulation (LQR) to the helicopter slung load system. LQR has been widely used for hover control of helicopter UAVs in the literature (see for instance [McLeana and Matsuda, 1998], [Jiang *et al.*, 2006], and [Cowling *et al.*, 2006]) and examples of LQR slung load control can be found in [Gupta and Bryson, 1976] and [Rodriguez and Athans, 1986]. If high speed flight should be required the hover controller can be extended to a wide range of flight conditions using gain scheduling.

8.2.1 Linear Quadratic Regulation

The discrete time linear system with the state vector $\boldsymbol{x}_s \in \mathbb{R}^n$ is described by

$$\boldsymbol{x}_s(k+1) = \boldsymbol{\Phi}_s \boldsymbol{x}_s(k) + \boldsymbol{\Gamma}_s \boldsymbol{u} \,, \tag{8.1}$$

where $\boldsymbol{u} \in \mathbb{R}^m$ is the input vector, $\boldsymbol{\Phi}_s \in \mathbb{R}^{n \times n}$ is the system matrix, and $\boldsymbol{\Gamma}_s \in \mathbb{R}^{n \times m}$ is the input matrix. The design process then consist of finding the feedback controller $\boldsymbol{L}_c \in \mathbb{R}^{m \times n}$ applied as

$$\boldsymbol{u}(k) = -\boldsymbol{L}_s \boldsymbol{e}(k) \,, \tag{8.2}$$

which stabilizes the plant and forces the error state vector $\boldsymbol{e} \in \mathbb{R}^n$ to zero. The error state vector is given as

$$\boldsymbol{e}(k) = \boldsymbol{x}_s(k) - \bar{\boldsymbol{x}}(k) \,. \tag{8.3}$$

where $\bar{\boldsymbol{x}} \in \mathbb{R}^n$ is the reference state vector. To suppress steady state errors (8.2) is augmented with integral action

$$\boldsymbol{u}(k) = -\boldsymbol{L}_s \boldsymbol{e}(k) - \boldsymbol{L}_i \boldsymbol{e}_i(k) \,. \tag{8.4}$$

The integral error state $\boldsymbol{e}_i \in \mathbb{R}^p$ is given as

$$\boldsymbol{e}_i(k+1) = \boldsymbol{H}_i \boldsymbol{e}(k) + \boldsymbol{e}_i(k) \tag{8.5}$$

where $\boldsymbol{H}_i \in \mathbb{R}^{p \times n}$ maps the states to the p integral states.

The optimal control law is then defined as the u that minimizes the following quadratic cost function

$$\mathcal{J} = \sum_{k=0}^{\infty} \left(\boldsymbol{e}^T(k) \boldsymbol{Q}_e \boldsymbol{e}(k) + \boldsymbol{e}_i^T(k) \boldsymbol{Q}_i \boldsymbol{e}_i(k) + \boldsymbol{u}^T(k) \boldsymbol{Q}_u \boldsymbol{u}(k) \right) , \tag{8.6}$$

where $\boldsymbol{Q}_e \in \mathbb{R}^{n \times n}$ is the error weight, $\boldsymbol{Q}_u \in \mathbb{R}^{m \times m}$ is the input weight, and $\boldsymbol{Q}_i \in \mathbb{R}^{p \times p}$ is the integral error weight.

8.2.2 Helicopter Slung Load Optimal Control

For any given suspension system linear models can be extracted using the methods presented in chapter 5 and used for the controller design. As described in chapter 6 only the rigid body states can reliably be estimated and the linear system used for the controller design therefore uses steady state solutions for flapping. The consequence of this is that the resonant helicopter short period modes that have a strong coupling to the flapping modes, especially the stabilizer bar, are not accurately represented in the rigid body linear model. This is important to be aware of when tuning the controller as it affects the system performance by limiting the achievable system bandwidth. Therefore, for the helicopter slung load system the input and the state vector is given by

$$\boldsymbol{u} = \begin{bmatrix} \theta_{\text{col}} \\ \theta_{\text{lat}} \\ \theta_{\text{lon}} \\ \omega_{\text{tail}} \end{bmatrix}_{4\times 1}, \quad \boldsymbol{x} = \begin{bmatrix} {}^{e}\boldsymbol{R}_{h} \\ {}^{e}\boldsymbol{\theta}_{h} \\ {}^{e}\boldsymbol{R}_{l} \\ {}^{e}\boldsymbol{\theta}_{l} \\ {}^{h}\boldsymbol{v}_{h} \\ {}^{h}\boldsymbol{\omega}_{h} \\ {}^{l}\boldsymbol{v}_{l} \\ {}^{l}\boldsymbol{\omega}_{l} \end{bmatrix}_{24\times 1}, \tag{8.7}$$

where the set of 24 states is a redundant representation of the constrained helicopter slung load system. For suspension system with yaw coupling the integral states are defined as

$$\boldsymbol{x}_i = \begin{bmatrix} {}^{e}\boldsymbol{R}_{l} \\ {}^{e}\boldsymbol{\psi}_{l} \end{bmatrix}_{4\times 1}. \tag{8.8}$$

For a system without yaw coupling the load yaw angle is replaced with helicopter yaw

$$\boldsymbol{x}_i = \begin{bmatrix} {}^{e}\boldsymbol{R}_{l} \\ {}^{e}\boldsymbol{\psi}_{h} \end{bmatrix}_{4\times 1}. \tag{8.9}$$

The linear model with the state vector (8.7) used for the controller design represent the system in trim in a hover flight condition. However, as positions and Euler angles are included in the state vector, a flight condition is no longer adequately represented by a speed, a flight plane angle, a sideslip angle, and a yaw angular velocity, as it was presented in section 5.2 on page 111. A yaw angle dependency is introduced by the transformation matrix between velocities and positions (see figure 4.4 on page 78), which means that a linear model represents a certain yaw angle. To handle arbitrary yaw angles, the controller

gain is mapped to follow the helicopter rotation as

$$\boldsymbol{L}_c^*(1:2,1:2) = \begin{bmatrix} \cos(-{}^e\psi_h) & \sin(-{}^e\psi_h) \\ -\sin(-{}^e\psi_h) & \cos(-{}^e\psi_h) \end{bmatrix} \boldsymbol{L}_c(1:2,1:2)\,, \tag{8.10}$$

$$\boldsymbol{L}_c^*(7:8,7:8) = \begin{bmatrix} \cos(-{}^e\psi_l) & \sin(-{}^e\psi_l) \\ -\sin(-{}^e\psi_l) & \cos(-{}^e\psi_l) \end{bmatrix} \boldsymbol{L}_c(7:8,7:8)\,, \tag{8.11}$$

$$\boldsymbol{L}_i^*(1:2,1:2) = \begin{bmatrix} \cos(-{}^e\psi_l) & \sin(-{}^e\psi_l) \\ -\sin(-{}^e\psi_l) & \cos(-{}^e\psi_l) \end{bmatrix} \boldsymbol{L}_i(1:2,1:2)\,. \tag{8.12}$$

The controller is tuned through the choice of the weighing matrices $\boldsymbol{Q}_e$, $\boldsymbol{Q}_u$, and $\boldsymbol{Q}_i$. Low gains are chosen for the slung load attitude state as these are only weakly controllable, while high gains are used for the slung load lateral and longitudinal states to dampen oscillation and ensure good tracking capabilities. When designing for a suspension system without yaw coupling, like the single wire slung load, the slung load attitude states are completely neglected such that the feedback from these becomes zero. This is equivalent to considering the slung load as a point mass.

Numerical Considerations

The fact that the nonlinear model describes the system using redundant coordinates has the effect that in the linear model there are multiple system modes representing the same dynamics depending on the chosen suspension system. For instance with the dual wire suspension system (see figure 4.1 (b) on page 70) the two wires couple the pitch and altitude dynamics of the helicopter and slung load. The consequence of this is that these multiple modes are ill-conditioned, which from a control theory point of view means that while the modes are controllable, they are not independently controllable: We cannot control one mode without controlling another.

This can be examined with the eigenvalue condition number κ_{λ_i} defined as [Moler, 2006]

$$\kappa_{\lambda_i} = \frac{\|\boldsymbol{w}_i\|\|\boldsymbol{v}_i\|}{\boldsymbol{w}_i^T\boldsymbol{v}_i} \tag{8.13}$$

where $\boldsymbol{v}_i \in \mathbb{C}^{n\times 1}$ is the right eigenvector and $\boldsymbol{w}_i \in \mathbb{C}^{1\times n}$ is the left eigenvector corresponding to the eigenvalue λ_i. Note that the condition number ranges from one to infinity and that a high condition number corresponds to an ill-conditioned mode. For a high condition number, the left and right eigenvectors are close to orthogonal and thereby linear independent. The ill-conditioned modes are very sensitive to small perturbations in the system and this results in problems when finding the optimal control law through optimization of (8.6).

The solution to this problem is to extract the linear system model with the numerical correction system (introduced in section 4.7.2 on page 100) enabled. This system places a spring and damper in parallel with each wire and while the input-output response of

the system is the same, it introduce a set of new modes into the system. These can be viewed as representing elastic wire modes and replace the ill-conditioned redundant coupled modes. Thereby we have achieve a well-conditioned system without changing the overall behavior of the system.

Simulation: Stabilization of Dual Wire Helicopter Slung Load system

In this simulated example the ability of the controller to stabilize the system is illustrated. The AAU Bergen Twin with the dual wire slung load is used as a test vehicle. The system is started in a off-trim situation with a lateral, longitudinal, and yaw offset on the slung load as shown in figure 8.2. The helicopter and slung load lateral and longitudinal

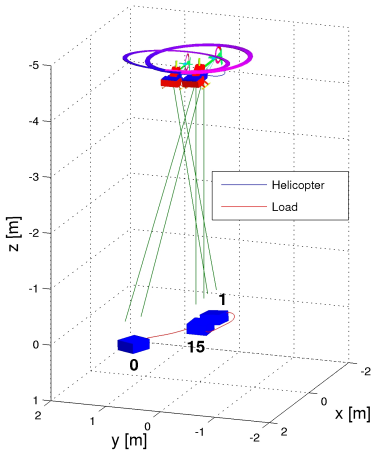

Figure 8.2: (Simulation) 3D plot of controller stabilization test.

positions are shown in figure 8.3. We can see that initially the slung load has a position offset in both directions and how the controller moves the helicopter out towards the slung load to counteract the offset and dampen oscillations. Figure 8.4 to the left shows how also the yaw angle offset and subsequent oscillations are suppressed. The controller effort as actuator signals is shown to the right in figure 8.4 together with saturation limits for cyclic pitch. This short simulation shows that the controller is capable of converging the system to a stable hover from an off-trim starting point.

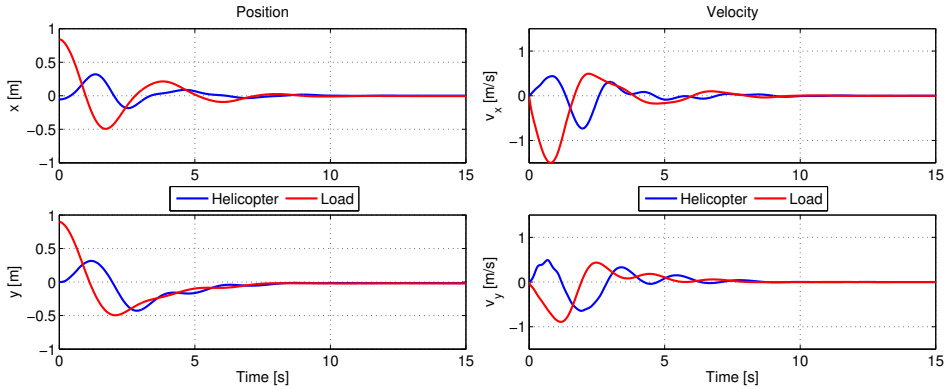

Figure 8.3: (Simulation). Helicopter and slung load longitudinal and lateral positions and velocities for the controller stabilization test.

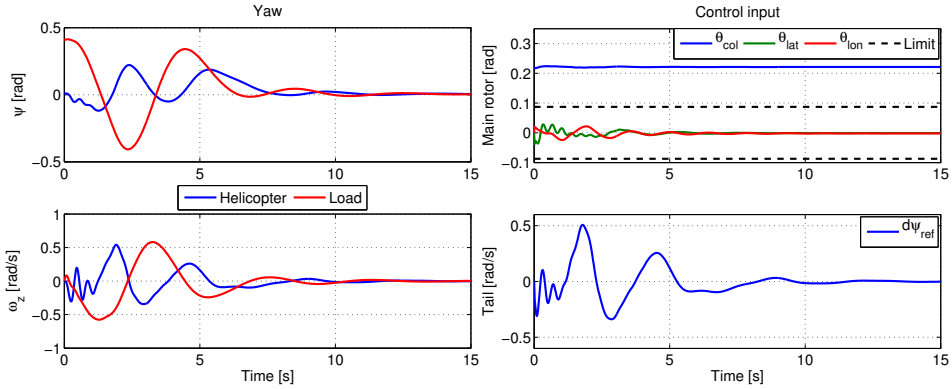

Figure 8.4: (Simulation). Controller stabilization test. Left: Helicopter and slung load yaw angle and rate. Right: Actuator signals generated by the controller.

8.3 Helicopter Slung Load Trajectories

The problem of generating trajectories for UAVs has been the subject of substantial research in the past years and a wide range of solutions to waypoint tracking, path planning, and obstacle avoidance have been presented. Many, like [Shim *et al.*, 2003], and [Inanc *et al.*, 2004], consider the need to plan trajectories in an environment with obstacles and different approaches to this have been suggested, ranging from Lyapounov functions in [Emilio Frazzoli, 2000] to potential fields in [Sigurd and How, 2003], and evolutionary al-

gorithms in [Rubio *et al.*, 2004]. In this research we will not focus on the actual trajectory generation for the helicopter slung load system, but instead on how to map an existing trajectory to the system.

8.3.1 Trajectory Mapping for Helicopter Slung Load System

The task here is to, given a desired slung load trajectory, calculate the corresponding feasible helicopter trajectory such that a full state reference trajectory is available for the controller. This means that we assume that a slung load velocity trajectory $\bar{\boldsymbol{\xi}}_l \in \mathbb{R}^4$ is given and that this trajectory is feasible such that tracking it is possible given the dynamics and saturations of the system. The trajectory is defined as

$$\bar{\boldsymbol{\xi}}_l = \begin{bmatrix} {}^l\bar{\boldsymbol{v}}_l \\ {}_e\bar{\dot{\boldsymbol{\psi}}}_l \end{bmatrix} , \tag{8.14}$$

calculated on the basis of a flight condition as described in (5.7) - (5.9) on page 112. The mapping of the reference trajectory into the slung load state space is defined as

$${}^l\bar{\dot{\boldsymbol{q}}}_l = \begin{bmatrix} 1 & 0 & 0 & 0 \\ 0 & 1 & 0 & 0 \\ 0 & 0 & 1 & 0 \\ 0 & 0 & 0 & 0 \\ 0 & 0 & 0 & 0 \\ 0 & 0 & 0 & 1 \end{bmatrix} \bar{\boldsymbol{\xi}}_l , \tag{8.15}$$

as we assume zero roll and pitch angles for the trajectory tracking problem which means that $\boldsymbol{T}_{\theta l}$ is a unity matrix.

When considering the particular problem of generating feasible trajectories for helicopters carrying slung loads, we must take into account some issues that are not applicable on normal UAVs. It is necessary to considered both kinematic and dynamic behavior of the system when mapping the slung load motion to the helicopter.

Dynamic Mapping

For velocity changes in the slung load trajectory, a map of corresponding helicopter accelerations must be found. If the system is in hover the correct way of transitioning into forward flight is: First the helicopter starts to accelerate forward and it flies in front of the slung load. This accelerates the slung load forward which shortly after catches up with the helicopter. The helicopter accelerates again and a smooth transition from hover to forward flight has been achieved. By examining this process we can identify that the behavior corresponds to that given by input shaping introduced in section 7.3 (see figure 7.7 on page 175). In fact by filtering the slung load trajectory through a ZV shaper, tuned to the pendulum oscillation period, a helicopter trajectory that allows for the dynamics of

the pendulum modes is achieved. However, for the slung load trajectory to fit to the generated helicopter trajectory it must be delayed with exactly half the length of the shaper, which is illustrated in figure 8.5. Should this time delay of the trajectory be unacceptable,

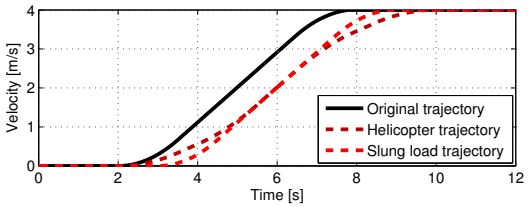

Figure 8.5: Dynamic mapping of trajectory.

it is possible to compensate by ”speeding up” the trajectory such that the system arrives at the required place at the required time. However, this must be done with consideration of the system dynamics such that the constraints of the system are not violated.

It is important to realize that the dynamic mapping achieved by the input shaper is only approximate as it is only applied to the lateral and longitudinal parts of the trajectories. Thereby an error arises on the distance between helicopter and load during the dynamics mapping, but the error is small for feasible trajectories and insignificant for the controller performance.

Kinematic Mapping

Another effect to consider is the swing out of the slung load during turns. This occurs when the helicopter is flying in a circle and the centrifugal force makes the slung load swing out in a larger circle as shown in figure 8.6. The radius of the slung load circle is given by

$$r_l = \frac{V_l}{\dot{\psi}_l} \,. \tag{8.16}$$

The swing out angle is given by the relationship between the centrifugal acceleration and the gravity and can then be calculated as

$$\nu = \arctan\left(\frac{a_{cf}}{g}\right) = \arctan\left(\frac{V_l \dot{\psi}_l}{g}\right) \,. \tag{8.17}$$

The difference in radius on the slung load circle and the helicopter circle is

$$\delta r = \sin(\nu) l \tag{8.18}$$

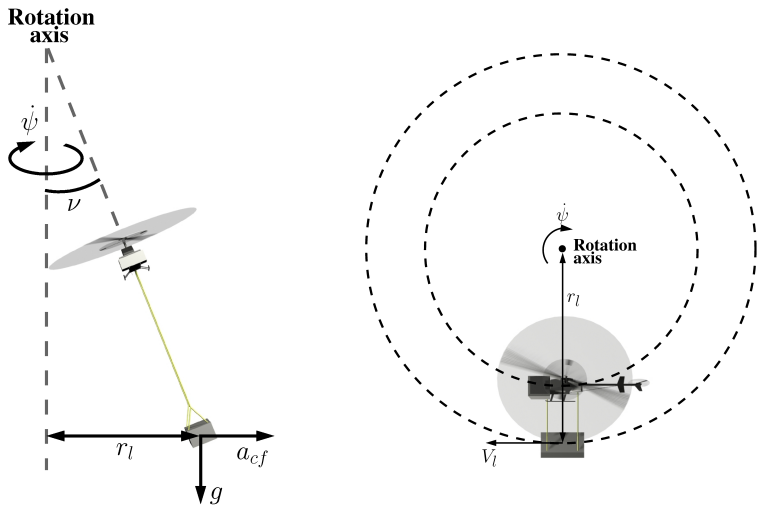

Figure 8.6: Illustration of the swing-out effect in circular flight with a helicopter slung load system.

where l is the length of the slung load suspension system. The position of the helicopter relative to the slung load can then be calculated as

$$\delta x = -\sin(\psi_l - \gamma_w)\delta r \,, \tag{8.19}$$
$$\delta y = \cos(\psi_l - \gamma_w)\delta r \,, \tag{8.20}$$
$$\delta z = -\cos(\nu) l \,. \tag{8.21}$$

Velocities can be found as time derivative of the positions.

The flow of the trajectory mapping is illustrated in figure 8.7.

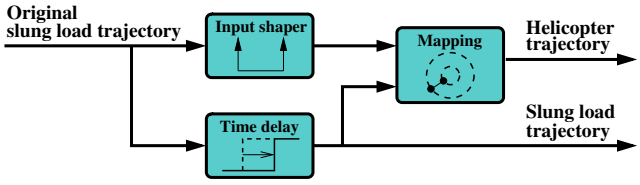

Figure 8.7: The mapping of trajectory to feasible helicopter and slung load trajectories.

Simulation: Slung Load Trajectory Mapping

To illustrate that the trajectory mapping an example is given here. The test trajectory is shown in figure 8.8 starts in hover, transitions into forward flight, makes a full left circle, goes straight, makes a 180° turn, and ends in hover. It can be seen how the helicopter trajectory turns in circles with a smaller radius that the slung load. It should also be noticed that the original trajectory is unchanged except for a time delay. The velocities

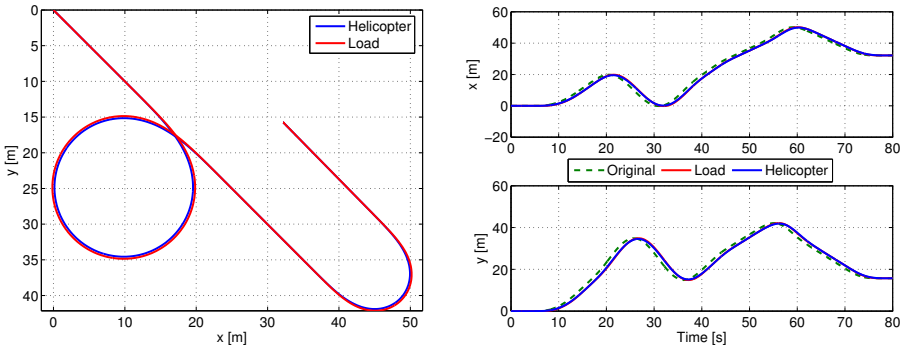

Figure 8.8: Trajectory mapping of position. Original trajectory plotted together with mapped trajectories.

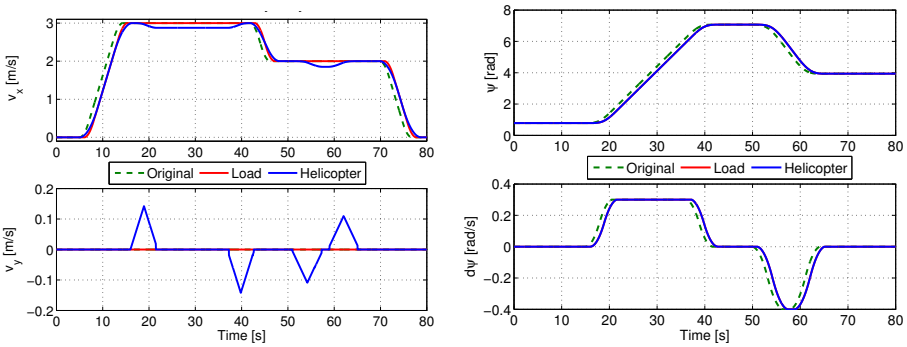

Figure 8.9: Trajectory mapping of velocity and heading. Original trajectory plotted together with mapped trajectories.

are show in figure 8.9 and we can see how the dynamic mapping has altered the original trajectory during velocity changes and how the kinematic mapping has altered it during the turns.

8.4 Simulation of Trajectory Tracking Slung Load Control

To illustrate the performance of the trajectory tracking controller we here present two difference simulation of the AAU Bergen Twin with the dual wire slung load. First one following the trajectory define in the previous example and then one that simulates a mine detection scenario. The simulations are done with the estimator in the loop as sensor noise and estimation errors have a significant effect on controller performance. Therefore, helicopter and slung load states shown in this example are estimated values and not true states. External wind modeled as a constant vector with sinusoids and random walks added is included in the simulations.

8.4.1 Simulation of Trajectory Tracking

In figure 8.10 and 8.11 a 3D and a topview plot of the helicopter and slung load are shown and we can see how the system seems capable of tracking the specified trajectory.

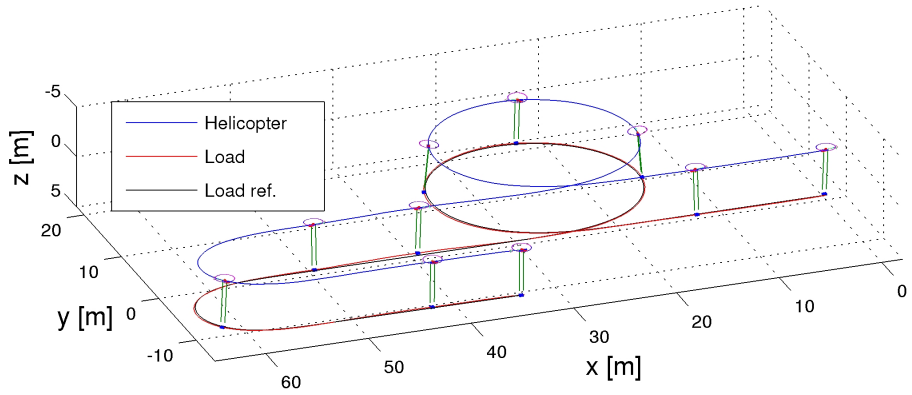

Figure 8.10: (Simulation) 3D plot of AAU Bergen Twin with dual wire slung load doing trajectory tracking.

Estimated states are shown together with references in figure 8.12 and we can see how the controller is tracking all references satisfactorily. The kinematic mapping is lowering the helicopter forward velocity reference when turning which otherwise would have resulted in a constant error during the turn.

For at close look at the controller performance, the error state vector and the integral error states are shown in figure 8.13. We can see how the controller is very good at

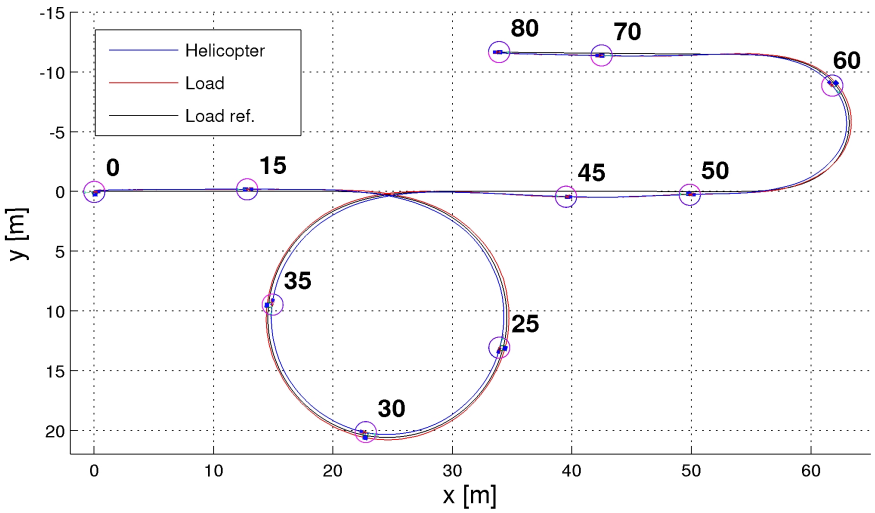

Figure 8.11: (Simulation) Topview plot of AAU Bergen Twin with dual wire slung load doing trajectory tracking.

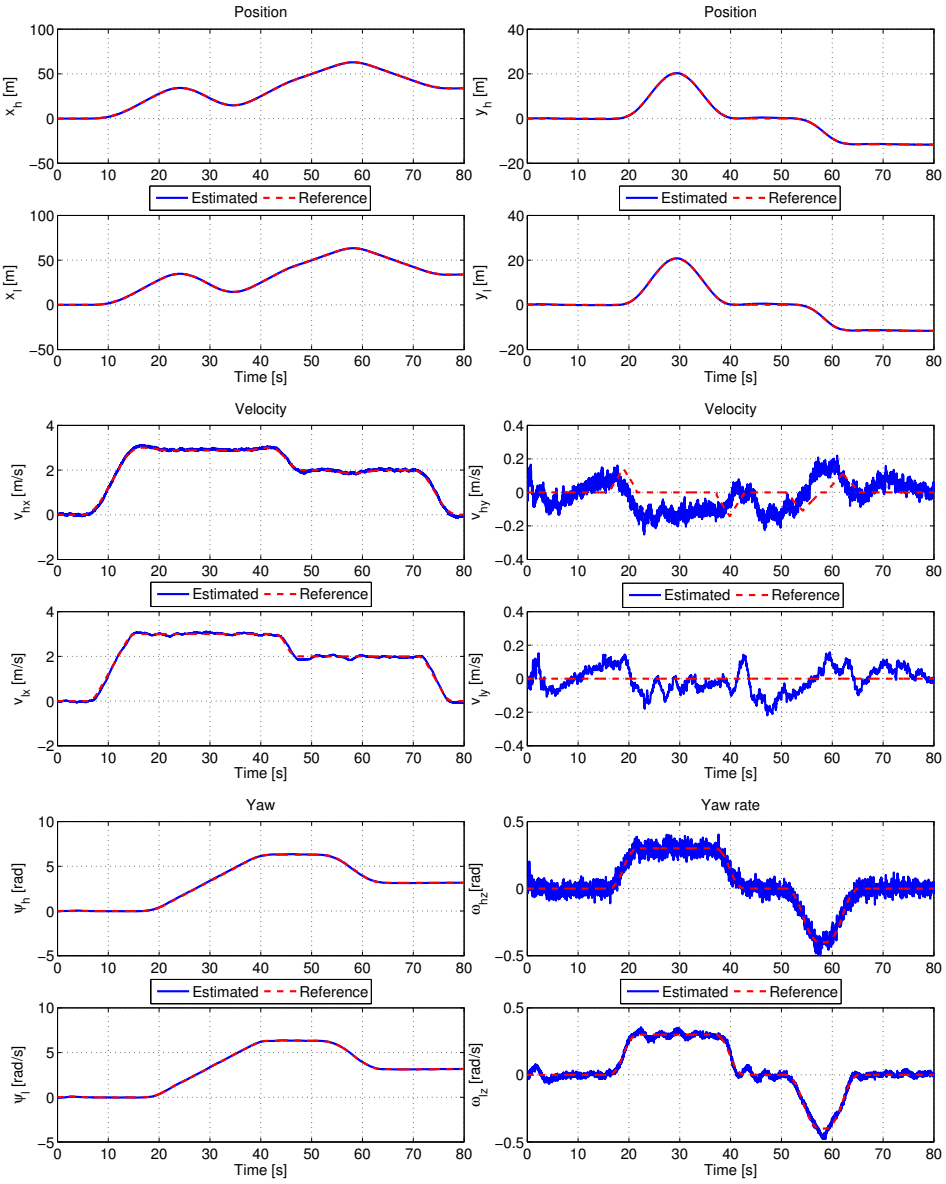

Figure 8.12: (Simulation) Estimated states and references for the AAU Bergen Twin with dual wire slung load doing trajectory tracking.

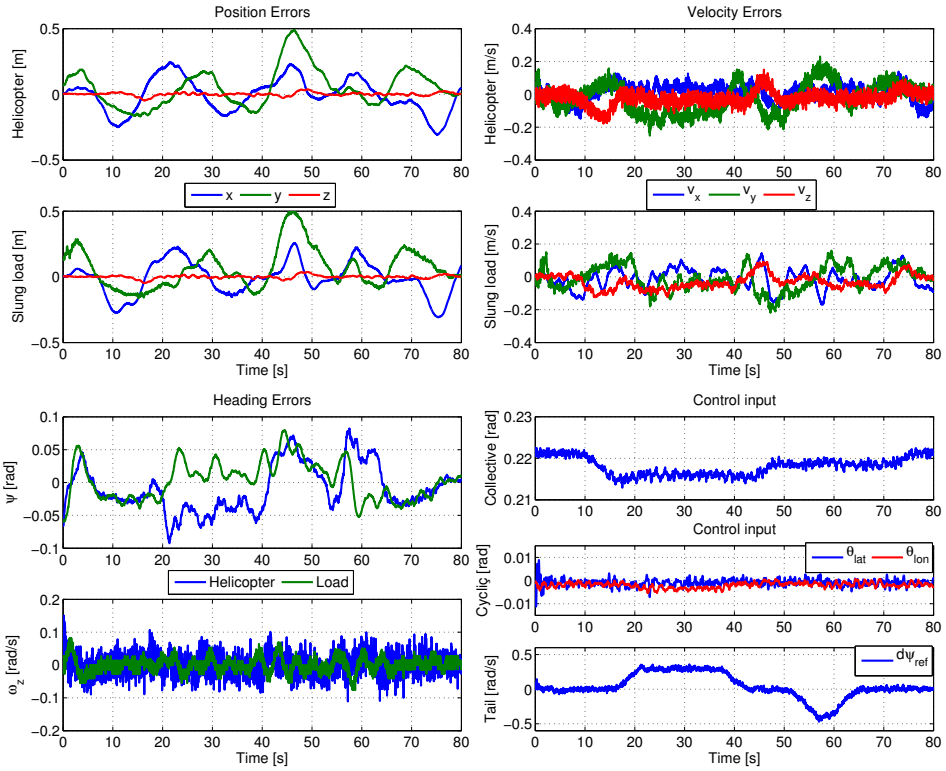

Figure 8.13: (Simulation) Error states and control signals for the AAU Bergen Twin with dual wire slung load doing trajectory tracking.

suppressing errors on the z-axis which is due to the good actuation the system have on this axis. For lateral and longitudinal errors are somewhat larger. In particular after the transition from turning to straight flight when leaving the 360° turn we can observe a peak can be seen on the y-axis error and the same can be seen on the heading error. This is due to the accumulated integrator state on yaw from the constant heading error during the long turn. The errors in the beginning of the simulation originates from estimator convergence. Control signals are also shown in figure 8.13 and we can see how noise on the state estimates propagate to the actuator signals, but the system still tracks the specified trajectory well.

8.4.2 Simulation of Terrain Tracking

This example simulates the helicopter slung load system used for the mine detection application. The system is equipped with laser range finder that measures the distance to the terrain and these measurements are used to generate a trajectory that allows the slung load to fly just over the terrain. In this simulated example the terrain is modeled as a low-pass filtered random walk and the laser range finder measures the distance between the load and the terrain. In figure 8.14 and 8.15 a 3D and a topview plot of the helicopter and slung load are shown and we can see how the trajectory is generated from the terrain as the helicopter flies forward and that the system seems capable of tracking it. The terrain

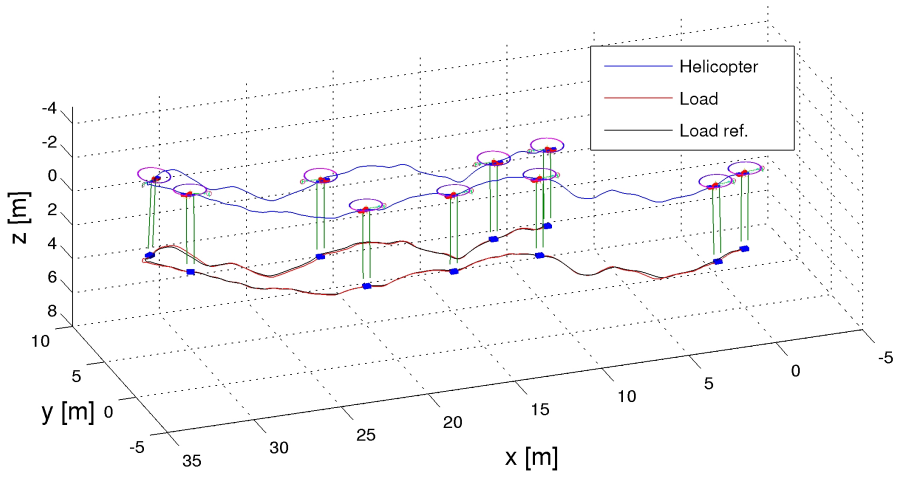

Figure 8.14: (Simulation) 3D plot of AAU Bergen Twin with dual wire slung load doing terrain tracking for mine detection.

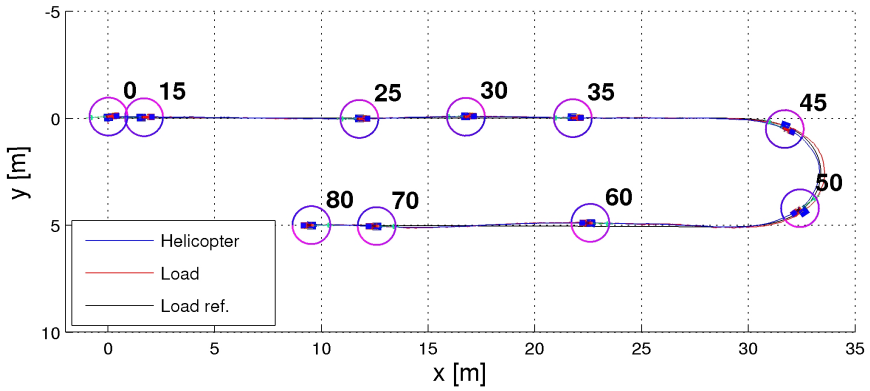

Figure 8.15: (Simulation) Topview plot of AAU Bergen Twin with dual wire slung load doing terrain tracking for mine detection.

trajectory and system altitude states are shown in figure 8.16 and also here we can see that the system is capable of tracking the trajectory. The changing altitude trajectory is reflected in the collective pitch signal that is used extensively compared to the previous example. The error states are show in figure 8.17 and again the errors in the beginning of the simulation originates from errors on the state estimates while the Kalman filter converges. We can see that the system can follow the terrain with a precision of ± 0.1 m.

8.5 Trajectory Tracking Control Summary and Discussion

A trajectory tracking controller was developed in this chapter. It is designed for close to hover flight with the mine detection application specifically in mind. The controller is designed using a linear optimal control approach and it was shown how it is capable of stabilizing the helicopter slung load system. Furthermore, a trajectory mapping algorithm was designed that is capable of taking a desired slung load trajectory and calculating a full state reference for the system. Through simulation it was shown how the controller is capable of satisfactorily tracking trajectories generated by the mapping algorithm. Finally it was shown how the control scheme can be used for mine detection where terrain tracking is necessary and a simulation verified that it can do so satisfactorily.

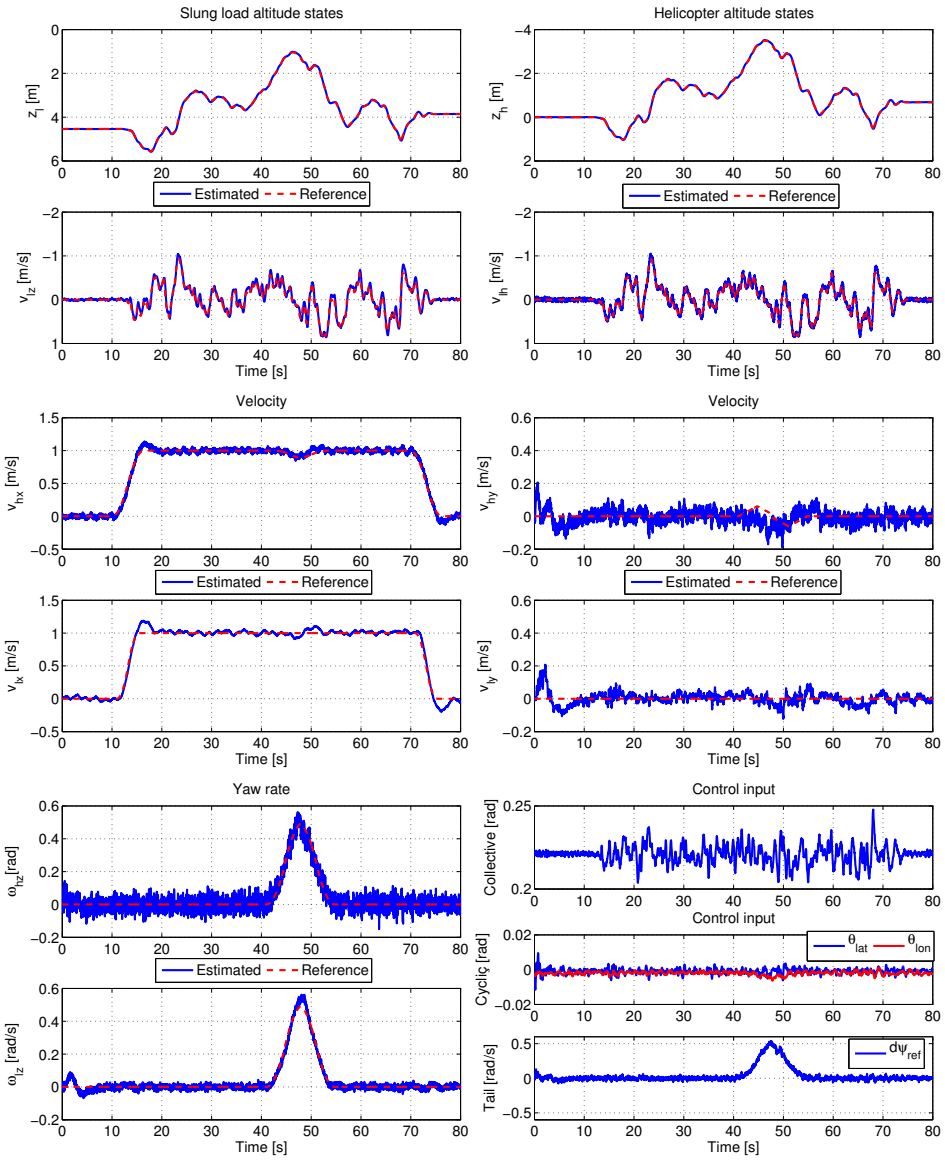

Figure 8.16: (Simulation) Error states and control signals for the AAU Bergen Twin with dual wire slung load doing terrain tracking for mine detection.

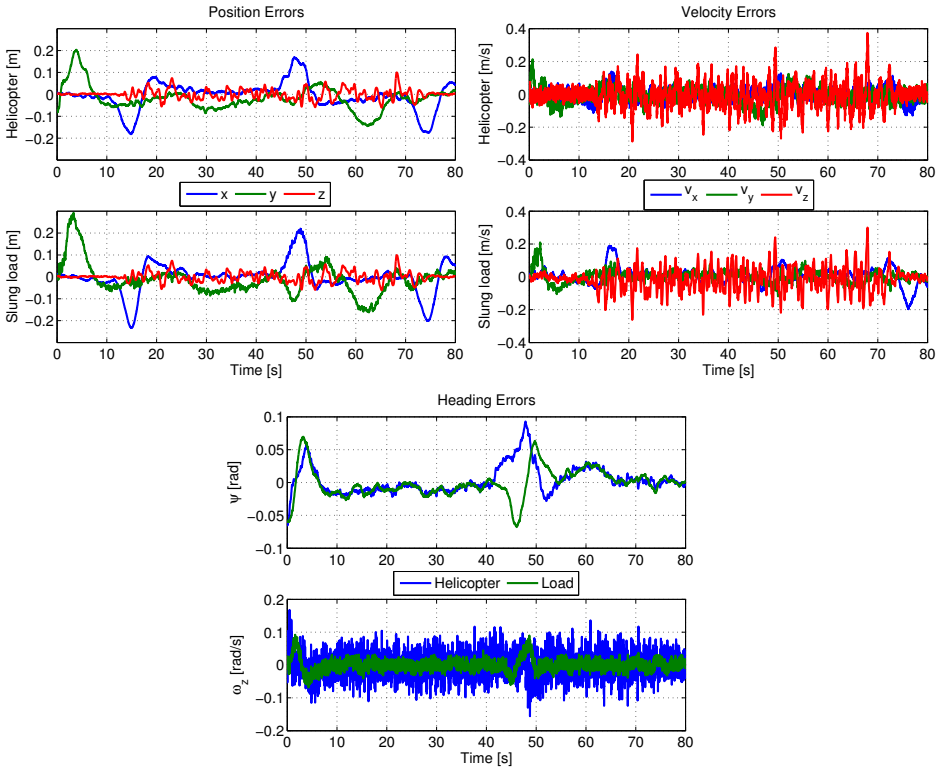

Figure 8.17: (Simulation) Error states and control signals for the AAU Bergen Twin with dual wire slung load doing terrain tracking for mine detection.

The linear controller design approach seems like an appropriate choice for the mine detection application where only slow flight is required. However, when doing terrain tracking, the system can reach quite high vertical velocities which can have a significant influence on the stability of the system. To improve the robustness of the controller a possibility would be to use a set of gain scheduled controllers for different vertical velocities. Another approach could be to parametrize the model with respect to the vertical velocity and use a parameter varying control approach.

The actual tracking performance could be improved by including the stabilizer bar dynamics in the linear model used for the controller design, as the current design is limited by the exclusion of resonant short period modes. This would require estimated stabilizer bar states from the sensor fusion, which are not readily available with the current design. However, it would be possible to design an observer using the linear model with rigid body and stabilizer bar dynamics for use in connection with the linear controller.

Part IV

Conclusion

This part contains a summary and conclusion of the thesis, a discussion of the thesis contributions, and considerations about future work.

Chapters

Chapter 9

Conclusion and Future Work

In this chapter a conclusion to this thesis is given. This is done by presenting an individual conclusion for each part of the thesis and summing up in a final conclusion. Finally suggestions is given for future work to further develop the thesis contributions.

9.1 Summary and Conclusion

The topic of this thesis has been the development of a methodology for autonomous helicopter slung load flight. Two different development branches have been pursued: One focusing on enabling slung load flight for general cargo transport with autonomous helicopter and one focusing on the development of a helicopter slung load system capable of precise trajectory tracking with a wide range of suspension systems.

Part I: Introduction

In chapter 1 the motivation behind this research was outlined and a specific application for precise trajectory tracking was presented, namely mine detection using an autonomous helicopter slung load system. Furthermore, a review of the previous work in the area was given and it was concluded that the specific topic of autonomous slung load flight has received little previous attention.

A overview of the physical test platforms used for test flights was given in chapter 2, introducing both the AAU Bergen Twin developed in connection with this research and the GTMax that has been made available for certain tests.

Part II: Modeling

A mathematical helicopter model was derived in chapter 3 using blade element theory for rotor forces and torques. Main rotor and stabilizer bar flapping dynamics were included

together with the effect of flapping hinge offset. Momentum theory was used to derive the induced inflow and a model of rotor downwash effect on the slung load was derived.

A rigid body model of the helicopter slung load system was derived in chapter 4 using the Udwaidia-Kalaba equation and a redundant coordinate formulation in which the wires were inserted as acceleration constraints. The model includes the ability of detect and respond to collapsing and tightening of wires in a dynamic way using impulse based collision theory and can be used to model multi-lift systems for multiple helicopters and loads.

The combined models from chapter 3 and chapter 4 were verified against flight data in chapter 5 and it was found that the model provides a satisfying description of the real system. A trim and linearization scheme was then developed and used for a linear analysis of the model. It was investigated how slung loads affect the behavior of the helicopter and how slung load parameter variations changes the system characteristic. It was concluded that the slung load introduces a set of weakly damped pendulous modes in the system and has a destabilizing effect on the helicopter.

Part III: Estimation and Control

In chapter 6 sensor fusion and state estimation algorithms were developed for the two application branches. For the cargo transport branch an estimator was designed specifically to augment autonomous helicopter state estimators. The update step was based entirely on vision based measurements which eliminates the need for sensors on the load. The estimator further includes the ability to estimate the wire length of the slung load and thus requires only basic knowledge of the load and suspension system, which makes it ideal for a general cargo transport application. Furthermore, a state estimator was designed as a stand-alone filter capable of delivering full state information for both helicopter and slung load. It requires acceleration and rate measurements from the load as well as vision based measurements of slung load position and heading. Both estimators were verified through test flights and simulations and it was concluded that both provides state estimates of satisfying quality for use in close loop.

The synthesis of a slung load swing damping control system was presented in chapter 7 with the focus on developing a controller for improving flight characteristic for autonomous helicopters flying with slung loads by suppressing load swing. The control system consists of a feedforward and a feedback part where the feedforward part shapes the reference signal to the helicopter controller such that excitations of the slung load pendulous modes are avoided. The feedback part is added to actively absorb load swing and when the two controller parts are combined, swing free slung load flight can be achieved. Both controller parts shows good performance individually during flight tests and future flight test will be performed to verify the overall performance of the swing damping control system.

In chapter 8 a control system for the helicopter slung load system was synthesized with focus on doing trajectory tracking with the mine detection application in mind. A linear optimal controller was designed for the system and it is capable of handling suspension

system both with and without yaw coupling. Furthermore, a trajectory mapping algorithm was developed for calculating the full state reference for the controller based on a given desired slung load trajectory. The control system was tested through simulation with a terrain tracking scenario and it was concluded that it yields satisfactorily performance. Future flight test will be performed to verify this result.

9.1.1 Thesis Conclusion

An overall methodology for autonomous helicopter slung load flight has been developed. To the best of the authors knowledge this work presents some of the very first flight results with autonomous helicopter slung load systems and this thesis is the most rigorous treatment of the subject ever published.

Two different development branches have been investigated, one focusing general slung load cargo transport and one focusing on slung load trajectory tracking and it can be concluded that both branches have resulted in solutions to the given slung load control problem. Through this development a highly flexible generic model has been derived that can be used for simulations of a wide range of helicopter slung load systems. A set of control systems with corresponding state estimators have been developed to respectively dampen slung load swing and to do trajectory tracking with the slung load.

9.2 Future Work

During this thesis a number of different issues that requires further consideration have been brought to attention and these are summarized here as suggestions for future work. The different suggestions range from specific improvements for the developed algorithms to general suggestions for research topics that could be investigated.

IMU Independent Dual Wire Slung Load State Estimation

In the discussion of the estimation chapter it was noted that the method developed for state estimation in slung load systems with yaw coupling to the helicopter requires an IMU mounted on the slung load. However, the estimator developed for point mass slung loads does not have this requirement and a natural next step could therefore be to extend this estimator for estimation of slung load heading. This could be achieved by using a bifilar pendulum model instead of the single wire pendulum model used presently.

Slung Load Mass Estimation

The wire length estimation algorithm provides frequency information of the pendulous slung load modes which can be used in online redesign of the control system to any wire length. However, it was concluded in the slung load swing damping chapter that in some cases it would be beneficial to know the slung load mass for redesign of the helicopter

altitude controller. Therefore, future work on the estimation could include the addition of a slung load mass estimator. By assuming that the helicopter mass is known it should be possible to estimate the slung load mass from its effect on the helicopter.

Given this mass estimate, the swing damping control scheme could be extended with an adaptive term capable of handling the change in heave dynamics imposed by the added mass.

Flight Envelope Expansion for Trajectory Tracking Controller

An obvious extension of the linear trajectory tracking controller is to use gain scheduling for expanding the flight envelope to include high speed flight.

Terrain Tracking Controller Design

The design of the trajectory tracking controller was done without specific attention to the fact that the mine detection application requires terrain tracking. It has been demonstrated that the controller is capable of satisfactorily tracking a terrain, but there is no doubt that the topic of terrain tracking control with slung load could benefit from further attention. If a forward looking laser range finder is mounted on the slung load, future terrain information is obtained, which could be used in a model predictive controller. A model predictive controller would also be capable of directly incorporating actuator saturation and system constraints.

Trajectory Generation using Inverse Dynamics

The trajectory mapping algorithm developed for the trajectory tracking controller relies on an approximate mapping of the system dynamics through the use of a ZV input shaper. It is assumed that a feasible slung load trajectory is available as input to the algorithm, but the generation of such a trajectory is no trivial matter. Therefore, attention could be put on using inverse system dynamics for generating full trajectories that does not violate system constraints.

Flight Testing

While most of the contributions of this thesis have been validated against flight data, two different flight test still remain. The joint feedback and feedforward swing damping control scheme should be flight tested to asses their combined effect on slung load swing. Both parts has been flight tested individually with satisfying results and it is expected that their combined effect will be slung load flight with virtually no load oscillations.

Furthermore, the trajectory tracking control scheme remains to be flight tested as only validation through simulation has been presented in this thesis. Based on experience from the other flight test carried out in this research we expect flight test results to be close to the simulation results.

Part V

Appendixes

In this part the supplemental appendixes created to support the preceding chapters are listed. Finally the bibliographic list of the thesis is given.

Chapters

Appendix A

Main and Tail Rotor Equations

In this appendix the resulting equations from the aerodynamic modeling in chapter 3 are presented.

A.1 Main Rotor Flapping Equations

When evaluating (3.29) the following trigonometric equations are used to discart all higher harmonics, e.g. $\sin(2\varphi)$, from the equations

$$\sin(\varphi)\cos(\varphi) = \frac{\sin(2\varphi)}{2}\,, \tag{A.1}$$

$$\sin^2(\varphi) = \frac{1}{2} - \frac{\cos(2\varphi)}{2}\,, \tag{A.2}$$

$$\cos^2(\varphi) = \frac{1}{2} + \frac{\cos(2\varphi)}{2}\,, \tag{A.3}$$

$$sin^3(\varphi) = \frac{3}{4}\sin(\varphi) - \frac{1}{4}\sin(3\varphi)\,, \tag{A.4}$$

$$\sin(\varphi)\cos^2(\varphi) = \frac{1}{4}\sin(\varphi) + \frac{1}{4}\sin(2\varphi)\,, \tag{A.5}$$

$$\sin^2(\varphi)\cos(\varphi) = \frac{1}{4}\cos(\varphi) - \frac{1}{4}\cos(2\varphi)\,. \tag{A.6}$$

The aerodynamic torque τ_a for the main rotor can be evaluated to yield (A.7).

$$\tau_a = \left(\frac{\rho C_l c \Omega^2 R^4}{2}\right)\left(\left(-1/2\,\frac{e}{R} + 1/3 + 1/2\,\mu_x\,\sin(\varphi) + \frac{e\mu_y\,\cos(\varphi)}{R} - \frac{e\mu_x\,\sin(\varphi)}{R} - 1/2\,\mu_y\,\cos(\varphi) + 1/2\,\frac{e^2\mu_x\,\sin(\varphi)}{R^2} - 1/2\,\frac{e^2\mu_y\,\cos(\varphi)}{R^2}\right)\lambda \right.$$
$$+ \left(-2/3\,\frac{e\mu_x\,\sin(\varphi)}{R} + 1/2\,\mu_x\,\sin(\varphi) - 1/4\,\frac{e}{R} + 1/5 - 2/3\,\mu_x\,\sin(\varphi)\,\mu_y\,\cos(\varphi) + 1/6\,{\mu_x}^2 - 1/4\,\frac{e{\mu_x}^2}{R} - 1/4\,\frac{e{\mu_y}^2}{R} + 1/6\,{\mu_y}^2 + 2/3\,\frac{e\mu_y\,\cos(\varphi)}{R}\right.$$
$$\left.- 1/2\,\mu_y\,\cos(\varphi) + \frac{e\mu_x\,\sin(\varphi)\,\mu_y\,\cos(\varphi)}{R}\right)\theta_t + \left(2\,\frac{e\mu_x\,\sin(\varphi)\,\mu_y\,\cos(\varphi)}{R} - 1/2\,\frac{e{\mu_x}^2}{R} + \frac{e\mu_y\,\cos(\varphi)}{R} - 1/2\,\frac{e{\mu_y}^2}{R} + 1/4\,{\mu_y}^2 - \frac{e\mu_x\,\sin(\varphi)}{R}\right.$$
$$\left.- \mu_x\,\sin(\varphi)\,\mu_y\,\cos(\varphi) - 1/3\,\frac{e}{R} + 2/3\,\mu_x\,\sin(\varphi) - 2/3\,\mu_y\,\cos(\varphi) + 1/4\,{\mu_x}^2 + 1/4\,\frac{e^2{\mu_y}^2}{R^2} + 1/4 + 1/4\,\frac{e^2{\mu_x}^2}{R^2} - \frac{e^2\mu_x\,\sin(\varphi)\,\mu_y\,\cos(\varphi)}{R^2}\right)\theta_{col}$$
$$+ \left(1/2\,\frac{e\sin(\varphi)\,{\mu_y}^2}{R} - \frac{e\mu_x\,\mu_y\,\cos(\varphi)}{R} - 1/3\,\mu_x + 1/2\,\mu_x\,\mu_y\,\cos(\varphi) - 1/4\,\sin(\varphi)\,{\mu_y}^2 + 1/2\,\frac{e^2\mu_x\,\mu_y\,\cos(\varphi)}{R^2} + 2/3\,\sin(\varphi)\,\mu_y\,\cos(\varphi)\right.$$
$$\left.- 3/8\,\sin(\varphi)\,{\mu_x}^2 + 1/3\,\frac{e\sin(\varphi)}{R} + 1/2\,\frac{e\mu_x}{R} - 3/8\,\frac{e^2\sin(\varphi)\,{\mu_x}^2}{R^2} - \frac{e\sin(\varphi)\,\mu_y\,\cos(\varphi)}{R} - 1/4\,\sin(\varphi) + 3/4\,\frac{e\sin(\varphi)\,{\mu_x}^2}{R} - 1/4\,\frac{e^2\sin(\varphi)\,{\mu_y}^2}{R^2}\right)\theta_{lon,mr}$$
$$+ \left(1/3\,\mu_y + 1/2\,\frac{e\cos(\varphi)\,{\mu_x}^2}{R} + \frac{\cos(\varphi)\,\mu_x\,\sin(\varphi)\,e}{R} + \frac{e\,(\cos(\varphi))^3\,{\mu_y}^2}{R} - 1/4\,\cos(\varphi)\,{\mu_x}^2 - 1/2\,\frac{e^2\,(\cos(\varphi))^3\,{\mu_y}^2}{R^2} - 1/2\,\left(\cos(\varphi)\right)^3\,{\mu_y}^2 - 1/4\,\cos(\varphi)\right.$$
$$\left.+ 1/2\,\mu_x\,\sin(\varphi)\,\mu_y - 1/2\,\frac{e\mu_y}{R} + 1/2\,\frac{e^2\mu_x\,\sin(\varphi)\,\mu_y}{R^2} - \frac{e\mu_x\,\sin(\varphi)\,\mu_y}{R} + 1/3\,\frac{e\cos(\varphi)}{R} - 2/3\,\cos(\varphi)\,\mu_x\,\sin(\varphi) - 1/4\,\frac{e^2\cos(\varphi)\,{\mu_x}^2}{R^2}\right)\theta_{lat,mr}$$
$$+ \left(-1/2\,{\mu_x}^2\cos(\varphi)\sin(\varphi) - \frac{e\sin(\varphi)\,{\mu_y}^2\cos(\varphi)}{R} - 1/3\,\mu_y\,\sin(\varphi) - 1/2\,\frac{e^2\cos(\varphi)\,{\mu_x}^2\sin(\varphi)}{R^2} + 1/2\,{\mu_y}^2\sin(\varphi)\cos(\varphi) + \frac{e\cos(\varphi)\,{\mu_x}^2\sin(\varphi)}{R}\right.$$
$$\left.- 1/3\,\mu_x\,\cos(\varphi) + 1/2\,\frac{e^2\sin(\varphi)\,{\mu_y}^2\cos(\varphi)}{R^2} + 1/2\,\frac{e\sin(\varphi)\,\mu_y}{R} + 1/2\,\frac{\mu_x\,\cos(\varphi)\,e}{R}\right)\beta + \left(-1/4\,\Omega^{-1} + \frac{e\mu_x\,\sin(\varphi)}{\Omega\,R} - 1/3\,\frac{\mu_x\,\sin(\varphi)}{\Omega} - \frac{e\mu_y\,\cos(\varphi)}{\Omega\,R}\right.$$
$$\left.+ \frac{e^2\mu_y\,\cos(\varphi)}{\Omega\,R^2} + 1/3\,\frac{\mu_y\,\cos(\varphi)}{\Omega} + 2/3\,\frac{e}{\Omega\,R} - 1/2\,\frac{e^2}{\Omega\,R^2} - \frac{e^2\mu_x\,\sin(\varphi)}{\Omega\,R^2}\right)\dot{\beta} + 1/4\,\frac{{}^{mr}\omega_{y_{mr}}\,\cos(\varphi)}{\Omega} - 1/4\,\frac{{}^{mr}\omega_{x_{mr}}\,\sin(\varphi)}{\Omega}$$
$$+ 1/3\,\frac{{}^{mr}\omega_{x_{mr}}\,\sin(\varphi)\,e}{\Omega\,R} - 1/6\,\frac{{}^{mr}\omega_{y_{mr}}\,\mu_y}{\Omega} + 1/3\,\frac{{}^{mr}\omega_{x_{mr}}\,\sin(\varphi)\,\mu_y\,\cos(\varphi)}{\Omega} - 1/2\,\frac{e^{mr}\omega_{y_{mr}}\,\cos(\varphi)\,\mu_x\,\sin(\varphi)}{\Omega\,R} + 1/4\,\frac{e^{mr}\omega_{y_{mr}}\,\mu_y}{\Omega\,R}$$
$$+ 1/4\,\frac{e^{mr}\omega_{x_{mr}}\,\mu_x}{\Omega\,R} + 1/3\,\frac{{}^{mr}\omega_{y_{mr}}\,\cos(\varphi)\,\mu_x\,\sin(\varphi)}{\Omega} - 1/6\,\frac{{}^{mr}\omega_{x_{mr}}\,\mu_x}{\Omega} - 1/3\,\frac{e^{mr}\omega_{y_{mr}}\,\cos(\varphi)}{\Omega\,R} - 1/2\,\frac{{}^{mr}\omega_{x_{mr}}\,\sin(\varphi)\,e\mu_y\,\cos(\varphi)}{\Omega\,R}\Bigg) \tag{A.7}$$

The main rotor flapping equations are shown in (A.8), (A.9), and (A.10).

$$
\begin{aligned}
\ddot{a}_{con} &= \Omega\gamma\left(-1/8\ -1/4\,\frac{e^2}{R^2}+1/3\,\frac{e}{R}\right)\dot{a}_{con}+\Omega\gamma\left(-1/4\,\frac{e^2\mu_y}{R^2}-1/12\,\mu_y+1/4\,\frac{e\mu_y}{R}\right)\dot{a}_{lon}\\
&+\Omega\gamma\left(1/4\,\frac{e\mu_x}{R}-1/12\,\mu_x-1/4\,\frac{e^2\mu_x}{R^2}\right)\dot{a}_{lat}+\Omega^2\left(-1+\frac{-\gamma\,eM_b-\gamma\,K_b}{R^4\rho\,ac}\right)a_{con}\\
&+\Omega^2\gamma\left(-1/4\,\frac{e^2\mu_x}{R^2}+1/8\,\frac{e\mu_x}{R}\right)a_{lon}+\Omega^2\gamma\left(-1/8\,\frac{e\mu_y}{R}+1/4\,\frac{e^2\mu_y}{R^2}\right)a_{lat}\\
&+\Omega^2\gamma\left(1/8\,{\mu_y}^2+1/8\,{\mu_x}^2+1/8\ +\frac{-1/6\,e-1/4\,e\mu_y{}^2-1/4\,e\mu_x{}^2}{R}+1/8e^2\,\frac{{\mu_y}^2+{\mu_x}^2}{R^2}\right)\theta_{col}\\
&+\Omega^2\gamma\left(1/12\,{\mu_y}^2+1/10\ +1/12\,{\mu_x}^2+\frac{-1/8\,e-1/8\,e\mu_x{}^2-1/8\,e\mu_y{}^2}{R}\right)\theta_t\\
&+\Omega^2\gamma\left(1/6\,\mu_y-1/4\,\frac{e\mu_y}{R}\right)\theta_{lat,mr}+\Omega^2\gamma\left(1/4\,\frac{e\mu_x}{R}-1/6\,\mu_x\right)\theta_{lon,mr}\\
&+\Omega^2\gamma\left(-1/4\,\frac{e}{R}+1/6\right)\lambda+\left(-\frac{\gamma\,M_b\,{}^hv_{xh}}{R^4\rho\,C_lc}-1/12\,\Omega\,\gamma\,\mu_y+1/8\,\frac{\Omega\,\gamma\,e\mu_y}{R}\right){}^h\omega_{y_h}\\
&+\left(1/8\,\frac{\Omega\,\gamma\,e\mu_x}{R}+\frac{\gamma\,M_b\,{}^hv_{y_h}}{R^4\rho\,C_lc}-1/12\,\Omega\,\gamma\,\mu_x\right){}^h\omega_{x_h}+\frac{\gamma\,M_b}{R^{4\,h}\dot{v}_{z_h}\rho\,C_lc}
\end{aligned}
\tag{A.8}
$$

$$
\begin{aligned}
\ddot{a}_{lon} &= \Omega\,\gamma\left(-1/2\,\frac{e^2\mu_y}{R^2}+1/2\,\frac{e\mu_y}{R}-1/6\,\mu_y\right)\dot{a}_{con}+\Omega\gamma\left(-1/8\ -1/4\,\frac{e^2}{R^2}+1/3\,\frac{e}{R}\right)\dot{a}_{lon}\\
&+\Omega^2\gamma\left(1/8\,\frac{e^2\mu_y\,\mu_x}{R^2}+1/8\,\mu_x\,\mu_y-1/4\,\frac{e\mu_y\,\mu_x}{R}+\frac{-eM_b}{R^4\rho\,C_lc}-\frac{K_b}{\Omega^2R^4\rho\,C_lc}\right)a_{lon}\\
&+\Omega^2\gamma\left(1/8\ +1/16\,{\mu_x}^2-1/16\,{\mu_y}^2+\frac{-1/8\,e\mu_x{}^2-1/3\,e+1/8\,e\mu_y{}^2}{R}\right.\\
&\left.+\frac{1/4\,e^2+1/16\,e^2\mu_x{}^2-1/16\,e^2\mu_y{}^2}{R^2}\right)a_{lat}\\
&+\Omega^2\gamma\left(1/6\,\mu_x-1/4\,\frac{e\mu_x}{R}\right)a_{con}+\Omega^2\gamma\left(1/4\,\frac{e\mu_y\,\mu_x}{R}-1/8\,\mu_x\,\mu_y-1/8\,\frac{e^2\mu_y\,\mu_x}{R^2}\right)\theta_{lon,mr}\\
&+\Omega^2\gamma\left(1/3\,\mu_y-1/2\,\frac{e\mu_y}{R}\right)\theta_{col,mr}+\Omega^2\gamma\left(-1/3\,\frac{e\mu_y}{R}+1/4\,\mu_y\right)\theta_t\\
&+\Omega^2\gamma\left(3/16\,{\mu_y}^2+1/16\,{\mu_x}^2+1/8\ +\frac{-1/8\,e\mu_x{}^2-1/6\,e-3/8\,e\mu_y{}^2}{R}\right.\\
&\left.+\frac{1/16\,e^2\mu_x{}^2+3/16\,e^2\mu_y{}^2}{R^2}\right)\theta_{lat,mr}+\Omega^2\gamma\left(1/4\,\frac{e^2\mu_y}{R^2}+1/4\,\mu_y-1/2\,\frac{e\mu_y}{R}\right)\lambda\\
&+\Omega\gamma\left(1/6\,\frac{e}{R}-1/8\right){}^h\omega_{y_h}+\left(2\,\Omega+2\,\frac{\Omega\,\gamma\,eM_b}{R^4\rho\,C_lc}\right){}^h\omega_{x_h}-{}^h\dot{\omega}_{y_h}+2\,\dot{a}_{lat}\,\Omega
\end{aligned}
\tag{A.9}
$$

$$
\begin{aligned}
\ddot{a}_{lat} &= \Omega\gamma\left(-1/2\,\frac{e^2\mu_x}{R^2}+1/2\,\frac{e\mu_x}{R}-1/6\,\mu_x\right)\dot{a}_{con}+\Omega\gamma\left(-1/8\,-1/4\,\frac{e^2}{R^2}+1/3\,\frac{e}{R}\right)\dot{a}_{lat}\\
&+\Omega^2\gamma\mu_y\left(1/4\,\frac{e}{R}-1/6\right)a_{con}+\Omega^2\gamma\left(1/4\,\mu_x-1/2\,\frac{e\mu_x}{R}+1/4\,\frac{e^2\mu_x}{R^2}\right)\lambda\\
&+\Omega^2\gamma\left(1/16\,({\mu_x}^2-{\mu_y}^2)-1/8+e^2\frac{1/16({\mu_x}^2-{\mu_y}^2)-1/4}{R^2}+e\frac{1/3+1/8({\mu_y}^2-{\mu_x}^2)}{R}\right)a_{lon}\\
&+\Omega^2\gamma\left(-1/8\,\mu_x\,\mu_y-1/8\,\frac{e^2\mu_y\,\mu_x}{R^2}+\frac{-eM_b}{R^4\rho\,C_lc}-\frac{-K_b}{\Omega^2R^4\rho\,C_lc}+1/4\,\frac{e\mu_y\,\mu_x}{R}\right)a_{lat}\\
&+\Omega^2\gamma\left(1/3\,\mu_x-1/2\,\frac{e\mu_x}{R}\right)\theta_{col}+\Omega^2\gamma\left(-1/3\,\frac{e\mu_x}{R}+1/4\,\mu_x\right)\theta_t\\
&+\Omega^2\gamma\left(1/8\,\frac{e^2\mu_y\,\mu_x}{R^2}+1/8\,\mu_x\,\mu_y-1/4\,\frac{e\mu_y\,\mu_x}{R}\right)\theta_{lat,mr}+\Omega^2\gamma\left(-3/16\,{\mu_x}^2-1/16\,{\mu_y}^2\right.\\
&\left.-1/8\,+e^2\frac{-1/16{\mu_y}^2-3/16\,{\mu_x}^2}{R^2}+e\frac{1/6+3/8{\mu_x}^2+1/8\,e{\mu_y}^2}{R}\right)\theta_{lon,mr}-2\,\Omega\,{}^h\omega_{y_h}\\
&+1/6\,\frac{\gamma\,\Omega\,{}^h\omega_{x_h}\,e}{R}-{}^h\dot{\omega}_{x_h}-2\,\frac{\Omega\,\gamma\,eM_b\,{}^h\omega_{y_h}}{R^4\rho\,C_lc}-2\,\dot{a}_{lon}\,\Omega-1/8\,\gamma\,\Omega\,{}^h\omega_{x_h}
\end{aligned}
\tag{A.10}
$$

A.2 Main Rotor Forces and Moments

The main rotor generated forces are shown in (A.11), (A.12), and (A.11)

$$
\begin{aligned}
F_z = -\frac{1}{2}\rho C_l bcR(\Omega R)^2\Bigg(&\left(1/2-1/2\,\frac{e^2}{R^2}\right)\lambda+\left(-1/2\,\mu_x+1/2\,\frac{\mu_x\,e^2}{R^2}\right)\theta_{lon,mr}\\
&+\left(1/3+1/2\,{\mu_x}^2-1/2\,\frac{e{\mu_x}^2}{R}+1/2\,{\mu_y}^2-1/2\,\frac{e{\mu_y}^2}{R}\right)\theta_{col}+1/2\mu_y\left(\frac{e^2}{R^2}-\frac{e}{R}\right)a_{lat}\\
&+1/2\mu_y\left(1-\frac{e^2}{R^2}\right)\theta_{lat,mr}+1/2\mu_x\left(\frac{e}{R}-\frac{e^2}{R^2}\right)a_{lon}+\left(-1/3\,\frac{1}{\Omega}+1/2\,\frac{e}{R\Omega}\right)\dot{a}_{con}\\
&+\left(1/2\,\frac{e\mu_y}{R\Omega}-1/4\,\frac{\mu_y\,e^2}{R^2\Omega}-1/4\,\frac{\mu_y}{\Omega}\right)\dot{a}_{lon}+\left(1/2\,\frac{\mu_x\,e}{R\Omega}-1/4\,\frac{\mu_x}{\Omega}-1/4\,\frac{\mu_x\,e^2}{R^2\Omega}\right)\dot{a}_{lat}\\
&+\left(-1/4\,\frac{\mu_y}{\Omega}+1/4\,\frac{\mu_y\,e^2}{R^2\Omega}\right){}^h\omega_{y_h}+\left(1/4\,\frac{\mu_x\,e^2}{R^2\Omega}-1/4\,\frac{\mu_x}{\Omega}\right){}^h\omega_{x_h}\\
&+\left(1/4\,-1/4\,\frac{e^2{\mu_y}^2}{R^2}-1/4\,\frac{e^2{\mu_x}^2}{R^2}+1/4\,{\mu_x}^2+1/4\,{\mu_y}^2\right)\theta_t\Bigg)
\end{aligned}
\tag{A.11}
$$

$$
F_x = \frac{1}{2}\rho C_l bcR^2(\Omega R)^2\left(F_{x1}+F_{x2}\right) \tag{A.12}
$$

$$
F_y = \frac{1}{2}\rho C_l bcR^2(\Omega R)^2\left(F_{y1}+F_{y2}\right) \tag{A.13}
$$

$$
\begin{aligned}
F_{x1} = & \left(-1/2\,\frac{\mu_x}{a} + 1/2\,\frac{e^2\mu_x}{aR^2} \right) C_d + \left(-1/2\,{\mu_y}^2 a_{lon} - 3/4\,\mu_y\, a_{con} - 1/2\,\mu_x\,\mu_y\, a_{lat} - 1/4\,\frac{\mu_x\,\dot{a}_{con}}{\Omega} - 1/6\,\frac{{}^{mr}\omega_{xmr}}{\Omega} + 1/2\,\frac{\mu_x\,\dot{a}_{con}\,e}{\Omega\,R} - 1/6\,\frac{\dot{a}_{lat}}{\Omega} \right. \\
& + 1/4\,\frac{a_{lon}\,e}{R} + 1/4\,\frac{e\dot{a}_{lat}}{\Omega\,R} + 1/2\,\mu_x\,\lambda + 1/2\,\frac{\mu_x\,\mu_y\,a_{lat}\,e}{R} + 3/4\,\frac{e^2\mu_y\,a_{con}}{R^2} - 1/4\,\frac{\mu_x\,\dot{a}_{con}\,e^2}{\Omega\,R^2} + 1/2\,\frac{{\mu_y}^2 a_{lon}\,e}{R} - 1/3\,a_{lon} - 1/2\,\frac{\mu_x\,\lambda\,e}{R} \Bigg) \theta_{col} \\
& + \left(3/8\,\frac{\mu_y\,a_{lon}\,e^2}{R^2} - 1/16\,\frac{\mu_x\,\dot{a}_{lon}}{\Omega} - 1/16\,\frac{\mu_x\,{}^{mr}\omega_{ymr}}{\Omega} - 1/2\,{\mu_y}^2 a_{con} - 1/16\,\frac{\mu_y\,\dot{a}_{lat}\,e^2}{\Omega\,R^2} \right. \\
& - 1/16\,\frac{\mu_y\,{}^{mr}\omega_{xmr}}{\Omega} - 1/8\,\frac{\mu_x\,a_{lat}\,e}{R} - 1/2\,\mu_y\,a_{lon} + 1/8\,\frac{\mu_x\,\dot{a}_{lon}\,e}{\Omega\,R} + 1/8\,\frac{\mu_x\,a_{lat}\,e^2}{R^2} + 1/16\,\frac{\mu_y\,e^{2mr}\omega_{xmr}}{\Omega\,R^2} - 1/16\,\frac{\mu_x\,\dot{a}_{lon}\,e^2}{\Omega\,R^2} \\
& + 1/16\,\frac{\mu_x\,e^{2mr}\omega_{ymr}}{\Omega\,R^2} + 1/8\,\frac{\mu_y\,\dot{a}_{lat}\,e}{\Omega\,R} + 1/2\,\frac{{\mu_y}^2 a_{con}\,e}{R} - 1/6\,a_{con} - 1/16\,\frac{\mu_y\,\dot{a}_{lat}}{\Omega} + 1/8\,\frac{\mu_y\,a_{lon}\,e}{R} \Bigg) \theta_{lat,mr} \\
& + \left(1/16\,\frac{\mu_y\,\dot{a}_{lon}}{\Omega} - 1/4\,\lambda + 1/4\,\mu_y\,a_{lat} - 1/8\,\frac{\mu_y\,\dot{a}_{lon}\,e}{\Omega\,R} + 3/16\,\frac{\mu_x\,{}^{mr}\omega_{xmr}}{\Omega} + 1/8\,\frac{e\mu_y\,a_{lat}}{R} + 3/16\,\frac{\mu_x\,\dot{a}_{lat}}{\Omega} - 3/8\,\frac{e^2\mu_y\,a_{lat}}{R^2} + 1/4\,\frac{e^2\lambda}{R^2} \right. \\
& - 3/16\,\frac{\mu_x\,e^{2mr}\omega_{xmr}}{\Omega\,R^2} + 1/16\,\frac{\mu_y\,{}^{mr}\omega_{ymr}}{\Omega} - 3/8\,\frac{\mu_x\,a_{lon}\,e}{R} - 1/16\,\frac{\mu_y\,e^{2mr}\omega_{ymr}}{\Omega\,R^2} - 3/8\,\frac{\mu_x\,\dot{a}_{lat}\,e}{\Omega\,R} + 1/2\,\mu_x\,\mu_y\,a_{con} + 1/6\,\frac{\dot{a}_{con}}{\Omega} \\
& + 1/4\,\mu_x\,a_{lon} + 1/8\,\frac{\mu_x\,a_{lon}\,e^2}{R^2} + 1/16\,\frac{\mu_y\,\dot{a}_{lon}\,e^2}{\Omega\,R^2} - 1/2\,\frac{\mu_x\,\mu_y\,a_{con}\,e}{R} + 3/16\,\frac{\mu_x\,\dot{a}_{lat}\,e^2}{\Omega\,R^2} - 1/4\,\frac{\dot{a}_{con}\,e}{\Omega\,R} \Bigg) \theta_{lon,mr} \\
& + \left(-1/8\,\frac{\dot{a}_{lat}}{\Omega} - 1/6\,\frac{\mu_x\,\dot{a}_{con}}{\Omega} + 1/4\,\frac{\mu_x\,\dot{a}_{con}\,e}{\Omega\,R} + 1/6\,\frac{e\dot{a}_{lat}}{\Omega\,R} - 1/4\,\frac{\mu_x\,e^2\lambda}{R^2} + 1/4\,\mu_x\,\lambda - 1/2\,\mu_y\,a_{con} + 1/6\,\frac{a_{lon}\,e}{R} \right. \\
& - 1/4\,{\mu_y}^2 a_{lon} - 1/4\,\mu_x\,\mu_y\,a_{lat} - 1/4\,a_{lon} + 1/4\,\frac{e^2{\mu_y}^2 a_{lon}}{R^2} + 1/4\,\frac{\mu_x\,e^2\mu_y\,a_{lat}}{R^2} - 1/8\,\frac{{}^{mr}\omega_{xmr}}{\Omega} \Bigg) \theta_t \\
& - 1/2\,\frac{\lambda\,\dot{a}_{lat}}{\Omega} + {\mu_y}^2 a_{con}\,a_{lat} + \left(-\frac{5}{16}\,\frac{e^2\mu_y\,a_{lon}}{\Omega\,R^2} + 1/6\,\frac{a_{con}}{\Omega} - 1/16\,\frac{\mu_x\,a_{lat}}{\Omega} + 1/16\,\frac{\mu_x\,a_{lat}\,e^2}{\Omega\,R^2} + \frac{5}{16}\,\frac{\mu_y\,a_{lon}}{\Omega} \right) {}^h\omega_{y_h} \\
& + \left(1/2\,\frac{e^2\lambda}{\Omega\,R^2} + \frac{7}{16}\,\frac{\mu_y\,a_{lat}}{\Omega} + 1/16\,\frac{\mu_x\,a_{lon}\,e^2}{\Omega\,R^2} - 1/16\,\frac{\mu_x\,a_{lon}}{\Omega} + 1/3\,\frac{\dot{a}_{con}}{\Omega^2} - \frac{7}{16}\,\frac{e^2\mu_y\,a_{lat}}{\Omega\,R^2} - 1/2\,\frac{\lambda}{\Omega} - 1/2\,\frac{\dot{a}_{con}\,e}{\Omega^2 R} \right) {}^h\omega_{x_h}
\end{aligned}
\tag{A.14}
$$

$$
\begin{aligned}
F_{x2} = & -1/2\,\frac{\lambda\,\dot{a}_{lat}\,e^2}{\Omega\,R^2} + \frac{\lambda\,a_{lon}\,e}{R} + \frac{7}{16}\,\frac{\dot{a}_{lat}\,\mu_y\,a_{lat}}{\Omega} + \frac{5}{16}\,\frac{\dot{a}_{lon}\,a_{lon}\,\mu_y}{\Omega} - 1/16\,\frac{\mu_x\,a_{lat}\,\dot{a}_{lon}}{\Omega} + 1/4\,\mu_y\,a_{lat}\,a_{lon} \\
& - 3/2\,\lambda\,\mu_y\,a_{con} - 3/2\,\frac{\dot{a}_{con}\,\mu_y\,a_{con}\,e}{\Omega\,R} - \frac{7}{8}\,\frac{\dot{a}_{lat}\,\mu_y\,a_{lat}\,e}{\Omega\,R} - 1/4\,\frac{\mu_y\,a_{lat}\,a_{lon}\,e}{R} - 3/4\,\lambda\,a_{lon} - 1/6\,a_{lat}\,a_{con} - \frac{{\mu_y}^2\,a_{con}\,a_{lat}\,e}{R} \\
& + \frac{\mu_x\,a_{lon}\,a_{con}\,\mu_y\,e}{R} - 1/4\,\mu_x\,{a_{con}}^2 - \mu_x\,a_{lon}\,a_{con}\,\mu_y + 1/6\,\frac{\dot{a}_{lon}\,a_{con}}{\Omega} + 1/2\,\frac{\dot{a}_{con}\,a_{lon}}{\Omega} + 3/4\,\frac{\dot{a}_{con}\,\mu_y\,a_{con}\,e^2}{\Omega\,R^2} + 3/2\,\frac{\lambda\,\mu_y\,a_{con}\,e}{R} \\
& + \frac{5}{16}\,\frac{\dot{a}_{lon}\,a_{lon}\,\mu_y\,e^2}{\Omega\,R^2} + 1/8\,\frac{\mu_x\,a_{lon}\,\dot{a}_{lat}\,e}{\Omega\,R} - 1/16\,\frac{\mu_x\,a_{lon}\,\dot{a}_{lat}\,e^2}{\Omega\,R^2} + 1/8\,\frac{\mu_x\,a_{lat}\,\dot{a}_{lon}\,e}{\Omega\,R} - 1/16\,\frac{\mu_x\,a_{lat}\,\dot{a}_{lon}\,e^2}{\Omega\,R^2} + \frac{\lambda\,\dot{a}_{lat}\,e}{\Omega\,R} \\
& - 5/4\,\frac{\dot{a}_{con}\,a_{lon}\,e}{\Omega\,R} - 1/4\,\mu_x\,{a_{lon}}^2 + \frac{\dot{a}_{con}\,a_{lon}\,e^2}{\Omega\,R^2} - 1/4\,\frac{\dot{a}_{lon}\,a_{con}\,e}{\Omega\,R} + 1/4\,\frac{a_{lat}\,a_{con}\,e}{R} - 1/4\,\frac{\lambda\,a_{lon}\,e^2}{R^2} + 1/8\,\frac{\mu_x\,{a_{lat}}^2\,e^2}{R^2} - 1/8\,\frac{\mu_x\,{a_{lat}}^2\,e}{R} \\
& + 3/4\,\frac{\dot{a}_{con}\,\mu_y\,a_{con}}{\Omega} + 1/8\,\frac{\mu_x\,{a_{lon}}^2\,e^2}{R^2} + 1/8\,\frac{\mu_x\,{a_{lon}}^2\,e}{R} + 1/4\,\frac{\mu_x\,{a_{con}}^2\,e^2}{R^2} - 1/16\,\frac{\mu_x\,a_{lon}\,\dot{a}_{lat}}{\Omega} + \frac{7}{16}\,\frac{\dot{a}_{lat}\,\mu_y\,a_{lat}\,e^2}{\Omega\,R^2} \\
& - 5/8\,\frac{\dot{a}_{lon}\,a_{lon}\,\mu_y\,e}{\Omega\,R} + \frac{\dot{a}_{con}\,\dot{a}_{lat}\,e^2}{\Omega^2\,R^2} - \frac{\dot{a}_{con}\,\dot{a}_{lat}\,e}{\Omega^2\,R} + 1/3\,\frac{\dot{a}_{con}\,\dot{a}_{lat}}{\Omega^2}
\end{aligned}
\tag{A.15}
$$

$$
\begin{aligned}
F_{y1} = & \left(-1/2\,\frac{\mu_y}{a} + 1/2\,\frac{e^2\mu_y}{aR^2} \right) Cd \\
& + \left(-1/4\,\frac{\mu_y\,\dot{a}_{con}\,e^2}{\Omega\,R^2} - 1/6\,\frac{{}^{mr}\omega_{y_{mr}}}{\Omega} - 1/2\,\frac{{\mu_x}^2\,a_{lat}\,e}{R} + 1/2\,\mu_y\,\lambda + 1/4\,\frac{\dot{a}_{lon}\,e}{\Omega\,R} - 1/2\,\frac{\mu_y\,\lambda\,e}{R} - 1/2\,\frac{\mu_y\,a_{lon}\,\mu_x\,e}{R} \right. \\
& \left. - 3/4\,\frac{\mu_x\,a_{con}\,e^2}{R^2} + 1/3\,a_{lat} - 1/4\,\frac{\mu_y\,\dot{a}_{con}}{\Omega} + 3/4\,\mu_x\,a_{con} + 1/2\,\frac{\mu_y\,\dot{a}_{con}\,e}{\Omega\,R} - 1/4\,\frac{a_{lat}\,e}{R} - 1/6\,\frac{\dot{a}_{lon}}{\Omega} + 1/2\,{\mu_x}^2\,a_{lat} + 1/2\,\mu_y\,a_{lon}\,\mu_x \right) \theta_{col} \\
& + \left(-1/6\,\frac{\dot{a}_{con}}{\Omega} - 3/16\,\frac{\mu_y\,\dot{a}_{lon}\,e^2}{\Omega\,R^2} - 1/2\,\frac{\mu_y\,a_{con}\,\mu_x\,e}{R} + 1/8\,\frac{\mu_x\,\dot{a}_{lat}\,e}{\Omega\,R} + 1/8\,\frac{\mu_x\,a_{lon}\,e}{R} - 3/16\,\frac{\mu_y\,\dot{a}_{lon}}{\Omega} \right. \\
& - 1/4\,\frac{e^2\lambda}{R^2} + 1/4\,\frac{\dot{a}_{con}\,e}{\Omega\,R} - 1/16\,\frac{\mu_x\,\dot{a}_{lat}}{\Omega} + 1/4\,\mu_x\,a_{lon} + 1/4\,\lambda + 1/16\,\frac{\mu_x\,e^{2mr}\omega_{x_{mr}}}{\Omega\,R^2} + 1/8\,\frac{\mu_y\,a_{lat}\,e^2}{R^2} - 3/16\,\frac{\mu_y\,{}^{mr}\omega_{y_{mr}}}{\Omega} \\
& \left. - 1/16\,\frac{\mu_x\,\dot{a}_{lat}\,e^2}{\Omega\,R^2} - 1/16\,\frac{\mu_x\,{}^{mr}\omega_{x_{mr}}}{\Omega} + 3/8\,\frac{\mu_y\,\dot{a}_{lon}\,e}{\Omega\,R} - 3/8\,\frac{\mu_y\,a_{lat}\,e}{R} + 3/16\,\frac{\mu_y\,e^{2\,mr}\omega_{y_{mr}}}{\Omega\,R^2} - 3/8\,\frac{\mu_x\,a_{lon}\,e^2}{R^2} + 1/2\,\mu_y\,a_{con}\,\mu_x + 1/4\,\mu_y\,a_{lat} \right) \theta_{lat,mr} \\
& + \left(1/16\,\frac{\mu_y\,{}^{mr}\omega_{x_{mr}}}{\Omega} + 1/2\,\frac{{\mu_x}^2\,a_{con}\,e}{R} + 3/8\,\frac{\mu_x\,a_{lat}\,e^2}{R^2} - 1/6\,a_{con} - 1/16\,\frac{\mu_y\,e^{2mr}\omega_{x_{mr}}}{\Omega\,R^2} + 1/8\,\frac{\mu_x\,a_{lat}\,e}{R} + 1/16\,\frac{\mu_x\,\dot{a}_{lon}\,e^2}{\Omega\,R^2} \right. \\
& \left. + 1/8\,\frac{\mu_y\,a_{lon}\,e^2}{R^2} + 1/16\,\frac{\mu_x\,\dot{a}_{lon}}{\Omega} + 1/16\,\frac{\mu_y\,\dot{a}_{lat}}{\Omega} - 1/16\,\frac{\mu_x\,e^{2mr}\omega_{y_{mr}}}{\Omega\,R^2} \right) \theta_{lon,mr} \\
& + \left(1/16\,\frac{\mu_y\,\dot{a}_{lat}\,e^2}{\Omega\,R^2} - 1/8\,\frac{\mu_y\,\dot{a}_{lat}\,e}{\Omega\,R} - 1/8\,\frac{\mu_x\,\dot{a}_{lon}\,e}{\Omega\,R} + 1/16\,\frac{\mu_x\,{}^{mr}\omega_{y_{mr}}}{\Omega} - 1/2\,{\mu_x}^2\,a_{con} - 1/2\,\mu_x\,a_{lat} - 1/8\,\frac{\mu_y\,a_{lon}\,e}{R} \right) \theta_{lon,mr} \\
& + \left(1/2\,\mu_x\,a_{con} - 1/6\,\frac{a_{lat}\,e}{R} - 1/4\,\frac{\mu_y\,e^2\lambda}{R^2} - 1/4\,\frac{e^2{\mu_x}^2 a_{lat}}{R^2} + 1/4\,{\mu_x}^2 a_{lat} + 1/4\,a_{lat} + 1/4\,\frac{\mu_y\,\dot{a}_{con}\,e}{\Omega\,R} - 1/6\,\frac{\mu_y\,\dot{a}_{con}}{\Omega} \right. \\
& \left. + 1/4\,\mu_y\,\lambda + 1/4\,\mu_y\,a_{lon}\,\mu_x - 1/8\,\frac{{}^{mr}\omega_{y_{mr}}}{\Omega} - 1/4\,\frac{\mu_y\,a_{lon}\,e^2\mu_x}{R^2} - 1/8\,\frac{\dot{a}_{lon}}{\Omega} + 1/6\,\frac{\dot{a}_{lon}\,e}{\Omega\,R} \right) \theta_t \\
& + \left(-1/6\,\frac{a_{con}}{\Omega} + 1/16\,\frac{\mu_y\,a_{lon}}{\Omega} - \frac{5}{16}\,\frac{\mu_x\,a_{lat}}{\Omega} - 1/16\,\frac{\mu_y\,a_{lon}\,e^2}{\Omega\,R^2} + \frac{5}{16}\,\frac{\mu_x\,a_{lat}\,e^2}{\Omega\,R^2} \right) {}^{h}\omega_{x_h} \\
& + \left(\frac{7}{16}\,\frac{\mu_x\,a_{lon}\,e^2}{\Omega\,R^2} + 1/2\,\frac{e^2\lambda}{\Omega\,R^2} - \frac{7}{16}\,\frac{\mu_x\,a_{lon}}{\Omega} + 1/16\,\frac{\mu_y\,a_{lat}}{\Omega} - 1/16\,\frac{\mu_y\,a_{lat}\,e^2}{\Omega\,R^2} - 1/2\,\frac{\lambda}{\Omega} - 1/2\,\frac{\dot{a}_{con}\,e}{\Omega^2\,R} + 1/3\,\frac{\dot{a}_{con}}{\Omega^2} \right) {}^{h}\omega_{y_h}
\end{aligned}
\tag{A.16}
$$

$$
\begin{aligned}
F_{y2} = {} & 3/2\,\lambda\,a_{con}\,\mu_x - 1/2\,\frac{\lambda\,\dot{a}_{lon}}{\Omega} + 1/3\,\frac{\dot{a}_{con}\,\dot{a}_{lon}}{\Omega^2} + 1/4\,\mu_x\,a_{lon}\,a_{lat} - 1/2\,\frac{\dot{a}_{con}\,a_{lat}}{\Omega} - 1/6\,\frac{\dot{a}_{lat}\,a_{con}}{\Omega} \\
& - 1/8\,\frac{\mu_y\,a_{lat}\,\dot{a}_{lon}\,e}{\Omega\,R} - \frac{5}{16}\,\frac{\dot{a}_{lat}\,\mu_x\,a_{lat}\,e^2}{\Omega\,R^2} - 1/6\,a_{lon}\,a_{con} - 1/4\,\frac{\mu_x\,a_{lon}\,a_{lat}\,e}{R} \\
& + 1/16\,\frac{\mu_y\,a_{lon}\,\dot{a}_{lat}\,e^2}{\Omega\,R^2} - 1/4\,\mu_y\,{a_{con}}^2 + 5/4\,\frac{\dot{a}_{con}\,a_{lat}\,e}{\Omega\,R} - \frac{\dot{a}_{con}\,\dot{a}_{lon}\,e}{\Omega^2 R} - 1/4\,\mu_y\,{a_{lat}}^2 + {\mu_x}^2 a_{con}\,a_{lon} \\
& + 1/16\,\frac{\mu_y\,a_{lon}\,\dot{a}_{lat}}{\Omega} - \frac{{\mu_x}^2 a_{con}\,a_{lon}\,e}{R} + \frac{\mu_y\,a_{con}\,\mu_x\,a_{lat}\,e}{R} + 1/8\,\frac{\mu_y\,{a_{lat}}^2 e^2}{R^2} - \frac{7}{16}\,\frac{\dot{a}_{lon}\,a_{lon}\,\mu_x\,e^2}{\Omega\,R^2} \\
& + \frac{7}{8}\,\frac{\dot{a}_{lon}\,a_{lon}\,\mu_x\,e}{\Omega\,R} + 5/8\,\frac{\dot{a}_{lat}\,\mu_x\,a_{lat}\,e}{\Omega\,R} + 1/16\,\frac{\mu_y\,a_{lat}\,\dot{a}_{lon}\,e^2}{\Omega\,R^2} - 1/2\,\frac{\lambda\,\dot{a}_{lon}\,e^2}{\Omega\,R^2} - \frac{\dot{a}_{con}\,a_{lat}\,e^2}{\Omega\,R^2} \\
& - 1/8\,\frac{\mu_y\,a_{lon}\,\dot{a}_{lat}\,e}{\Omega\,R} + 1/16\,\frac{\mu_y\,a_{lat}\,\dot{a}_{lon}}{\Omega} - \frac{5}{16}\,\frac{\dot{a}_{lat}\,\mu_x\,a_{lat}}{\Omega} + 1/4\,\frac{a_{lon}\,a_{con}\,e}{R} + 1/8\,\frac{\mu_y\,{a_{lat}}^2 e}{R} \\
& + \frac{\lambda\,\dot{a}_{lon}\,e}{\Omega\,R} + 1/4\,\frac{\dot{a}_{lat}\,a_{con}\,e}{\Omega\,R} + \frac{\dot{a}_{con}\,\dot{a}_{lon}\,e^2}{\Omega^2 R^2} + 3/2\,\frac{\dot{a}_{con}\,a_{con}\,\mu_x\,e}{\Omega\,R} - 3/4\,\frac{\dot{a}_{con}\,a_{con}\,\mu_x\,e^2}{\Omega\,R^2} - 3/2\,\frac{\lambda\,a_{con}\,\mu_x\,e}{R} \\
& - \frac{\lambda\,a_{lat}\,e}{R} - \mu_y\,a_{con}\,\mu_x\,a_{lat} - 1/8\,\frac{\mu_y\,{a_{lon}}^2 e}{R} + 1/8\,\frac{\mu_y\,{a_{lon}}^2 e^2}{R^2} - \frac{7}{16}\,\frac{\dot{a}_{lon}\,a_{lon}\,\mu_x}{\Omega} + 1/4\,\frac{\lambda\,a_{lat}\,e^2}{R^2} \\
& + 1/4\,\frac{\mu_y\,{a_{con}}^2 e^2}{R^2} + 3/4\,\lambda\,a_{lat} - 3/4\,\frac{\dot{a}_{con}\,a_{con}\,\mu_x}{\Omega}
\end{aligned}
\tag{A.17}
$$

The main rotor generated torques are shown in (A.18), (A.19), and (A.20).

$$\begin{aligned}\tau_x = &\left(1/2\rho C_l bc\Omega^2 R^4\right)\left(1/2\,\frac{e\,\mu_x}{R}\theta_{col} + \left(-1/4\,\frac{e^2\mu_y\,\mu_x}{R^2} + 1/4\,\frac{e\mu_y\,\mu_x}{R}\right)\theta_{lat,mr}\right.\\
&+\left(-1/8\,\frac{e{\mu_y}^2}{R} + 1/8\,\frac{e^2{\mu_y}^2}{R^2} - 1/6\,\frac{e}{R} - 3/8\,\frac{e{\mu_x}^2}{R} + 3/8\,\frac{e^2{\mu_x}^2}{R^2}\right)\theta_{lon,mr}\\
&+1/3\,\frac{e\theta_t\,\mu_x}{R} + \left(-1/2\,\frac{e^2\mu_x}{R^2} + 1/2\,\frac{e\mu_x}{R}\right)\lambda\\
&+\left(-1/4\,\frac{e\mu_x}{\Omega\,R} + 1/2\,\frac{e^2\mu_x}{\Omega\,R^2}\right)\dot{a}_{con} + \left(-1/6\,\frac{e}{\Omega\,R} + 1/4\,\frac{e^2}{\Omega\,R^2}\right)\dot{a}_{lat}\\
&+\left(1/4\,\frac{e^2}{R^2} - 1/8\,\frac{e{\mu_y}^2}{R} - 1/6\,\frac{e}{R} - 1/8\,\frac{e^2{\mu_x}^2}{R^2} + 1/8\,\frac{e{\mu_x}^2}{R} + 1/8\,\frac{e^2{\mu_y}^2}{R^2}\right)a_{lon}\\
&\left.+2\,\frac{K_b\,a_{lat}}{\rho\,C_l bc\Omega^2 R^4} - 1/4\,\frac{e\mu_y\,a_{con}}{R} + 1/4\,\frac{e^2\mu_x\,a_{lat}\,\mu_y}{R^2} - 1/6\,\frac{e^{mr}\omega_{x\,mr}}{\Omega\,R} - 1/4\,\frac{e\mu_x\,a_{lat}\,\mu_y}{R}\right)\end{aligned} \tag{A.18}$$

$$\begin{aligned}\tau_y = &\left(1/2\rho C_l bc\Omega^2 R^4\right)\left(1/2\,\frac{e\,\mu_y}{R}\theta_{col}\right.\\
&+\left(3/8\,\frac{e{\mu_y}^2}{R} + 1/6\,\frac{e}{R} + 1/8\,\frac{e{\mu_x}^2}{R} - 1/8\,\frac{e^2{\mu_x}^2}{R^2} - 3/8\,\frac{e^2{\mu_y}^2}{R^2}\right)\theta_{lat,mr}\\
&+\left(-1/4\,\frac{e\mu_x\,\mu_y}{R} + 1/4\,\frac{e^2\mu_x\,\mu_y}{R^2}\right)\theta_{lon,mr} + 1/3\,\frac{e\theta_t\,\mu_y}{R} + \left(1/2\,\frac{e\mu_y}{R} - 1/2\,\frac{e^2\mu_y}{R^2}\right)\lambda\\
&+\left(1/2\,\frac{e^2\mu_y}{\Omega\,R^2} - 1/4\,\frac{e\mu_y}{\Omega\,R}\right)\dot{a}_{con} + \left(1/4\,\frac{e\mu_x\,\mu_y}{R} + 2\,\frac{K_b}{\rho\,abc\Omega^2 R^4} - 1/4\,\frac{e^2\mu_x\,\mu_y}{R^2}\right)a_{lon}\\
&-1/6\,\frac{e\dot{a}_{lon}}{\Omega\,R} - 1/6\,\frac{e^{mr}\omega_{y\,mr}}{\Omega\,R} + 1/4\,\frac{e^2\dot{a}_{lon}}{\Omega\,R^2} + 1/6\,\frac{ea_{lat}}{R} + 1/4\,\frac{e\mu_x\,a_{con}}{R} + 1/8\,\frac{e^2{\mu_y}^2 a_{lat}}{R^2}\\
&\left.-1/4\,\frac{e^2 a_{lat}}{R^2} - 1/8\,\frac{e{\mu_y}^2 a_{lat}}{R} + 1/8\,\frac{e{\mu_x}^2 a_{lat}}{R} - 1/8\,\frac{e^2{\mu_x}^2 a_{lat}}{R^2}\right).\end{aligned} \tag{A.19}$$

$$\tau_z = \frac{1}{2}\rho C_l bcR^2(\Omega R)^2\left(\tau_{z1} + \tau_{z2}\right), \tag{A.20}$$

$$
\begin{aligned}
\tau_{z1} = &\left(-1/4\, a^{-1} - 1/4\, \frac{{\mu_x}^2}{a} + 1/4\, \frac{e^2 {\mu_x}^2}{a R^2} - 1/4\, \frac{{\mu_y}^2}{a} + 1/4\, \frac{e^2 {\mu_y}^2}{a R^2} \right) C_d \\
&+ \left(1/3\, \frac{\dot{a}_{con}\, e}{\Omega\, R} - 1/4\, \frac{\mu_y\, a_{lat}\, e}{R} + 1/4\, \frac{\mu_x\, \dot{a}_{lat}\, e}{\Omega\, R} + 1/4\, \frac{\mu_x\, a_{lon}\, e}{R} + 1/3\, \lambda + 1/4\, \frac{\mu_y\, \dot{a}_{lon}\, e}{\Omega\, R} \right. \\
&\left. - 1/4\, \frac{\dot{a}_{con}}{\Omega} - 1/6\, \frac{\mu_y\, \dot{a}_{lon}}{\Omega} - 1/6\, \frac{\mu_x\, \dot{a}_{lat}}{\Omega} - 1/6\, \frac{\mu_y\, {}^{mr}\omega_{y_{mr}}}{\Omega} - 1/6\, \frac{\mu_x\, {}^{mr}\omega_{x_{mr}}}{\Omega} \right) \theta_{col} \\
&+ \left(1/8\, \mu_x\, \mu_y\, a_{lon} - 1/8\, \frac{e^2 \mu_x\, \mu_y\, a_{lon}}{R^2} + 1/16\, {\mu_x}^2 a_{lat} + 1/6\, \mu_x\, a_{con} - 1/4\, \frac{e^2 \mu_y\, \lambda}{R^2} \right. \\
&- 1/6\, \frac{a_{lat}\, e}{R} - 1/6\, \frac{\mu_y\, \dot{a}_{con}}{\Omega} + 1/16\, \frac{e^2 {\mu_y}^2 a_{lat}}{R^2} + 1/4\, \mu_y\, \lambda + 1/8\, a_{lat} - 1/8\, \frac{{}^{mr}\omega_{y_{mr}}}{\Omega} \\
&\left. + 1/4\, \frac{\mu_y\, \dot{a}_{con}\, e}{\Omega\, R} - 1/16\, \frac{e^2 {\mu_x}^2 a_{lat}}{R^2} - 1/8\, \frac{\dot{a}_{lon}}{\Omega} + 1/6\, \frac{\dot{a}_{lon}\, e}{\Omega\, R} - 1/16\, {\mu_y}^2 a_{lat} \right) \theta_{lat,mr} \\
&+ \left(-1/4\, \mu_x\, \lambda - 1/6\, \frac{\dot{a}_{lat}\, e}{\Omega\, R} + 1/16\, {\mu_y}^2 a_{lon} + 1/8\, a_{lon} + 1/8\, \frac{{}^{mr}\omega_{x_{mr}}}{\Omega} - 1/16\, \frac{e^2 {\mu_y}^2 a_{lon}}{R^2} \right. \\
&- 1/8\, \frac{e^2 \mu_x\, \mu_y\, a_{lat}}{R^2} + 1/16\, \frac{e^2 {\mu_x}^2 a_{lon}}{R^2} + 1/8\, \mu_y\, \mu_x\, a_{lat} + 1/4\, \frac{e^2 \mu_x\, \lambda}{R^2} + 1/6\, \mu_y\, a_{con} + 1/8\, \frac{\dot{a}_{lat}}{\Omega} \\
&\left. - 1/6\, \frac{a_{lon}\, e}{R} - 1/4\, \frac{\mu_x\, \dot{a}_{con}\, e}{\Omega\, R} - 1/16\, {\mu_x}^2 a_{lon} + 1/6\, \frac{\mu_x\, \dot{a}_{con}}{\Omega} \right) \theta_{lon,mr} + \left(-1/2\, \frac{e^2}{R^2} + 1/2 \right) \lambda^2 \\
&+ \left(-1/2\, \frac{e^2 \mu_x\, a_{lon}}{R^2} + 1/2\, \frac{e^2 \mu_y\, a_{lat}}{R^2} + \frac{\dot{a}_{con}\, e}{\Omega\, R} + 1/2\, \mu_x\, a_{lon} - 2/3\, \frac{\dot{a}_{con}}{\Omega} - 1/2\, \mu_y\, a_{lat} \right) \lambda \\
&+ \left(-1/6\, \frac{\mu_y\, a_{lat}\, e}{R} - 1/8\, \frac{\mu_x\, {}^{mr}\omega_{x_{mr}}}{\Omega} - 1/5\, \frac{\dot{a}_{con}}{\Omega} + 1/6\, \frac{\mu_y\, \dot{a}_{lon}\, e}{\Omega\, R} - 1/8\, \frac{\mu_x\, \dot{a}_{lat}}{\Omega} + 1/4\, \lambda \right. \\
&\left. + 1/4\, \frac{\dot{a}_{con}\, e}{\Omega\, R} - 1/8\, \frac{\mu_y\, \dot{a}_{lon}}{\Omega} + 1/6\, \frac{\mu_x\, a_{lon}\, e}{R} + 1/6\, \frac{\mu_x\, \dot{a}_{lat}\, e}{\Omega\, R} - 1/8\, \frac{\mu_y\, {}^{mr}\omega_{y_{mr}}}{\Omega} \right) \theta_t \\
&+ \left(1/3\, \frac{\mu_y\, a_{con}}{\Omega} + 1/4\, \frac{a_{lon}}{\Omega} - 1/3\, \frac{\dot{a}_{lat}\, e}{\Omega^2 R} - 1/3\, \frac{a_{lon}\, e}{\Omega\, R} + 1/4\, \frac{\dot{a}_{lat}}{\Omega^2} \right) {}^{mr}\omega_{x_{mr}} \\
&+ \left(1/3\, \frac{a_{lat}\, e}{\Omega\, R} + 1/4\, \frac{\dot{a}_{lon}}{\Omega^2} - 1/3\, \frac{\mu_x\, a_{con}}{\Omega} - 1/3\, \frac{\dot{a}_{lon}\, e}{\Omega^2 R} - 1/4\, \frac{a_{lat}}{\Omega} \right) {}^{mr}\omega_{y_{mr}}\,, \qquad \text{(A.21)}
\end{aligned}
$$

$$
\begin{aligned}
\tau_{z2} = & -1/4\,\frac{\dot{a}_{lon}\,a_{lat}}{\Omega} - 1/3\,\frac{{a_{lon}}^2 e}{R} + 1/4\,\frac{{a_{lon}}^2 e^2}{R^2} + 1/3\,\mu_x\,a_{con}\,a_{lat} + 1/3\,\mu_y\,a_{con}\,a_{lon} \\
& + 3/16\,{\mu_x}^2 {a_{lon}}^2 + 1/4\,{\mu_x}^2 {a_{con}}^2 + 1/8\,{a_{lat}}^2 + 1/4\,{\mu_y}^2 {a_{con}}^2 - 1/2\,\frac{\dot{a}_{con}\,\mu_y\,a_{lat}\,e}{\Omega\,R} + 3/16\,{\mu_y}^2 {a_{lat}}^2 \\
& + 1/4\,\frac{{a_{lat}}^2 e^2}{R^2} + 1/4\,\frac{\dot{a}_{lat}\,a_{lon}}{\Omega} - 1/3\,\frac{{a_{lat}}^2 e}{R} - 1/2\,\frac{\mu_x\,a_{con}\,a_{lat}\,e}{R} - 2/3\,\frac{\dot{a}_{lat}\,a_{lon}\,e}{\Omega\,R} \\
& + 1/2\,\frac{\dot{a}_{lat}\,a_{lon}\,e^2}{\Omega\,R^2} + 1/2\,\frac{\dot{a}_{lon}\,\mu_x\,a_{con}\,e}{\Omega\,R} + 1/4\,\frac{e^2 \mu_x\,a_{lon}\,\mu_y\,a_{lat}}{R^2} + 1/4\,\frac{\dot{a}_{lat}^2 e^2}{\Omega^2 R^2} \\
& - 1/3\,\frac{\dot{a}_{lat}^2 e}{\Omega^2 R} + 1/3\,\frac{\dot{a}_{lat}\,\mu_y\,a_{con}}{\Omega} + 1/3\,\frac{\dot{a}_{con}\,\mu_y\,a_{lat}}{\Omega} - 1/4\,\frac{e^2 {\mu_x}^2 {a_{con}}^2}{R^2} + 2/3\,\frac{\dot{a}_{lon}\,a_{lat}\,e}{\Omega\,R} \\
& - 1/2\,\frac{\dot{a}_{lon}\,a_{lat}\,e^2}{\Omega\,R^2} + 1/8\,{a_{lon}}^2 + 1/8\,\frac{{}^{mr}\omega_{y_{mr}}{}^2}{\Omega^2} - 1/2\,\frac{\mu_y\,a_{con}\,a_{lon}\,e}{R} + 1/2\,\frac{\dot{a}_{con}\,\mu_x\,a_{lon}\,e}{\Omega\,R} \\
& - 1/2\,\frac{\dot{a}_{lat}\,\mu_y\,a_{con}\,e}{\Omega\,R} + 1/4\,\frac{\dot{a}_{con}^2}{\Omega^2} + 1/16\,{\mu_y}^2 {a_{lon}}^2 + 1/16\,{\mu_x}^2 {a_{lat}}^2 + 1/8\,\frac{{}^{mr}\omega_{x\,mr}{}^2}{\Omega^2} + 1/8\,\frac{\dot{a}_{lat}^2}{\Omega^2} \\
& + 1/8\,\frac{\dot{a}_{lon}^2}{\Omega^2} - 2/3\,\frac{\dot{a}_{con}^2 e}{\Omega^2 R} - 3/16\,\frac{e^2 {\mu_x}^2 {a_{lon}}^2}{R^2} - 1/3\,\frac{\dot{a}_{con}\,\mu_x\,a_{lon}}{\Omega} - 1/16\,\frac{e^2 {\mu_y}^2 {a_{lon}}^2}{R^2} \\
& - 1/4\,\frac{e^2 {\mu_y}^2 {a_{con}}^2}{R^2} - 1/3\,\frac{\dot{a}_{lon}\,\mu_x\,a_{con}}{\Omega} - 3/16\,\frac{e^2 {\mu_y}^2 {a_{lat}}^2}{R^2} + 1/4\,\frac{\dot{a}_{lon}^2 e^2}{\Omega^2 R^2} \\
& - 1/3\,\frac{\dot{a}_{lon}^2 e}{\Omega^2 R} + 1/2\,\frac{\dot{a}_{con}^2 e^2}{\Omega^2 R^2} - 1/16\,\frac{e^2 {\mu_x}^2 {a_{lat}}^2}{R^2} - 1/4\,\mu_x\,a_{lon}\,\mu_y\,a_{lat}\,. \qquad \text{(A.22)}
\end{aligned}
$$

A.3 Stabilizer Bar Flapping Equation

The longitudinal and lateral stabilizer bar flapping equations are shown in (A.23) and (A.24).

$$
\begin{aligned}
\ddot{a}_{lon,sb} = & \,\Omega\,\gamma_{sb}\left(-1/8 + 1/8\,\frac{{R_i}^4}{{R_o}^4}\right)\dot{a}_{lon,sb} + 2\,\dot{a}_{lat,sb}\,\Omega + \Omega^2\gamma_{sb}\left(1/8\,\mu_x\,\mu_y - 1/8\,\frac{{R_i}^2 \mu_x\,\mu_y}{{R_o}^2}\right)a_{lon,sb} \\
& + \Omega^2\gamma_{sb}\left(1/16\,{\mu_x}^2 - 1/16\,\frac{{R_i}^2 {\mu_x}^2}{{R_o}^2} + 1/16\,\frac{{R_i}^2 {\mu_y}^2}{{R_o}^2} - 1/16\,{\mu_y}^2 + 1/8 - 1/8\,\frac{{R_i}^4}{{R_o}^4}\right)a_{lat,sb} \\
& + \Omega^2\gamma_{sb}\left(-1/8\,\frac{{R_i}^4}{{R_o}^4} + 1/8 - 3/16\,\frac{{R_i}^2 {\mu_y}^2}{{R_o}^2} + 3/16\,{\mu_y}^2 + 1/16\,{\mu_x}^2 - 1/16\,\frac{{R_i}^2 {\mu_x}^2}{{R_o}^2}\right)\theta_{lat} \\
& + \Omega^2\gamma_{sb}\left(1/8\,\frac{{R_i}^2 \mu_x\,\mu_y}{{R_o}^2} - 1/8\,\mu_x\,\mu_y\right)\theta_{lon} + \Omega^2\gamma_{sb}\left(-1/4\,\frac{{R_i}^2 \mu_y}{{R_o}^2} + 1/4\,\mu_y\right)\lambda \\
& - {}^{mr}\dot{\omega}_{y,m} + 1/8\,\frac{\gamma_{sb}\,\Omega\,{R_i}^4}{{R_o}^4}\,{}^{mr}\omega_{y_{mr}} - 1/8\,\gamma_{sb}\,\Omega\,{}^{mr}\omega_{y_{mr}} + 2\,\Omega\,{}^{mr}\omega_{x\,mr}\,. \qquad \text{(A.23)}
\end{aligned}
$$

$$
\begin{aligned}
\ddot{a}_{lat,st} = & -2\,\dot{a}_{lon,sb}\,\Omega + \Omega\,\gamma_{sb}\left(-1/8\ + 1/8\,\frac{{R_i}^4}{{R_o}^4}\right)\dot{a}_{lat,sb} + \Omega^2\gamma_{sb}\left(1/4\,\mu_x - 1/4\,\frac{{R_i}^2\mu_x}{{R_o}^2}\right)\lambda \\
& + \Omega^2\,\gamma_{sb}\left(-1/16\,\frac{{R_i}^2{\mu_x}^2}{{R_o}^2} + 1/16\,\frac{{R_i}^2{\mu_y}^2}{{R_o}^2} + 1/16\,{\mu_x}^2 - 1/16\,{\mu_y}^2 + 1/8\,\frac{{R_i}^4}{{R_o}^4} - 1/8\right)a_{lon,sb} \\
& + \Omega^2\gamma_{sb}\left(1/8\,\frac{{R_i}^2\mu_x\,\mu_y}{{R_o}^2} - 1/8\,\mu_x\,\mu_y\right)a_{lat} + \Omega^2\gamma_{sb}\left(1/8\,\mu_x\,\mu_y - 1/8\,\frac{{R_i}^2\mu_x\,\mu_y}{{R_o}^2}\right)\theta_{lat} \\
& + \Omega^2\gamma_{sb}\left(3/16\,\frac{{R_i}^2{\mu_x}^2}{{R_o}^2} - 1/16\,{\mu_y}^2 + 1/16\,\frac{{R_i}^2{\mu_y}^2}{{R_o}^2} - 1/8\ - 3/16\,{\mu_x}^2 + 1/8\,\frac{{R_i}^4}{{R_o}^4}\right)\theta_{lon} \\
& - {}^{mr}\dot{\omega}_{x,m} + 1/8\,\frac{\gamma_{sb}\,\Omega\,{R_i}^4}{{R_o}^4}\,{}^{mr}\omega_{x\,mr} - 1/8\,\gamma_{sb}\,\Omega\,{}^{mr}\omega_{x\,mr} - 2\,\Omega\,{}^{mr}\omega_{y_{mr}}\,. \qquad \text{(A.24)}
\end{aligned}
$$

A.4 Tail Rotor Force and Torque

The tail rotor force and torque are shown in (A.25) and (A.26).

$$
\begin{aligned}
F_{y_{tr}} = & \left(\frac{1}{2}\rho C_{l_{tr}} b_{tr} c_{tr} \Omega_{tr}^2 R_{tr}^4\right)\left(1/2\,\lambda_{tr} + \left(1/3 + 1/2\,{\mu_{x_{tr}}}^2 + 1/2\,{\mu_{z_{tr}}}^2\right)\theta_{tr}\right. \\
& \left. + 1/4\,\frac{{}^{tr}\omega_{z,t}\,\mu_{z_{tr}}}{\Omega_{tr}} + 1/4\,\frac{{}^{tr}\omega_{x,t}\,\mu_{x_{tr}}}{\Omega_{tr}}\right) \qquad \text{(A.25)} \\
\tau_{y_{tr}} = & \left(\frac{1}{2}\rho C_{l_{tr}} b_{tr} c_{tr} \Omega_{tr}^2 R_{tr}^4\right)\left(\left(\frac{-1}{4\,C_{l_{tr}}} - 1/4\,\frac{{\mu_{z_{tr}}}^2}{C_{l_{tr}}} - 1/4\,\frac{{\mu_{x_{tr}}}^2}{C_{l_{tr}}}\right)C_{d_{tr}} + 1/2\,{\lambda_{tr}}^2\right. \\
& \left. + \left(1/6\,\frac{\mu_{x_{tr}}\,{}^{tr}\omega_{x,t}}{\Omega_{tr}} + 1/3\,\lambda_{tr} + 1/6\,\frac{\mu_{z_{tr}}\,{}^{tr}\omega_{z_{tr}}}{\Omega_{tr}}\right)\theta_{tr} + 1/8\,\frac{{}^{tr}\omega_{z_{tr}}{}^2}{{\Omega_{tr}}^2} + 1/8\,\frac{{}^{tr}\omega_{x_{tr}}{}^2}{{\Omega_{tr}}^2}\right) \qquad \text{(A.26)}
\end{aligned}
$$

Appendix B

Model Parameters

The parameters for the model derived in chapter 3 and 4 are presented in this appendix. Parameters was determined in connection with the model verification in chapter 5.

B.1 Helicopter Parameters

The parameters the AAU Bergen Industrial Twin is shown in table B.1 to B.6.

Empennage Parameters			
Parameter	**Describtion**	**Value**	**Unit**
A_{tf}	Area of tail fin	0.015	[m^2]
A_{tp}	Area of tail plane	0.02	[m^2]
A_{fp}	Area of front plane	0.085	[m^2]
d_{tf}	Tail fin drag coefficient	1.0	[·]
d_{tp}	Tail plane drag coefficient	1.0	[·]
d_{fp}	Front plane drag coefficient	1.0	[·]
K_{tf}	Ratio of tail fin in tail rotor wake	0.95	[·]
A_{x_h}	Area of helicopter along x axis	0.05	[m^2]
A_{y_h}	Area of helicopter along y axis	0.185	[m^2]
A_{z_h}	Area of helicopter along z axis	0.05	[m^2]
d_{x_h}	Helicopter x axis drag coefficient	0.8	[·]
d_{y_h}	Helicopter y axis drag coefficient	0.8	[·]
d_{z_h}	Helicopter z axis drag coefficient	0.8	[·]

Table B.1: Empennage parameters

Main Rotor Parameters			
Parameter	**Describtion**	**Value**	**Unit**
b_{mr}	Number of main rotor blades	2	[·]
$C_{l\,mr}$	Main rotor blade lift curve slope	6.0	[·]
$C_{d\,mr}$	Main rotor blade drag coefficient	0.008	[·]
c_{mr}	Main rotor blade cord	0.088	[m]
R_{mr}	Main rotor radius	0.978	[m]
$M_{b\,mr}$	Main rotor blade first moment of mass	0.22	[kg m]
$I_{b\,mr}$	Main rotor blade moment of inertia	0.16	[kg m^2]
$K_{s\,mr}$	Main rotor blade spring constant	190	[N/rad]
e_{mr}	Main rotor hinge offset	0.05	[·]
$\theta_{t\,mr}$	Main rotor twist angle	-8.7	[^{o}]
K_B	Bell ratio	1.0	[·]
K_H	Hiller ratio	0.641	[·]
K_{st}	Stabilizer bar to main rotor pitch ratio	4.0	[·]
E_g	Engine to main rotor gear ratio	90/10	[·]

Table B.2: Main rotor parameters

Tail Rotor Parameters			
Parameter	**Describtion**	**Value**	**Unit**
b_{tr}	Number of tail rotor blades	2	[·]
$C_{l\,tr}$	Tail rotor blade lift curve slope	5.5	[·]
$C_{d\,tr}$	Tail rotor blade drag coefficient	0.005	[·]
c_{tr}	Tail rotor blade cord	0.035	[m]
R_{tr}	Tail rotor radius	0.17	[m]
E_t	Main rotor to tail rotor gear ratio	70/15	[·]

Table B.3: Tail rotor parameters

Stabilizer Bar Parameters			
Parameter	**Describtion**	**Value**	**Unit**
$C_{l\,sb}$	Stabilizer bar lift curve slope	1.4	[·]
c_{sb}	Stabilizer bar cord	0.055	[m]
R_o	Stabilizer bar outer radius	0.305	[m]
R_i	Stabilizer bar inner radius	0.215	[m]
$I_{b\,sb}$	Stabilizer bar moment of inertia	0.0015	[kg m^2]

Table B.4: Stabilizer bar parameters

Helicopter Physical Parameters			
Parameter	**Describtion**	**Value**	**Unit**
m_h	Helicopter mass (no fuel)	14.0	[kg]
I_{hxx}	Helicopter moment of inertia x axis	0.35	[kg m^2]
I_{hyy}	Helicopter moment of inertia y axis	2.4	[kg m^2]
I_{hzz}	Helicopter moment of inertia z axis	2.2	[kg m^2]
I_{hxy}	Helicopter moment of inertia x-y	0.0	[kg m^2]
I_{hxz}	Helicopter moment of inertia x-z	0.3	[kg m^2]
I_{hyz}	Helicopter moment of inertia y-z	0.0	[kg m^2]
$\boldsymbol{\kappa}_{mr}$	Main rotor position wrt. CM	$\begin{bmatrix} 0.0 \\ 0.0 \\ 0.28 \end{bmatrix}$	[m]
$\boldsymbol{\kappa}_{tr}$	Tail rotor position wrt. CM	$\begin{bmatrix} -1.1 \\ 0.0 \\ -0.1 \end{bmatrix}$	[m]
$\boldsymbol{\kappa}_{tf}$	Tail fin position wrt. CM	$\begin{bmatrix} -1.09 \\ 0.0 \\ 0.0 \end{bmatrix}$	[m]
$\boldsymbol{\kappa}_{tp}$	Tail plane position wrt. CM	$\begin{bmatrix} -0.79 \\ 0.0 \\ 0.0 \end{bmatrix}$	[m]
$\boldsymbol{\kappa}_{fp}$	Front plane position wrt. CM	$\begin{bmatrix} 0.2 \\ 0.0 \\ 0.0 \end{bmatrix}$	[m]

Table B.5: Physical parameters

Helicopter Suspension System Parameters			
Parameter	**Describtion**	**Value**	**Unit**
$\boldsymbol{R}_{ha1}$	Dual wire attachment point vector 1	$\begin{bmatrix} 0.2 \\ 0.0 \\ 0.09 \end{bmatrix}$	[m]
$\boldsymbol{R}_{ha2}$	Dual wire attachment point vector 2	$\begin{bmatrix} -0.2 \\ 0.0 \\ 0.09 \end{bmatrix}$	[m]
$\boldsymbol{R}_{ha}$	Single wire attachment point vector	$\begin{bmatrix} 0.0 \\ 0.0 \\ 0.18 \end{bmatrix}$	[m]

Table B.6: Suspension system parameters

B.2 Slung Load Parameters

The parameters for the two slung load used together with the AAU Bergen Industrial Twin is shown in table B.7 and B.8. The first slung load is the bucket used for single wire suspension flights and the second is the box used for multi wire suspension flights.

Single Wire Slung Load Parameters			
Parameter	**Describtion**	**Value**	**Unit**
m_l	Load mass	0.95	[kg]
$I_{l_{xx}}$	Load moment of inertia x axis	0.05	[kg m^2]
$I_{l_{yy}}$	Load moment of inertia y axis	0.05	[kg m^2]
$I_{l_{zz}}$	Load moment of inertia z axis	0.01	[kg m^2]
$I_{l_{xy}}$	Load moment of inertia x-y	0.0	[kg m^2]
$I_{l_{xz}}$	Load moment of inertia x-z	0.0	[kg m^2]
$I_{l_{yz}}$	Load moment of inertia y-z	0.0	[kg m^2]
$\boldsymbol{R}_{la}$	Attachment point vector	$\begin{bmatrix} 0.0 \\ 0.0 \\ -0.35 \end{bmatrix}$	[m]
$\boldsymbol{R}_{lm}$	Marker vector	$\begin{bmatrix} 0.0 \\ 0.0 \\ -0.20 \end{bmatrix}$	[m]
A_{xl}	Area of load along x axis	0.16	[m^2]
A_{yl}	Area of load along y axis	0.16	[m^2]
A_{zl}	Area of load along z axis	0.1	[m^2]
d_{xl}	Load x axis drag coefficient	0.4	[$\cdot$]
d_{yl}	Load y axis drag coefficient	0.4	[$\cdot$]
d_{zl}	Load z axis drag coefficient	0.8	[$\cdot$]

Table B.7: Single wire slung load

Dual Wire Slung Load Parameters			
Parameter	**Describtion**	**Value**	**Unit**
m_l	Load mass	2.2	[kg]
$I_{l_{xx}}$	Load moment of inertia x axis	0.03	[kg m^2]
$I_{l_{yy}}$	Load moment of inertia y axis	0.11	[kg m^2]
$I_{l_{zz}}$	Load moment of inertia z axis	0.11	[kg m^2]
$I_{l_{xy}}$	Load moment of inertia x-y	0.0	[kg m^2]
$I_{l_{xz}}$	Load moment of inertia x-z	0.0	[kg m^2]
$I_{l_{yz}}$	Load moment of inertia y-z	0.0	[kg m^2]
$\boldsymbol{R}_{la1}$	Attachment point vector 1	$\begin{bmatrix} 0.2 \\ 0.0 \\ -0.45 \end{bmatrix}$	[m]
$\boldsymbol{R}_{la2}$	Attachment point vector 2	$\begin{bmatrix} -0.2 \\ 0.0 \\ -0.45 \end{bmatrix}$	[m]
$\boldsymbol{R}_{lm}$	Marker vector	$\begin{bmatrix} -0.2 \\ 0.0 \\ -0.24 \end{bmatrix}$	[m]
A_{xl}	Area of load along x axis	0.03	[m^2]
A_{yl}	Area of load along y axis	0.15	[m^2]
A_{zl}	Area of load along z axis	0.15	[m^2]
d_{xl}	Load x axis drag coefficient	0.8	[·]
d_{yl}	Load y axis drag coefficient	0.8	[·]
d_{zl}	Load z axis drag coefficient	0.8	[·]

Table B.8: Dual wire slung load

Bibliography

[ADS-33E-PRF, 2000] ADS-33E-PRF. *Aeronautical Design Standard, Performance Specification, Handling Qualities Requirements for Military Rotorcraft*. United States Army Aviation and Missile Command, Aviation Engineering Directorate, 2000.

[Ascher *et al.*, 1994] Uri M. Ascher, Hongsheng Chin, Linda R. Petzold, and Sebastian Reich. *Stabilization of constrained mechanical systems with DAEs and invariant manifolds*. Numerische Mathematik, 1994.

[Baerveldt and Klang, 1997] Albert-Jan Baerveldt and Robert Klang. *A Low-cost and Low-weight Attitude Estimation System for an Autonomous Helicopter*. IEEE International Conference on Inteligent Engineering Systmes, pp. 391-395, 1997.

[Banerjee *et al.*, 2001] A. Banerjee, N. Pedreiro, and W. Singhose. *Vibration Reduction for Flexible Spacecraft Following Momentum Dumping with/without Slewing*. American Control Conference, 2001.

[Baumgarte, 1972] J. Baumgarte. *Stabilization of Constraints and Integrals of Motion in Dynamical Systems*. Computer Methods in Applied Mechanics, Vol 1, pp 1-16, 1972.

[Bhat and Miu, 1991] S. P. Bhat and D. K. Miu. *Solutions to Point-to-Point Control Problems Using Laplace Transform Technique*. Journal of Dynamic Systems, Measurement, and Control, 1991.

[Bisgaard *et al.*, 2005] Morten Bisgaard, Dennis Vinther, Kasper Østergaard, Jan Bendtsen, and Roozbeh Izadi-Zamanabadi. *Sensor Fusion and Model Verification for a Mobile Robot*. 16th IASTED International Conference on Modelling and Simulation, 2005.

[Bisgaard *et al.*, 2006] Morten Bisgaard, Jan Dimon Bendtsen, and Anders la Cour-Harbo. *Modelling of a Generic Slung Load System*. AIAA Modeling and Simulation Technologies Conference and Exhibit, 2006.

[Bisgaard *et al.*, 2007a] Morten Bisgaard, Jan Dimon Bendtsen, and Anders la Cour-Harbo. *Modelling of a Generic Slung Load System*. Journal of Guidance, Control, and Dynamics, 2007. Submitted.

[Bisgaard *et al.*, 2007b] Morten Bisgaard, Anders la Cour-Harbo, and Jan Dimon Bendtsen. *Full State Estimation for Helicopter Slung Load System*. AIAA Guidance, Navigation and Control Conference, 2007.

[Bisgaard *et al.*, 2007c] Morten Bisgaard, Anders la Cour-Harbo, Eric N. Johnson, and Jan Dimon Bendtsen. *Vision Aided State Estimator for Helicopter Slung Load System*. 17th IFAC Symposium On Automatic Control In Aerospace, 2007.

[Bogdanov *et al.*, 2004] A. Bogdanov, E. Wan, and G. Harvey. *SDRE Flight Control for X-Cell and R-Max Autonomous Helicopters*. The 43rd IEEE Conference on Decision and Control, 2004.

[Bramwell, 1976] A. R. S. Bramwell. *Helicopter Dynamics*. Edward Arnold Ltd, 1976.

[Chen, 1979] Robert T. N. Chen. *A Simplified Rotor System Mathematical Model for Piloted Flight Dynamics Simulation*. Nasa, 1979.

[Chen, 1980] Robert T. N. Chen. *Effects of Primary Rotors Parameters on Flapping Dynamics*. Nasa, 1980.

[Chen, 1990] Robert T. N. Chen. *A Survey of Non-Uniform Inflow Models For Rotorcraft Flight Dynamics and Control Applications*. Vertica, Vol. 14, pp 147-184, 1990.

[Cicolani and Kanning, 1992] Luigi S. Cicolani and Gerd Kanning. *Equations of Motion of Slung-Load Systems, Including Multilift Systems*. NASA, 1992. NASA-TP-3280.

[Cicolani *et al.*, 1995] Luigi S. Cicolani, Gerd Kanning, and Robert Synnestvedt. *Simulation of the Dynamics of Helicopter Slung Load Systems*. Journal of the American Helicopter Society, Vol. 40, pp 44-61, 1995.

[Civita, 2002] Marco La Civita. *Integrated Modeling and Robust Control for Full-Envelope Flight of Robotic Helicopters*. Carnegie Mellon University, 2002. PhD Thesis.

[Clien and Pai, 2003] Michael B. Clien and Dinesh K. Pai. *Post-Stabilization for Rigid Body Simulation with Contact and Constraints*. In Proceedings of the IEEE International Conference on Robotics and Automation, 2003.

[Cowling *et al.*, 2006] Ian D. Cowling, James F. Whidborne, and Alastair K. Cooke. *Optimal Trajectory Planning and LQR Control for a Quadrotor UAV*. International Conference on Control, 2006.

[Dukes, 1973a] Theodor A. Dukes. *Maneuvering Heavy Sling Loads Near Hover Part I: Damping the Pendulous Motion*. Journal of the American Helicopter Society, Vol. 18, No. 2, pp. 2-11, 1973.

[Dukes, 1973b] Theodor A. Dukes. *Maneuvering Heavy Sling Loads Near Hover Part II: Some Elementary Maneuvers*. Journal of the American Helicopter Society, Vol. 18, No. 3, pp. 2-11, 1973.

[Elmali *et al.*, 2000] Hakan Elmali, Mark Renzulli, and Nejat Olgac. *Experimantal Comparision of Delayed Resonator and PD Controlled Vibration Absorbers Using Electromagnetic Actuators*. Journal of Dynamic Systems, Measurement, and Control, Vol. 122, No. 3, pp. 514-520, 2000.

[Emilio Frazzoli, 2000] Eric Feron Emilio Frazzoli, Munther A. Dahleh. *Real-Time Motion Planning For Agile Autonomous Vehicles*. AIAA Conference on Guidance, Navigation and Control, 2000.

[Faille and Weiden, 1995] D. Faille and A. J. J. var der Weiden. *Robust regulation of a flying crane*. The 4th IEEE Conference on Control Applications, 1995.

[Fester *et al.*, 1977] L. Fester, C. Poli, and R. Krichhoff. *Dynamics of a Slung Load*. Journal of Aircraft, Vol 12, pp. 115-121, 1977.

[Fusato *et al.*, 2002] Dario Fusato, Giorgio Guglieri, and Roberto Celi. *Flight Dynamics of an Articulated Rotor Helicopter with an External Slung Load*. Journal of the American Helicopter Society, Vol 39, No 4, pp 577-586, 2002.

[Gauss, 1829] Karl Friedrich Gauss. *Uber ein neues allgemeines Grundgesatz der Mechanik*. Journal fr die Reine und Angewandte Mathematik, 4, pp. 232-235, 1829.

[Gavrilets *et al.*, 2001a] V. Gavrilets, B. Mettler, and E. Feron. *Nonlinear Model for a Small-Size Acrobatic Helicopter*. AIAA Guidance, Navigation, and Control Conference and Exhibit, 2001.

[Gavrilets *et al.*, 2001b] V. Gavrilets, A. Shterenberg, M. A. Dahleh, and E. Feron. *Avionics System For A Small Unmanned Helicopter Performing Agressive Maneuvers*. IEEE Aerospace and Electronic Systems Magazine, 2001.

[Gavrilets *et al.*, 2002] V. Gavrilets, I. Martinos, B. Mettler, and E. Feron. *Control Logic for Automated Aerobatic Flight of a Miniature Helicopter Monterey, California*. AIAA Guidance, Navigation, and Control Conference and Exhibit, 2002.

[Gieck and Gieck, 2006] Kurt Gieck and Reiner Gieck. *Engineering Formulas, 8'th Edition*. McGraw-Hill, 2006.

[Glauert, 1930] H. Glauert. *The Stability of a Body Towed by a Light Wire*. Great Britain Aeronautical research Committee, R & M 1312, 1930.

[Gros and Bruschini, 1996] Bertrand Gros and Claudio Bruschini. *Sensor Technologies for the Detection of Antipersonnel Mines, A Survay of Current Research and System Developments*. International Symposium on Measurement and Control in Robotics, 1996.

[Gupta and Bryson, 1976] Narendra K. Gupta and Arthur E. Bryson, Jr. *Near-Hover Control of a Helicopter with a Hanging Load*. Journal of Aircraft, Vol. 13, No. 3, pp. 217-222, 1976.

[H. C. Curtiss, 1988] Jr H. C. Curtiss. *Studies of the Dynamics of the Twin-Lift System*. NASA, 1988. NASA-CR-183273.

[Heffley and Mnich, 1988] Robert K. Heffley and Marc A. Mnich. *Minimum-Complexity Helicopter Simulation Math Model*. Nasa, 1988.

[Hillsley and Yurkovich, 1993] K.L. Hillsley and S. Yurkovich. *Vibration Control of a Two-Link Flexible Robot Arm*. Journal of Dynamics and Control, Vol. 3, No. 3, pp. 261-280, 1993.

[Hoh *et al.*, 2006] Roger H. Hoh, Robert K. Heffley, and David G. Mitchell. *Development of Handling Qualities Criteria for Rotorcraft with Externally Slung Loads*. NASA, 2006.

[Human Rights Watch, 2004] Human Rights Watch. *Landmine Monitor Report*. Landmine Monitor Core Group, 2004.

[Inanc *et al.*, 2004] Tamer Inanc, Kathy Misovec, and Richard M. Murray. *Nonlinear Trajectory Generation for Unmanned Air Vehicles with Multiple Radars*. Conference on Decision and Control, 2004.

[Jeon *et al.*, 2004] Hongjun Jeon, Min-Hyung Choi, and Min Hong. *Numerical Stability and Convergence Analysis of Geometric Constraint Enforcement in Dynamic Simulation Systems*. International Conference on Modeling, Simulation and Visualization Methods, 2004.

[Jiang *et al.*, 2006] Zhe Jiang, Jianda Han, Yuechao Wang, and Qi Song. *Enhanced LQR Control for Unmanned Helicopter in Hover*. 1st International Symposium on Systems and Control in Aerospace and Astronautics, 2006.

[Johnson and Kannan, 2005] Eric N. Johnson and Suresh K. Kannan. *Adaptive Trajectory Control for Autonomous Helicopters*. AIAA Journal of Guidance, Control, and Dynamics, Vol 28, No 3, 2005.

[Johnson, 1980] Wayne Johnson. *Helicopter Theory*. Dover Publications Inc, 1980.

[Jones, 1994] S. D. Jones. *Control Input Shaping for Coordinate Measuring Machines*. American Control Conference, 1994.

[Julier and Uhlmann, 1997a] Simon J. Julier and Jeffrey K. Uhlmann. *A Consistent, Debiased Method for Converting Between Polar and Cartesian Coordiante Systems*. In proceedings of AeroSense, the 11th International Symposium on Aerospace/Defense Sensing, Simulation and Control Conference, 1997.

[Julier and Uhlmann, 1997b] Simon J. Julier and Jeffrey K. Uhlmann. *A New Extension of the Kalman Filter to Nonlinear Systems*. University of Oxford, 1997.

[Julier, 2000] Simon J. Julier. *The Scaled Unscented Transformation*. In proceedings of the American Control Conference, 2000.

[Jun *et al.*, 1999] Myungsoo Jun, Stergios I. Roumeliotis, and Gaurav S. Sukhatme. *State Estimation of an Autonomous Helicopter Using Kalman Filtering*. International Conference on Intelligent Robots and Systems, 1999.

[Kim *et al.*, 1990] Frederick D. Kim, Roberto Celi, and Mark B. Tischler. *High-Order State Space Simulation Models of Helicopter Flight Mechanics*. 16th European Rotorcraft Forum, 1990.

[Kim *et al.*, 1993] Frederick D. Kim, Roberto Celi, and Mark B. Tischler. *Forward Flight Trim and Frequency Response Validation of a Helicopter Simulation Model*. Journal of Aircraft, Vol 30, No 6, pp 854-863, 1993.

[Koo and Sastry, 1998] T. John Koo and S. Sastry. *Output Tracking Control design of a Helicopter Model Based on Approximate Linearization*. The 37th IEEE Conference on Decision and Control, 1998.

[Lin, 2002] Shih-Tin Lin. *Stabilization of Baumgarte's Method Using the Runge-Kutta Approach*. Journal of Mechanical Design, Vol. 124, pp 633-641, 2002.

[Lucassen and Sterk, 1965] L. B. Lucassen and F. J. Sterk. *Dynamic Stability Analysis of a Hovering Helicopter with a Sling Load*. Journal of the American Helicopter Society, Vol. 10, pp 6-12, 1965.

[Luo *et al.*, 1993] Chi-Chung Luo, Chien-Chung Kung, Po-Wei Chang, Ciann-Dong Yang, and Yeong-Hwa Chang. *Linear Helicopter Model for Global Fligth Envelope Control*. Journal of C.C.I.T., Vol 32, No 1, 1993.

[Mächler, 1995] Philip Mächler. *Detection technologies for Anti-Personnel Mines*. Symposium on Autonomous Vehicles in Mine Countermeasures, 1995.

[Masoud and Nayfeh, 2003] Ziyad N. Masoud and Ali H. Nayfeh. *Sway Reduction on Container Cranes Using Delayed Feedback Controller*. Journal of Nonlinear Dynamics, Vol. 34, pp. 347-358, 2003.

[Masoud *et al.*, 2004] Ziyad N. Masoud, Mohammed F. Daqaq, and Ali H. Nayfeh. *Pendulation Reduction on Small Ship-Mounted Telescopic Cranes*. Journal of Vibration and Control, Vol. 10, pp. 1176-1179, 2004.

[Matsuoka *et al.*, 2005] Masa Matsuoka, Alan Chen Surya Singh, Adam Coates, Andrew Y. Ng, and Sebastian Thrun. *Autonomous Helicopter Tracking and Localization Using a Self-Calibrating Camera Array*. Proceedings of the Fifth International Conference on Field Service Robotics, 2005.

[McAslan, 2004] Alastair McAslan. *A Framework of International Mine Action Standards and Guidelines*. UNMAS, 2004.

[McLeana and Matsuda, 1998] D. McLeana and H. Matsuda. *Helicopter station-keeping: Comparing LQR, fuzzy-logic and neural-net controllers*. Engineering Applications of Articial Intelligence, Vol. 11, pp. 411-418, 1998.

[Mettler *et al.*, 1999] Bernard Mettler, Mark B. Tischler, and Takeo Kanade. *System Identification of Small-Size Unmanned Helicopter Dynamics*. Presented at the American Helicopter Society 55th Forum, 1999.

[Mettler *et al.*, 2002] Bernard Mettler, Mark B. Tischler, and Takeo Kanade. *System Identification Modeling of a Small-Scale Unmanned Rotorcraft for Flight Control Design*. Journal of the American Helicopter Society, Vol 47, pp 50-63, 2002.

[Micale and Poli, 1973] E. C. Micale and C. Poli. *Dynamics of Slung Bodies using a Rotating Wheel for Stability*. Journal of Aircraft, Vol. 10, pp 80-86, 1973.

[Miller *et al.*, 1997] Ryan Miller, Bernard Mettler, and Omead Amidi. *Carnegie Mellon University's 1997 International Aerial Robotics Entry*. Association for Unmanned Vehicle Systems International, 1997.

[Mittal *et al.*, 1991] M. Mittal, J.V.R. Prasad, and D.P. Schrage. *Nonlinear adaptive control of a twin lift helicopter system*. IEEE Control Systems Magazine, Vol. 11, No. 3, pp. 39-45, 1991.

[Moler, 2006] Cleve B. Moler. *Numerical Computing with Matlab*. Society for Industrial & Applied Mathematics, 2006.

[Musial *et al.*, 2004] Marek Musial, Carsten Deeg, Volker Remuss, and Günter Hommel. *Orientation Sensing for Helicopter UAVs under Strict Resource Constraints*. First European Micro Air Vehicle Conference, 2004.

[Nagabhushan, 1983] B. L. Nagabhushan. *Dynamical Stability of a Buoyant Quad-Rotor Aircraft*. Journal of Aircraft, Vol. 20, No. 3, pp 243-249, 1983.

[Ng *et al.*, 2004] Andrew Y. Ng, Adam Coates, Mark Diel, Varun Ganapathi, Jamie Schulte, Ben Tse, Eric Berger, and Eric Liang. *Inverted autonomous helicopter flight via reinforcement learning*. International Symposium on Experimental Robotics, 2004.

[Oh *et al.*, 2006] So-Ryeok Oh, Ji-Chul Ryu, and Sunil K. Agrawal. *Dynamics and Control of a Helicopter Carrying a Payload Using a Cable-Suspended Robot*. Journal of Mechanical Design, Vol. 128, Issue 5, pp. 1113-1121, 2006.

[Olgac and Holm-Hansen, 1994] N. Olgac and B. T. Holm-Hansen. *A Novel Active Vibration Absorption Technique: Delayed Resonator*. Journal of Sound and Vibration, Vol. 176, No. 1, pp. 93-104, 1994.

[Olgac *et al.*, 1996] N. Olgac, H. Elmali, and S. Vijayan. *Introduction to the Dual Frequency Fixed Delayed Resonator*. Journal of Sound and Vibration, Vol. 189, No. 3, pp. 355-367, 1996.

[Padfield, 1996] Gareth D. Padfield. *Helicopter Flight Dynamics: The Theory and Application of Flying Qualities and Simulation Modeling*. AIAA, 1996.

[Peters and Barwey, 1996] David A. Peters and Dinesh Barwey. *A General Theory of Rotorcraft Trim*. Mathematical Problems in Engineering, Vol 2, No 1,pp 1-34, 1996.

[Peters, 2005] Jan Peters. *About a Novel General Underlying Principle of Mechanics*. http://manet.usc.edu/˜jrpeters/uploads/Research/GaussEng.pdf, 2005.

[Pitt and Peters, 1981] Dale M. Pitt and David A. Peters. *Theoretical Prediction of Dynamic-Inflow Derivatives*. Vertica, Vol. 5, pp 21-34, 1981.

[Poli and Cromack, 1973] Corrado Poli and Duane Cromack. *Dynamics of Slung Bodies Using a Single-Point Suspension System*. Journal of Aircraft, Vol 10, pp. 80-86, 1973.

[Prabhakar, 1978] A. Prabhakar. *Stability of a Helicopter Carrying an Underslung Load*. Vertica, Vol. 2, pp 121-143, 1978.

[Prouty, 1989] Raymond W. Prouty. *Helicopter Performance, Stability and Control*. PWS Publishers, 1989.

[Rao and Mitra, 1972] C. Radhakrishna Rao and Sujit Kumar Mitra. *Generalized Inverse of Matrices and Its Applications*. John Wiley & Sons, Inc., 1972.

[Raz *et al.*, 1989] Reuben Raz, Aviv Rosen, and Tuvia Ronen. *Active Aerodynamic Stabilization of a Helicopter/Sling-Load System*. Journal of Aircraft, Vol. 26, No. 9, pp. 822-828, 1989.

[Reynolds and Rodriguez, 1992] H.K. Reynolds and A.A. Rodriguez. *$\mathcal{H}_\infty$ control of a twin lift helicopter system*. The 31st IEEE Conference on Decision and Control, 1992.

[Rock *et al.*, 1998] Stephen M. Rock, Eric W. Frew, Hank Jones, Edward A. LeMaster, and Bruce R. Woodley. *Combined CDGPS and Vision-Based Control of a Small Autonomous Helicopter*. Proceedings of the American Control Conference, pp. 694-698, 1998.

[Rodriguez and Athans, 1986] Armando A. Rodriguez and Michael Athans. *Multivariable control of a twin lift helicopter system using the LQG/LTR design methodology*. Laboratory for Information and Decision Systems, Massachusetts Institute of Technology, 1986.

[Ronen *et al.*, 1986] Tuvya Ronen, Arthur E. Bryson, and William S. Hindson. *Dynamics of a Helicopter with a Sling Load*. AIAA Atmospheric Flight Mechanics Conference, 1986. AIAA number 86-2288.

[Rubio *et al.*, 2004] Juan Carlos Rubio, Juris Vagners, and Rolf Rysdyk. *Adaptive Path Planning for Autonomous UAV Oceanic Search Missions*. AIAA 1st Intelligent Systems Technical Conferencen, 2004.

[Sampath, 1980] Prasad Sampath. *Dynamics of a Helicopter-Slung Load System*. Maryland University, 1980. PhD Thesis.

[Saripoalli *et al.*, 2003] Srikanth Saripoalli, Jonathan M. Roberts, Peter I. Corke, and Gregg Buskey. *A Tale of Two Helicopters*. Proceedings of IEEE/RSJ International Conference on Intelligent Robots and Systems, pp. 805-810, 2003.

[Schierman *et al.*, 2000] J. D. Schierman, D. G. Ward, J. F. Monaco, and J. R. Hull. *On-line identification and nonlinear control of rotorcraft/external-load systems*. AIAA Guidance, Navigation, and Control Conference and Exhibit, 2000.

[Sheldon, 1977] D. F. Sheldon. *An Appreciation of the Dynamic Problems Associated with the External Transportation of Loads from a Helicopter - State of the Art*. Vertica, Vol. 1, pp 281-290, 1977.

[Shim *et al.*, 1998] H. Shim, T. J. Koo, F. Hoffmann, and S. Sastry. *A Comprehensive Study of Control Design for an Autonomous Helicopter*. The 37th IEEE Conference on Decision and Control, 1998.

[Shim *et al.*, 2002] D. H. Shim, H. J. Kim, and S. Sastry. *Nonlinear Model Predictive Tracking Control for Rotorcraft-based Unmanned Aerial Vehicles*. American Control Conference, 2002.

[Shim *et al.*, 2003] David H. Shim, H. Jin Kim, and Shankar Sastry. *Decentralized Reflective Model Predictive Control of Multiple Flying Robots in Dynamic Environment*. Proceedings of the IEEE Conference on Decision and Control, 2003.

[Sigurd and How, 2003] K. Sigurd and J. How. *UAV Trajectory Design Using Total Field Collision Avoidance*. AIAA Conference on Guidance, Navigation and Control, 2003.

[Singer, 1983] Neil Cooper Singer. *Residual Vibration Reduction in Computer Controlled Machines*. Massachusetts Institute of Technology, 1983. PhD Thesis.

[Singh and Singhose, 2002] Tarunraj Singh and William Singhose. *Tutorial on Input Shaping/Time Delay Control of Maneuvering Flexible Structures*. American Control Conference, 2002.

[Singhose and Seering, 1991] W. Singhose and W. Seering. *Generating Vibration-Reducing Inputs with Vector Diagrams*. The 8th World Conference on the Theory of Machines and Mechanisms, 1991.

[Singhose *et al.*, 1994] William Singhose, Warren Seering, and Neil Singer. *Residual Vibration Reduction Using Vector Diagrams to Generate Shaped Inputs*. ASME Journal of Mechanical Design, Vol. 116, pp. 654-659, 1994.

[Singhose *et al.*, 1995] William Singhose, Neil Singer, and Warren Seering. *Comparison of Command Shaping Methods for Reducting Residual Vibration*. Proceedings of the European Control Conference, 1995.

[Singhose *et al.*, 1997] William E. Singhose, Arun K. Banerjee, and Warren P. Seering. *Slewing Flexible Spacecraft with Deflection-Limiting Input Shaping*. Journal of Guidance, Control, and Dynamics, Vol. 20, No. 2, pp. 291-298, 1997.

[Singhose, 1997] William E. Singhose. *Command Generation for Flexible Systems*. Massachusetts Institute of Technology, 1997. PhD Thesis.

[Smith, 1957] O. J. M. Smith. *Posicast Control of Damped Oscillatory Systems*. Proceedings of the IRE, Vol. 45, No. 9, pp. 1249-1255, 1957.

[Starr, 1985] G. P. Starr. *Swing-Free Transport of Suspended Objects With a Robot Manipulator*. Journal of Dynamic Systems, Measurement and Control, Vol. 107, pp. 97-100, 1985.

[Stephan, 2004] Christine Stephan. *The Landmine Action Smart Book*. Mine Action Information Center, 2004.

[Stuckey, 2002] R. A. Stuckey. *Mathematical Modelling of a Helicopter Slung-Load Systems*. Air Operations Division Aeronautical and Maritime Research Laboratory, 2002.

[Talbot *et al.*, 1982] P. D. Talbot, B. E. Tinling, W. A. Decker, and R. T. N. Chen. *A Mathematical Model of a Single Main Rotor Helicopter for Piloted Simulation*. Nasa, 1982.

[Udwadia and Kalaba, 1992] Firdaus E. Udwadia and Robert E. Kalaba. *A new perspective on constrained motion*. In Proceedings: Mathematical and Physical Sciences, Vol 439, Issue 1906, pp 407-410, 1992.

[Udwadia and Kalaba, 1995] Firdaus E. Udwadia and Robert E. Kalaba. *An Alernate Proof for the Equation of Motion for Constrained Mechanical Systems*. Applied Mathematics and Computation, Vol 70, pp 339-342, 1995.

[Udwadia and Phohomsiri, 2005] Firdaus E. Udwadia and Phailaung Phohomsiri. *Active Control of Structures using Time Delay Positive Feedback Proportional Control Designs*. Journal of Structural Control and Health Monitoring, Vol. 13, pp. 536-552, 2005.

[Udwadia, 1996] Firdaus E. Udwadia. *Equations of Motion for Mechanical Systems: A Unified Approach*. Internation Journal of Non-Lienar Mechaics, Vol 31, No. 6, pp 951-958, 1996.

[U.S. Department of Defense, 2001] U.S. Department of Defense. *Humanitarian Demining: Developmental Technologies 2000-2001*. Pentagon, 2001.
http://www.humanitarian-demining.org/demining/pubs/catalog/pdfs/catalog.pdf.

[van der Merwe *et al.*, 2004] R. van der Merwe, E. Wan, S. Julier, A. Bogdanov, G. Harvey, and J. Hunt. *Sigma-Point Kalman Filters for Nonlinear Estimation and Sensor Fusion: Applications to Integrated Navigation*. AIAA Guidance Navigation & Control Conference, 2004.

[Wan and Bogdanov, 2001] E. A. Wan and A. A. Bogdanov. *Model predictive neural control with applications to a 6 DoF helicopter model*. American Control Conference, 2001.

[Wan and van der Merwe, 2000] Eric A. Wan and Rudolph van der Merwe. *The Unscented Kalman Filter for Nonlienar Estimation*. Oregon Graduate Institute of Science and Technology, 2000.

[Whittaker, 1964] E. T. Whittaker. *A Treatise on the Analytical Dynamics of Particles and Rigid Bodies*. Cambridge University Press, 1964.